MECHANISMS OF MAGMA DISAGGREGATION IN A COOLER HOST:

VOLCANIC, PLUTONIC, AND THEORETICAL CONSIDERATIONS

By

Tenley Jill Banik

Thesis

Submitted to the Faculty of the

Graduate School of Vanderbilt University

in partial fulfillment of the requirements

for the degree of

MASTER OF SCIENCE

in

Earth and Environmental Sciences

August 8, 2008

Nashville, Tennessee

Approved:

Professor Calvin F. Miller

Professor David Jon Furbish

To my brother

ACKNOWLEDGEMENTS

TABLE OF CONTENTS

Page

Chapter

I.   INTRODUCTION

II.   METHODS

III.   A VOLCANIC EXAMPLE OF MAGMA-HOST INTERACTION: INJECTION
        AND DISAGGREGATION OF BASALTIC LAVA IN HYALOCLASTITE,
        SOUTH ICELAND

LIST OF TABLES

LIST OF FIGURES

LIST OF SYMBOLS and PRONUNCIATIONS

Symbol	Meaning	Units
μ	dynamic viscosity	Pa s
ρ	density	kg m^{-3}
T	temperature	°C
v	velocity	m s^{-1}
q	Darcy flux (specific discharge)	m^3 m^{-2} s^{-1}
h	hydraulic head	m
K	hydraulic conductivity	m s^{-1}
k	permeability	m^2
p	pressure	Pa (kg m^{-1} s^{-2})
g	acceleration due to gravity	m s^{-2}

Symbol	Pronunciation Guide

Due to the unfamiliarity of most readers with the Icelandic language, this list of Icelandic letters used in this manuscript is included to ease the difficulty in reading foreign words.

á	"ow", as in the "ou" in *house*
æ	Like the word *eye*
í	A long "e", as in *seen*
ó	A long "o", as in *boat*
ö	Like the "u" in *turn*
ú	A double "o", as in *soon*
Þ, þ	The letter Thorn, pronounced as a hard "th", as in *thorn* or *thing*
Ð, ð	The letter Edth, pronounced as a soft "th", as in *the* or *there*

CHAPTER I

INTRODUCTION

Background

The physical processes by which mafic magmas separate from parental sheets (either dikes, sills, or flows) in a cooler slurry host are poorly understood. Physical properties of these magmas and the material they intrude, such as temperature, dynamic viscosity, velocity, and density—all of which are likely to undergo rapid change during interaction—play critical roles in determining the rheologies of the materials; yet, no relationship between these factors has been proposed that can be applied to magmatic systems in a broad sense. This research has been motivated by a desire to determine: a) if such a relationship exists that can be applied to a range of magmatic processes; and b) if there are similarities in the responses of magmatic interaction with another material in two very different environments.

Terminology

Before proceeding, definitions of terms commonly used in this manuscript must be stated so that no reader is confused at the onset. Please note that the definitions given below have arisen from a combination of literary convention, colloquial usage within the author's research group, and personal taste. No disrespect to previous researchers was intended if their terminology was overlooked or modified; these are simply the author's preferred terms for the sake of continuity and avoiding personal confusion.

apophyses—vertically elongate structures that protrude from the upper surface of

lava flows into hyaloclastite; they resemble flame structures, although their

formation is not gravity-induced (after Smellie, 2008)

cube jointing—irregular jointing where the joint spacings are equidimensional,

usually small (20-30 cm), and irregularly curved; interpreted to be associated with

rapid cooling during contact with water (Bergh and Sigvaldason, 1991)

diamictite—sedimentary facies consisting of pebbly-to-cobbly mudstones, with

occasional boulders; many diamictites in Iceland are interpreted to be tillites, and

the two terms are often used interchangeably there (Bergh and Sigvaldason, 1991)

hyaloclastite—a coarse volcanic rock composed of angular glassy fragments that

formed from quenching of magma from a non-explosive eruption into water

(Batiza and White, 2000; Smellie, 2000)

jökulhlaup—a glacial outburst flood that commonly results from sub-ice volcanic

eruptions (Smellie, 2000)

quenching—the process of cooling magma rapidly to form a glass (Batiza and

White, 2000)

Purpose

This project addresses mechanisms by which mafic magma injects into or onto

and disaggregates in a cooler, liquid-bearing host (either wet sediments or felsic crystal-

bearing magma and mush) in two geologically distinct settings. By examining,

comparing, and contrasting the products of these interactions, I intend to establish a better

understanding of magma rheology under specific circumstances that can be extrapolated

for application to magmatic systems in general. Establishing a better understanding of the behavior of magma interacting with other materials in shallow crustal and surface settings has implications for eruption triggering and hazard mitigation (e.g. Pallister et al., 1992).

Geologic Settings

Field research for this study was conducted in the Siða-Fljotshverfi district of southern Iceland (Figure 1.1) and Aztec Wash pluton (AWP), Nevada (Figure 1.2).

In southern Iceland, Plio-Pleistocene strata are exposed in paleo-seacliffs along the main "Ring Road" for approximately 75 km (Bergh, 1985; Bergh and Sigvaldason, 1991; Smellie, 2008). Within these cliffs, basaltic lava intermingles with overlying massive hyaloclastite, resulting in structures ranging from dikes to flame-like apophyses to discrete pods on meters to 10s of m scale (Figure 1.3). For a more detailed description of the field area and its geologic history, please see Chapter III.

In Nevada, the 15.7 Ma Aztec Wash pluton (AWP) is exposed over an area of 50 km^2 in the Eldorado Mountains approximately 80 km south of Las Vegas in the Colorado River extensional corridor (CREC)(Falkner et al., 1995)(Figure 1.4). Post-emplacement tilting of the eastern portion by 50-90° ENE presents a continuous vertical cross-section of the 4-7 km-deep pluton (Patrick and Miller, 1997; Harper et al., 2004). AWP includes a smaller zone of homogeneous granite and a larger area of intermingling between mafic rocks and granite. Sheets and pillow-like structures (PLS) of mafic rock in a variably hybridized granitic host are widespread in this zone of mingling. For a more detailed description of the field area, please see Chapter V.
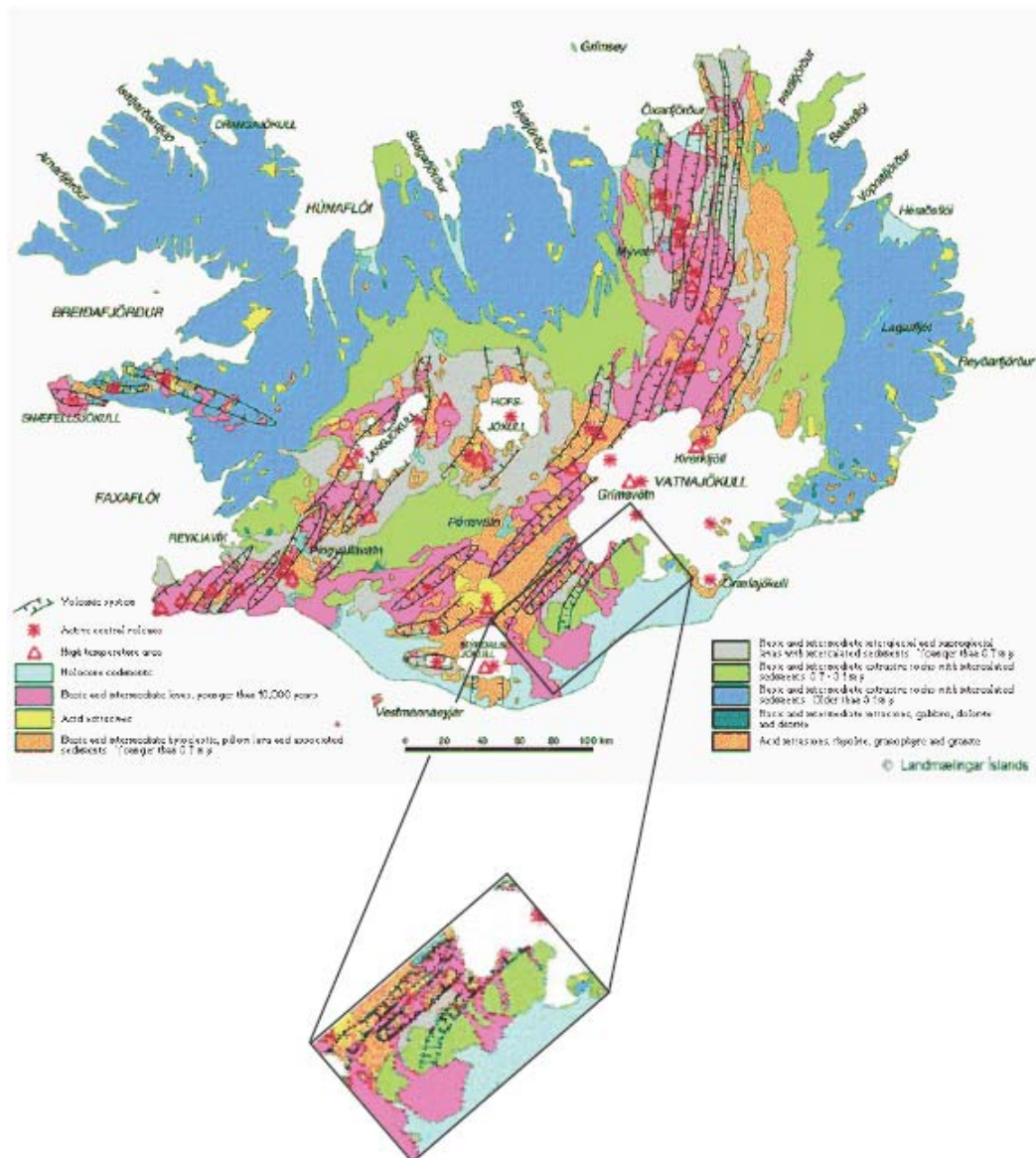
Figure 1.1: Geologic map of Iceland. Study area shown in inset and the Siða-Fljotshverfi deposits are in green.
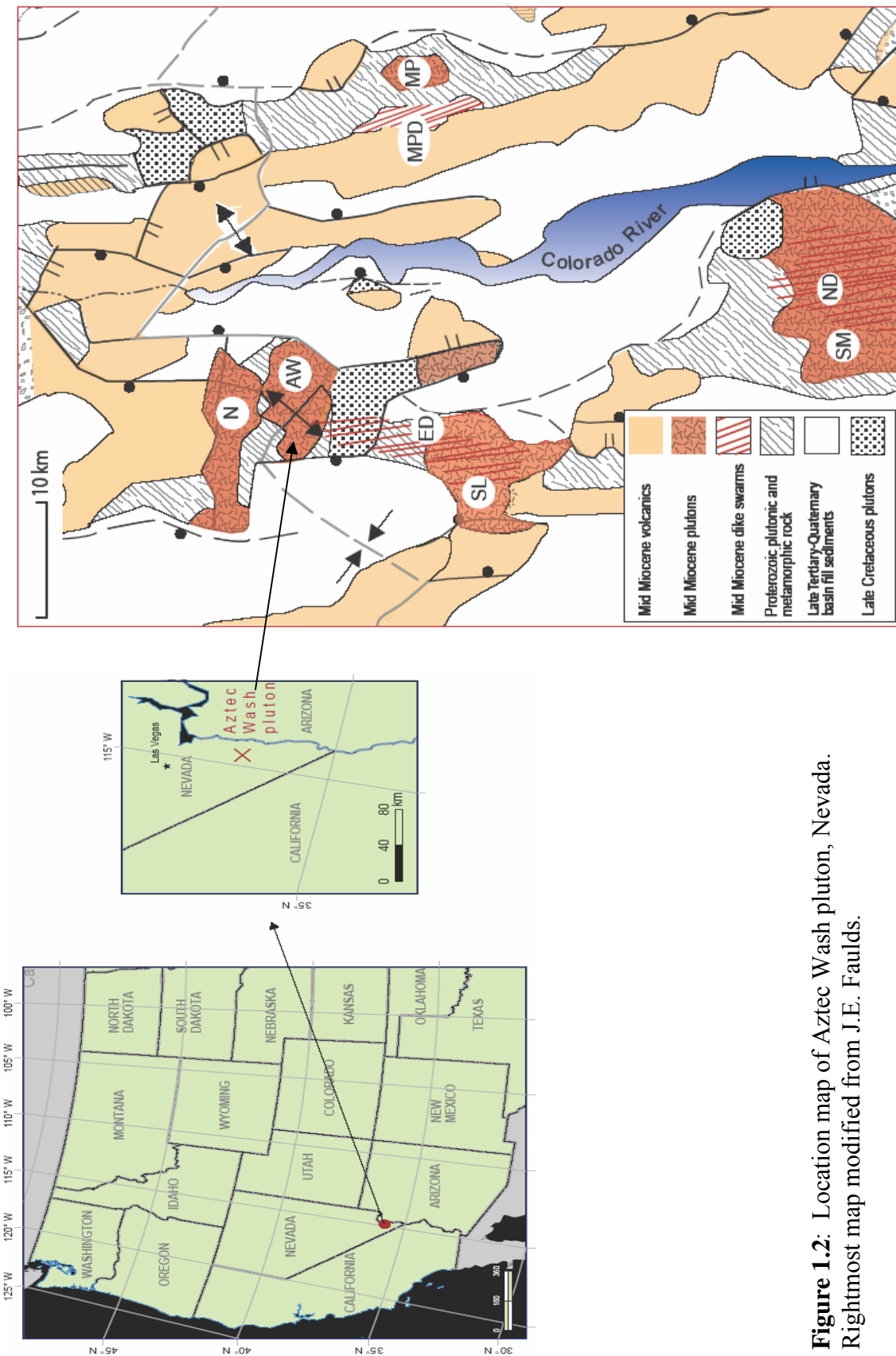
Figure 1.2: Location map of Aztec Wash pluton, Nevada. Rightmost map modified from J.E. Faulds.

Previous Work

This research builds on several studies carried out previously in both Iceland and AWP. Noe-Nygaard (1940) and Walker and Blake (1966) performed preliminary reconnaissance in south Iceland, interpreting geologic histories and general relationships of similar areas. Noe-Nygaard's pioneering work mapping and describing the general geological relationships between lava, hyaloclastite, and diamictite evident within the Siða-Fljotshverfi cliff faces exposed the complexity of this system, but he did not speculate on the formation of large basaltic flame and disaggregated basalt structures. Walker and Blake's (1966) study focused on a similar system farther east along the coast of southern Iceland, but was instrumental in describing not only relationships between lava, hyaloclastite, and diamictite, but also emplacement mechanisms relating to glacial origin and potential eruptive sources, lending key insight into the larger-scale processes defining the system, notably with regard to jökulhlaup transport and lava-ice interaction. Bergh and Sigvaldason (1991) conducted a detailed field-based investigation of the sequences exposed in cliff transects and identified what they termed a "standard depositional unit". Based on their transect maps and observations of lithologies and field relationships, they hypothesized submarine eruption and emplacement of these units. Bergh and Sigvaldason's field area is the setting for this study, and their contribution to the interpretation of the south Iceland basalt-hyaloclastite sequence is noteworthy. Although this study reaches very different conclusions, their work proved very useful. Most recently, Smellie (2008) reported on the subglacial origin of the Siða-Fljotshverfi district, suggesting that the sequences are not only the product of a sequence of subglacial eruptions, but that the entire emplacement process occurred subglacially.

In AWP, this study builds on previous research by C.F. Miller and his students. Falkner et al. (1995) first identified the occurrence of mafic PLS in the granites of the pluton. Patrick and Miller (1997) further described mafic-felsic interaction in the forms of load-cast structures, mafic sheets, and felsic pipes, and interpreted repeated injections of mafic material in AWP to be lava flows that spread atop crystal-rich mush at the floor of a felsic magma chamber (cf. Wiebe, 1994; Miller and Miller, 2002). This study seeks to build upon these existing interpretations by establishing a formation mechanism for mafic PLS within the pluton.

The findings of several workers were extremely useful in helping establish general ideas about disaggregation and magma-fluid interaction, particularly with regard to traditional pillow basalts and peperites. Moore's (1975) studies of pillow lava morphology and formation provide a basis for conceptualizing disaggregation processes and PLS formation. Although pillow formation in a submarine setting is unquestionably different than pillow formation within a crystal-rich host, similarities can be inferred between processes in the two settings. Moore's (1975) description of pillow lavas as interconnected flow lobes that are frequently elliptical or circular in cross-section, with isolated PLS occurring only rarely, was instrumental in evaluating PLS-forming processes in Aztec Wash pluton, as were his observations on the nature of the outermost pillow surfaces. Publications by Gass (1968) and Walker (1992) were also helpful. Work by White and Houghton (2006), Squire and McPhie (2002) and Skilling et al. (2002) on differentiating between hyaloclastite and peperite deposits was highly relevant to interpreting interactions in Iceland. Although by definition peperite—a rock produced by active mixing and mingling of molten lava and poorly consolidated, water-rich

sediments (Batiza and White, 2000)—sounds similar to the disaggregation products of lava-hyaloclastite in Iceland, there are fundamental differences, primarily with regard to water content and disaggregation forms produced. Although hyaloclastites are initially water-borne, they dewater quickly due to their high permeability, and are already coherent by the time lava disaggregation occurs (Cas and Wright, 1987; Stroncik and Schminke, 2001). This contrasts with peperite formation conditions, in which the sediment is frequently described as "fluidised" (Skilling et al., 2002).

In addition, work by Sparks and Sigurdsson (1977), Sparks and Marshall (1986), Hawkins and Wiebe (2004), Wiebe (1996), Whitehead (1988), and Whitehead and Luther (1975) were critical to understanding mafic-felsic interaction and general fluid mechanics in magmatic systems.

Figure 1.3: Field photograph of cliffs exposed at Þverárnúpur.

Figure 1.4: Field photograph of mafic PLS within a granite host at AWP.

CHAPTER II

METHODS

Field Observations and Measurements

In both Iceland and Nevada, field observations were critical to understanding the

interaction of mafic magma with a cooler, liquid-bearing host. In Iceland, the majority of

field observations were carried out in May 2007, with additional observations taken

during a long weekend in October 2007. Observation strategy consisted of taking

measurements of features relevant to lava-hyaloclastite interactions at and near 23

individual basalt flame injections in varying locations within the cliff exposure

(Lómagnúpur, Eystrikinnar, Keldunúpur, Rauða Canyon, Þverárnúpur, Kotafjoll, and

Djúpa River) (Figures 2.1, 2.2; Pocket map); identifying depositional units and

comparing cliff transects with those identified by Bergh (1985) and Bergh and

Sigvaldason (1991); locating and characterizing instances of isolated, disaggregated

basaltic pods in the hyaloclastite; and noting specific characteristics of the lava and

hyaloclastite units regarding vesiculation, quenching, and rock fabric. Measurements

were taken using a hand-held laser distance sensor.

At Aztec Wash pluton, field observations were carried out in 5 locations (Figure

5.1), with emphasis on describing mafic-felsic contacts, orientation of pillow-like

structures in the area, and orientation of the parental mafic magma sheet. Measurements

of PLS orientations and dimensions were obtained using a tape measure and compass

(Figure 2.3), and are displayed in Table 5.2.
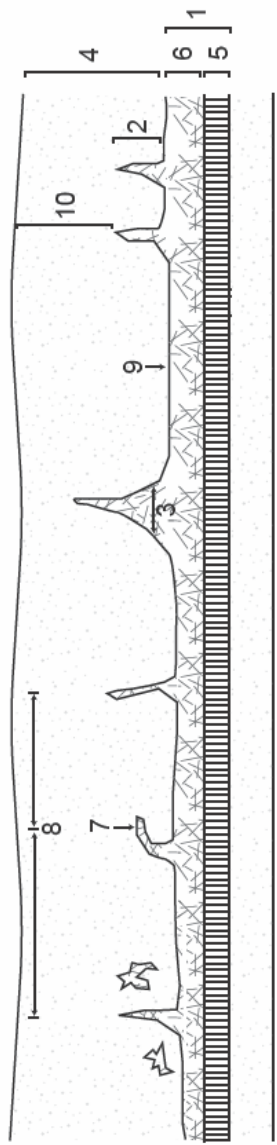
Figure 2.1: Locations of measurements taken in Iceland. 1: Thickness of lava; 2: Height of flame; 3: Thickness of flame; 4: Thickness of hyaloclastite; 5: Thickness of columnar-jointed lava; 6: Thickness of cube-jointed lava; 7: Direction of flame; 8: Spacing of flames; 9: Thickness of chilled margin; 10: Distance from top of flame to top of hyaloclastite unit.
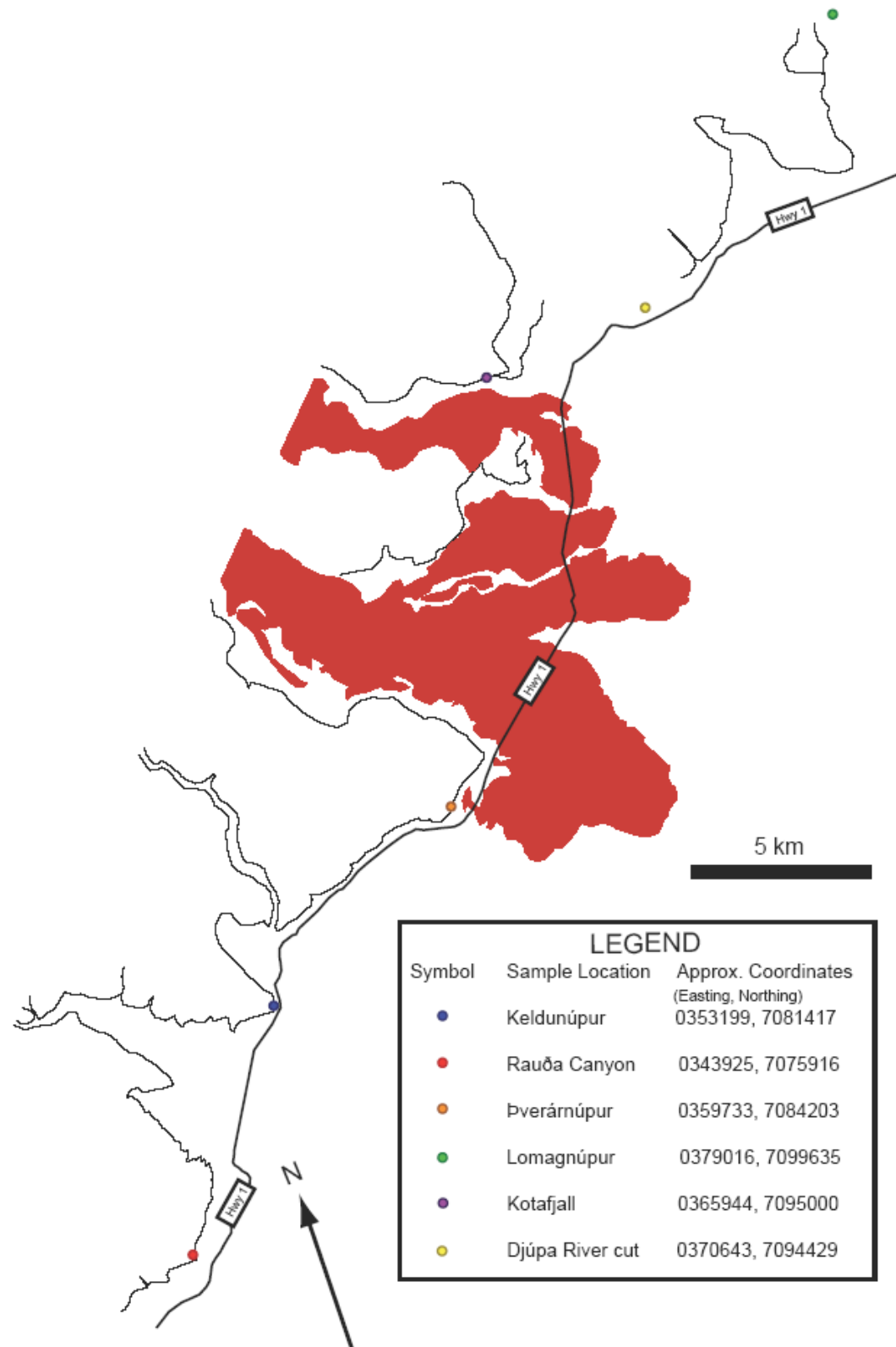
Figure 2.2: Map showing sample/measurement locations. Red area is 1783 Laki eruption lava flow.
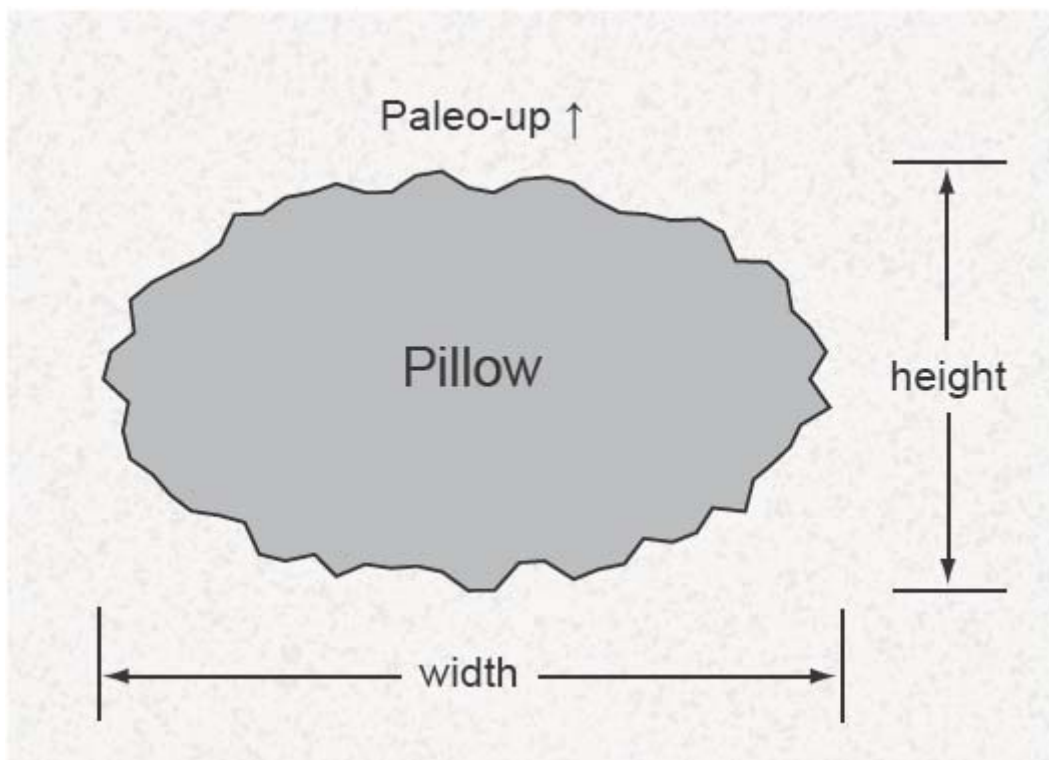
Figure 2.3: Measurement parameters of pillows in Aztec Wash pluton.

Rock samples were gathered from both Iceland and AWP for petrographic and elemental analysis. In Iceland, samples were gathered from chilled, glassy margins of basaltic lavas, and from glassy fragments in the overlying hyaloclastite at 7 locations, with 3 being heavily studied (see Chapter III). At AWP, samples of mafic-felsic boundaries were obtained from 3 locations within the pluton, although 5 locations were observed in detail (see Chapter V).

Petrographic Analysis

Forty-eight thin (30μm) and thick (60 μm) sections were obtained and examined from the rock samples collected in Iceland and AWP. Sample billets were shipped to both Idaho Petrographics and Burnham Petrographics for thick and thin section production. Samples from Iceland were examined primarily for the presence of glass, but also to identify phenocrysts and characterize vesicularity and grain size of quenched margins. In thin sections from AWP, semi-quantitative (visual) estimates of mineral abundances were made using standard optical microscopy. Examination focused on examining textural (quenching, grain size, shape, and distribution) and mineralogical variations at the mafic-felsic contact that might help clarify the mafic disaggregation processes operating in the pluton. Petrographic descriptions can be found in Appendix C.

Elemental Analysis

Elemental analysis was conducted on samples from Iceland using both laser-ablation inductively-coupled plasma mass-spectrometry (LA-ICP-MS) and electron microprobe (EMP). Trace element analysis of 21 samples using LA-ICPMS was carried

out over the course of 3 days in July 2007, and 1 day in January 2008 at Vanderbilt University. In addition, major element analysis of 22 samples using EMP was conducted on 2 days in July 2007 and November 2007 at the University of Tennessee-Knoxville. See Appendices D and E, respectively, for instrument details and operating conditions used for in situ LA-ICP-MS and EMP analyses.

Samples were prepared by chipping small ($<50mm^2$) pieces of glass-bearing rock off the hand sample and creating a 1-inch diameter polished epoxy mount, with approximately 4-5 sample pieces in each mount. These mounts were then used for both LA-ICPMS and EMP analysis, with the goal of comparing compositions of lava and hyaloclastite units at varying locations, and possibly constraining the eruptive source.

Application of MELTS

Once compositions of Icelandic lava and hyaloclastite pairs were determined, the MELTS software program (Ghiorso and Sack, 1995) was used to test possible relationships between lavas and hyaloclastites. After entering the major element compositions of hyaloclastite glasses at each location, pressure and temperature were varied to simulate possible within-magma-chamber and within-flow fractionation in order to constrain relationships between the hyaloclastite glasses and glass in underlying lavas and determine a plausible sequence of events by which they might be related.

In addition, MELTS was used to determine changes in volume and density during crystallization of mafic magma injected into the felsic reservoir at Aztec Wash pluton. Observing simulations of this behavior yielded data necessary for the modeling of this aspect of the project.

CHAPTER III

A VOLCANIC EXAMPLE OF MAGMA-HOST INTERACTION: INJECTION AND DISAGGREGATION OF BASALTIC LAVA IN HYALOCLASTITE, SOUTH ICELAND

Geologic History

Iceland is geologically unique due to its current location atop both the Mid-Atlantic Ridge and a hotspot (Thordarson and Höskuldsson, 2003). In addition, its northerly maritime location results in exposure to a wide variety of weather- and climate-related agents. Accordingly, many geologic processes—such as erosion, volcanism, debris transport, glaciation, faulting, and sea level change—have actively and rapidly shaped Iceland over its 25 Ma history. South Iceland has been shaped most recently—within the last 3 Ma—by glaciations, the related effects of transgression and regression, very active mafic to felsic volcanism, and glacier-derived debris flows (jökulhlaups).

Description of Study Area

The study area for this research comprises ~50 km of exposed paleo-seacliffs of Plio-Pleistocene age in south Iceland along the Ring Road in the Siða-Fljotshverfi district (Figure 2.2, or see back cover pocket for map).   The cliffs display relief ranging from 50 to 600 m, with a maximum elevation of 671 m at Lómagnúpur at the eastern end of the exposure. They are composed of repeating sequences of, from bottom to top, basaltic lava, hyaloclastite sediments, and bedded diamictite, although one or more of these units may be missing at any location (Bergh and Sigvaldason, 1991)(Figures A7 and A8 in

Appendix A). These depositional units range from almost nonexistent to 200 m in thickness. Contacts between depositional units are frequently irregular due to post-emplacement erosion. Hyaloclastite units host basaltic apophyses, pillow-like forms, and pods of lava in varying states of disaggregation. These features are visible on the dm to 10's of m scale, and are described in detail in the next section. The basalt and hyaloclastite source is proposed here and in Bergh and Sigvaldason (1991) to be a series of fissures roughly 50 km northwest of the terminus of the flows (see Figure 1.1), from either proto-Laki fissures or fissures parallel to those that have fed modern eruptions. The majority of observations for this study were at or near the modern termini of the flows, which have been eroded inland from their emplacement termini.

Overall, the depositional units dip slightly (~5°) southeast, roughly perpendicular to the coast. It should be noted, however, that this dip was not likely the case during emplacement. Iceland was subject to extreme glaciation during the Pliocene and Pleistocene, most notably in the interior of the island, but also stretching past modern-day coasts as well. Since the interior of Iceland was the most heavily glaciated, it has also experienced the most extreme effects of glacial rebound (~300-500 m; Sigmundsson, 1991, in Smellie, 2008), meaning that the dip of these depositional units is likely slightly exaggerated from what it was at the time of deposition, even though only a maximum of 100-120 m of rebound has occurred in the Siða-Fljotshverfi district (Sigmundsson, 1991, in Smellie, 2008).

<center>**Depositional Unit Components and Field Observations**</center>

As previously mentioned, the three main components of the "standard

depositional unit" (Bergh and Sigvaldason, 1991) in south Iceland are basalt lava,

hyaloclastite, and diamictite, although any component might be absent at a given

location. Each is discussed in detail below; photographs displaying key relations in

Appendix A are cited within the discussion.

Basalt Lava

The standard basalt sequence consists of columnar basalt ~10-30 m thick overlain

by cube-jointed ("cubey") basalt ~5-20 m thick (Figure A12). In some areas, such as

Kotafjall, basalt is also present in massive, unjointed flow units. The columnar basalt is

not always present, but wherever it is present it is overlain by the cube-jointed basalt.

Jointing in the columnar basalt most often is vertical, although in some sections

joints curve in wave-like fashion, sometimes forming almost complete circles of columns

(Figures A5, A23). Proposed formation mechanisms for these structures include cooling

of lavas within paleo-lava tubes, which would have been insulated to allow columnar-

jointing formation, or, perhaps more likely, within the cavities left by a melted iceberg

after it was entrained in the lava flow (Smellie, 2008).   In some localities, columns are at

orientations 180° from normal vertical orientation, with the hexagonal ends of the

columns the only exposed part of the column amidst normal vertical columns. The

reasons for this arrangement are unclear.

The basalt that comprises both the columnar- and cube-jointed portions of the lava

flow is aphanitic with sparse olivine, pyroxene, and plagioclase phenocrysts. At

<center>19</center>

Keldunúpur, phenocrystic pyroxenes are rimmed by olivine. Aggregates of calcite crystals are widespread and represent post-emplacement alteration.

Basalts throughout the units display varying degrees of vesicularity. At Keldunúpur, vesicularity in lava ranges from virtually non-existent to roughly 5%. Vesicles are 2-10 mm in diameter, and display a tubular, straw-like shape that extends into the rock—normal to the overall flow surface—for several mm up to 5 cm. Similarly, basalts from Lómagnúpur generally show no vesiculation, but locally display tubular vesicles 2-5 mm in diameter and up to 5 cm deep oriented toward the paleo-outside (primarily the top) of the flow. At the Rauða River outcrop, the basalts show no readily visible vesiculation, either in the main flow or the apophyses.

In striking contrast to these observations, at Kotafjall non-apophysis basalt shows a mixture of vesiculated (Figure A19) and non-vesiculated lava, often with both types occurring within a meter of two of each other, and sometimes within the same rock (Figure A21). Some tubular vesicles similar to those of Keldunúpur are also present. Small "bubble dikes" that propagated horizontally are located within 10 m of highly vesiculated basalt (Figure A20). In an even more extreme case of vesiculation and non-vesiculation near Kotafjall, a 300 m-long outcrop along the Djúpa River displayed a lava flow 12 m high with vesicles ranging from less than 500 μm to over 1 cm in diameter. This basalt flow graded from scoria-like texture in the lower 2 m, to 2 m of non-vesiculated basalt, 2 m of moderately vesiculated basalt interspersed with areas of non-vesiculation, 4 m of highly vesiculated basalt interspersed with areas of non-vesiculation and capped with 2 m of extremely vesiculated basalt (Figure A25). However, the

correlation with the previously mentioned sites is in doubt; this lava may be significantly younger than the units that are the subject of this research.

The basalt from which the flame-like apophyses and hyaloclastite-borne fragmented lava pods are derived is almost always cubey (Figure A14), although some apophyses appear to lack joints (Figure A18). The outer edges of the apophyses invariably display glassy, chilled margins ranging anywhere from several millimeters to ~2 cm in thickness, as do the rinds of fragmented pods. The cube-jointed basalt flows from which these structures originate display the same chilled margins with glassy rinds about 50% of the time at their upper contact against hyaloclastite (Figure A22)—the interiors and remaining 50% of the upper contact of the lava flow show minimal chilling, and no glassy rims. The interiors of the apophyses are always non-vesiculated, although some fragmented pods or clasts display minor vesiculation (Figure A24).

Basaltic pillow-like pods and en echelon dikes are also present throughout the district. Pillow-like structures are confined to the lower portions of hyaloclastite units at many locations, and are acutely fractured, and vesiculated near their outer rims. The pillows are 1-4 dm in diameter. En echelon dikes (Figure A9) are most prominent in the cliffs at Eystrikinnar, where they can be seen originating from a lava flow and intruding the overlying hyaloclastite unit for 10s of m. These small dikes are also seen throughout the cliffs. Larger and more abundant dikes intrude hyaloclastite at Fagrifoss waterfall (~0336100, 7085500), about 15 km northwest of the study area (toward the presumed eruption site). They may be part of a vent system and indicate proximity to the source fissure(s). Substantial amounts of basaltic pillows were also seen at Fagrifoss.

Hyaloclastite

The hyaloclastite observed in the Siða-Fljotshverfi district erupted as basaltic
sideromelane glass as a product of non-explosive lava shattering due to contact with
(presumably eruption into) water. Basaltic glass is thermodynamically highly unstable in
the cold, wet environment where hyaloclastite forms, and therefore extremely sensitive to
alteration (Frolova et al., 2005). Accordingly, sideromelane rapidly alters to palagonite,
the first replacement product of mafic glass alteration (Stroncik and Schminke, 2001).
Palagonization is responsible for the first cementation of glass shards into consolidated
rock (Frolova et al., 2005). As a result of the majority of the material being sideromelane
with altered palagonite rims, the hyaloclastite has a ubiquitous tannish color, which
darkens with weathering and alteration (Figure A1).

Hyaloclastite units in the Siða-Fljotshverfi district are 10-115 m thick, with an
average thickness of ~40 m, comparable to the measurements taken by Smellie (2008).
The contact with the overlying layer is highly variable. In many locations where
diamictite overlies the hyaloclastite, there is gradual gradation from one to the other.
Other areas display an undulating hyaloclastite/diamictite boundary that shows evidence
of erosion.

All observed hyaloclastite units contain both the sideromelane/palagonite matrix
and substantial amounts of lava clasts up to 2 dm in diameter. The lava clasts almost
always display more abundant vesicles than the underlying lava flow and commonly have
1- 5 mm glass rinds. Basaltic clasts vary in appearance from juvenile and unaltered to
older and more weathered, although this is likely a result of post-emplacement

weathering in more exposed areas. The majority of basaltic fragments are juvenile and partly to entirely surrounded by quenched, glassy margins (Figures A15, A16).

The hyaloclastite displays varying grain sizes and sorting. For example, at Keldunúpur hyaloclastites both immediately underlie and overlie a prominent basalt layer, but the hyaloclastite below the lava is better sorted than the overlying hyaloclastite, with fewer large, angular fragments in the matrix (Figures A7, A8). However, there are ~0.5 m-diameter boulders in the underlying hyaloclastite. The opposite is true at Lómagnúpur, where the lower hyaloclastite unit is very rich in basalt clasts up to 1 dm in diameter, but the overlying unit displays a uniformly fine-grained and clast-free matrix.

A subtle feature at Keldunúpur that becomes readily apparent upon closer observation is the presence of baked or burned hyaloclastite at the contact with the underlying lava (Figure A13). These baked margins are 3-10 cm thick, and have a deep orange-brown color. They presumably result from heating by the underlying lava.

Diamictite/Sedimentary Strata

Diamictite and similar sedimentary rocks comprise the smallest volume percentage in the Siða cliffs. These strata overlie hyaloclastites and rarely basaltic lava, and also form lenses within hyaloclastite units. Diamictites more frequently cap the entire cliff as the final layer than they appear as a within-cliff unit. Diamictite strata are variable in thickness, but are generally 5-50 m thick, with an average of around 15 m (Bergh and Sigvaldason, 1991). They are characterized by monolithologic cobbles and boulders in a fine-grained mudstone matrix. In one area of recent jökulhlaup activity, the sandur was bedded in a fines-boulders-fines arrangement, with sideromelane/palagonite

integrated into the "fines". It is probable that the boulders represent the start of a new wave or outburst, since the initial force would be enough to carry material off the valley walls and deposit it downstream. However, the boulders might also be the top of a sequence, because they drop out as energy decreases while fines are carried further. These modern deposits appear to be very similar to those interbedded with the lava and hyaloclastite of the -Fljotshverfi district.

At a few study area locations, sedimentary strata (diamictites and sandstones) are clast-poor. Larger clasts within the mud matrix are almost invariably rounded, although in a few locations angular fragments are present. At Þverárnúpur, diamictites host large (>1 m) breccias composed of angular clasts. Similar features are also seen at Lómagnúpur, and large conglomerates with rounded clasts are also seen at Keldunúpur. The diamictites locally tend to fill in paleovalleys and thicken in topographic lows (cf. Bergh, 1985; Bergh and Sigvaldason, 1991).

Field Observations of Apophyses and Fragmentation Structures

Since the main focus of this portion of research was the formation of flame-like apophyses, a large amount of time was devoted to their observation and measurement. Measurements were conducted according to the scheme outlined in Figure 2.1—the corresponding measurements are listed in Table 3.1.

As previously mentioned, apophyses originate from a cube-jointed lava flow and propagate upward into overlying hyaloclastite for up to 40 m (~13 m average), although Smellie (2008) observed these structures reaching over 60 m in height and up to 15m in width. Measured apophysis widths for this study range from <1-10 m wide. The

apophyses have chilled and fragmented margins and commonly have glassy rims with non-vesiculated interiors (Figure A11).

Although commonly elongate in the vertical dimension, apophyses usually display bending, undulating margins, and their margins are generally fragmented and rarely smooth (Figures A6, A10, A11). Many apophyses are vertical, although a few lean toward the NW (opposite the presumed transport direction)(Table 3.1). Apophysis height does not correlate with thickness of the underlying lava flow, and apophyses can be 40 to 1500% the height of their parental lava sheet (see Table 3.1). On the other hand, apophysis height does appear to be linked to the thickness of the hyaloclastite deposit overlying it. This relationship, and the formation mechanism of the apophyses, will be discussed in detail in the next chapter.

Petrographic Observations

Petrographic analysis was carried out on 36 rock samples obtained in Iceland. Please refer to table 3.2 for a list of samples and their locations. Both the basaltic lava and the hyaloclastite in the Siða-Fljotshverfi district are composed of the same phases, although the relative percentages of each vary. Hyaloclastites are invariably composed of palagonitized glass (60-95%), zeolites (5-35%), and trace amounts of opaques, plagioclase feldspar, olivine, and clinopyroxene (Figures A1, A2). The hyaloclastites, which display a wide range of porosities, show large amounts (up to 20% of the total rock volume) of void spaces in some samples. The void spaces result from evacuation of water after emplacement, and are subsequently filled by zeolites, which form secondarily in pores and void spaces in the hyaloclastite sediments after emplacement (Stroncik and

Table 3.1: Measurements of apophyses. Description numbers correspond to measurements shown in Figure 2.1.

ID	Location Name	UTM Easting	UTM Northing†	Latitude	Longitude	1: Lava thickness (m)						
						1	2	3	4	5	6	7
LOM101m	Lómagnúpur	0378468	7098032	N63 29.045'	W17 29.045'	18	19	28	21	34	28	23
EYS101m	Eystrikinnar	0374722	7097337	N63 58.805'	W17 33.594'	3	1.9	2.2	2	2	1.4	2.5
EYS102m	Eystrikinnar	0374722	7097337	N63 58.805'	W17 33.594'	3	1.9	2.2	2	2	1.4	2.5
EYS103m	Eystrikinnar	0374722	7097337	N63 58.805'	W17 33.594'	3	1.9	2.2	2	2	1.4	2.5
RAU101m	Rauða Canyon	0343925	7075516	N63 46.655'	W18 04.778'	0.2	0.26	0.23	0.29	0.24	0.28	0.29
LOM201m	Lómagnúpur	0378079	7095849	N63 58.090'	W17 29.421'	5	7	8	7	4	9	4
LOM202m	Lómagnúpur	0378079	7095849	N63 58.090'	W17 29.421'	5	7	8	7	4	9	4
LOM203m	Lómagnúpur	0378082	7095849	N63 58.090'	W17 29.421'	11	8	10	14	16	13	10
LOM301m	Lómagnúpur	0378082	7096375	N63 58.372'	W17 29.463'	29	31	31	29	24	23	26
LOM302m	Lómagnúpur	0378082	7096375	N63 58.372'	W17 29.463'	25	29	26	22	24	21	24
LOM303m	Lómagnúpur	0378082	7096375	N63 58.372'	W17 29.463'	25	29	26	22	24	21	24
TVE101m	Thverárnúpur	0361378	7084666	N63 51.673'	W17 49.289'	4	5	4	5	5	6	5
TVE102m	Thverárnúpur	0361378	7084666	N63 51.673'	W17 49.289'	17.3	16.9	18	13	16.8	16.6	16.5
TVE103m	Thverárnúpur	0361378	7084666	N63 51.673'	W17 49.289'	5	5	7	6	4	4	3
TVE201m	Thverárnúpur	0360673	7084331	N63 51.503	W17 50.092'							
KEL101m	Keldunúpur	0353015	7081034	N63 49.550'	W17 59.247"	1	1.8	1	1.4	1	2.8	1.2
KEL102m	Keldunúpur	0353015	7081034	N63 49.550'	W17 59.247'	6.1	7.1	6.5	6.6	6.9	6.2	7
KEL103m	Keldunúpur	0353015	7081034	N63 49.550'	W17 59.247'	4.6	4.4	4.5	4.2	4.9	5.1	4.9
KEL201m	Keldunúpur					1	0.9	1.1	1.2	0.9	1	0.9
LOM401m	Lómagnúpur	0379016	7099235	N63 59.953'	W17 28.436'	4.8	4.8	5.5	5	4.8	5.3	5.1
LOM402m	Lómagnúpur	0379016	7099235	N63 59.953'	W17 28.436'	8	8.9	8.7	9	9.1	8	8.2
LOM404m	Lómagnúpur	0379016	7099235	N63 59.953'	W17 28.436'	2.4	2.1	1.8	2.1	2	2	1.9
LOM405m	Lómagnúpur	0379016	7099235	N63 59.953'	W17 28.436'	2	1.9	1.8	2	2	2	1.9

†GPS underestimates Northing value by ~400 m

26

Table 3.1 cont: Measurements of apophyses. Description numbers correspond to measurements shown in Figure 2.1.

ID	2: Flame Height (m)							3: Flame Width							4: Hyaloclastite Thickness						
	1.0	2.0	3.0	4.0	5.0	6.0	7.0	1	2	3	4	5	6	7	1.0	2.0	3.0	4.0	5.0	6.0	7.0
LOM101m															29.0	28.0	54.0	60.0	70.0	28.0	28.0
EYS101m	5.8	6.4	8.3	4.5	5.7	5.2	6.3	2.41							15.1	16.4	15.5	17.2	16.8	18.3	15.3
EYS102m	7.5	8.5	9.1	8.0	7.5	9.7	6.4	3.3	3.6						15.1	16.4	15.5	17.2	16.8	18.3	15.3
EYS103m	9.0	9.0	10.0	7.5	7.7	9.6	8.6	6.45							15.1	16.4	15.5	17.2	16.8	18.3	15.3
RAU101m	3.1	3.4	4.2	3.8	3.5	2.9	3.4	0.33	0.28	0.32	0.31	0.36	0.35	0.32	Can't see top of unit (>5m)						
LOM201m	15.0	15.0	13.0	15.0	16.0	14.0	17.0	2.3							45.0	37.0	43.0	44.0	42.0	41.0	43.0
LOM202m	4.0	5.0	5.0	3.0	5.0	3.0	5.0	0.76							45.0	37.0	43.0	44.0	42.0	41.0	43.0
LOM203m	19.0	18.0	15.0	17.0	14.0	13.0	18.0	4							70.0	70.0	69.0	66.0	68.0	73.0	70.0
LOM301m	20.0	18.0	28.0	19.0	25.0	--		5.2							31.0	34.0	33.0	33.0	32.0	34.0	32.0
LOM302m	14.0	15.0	19.0	20.0	18.0	21.0	17.0	4.65							45.0	46.0	45.0	42.0	43.0	44.0	43.0
LOM303m	14.0	17.0	16.0	17.0	18.0	17.0	15.0	5.3							45.0	41.0	43.0	43.0	45.0	42.0	46.0
TVE101m	9.0	9.0	8.0	10.0	8.0	9.0	10.0	4.2							23.0	21.0	24.0	25.0	23.0	20.0	22.0
TVE102m	6.6	6.7	6.4	6.9	7.0	6.8	7.0	3.32							9.0	10.3	10.1	9.4	10.0	10.0	9.3
TVE103m	15.0	13.0	15.0	15.0	13.0	14.0	14.0								19.0	19.0	19.0	19.0	20.0	19.0	18.0
TVE201m	9.0	9.0	11.0	9.0	10.0	12.0	9.0	2.47							43.0	44.0	43.0	42.0	39.0	42.0	43.0
KEL101m	4.6	6.4	6.4	5.4	5.9	6.5	5.2	6.9							44.1	44.0	41.7	41.8	44.0	44.9	43.0
KEL102m	10.9	11.0	11.6	10.0	12.5	11.7	10.5	1.35							38.0	38.5	37.9	38.7	38.5	38.0	38.9
KEL103m	26.9	27.3	26.8	26.6	27.1	25.7	27.6	9.37							41.6	41.4	41.0	40.4	41.3	39.4	39.9
KEL201m	4.0	4.0	4.1	5.0	5.0	4.0	6.0								18.0	20.0	19.0	20.0	20.0	19.0	18.0
LOM401m	4.8	4.6	4.0	4.1	5.0	5.3	5.4	1.8							23.0	21.0	21.2	22.1	24.0	27.5	21.7
LOM402m	36.5	37.0	37.4	37.9	68.0	36.3	37.0	11.5							37.0	37.0	35.0	37.4	35.3	35.7	36.9
LOM404m	20.0	16.8	19.6	19.3	20.1	19.9	18.9	1.6							64.4	64.9	66.2	64.3	61.3	66.4	66.6
LOM405m	19.4	21.0	20.0	19.7	20.0	19.8	20.3	3.38							62.7	61.0	62.0	59.9	68.4	66.6	63.1

Table 3.1 cont.: Measurements of apophyses. Description numbers correspond to measurements shown in Figure 2.1.

ID	5: Column Height							6: Cubes Height							7: Flame Orientation	
	1	2	3	4	5	6	7	1	2	3	4	5	6	7	Face	Strike
LOM101m	12	7	11	9	13										Flames point toward source	002
EYS101m	none							same as 1							Flame points toward source	340
EYS102m	none							same as 1							Flame points toward source	340
EYS103m	none							same as 1							Flame points toward source	340
RAU101m	none							same as 1							X-section? On SW face	?
LOM201m	8	10	7	8	11	6	7	same as 1							Flame points toward source	330
LOM202m	8	10	7	8	11	6	7	same as 1							Vertical	330
LOM203m	18	22	13	21	16	14	19	same as 1							Vertical	330
LOM301m	18	15	14	19	18	18	17	13	8	13	15	16	14	15	Flame points toward source	006
LOM302m	22	15	15	15	18	16	13	8	7	7	5	7	6	8	Points away from source	006
LOM303m	22	15	15	15	18	16	13	8	7	7	5	7	6	8	Vertical	006
TVE101m	none														Vertical	045
TVE102m	8.4	9.1	8.2	8.2	9.0	8.5	9.1	7	10.0	8.5	8.6	9.7	12.0	9.0	X-section?	074
TVE103m	4	3.0	2.0	2.0	3.0	3.0	3.0	2	2.0	2.0	2.0	1.0	2.0	2.0	Vertical	082
TVE201m	none							3	3	5	2	5	1	2	Vertical, slightly to source	077
KEL101m	none							same as 1							Bent back full circle	011
KEL102m	2.7	3.0	2.7	1.7	2.1	3.0	2.8	3.8	4.8	3.4	3.9	4.7	3.0	3.3	Vertical	011
KEL103m	none							same as 1							Vertical	011
KEL201m	none							same as 1							Vertical	022
LOM401m	11.8	11.1	11.8	12.9	13.0	12.3	11.9	7	6.0	6.2	6.1	5.6	6.4	7.0		000
LOM402m																000
LOM404m															Vert, slight lean to sea	024
LOM405m															Vertical	024

Table 3.1 cont.: Measurements of apophyses. Description numbers correspond to measurements shown in Figure 2.1.

ID	10: Surface Proximity						
	1.0	2.0	3.0	4.0	5.0	6.0	7.0
LOM101m							
EYS101m	9.6	10.0	8.9	9.5	11.59	9.6	9.4
EYS102m	5.0	5.7	3.4	6.7	4.3	4.8	4.3
EYS103m	5.6	6.7	6.9	7.0	5.3	6.0	6.9
RAU101m	Can't see top of unit (>5m)						
LOM201m	32.0	27.0	30.0	31.0	34.0	24.0	31.0
LOM202m	41.0	39.0	35.0	40.0	47.0	43.0	46.0
LOM203m	68.0	63.0	56.0	59.0	52.0	58.0	49.0
LOM301m	12.0	16.0	12.0	8.0	13.0	14.0	15.0
LOM302m	17.0	17.0	17.0	16.0	16.0	18.0	17.0
LOM303m	27.0	28.0	28.0	26.0	29.0	27.0	26.0
TVE101m	13.0	13.0	12.0	11.0	11.0	11.0	13.0
TVE102m	3.2	5.0	5.5	4.0	5.2	5.0	4.0
TVE103m	5.0	5.0	6.0	4.0	5.0	6.0	4.0
TVE201m	33.0	35.0	39.0	33.0	32.0	36.0	35.0
KEL101m	41.6	39.7	39.0	37.9	37.7	38.0	37.7
KEL102m	25.5	26.1	24.0	25.3	26.1	25.6	24.9
KEL103m	13.1	12.7	13.6	13.9	14.5	13.9	12.9
KEL201m	12.5	12.0	13.0	13.9	14.0	13.0	13.0
LOM401m	16.3	17.9	18.1	17.3	17.0	17.1	17.7
LOM402m							
LOM404m	56.4	59.2	54.1	58.1	53.3	57.7	53.6
LOM405m	48.8	36.9	32.4	34.4	37.2	40.4	36.7

Schminke, 2001). In addition to voids, basalt clasts up to 3mm diameter are present in many samples. Palagonitized sideromelane grains are 0.5-3 mm diameter, and frequently show alteration rims. They also usually display trace phenocrysts <100 μm diameter of plagioclase and olivine in the glass. Plagioclase and olivine phenocrysts are also seen throughout the hyaloclastite matrix.

Basaltic lavas have predominantly plagioclase feldspar (up to 90%) phenocrysts, with clinopyroxene and olivine as the other major mineral constituents (Figures A3, A4). Opaques and glass are trace components in the lava. Lavas display 0 to ~20% of small vesicles in thin section. Vesicles can reach up to 200 μm in diameter, particularly in samples from the top of the cube-jointed basalt lava flow.

Thin sections of boundaries between basalt lava and hyaloclastite reveal several interesting characteristics of both materials. Glass content in basalt is inversely proportional to distance from boundary zone, with the basalt at the boundary virtually 100% quenched glass. In addition, vesiculation increases from no interior vesicles to ~20% adjacent to the boundary. Plagioclase phenocrysts also display this pattern, with phenocrysts present throughout the sample, but concentrated near the boundary. At the basalt-hyaloclastite boundary itself, basalt is frequently seen "splintering" and forming finger-like projections into the hyaloclastite for up to 3 mm (Figure A2). Some projections appear slightly angled. The boundary zone itself—the area where basalt and hyaloclastite intermingle—is 0-3 mm wide.

The hyaloclastite side of the boundary is fairly nondescript, although it does generally show increased concentration of zeolites and often contains large plagioclase

feldspar and olivine phenocrysts. For detailed petrographic descriptions of lava and hyaloclastite samples, please see Appendix C.

Elemental Data

Major element compositions were determined for 22 total samples of fresh glass from basalt lava and hyaloclastite from 3 locations: Rauða Canyon, Keldunúpur, and Lómagnúpur (see Figure 2.2 or pocket map). All samples were analyzed for SiO_2, TiO_2, Al_2O_3, FeO, MnO, MgO, CaO, Na_2O, K_2O, and P_2O_5, while some samples were also analyzed for SO_2 and Cr_2O_3 (Figures 3.1-3.9; Appendix D). The largest discrepancy between lava and hyaloclastite data within a location is seen at Lómagnúpur, where the lavas are clearly more fractionated with significantly higher SiO_2, TiO_2, K_2O, FeO, and P_2O_5; slightly higher Na_2O and MnO; and lower Al_2O_3, CaO, and MgO (Table 3.3).

Rauða Canyon and Keldunúpur glasses are very similar (Table 3.3) and are somewhat more evolved than Lómagnúpur hyaloclastites. At Rauða Canyon, glasses from lavas and hyaloclastites are almost identical (Figures 3.1-3.9). Keldunúpur hyaloclastites appear to be very slightly more evolved than the Rauða Canyon hyaloclastites, and at Keldunúpur lavas are slightly, but distinctly, more evolved than hyaloclastites.

Rare earth element (REE) patterns from analyses of 21 samples show some slightly different trends (Figures 3.10-3.12). Data are overwhelmingly concentrated by location. Lómagnúpur lavas are once again the most evolved samples, and show a slightly "steeper", more light REE (LREE)-enriched pattern. Analyses of lavas and hyaloclastites from Keldunúpur and Rauða Canyon display a flatter pattern than

31

Table 3.2: Iceland sample locations and descriptions.

ID	Location Name	UTM Easting	UTM Northing[†]	Latitude	Longitude	Description of Source
KEL101*	Keldunúpur	0353199	7081017	N63 49.537'	W17 59.018'	Hyaloclastite under cubey basalt
KEL102	Keldunúpur	0353137	7080981	N63 49.520'	W17 59.090'	Hyaloclastite over cubey basalt, proximal to flame
KEL103*	Keldunúpur	0353139	7081020	N63 49.517'	W17 59.082'	Interior of cubey basalt
KEL104*	Keldunúpur	0352983	7080922	N63 49.479'	W17 59.302'	Basalt from upper margin w/hyaloclastite
KEL105*	Keldunúpur	0353138	7080985	N63.49.520'	W17 59.076'	Basalt from flame margin
KEL106*	Keldunúpur	0353138	7080985	N63.49.520'	W17 59.076'	Basalt from flame interior
KEL107	Keldunúpur	0353138	7080985	N63.49.520'	W17 59.076'	Hyaloclastite near boundary w/ underlying basalt
KEL108	Keldunúpur	0353138	7080985	N63.49.520'	W17 59.076'	Hyaloclastite from interior of deposit
KEL201[+]	Keldunúpur	0353015	7081034	N63 49.550'	W17 59.247'	Interior of cubey basalt
KEL202[+]	Keldunúpur	0353015	7081034	N63 49.550'	W17 59.247'	Basalt from upper glassy margin w/hyaloclastite
KEL203[+]	Keldunúpur	0353015	7081034	N63 49.550'	W17 59.247'	Basalt from flame margin
KEL204[+]	Keldunúpur	0353015	7081034	N63 49.550'	W17 59.247'	Basalt from flame interior
KEL205[+]	Keldunúpur	0353015	7081034	N63 49.550'	W17 59.247'	Hyaloclastite near boundary w/ underlying basalt
KEL206[+]	Keldunúpur	0353015	7081034	N63 49.550'	W17 59.247'	Hyaloclastite over cubey basalt, proximal to flame
KEL207[+]	Keldunúpur	0353015	7081034	N63 49.550'	W17 59.247'	Hyaloclastite from interior of deposit
RAU101	Rauðá Canyon	0343925	7075516	N63 46.655'	W18 04.778'	Basalt from flame interior
RAU102	Rauðá Canyon	0343925	7075516	N63 46.655'	W18 04.778'	Basalt from upper margin w/hyaloclastite
RAU103	Rauðá Canyon	0343925	7075516	N63 46.655'	W18 04.778'	Basalt from flame margin
RAU104	Rauðá Canyon	0343925	7075516	N63 46.655'	W18 04.778'	Hyaloclastite over cubey basalt, proximal to flame
RAU105	Rauðá Canyon	0343925	7075516	N63 46.655'	W18 04.778'	Interior of cubey basalt
RAU106	Rauðá Canyon	0343925	7075516	N63 46.655'	W18 04.778'	Hyaloclastite near boundary w/ underlying basalt
RAU107	Rauðá Canyon	0343925	7075516	N63 46.655'	W18 04.778'	Hyaloclastite from interior of deposit
TVE301[+]	Þverárnúpur	0359733	7083803	N63 51.191'	W17 51.193'	Hyaloclastite near boundary w/ underlying basalt
TVE302[+]	Þverárnúpur	0359733	7083803	N63 51.191'	W17 51.193'	Hyaloclastite near boundary w/ underlying basalt
LOM401	Lómagnúpur	0379016	7099235	N63 59.953'	W17 28.436'	Interior of cubey basalt
LOM402	Lómagnúpur	0379016	7099235	N63 59.953'	W17 28.436'	Basalt from upper glassy margin w/hyaloclastite
LOM403	Lómagnúpur	0379016	7099235	N63 59.953'	W17 28.436'	Basalt from flame margin
LOM404	Lómagnúpur	0379016	7099235	N63 59.953'	W17 28.436'	Basalt from flame interior

[†]GPS underestimates Northing value by ~400 m

*No viable LA-ICPMS or EMP data obtained

[+]Sample did not undergo analysis

Table 3.2 cont.: Iceland sample locations and descriptions.

ID	Location Name	UTM Easting	UTM Northing†	Latitude	Longitude	Description of Source	Additional Notes
LOM405	Lómagnúpur	0379016	7099235	N63 59.953'	W17 28.436'	Hyaloclastite near boundary w/ underlying basalt	
LOM406	Lómagnúpur	0379016	7099235	N63 59.953'	W17 28.436'	Hyaloclastite over cubey basalt, proximal to flame	
LOM407	Lómagnúpur	0379016	7099235	N63 59.953'	W17 28.436'	Hyaloclastite from interior of deposit	
LOM408	Lómagnúpur	0379016	7099235	N63 59.953'	W17 28.436'	Hyaloclastite under basalt, uniform matrix	
LOM409	Lómagnúpur	0379016	7099235	N63 59.953'	W17 28.436'	Hyaloclasitite under basalt, basalt clast rich	
LOM410	Lómagnúpur	0379016	7099235	N63 59.953'	W17 28.436'	Quenched basalt	
LOM411	Lómagnúpur	0379016	7099235	N63 59.953'	W17 28.436'	Quenched basalt	
KOT101*	Kotafjall	0365944	7094600	N63 57.174'	W17 44.138'	Hyaloclastite from immediately above vesiculated basalt	
KOT102*	Kotafjall	0365944	7094600	N63 57.174'	W17 44.138'	Strange basalt vesiculation	
KOT103*	Kotafjall	0365944	7094600	N63 57.174'	W17 44.138'	Basalt pillow rim	
KELX01	Keldunúpur	0352986	7080863	N63 49.558'	W17 59.256'	Basalt glass from upper margin w/ hyaloclastite	
KELX02	Keldunúpur	0352984	7080881			Basalt glass from upper margin w/ hyaloclastite	
KELX03	Keldunúpur	0352984	7080881			Basalt glass from upper margin w/ hyaloclastite	
KELX04	Keldunúpur	0353100	7081200			Basalt glass from upper margin w/ hyaloclastite	GPS malfuncation; Estimated values given (no correction needed)
KELX05	Keldunúpur	0353100	7081200			Basalt glass from upper margin w/ hyaloclastite	GPS malfuncation; Estimated values given (no correction needed)
KELX06	Keldunúpur	0352879	7080933			Basalt glass from upper margin w/ hyaloclastite	
KELX07	Keldunúpur	0353073	7081005	N63 49.526'	W17 59.170'	Basalt from upper glassy margin w/ burned hyaloclastite	
RAUX01	Rauðá Canyon	0343935	7075330			Basalt glass from side margin w/ hyaloclastite	
RAUX02	Rauðá Canyon	0343950	7075650			Basalt glass from upper margin w/ hyaloclastite	GPS malfuncation; Estimated values given (no correction needed)
RAUX03	Rauðá Canyon	0343950	7075650			Basalt glass from upper margin w/ hyaloclastite	GPS malfuncation; Estimated values given (no correction needed)
RAUX04	Rauðá Canyon	0343950	7075650			Basalt glass from upper margin w/ hyaloclastite	GPS malfuncation; Estimated values given (no correction needed)
RAUX05	Rauðá Canyon	0343950	7075650			Basalt glass from upper margin w/ hyaloclastite	GPS malfuncation; Estimated values given (no correction needed)
RAUX06	Rauðá Canyon	0343950	7075650			Basalt glass from upper margin w/ hyaloclastite	GPS malfuncation; Estimated values given (no correction needed)
RAUX07	Rauðá Canyon	0343950	7075650			Hyaloclastite from layer above samples RAUX05 and RAUX06	GPS malfuncation; Estimated values given (no correction needed)
DJÚ101*	Djúpa River cut	0370643	7094029			Base of lava flow crust, 12 m below flow surface	
DJÚ102*	Djúpa River cut	0370643	7094029			Base of lava flow crust, 12 m below flow surface	
DJÚ103*	Djúpa River cut	0370643	7094029			Base of lava flow crust, 12 m below flow surface	
DJÚ104*	Djúpa River cut	0370643	7094029			Basalt with minor vesiculation, 8 m below flow surface	
DJÚ105*	Djúpa River cut	0370643	7094029			Basalt with major vesiculation, 6 m below flow surface	

†GPS underestimates Northing value by ~400 m   *No viable LA-ICPMS or EMP data obtained   *Sample did not undergo analysis

Table 3.3: Average major element compositions by material and location.

Location	Material	Average weight %									
		SiO_2	TiO_2	Al_2O_3	MgO	CaO	MnO	FeO	Na_2O	K_2O	P_2O_5
Keldunúpur	Lava	49.00	2.68	13.26	6.38	11.40	0.239	13.96	2.62	0.261	0.221
	Hyaloclastite	49.16	2.62	13.22	6.53	11.52	0.268	13.50	2.60	0.259	0.235
Rauða Canyon	Lava	49.32	2.55	13.50	6.66	11.76	0.238	13.02	2.45	0.258	0.241
	Hyaloclastite	49.05	2.55	13.46	6.84	11.67	0.292	13.02	2.46	0.293	0.234
Lomagnúpur	Lava	50.57	4.23	11.29	3.60	8.61	0.393	16.98	2.97	0.747	0.532
	Hyaloclastite	48.53	2.37	13.62	7.06	12.21	0.250	12.93	2.48	0.237	0.211

Lómagnúpur lavas. Lavas from Keldunúpur show a much broader range of REE concentrations than Rauða Canyon lavas, which are very homogeneous and fall in the middle of the Keldunúpur lava range.

Lómagnúpur hyaloclastites are uniformly the least evolved of all samples (as with major elements), although a single analysis from Keldunúpur plots with them. Keldunúpur hyaloclastites show a wide range of concentrations, but appear to have 2 sample sets, as only 4 analyses constitute the entire lower range (La between 20 and 30 ppm) while the remaining analyses uniformly show La concentrations of 35-45 ppm. REE concentrations in Rauða Canyon hyaloclastite glasses are practically identical, whereas Keldunúpur hyaloclastites extend to more evolved (REE-rich) compositions.
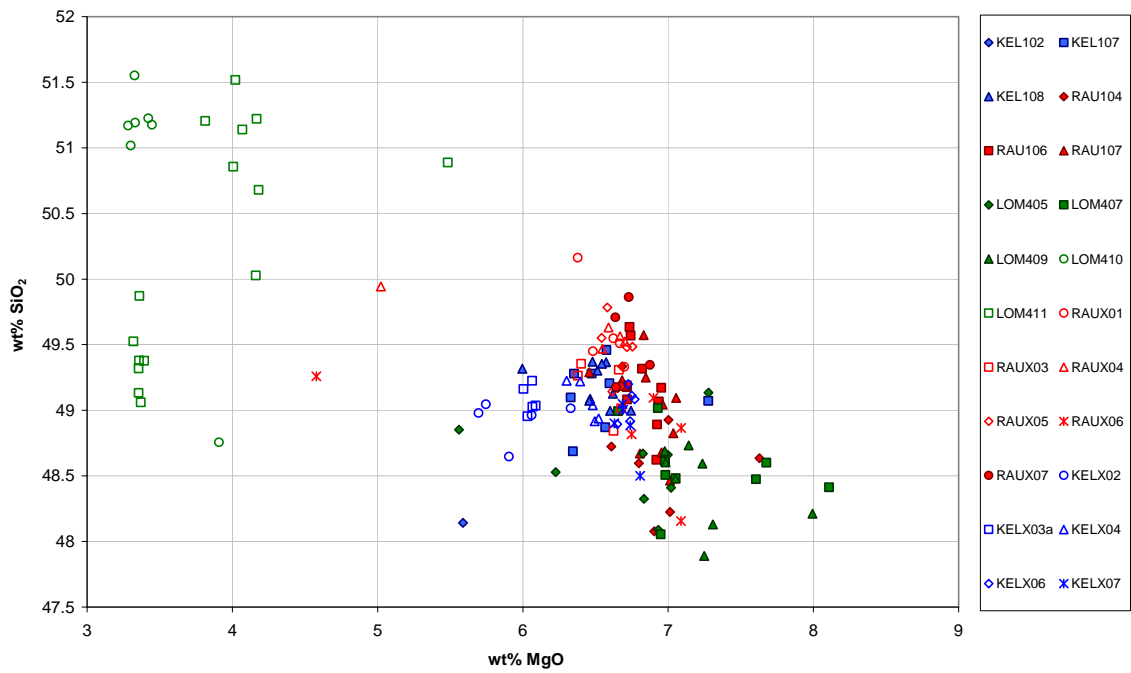
Figure 3.1 (above): SiO$_2$ vs. MgO for Icelandic samples.
Figure 3.2 (below): TiO$_2$ vs. MgO for Icelandic samples. Solid symbols indicate hyaloclastite, open symbols indicate lava. Data points are color-coded by location.
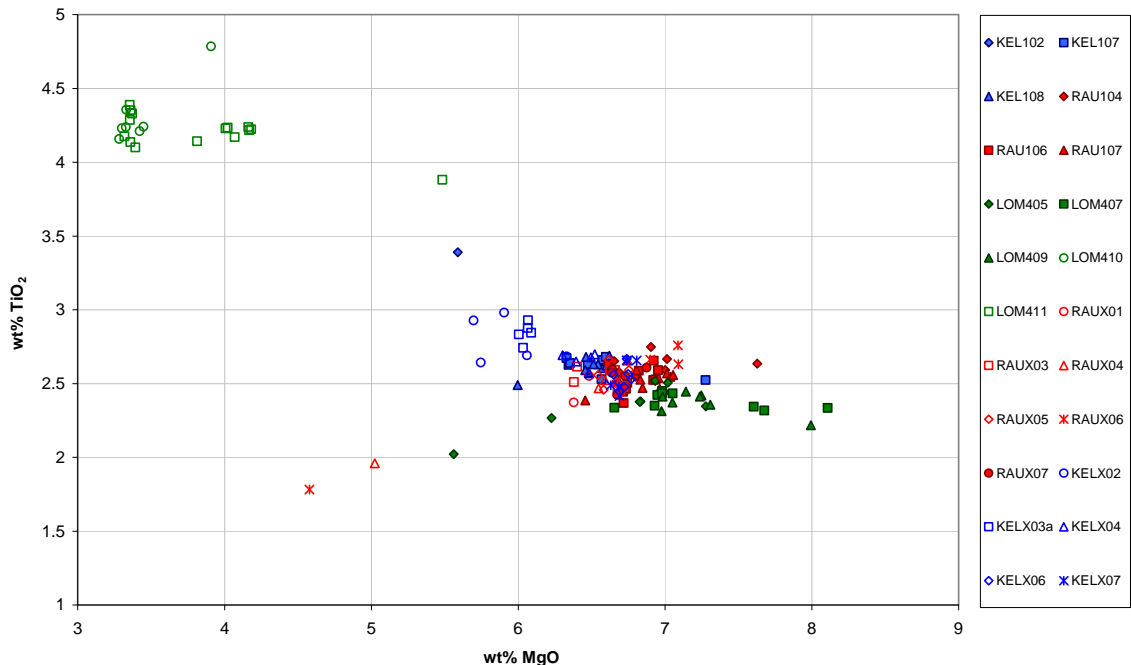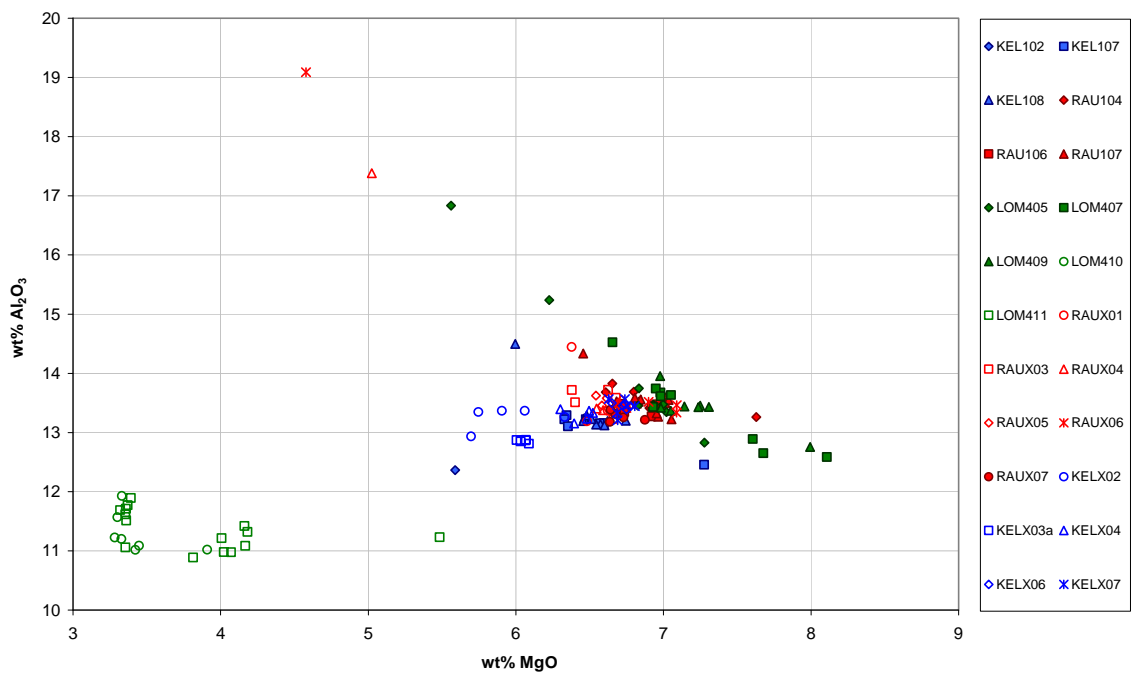
Figure 3.3 (above): Al₂O₃ vs. MgO for Icelandic samples.
Figure 3.4 (below): MnO vs. MgO for Icelandic samples. Solid symbols indicate hyaloclastite, open symbols indicate lava. Data points are color-coded by location.

36
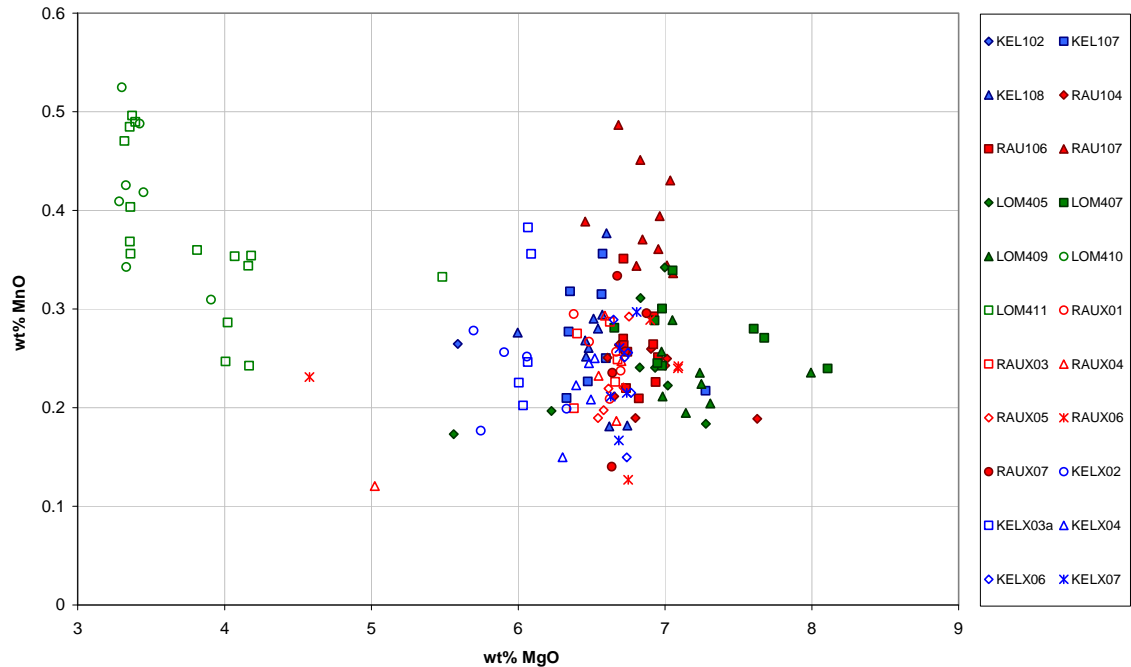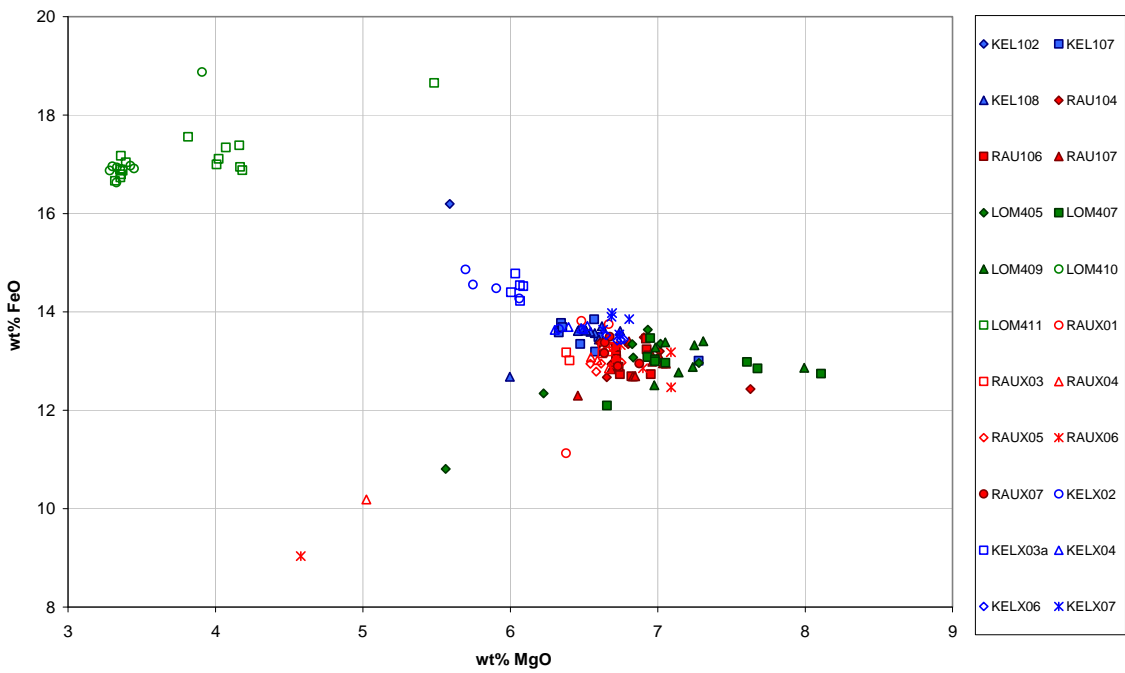
Figure 3.5 (above): FeO vs. MgO for Icelandic samples.
Figure 3.6 (below): CaO vs. MgO for Icelandic samples. Solid symbols indicate hyaloclastite, open symbols indicate lava. Data points are color-coded by location.
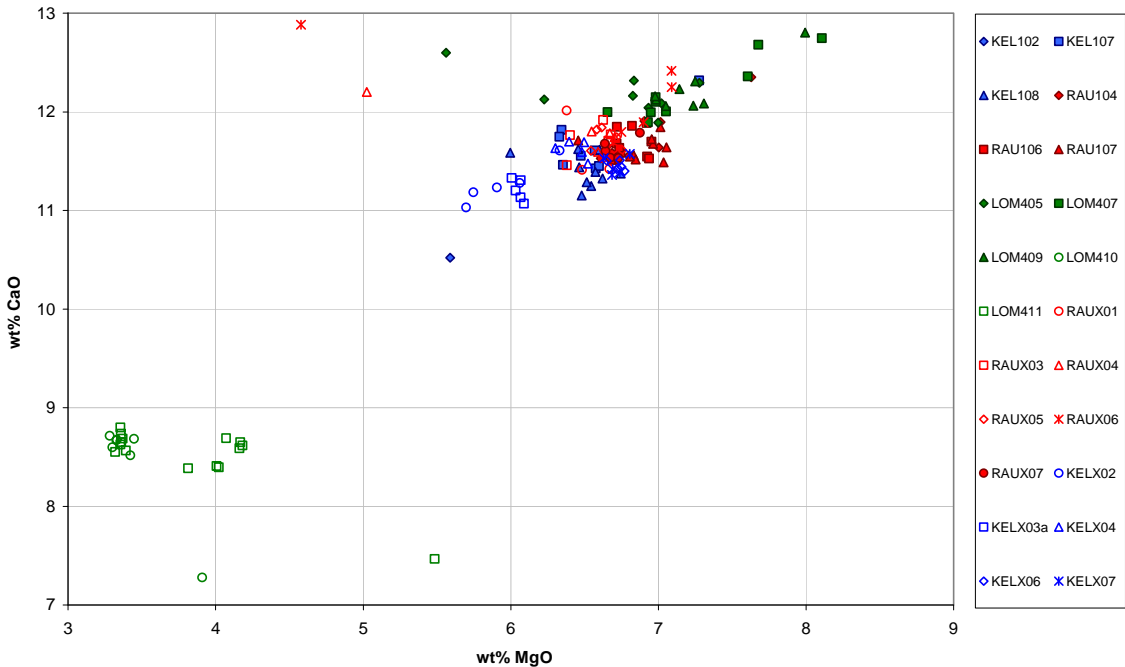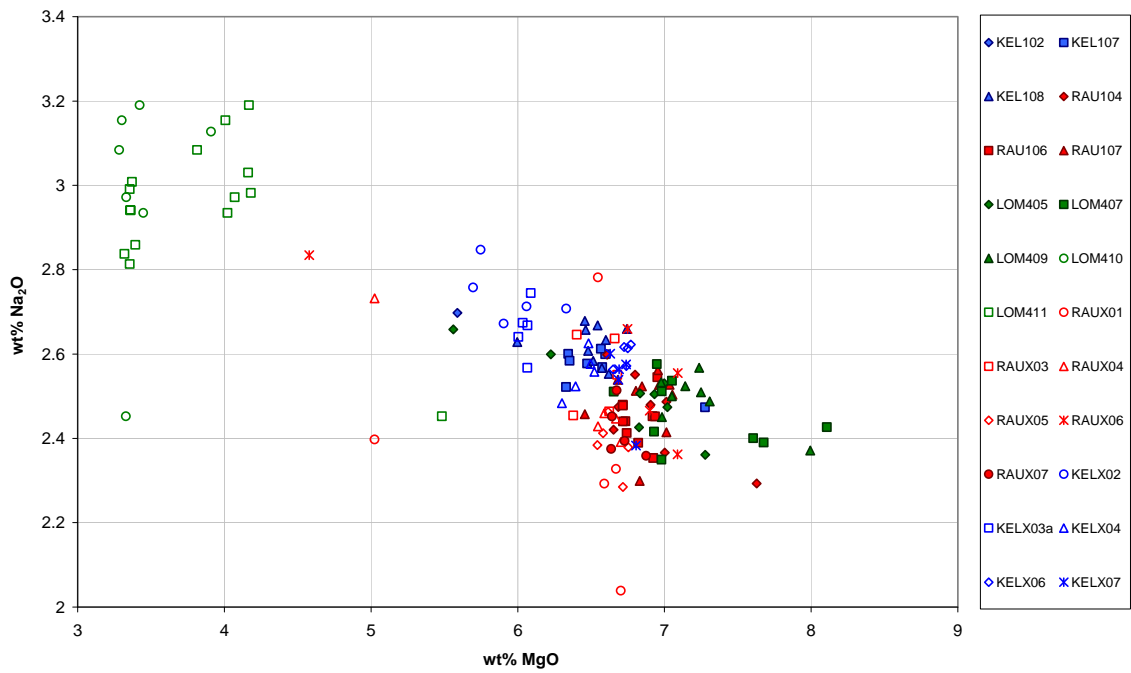
Figure 3.7 (above): Na₂O vs. MgO for Icelandic samples.
Figure 3.8 (below): K₂O vs. MgO for Icelandic samples. Solid symbols indicate hyaloclastite, open symbols indicate lava. Data points are color-coded by location
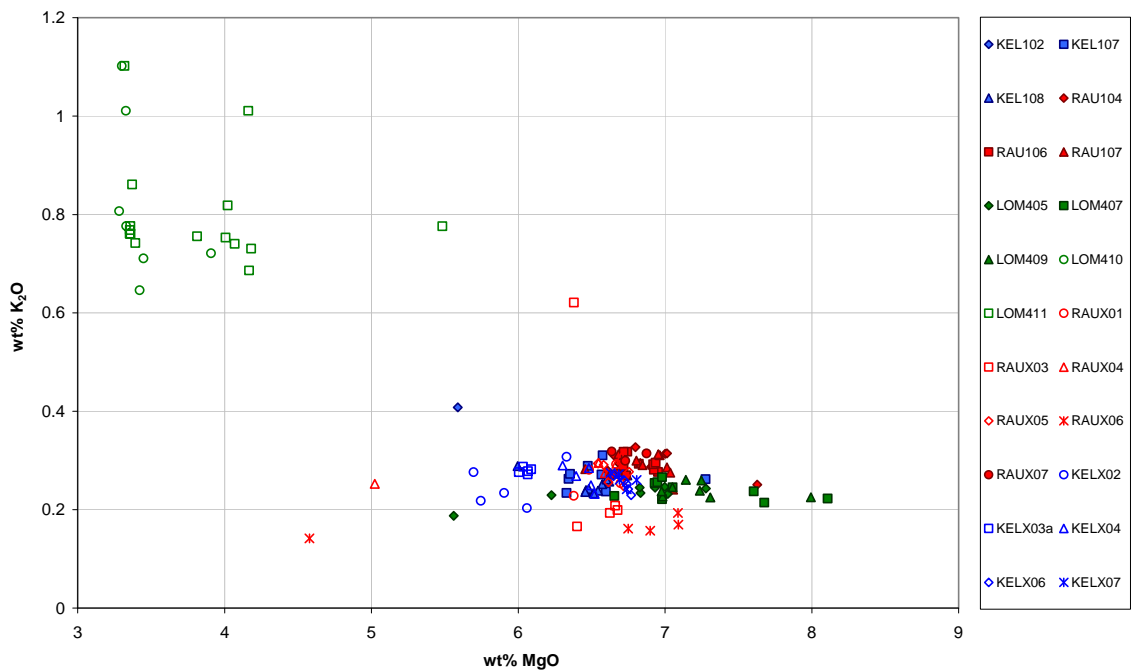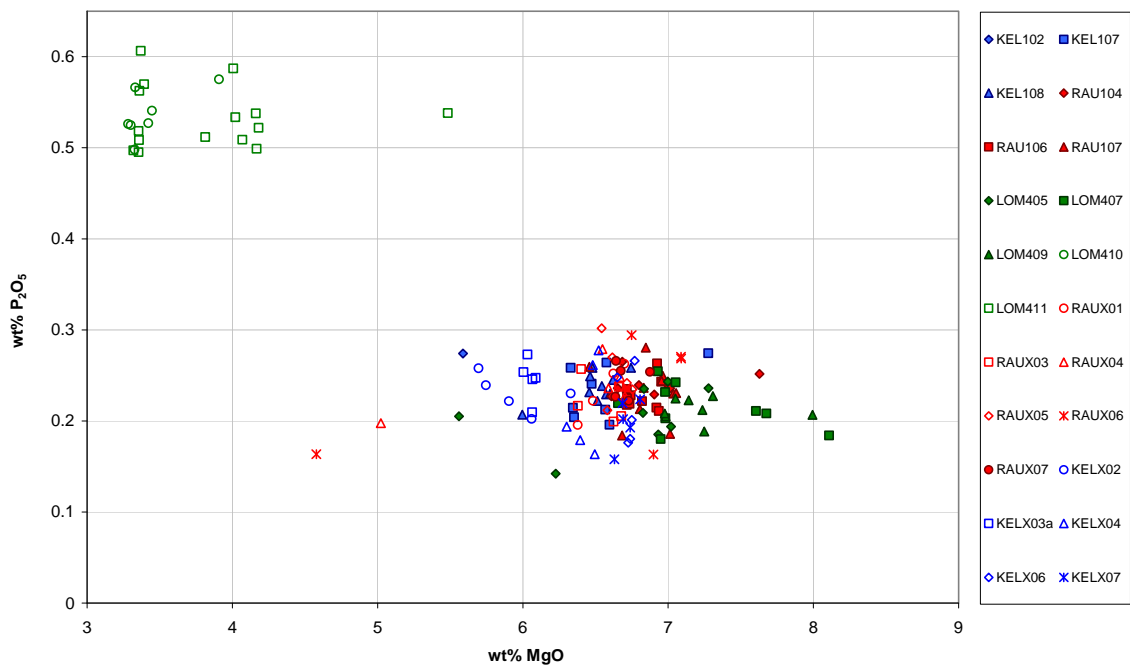
Figure 3.9: P_2O_5 vs. MgO for Icelandic samples. Solid symbols indicate hyaloclastite, open symbols indicate lava. Data points are color-coded by location.

Figure 3.10: REE patterns for Icelandic samples. Solid symbols with dashed lines indicate hyaloclastite, open symbols with solid lines indicate lava. Data points are color-coded by location.
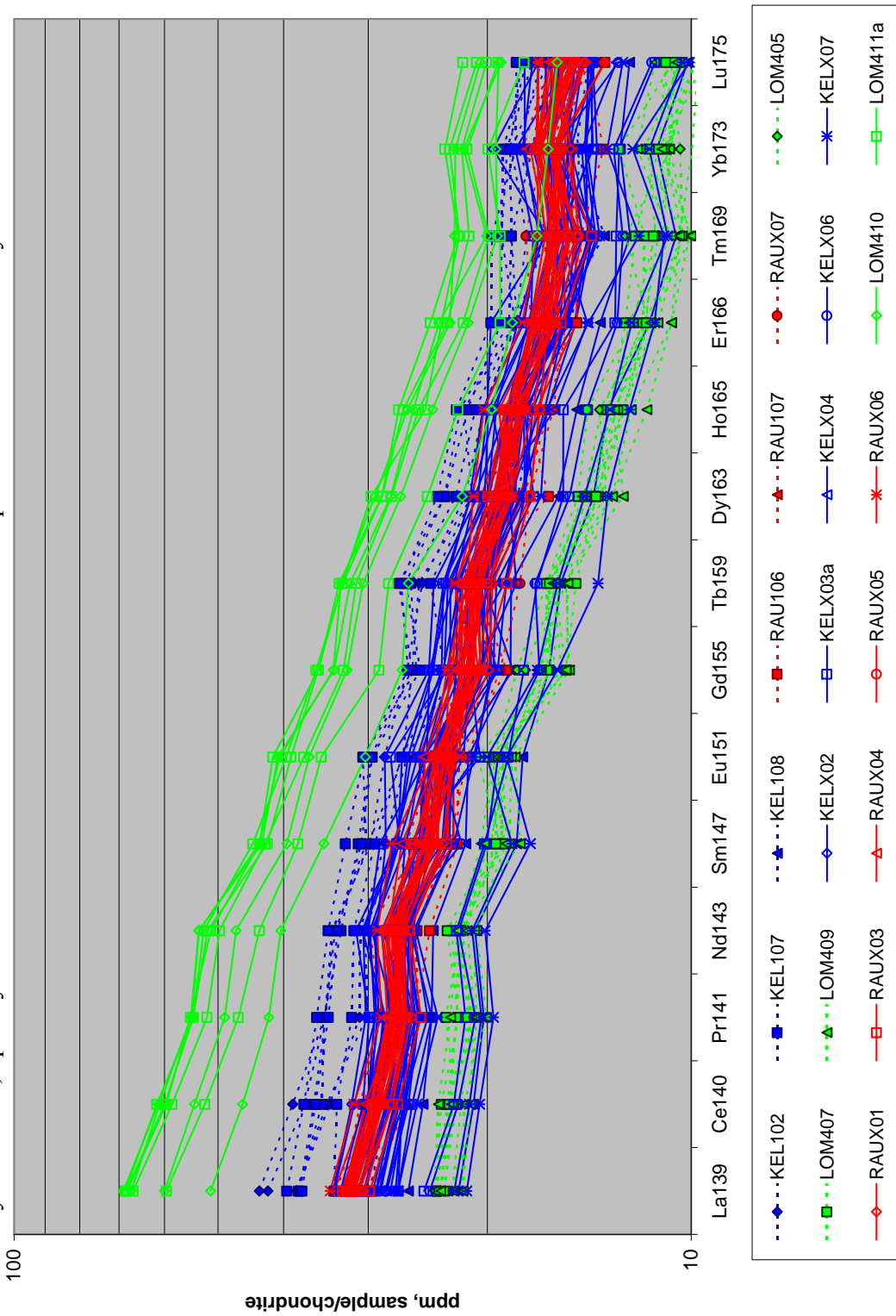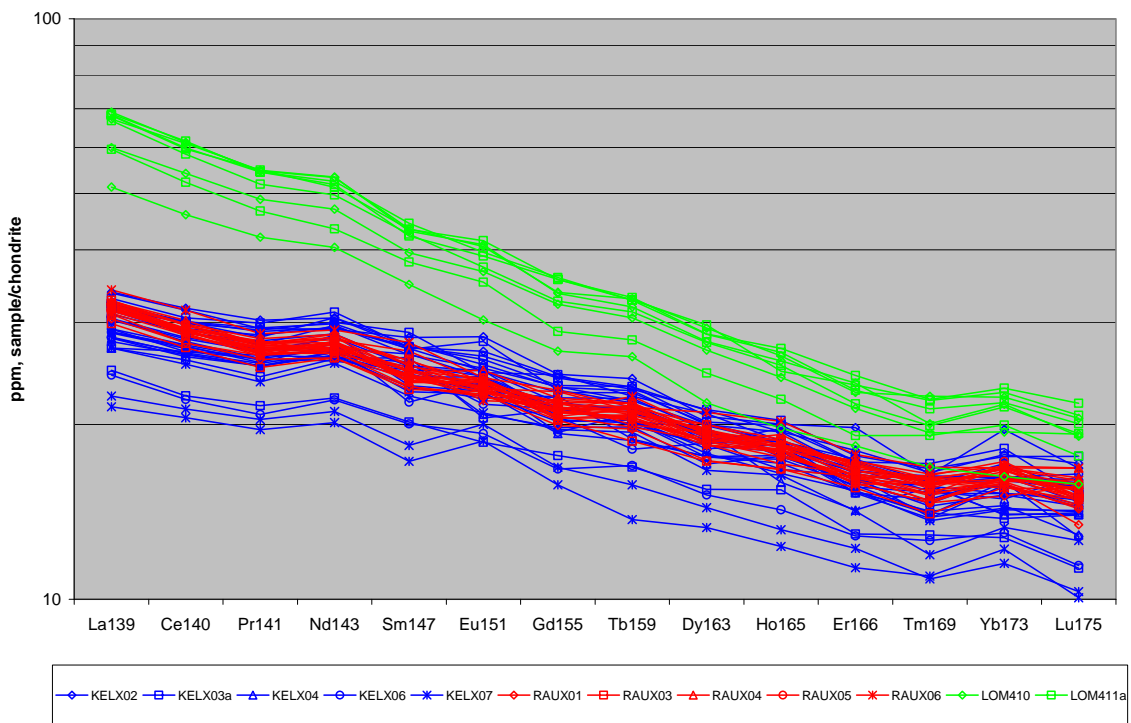
Figure 3.11 (above): REE in Icelandic lava samples.

Figure 3.12 (below): REE in Icelandic hyaloclastite samples. Solid symbols with dashed lines indicate hyaloclastite, open symbols with solid lines indicate lava. Data points are color-coded by location.
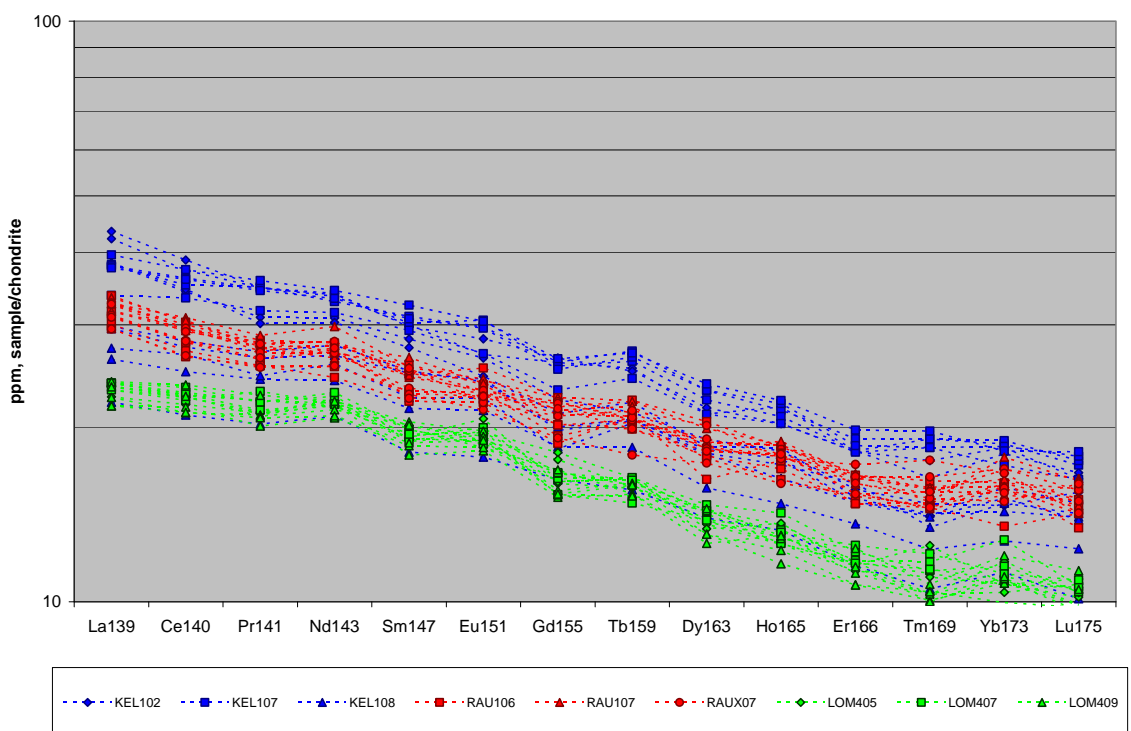
CHAPTER IV

DISCUSSION AND IMPLICATIONS OF VOLCANIC MAGMA-HOST
INTERACTION IN SOUTH ICELAND

The potential eruption sequence presented below is provided to help in visualization of apophysis-forming processes, which will be discussed in the subsequent section of this chapter.

Proposed General Eruption Sequence

Although no source fissures have been identified previously, geochemical data collected in this study are consistent with origin from fissures similar to modern Laki, or perhaps nearby parallel fissures approximately 50 km northwest of the observed termini of the flows. Hyaloclastite—which requires sub-aqueous magma effusion—overlying lava which is cube-jointed at the contact and columnar-jointed beneath suggests that both subaerial and subaqueous eruptions happened in relatively quick succession. Some areas of hyaloclastite display fragments of basaltic pillows, which are also indicative of lava interacting with water. I propose that cube-jointed basalt represents the upper portion of an initially subaerial lava flow that was quenched and fractured due to deposition of wet, relatively cool hyaloclastite. Its formation allowed the inner hot magma to remain insulated, cooling much more slowly over many months, which yielded the columnar basalts commonly seen in these eruptive units. The fact that cube-jointing is always seen over columns is strong motivation for adopting a partly subaerial eruptive and emplacement sequence.

It seems likely that an eruption along the source fissure(s) propagated from a subaerial portion of the fissure—yielding the basaltic lavas, which began flowing down-slope—to a subglacial portion of the fissure. Since volcanoes with subglacial conduits typically melt the surrounding ice to create a sub- or intra-glacial lake even in times of quiescence (Thordarsson and Höskuldsson, 2003), once this particular fissure started erupting subglacially, eruption into this lake led to formation of the large volume of hyaloclastite observed. Such an eruption would have led to increased meltwater production, which led to the volume of water and hyaloclastite exceeding the capacity of the lake. In order to relieve pressure of this material within or under the glacier, a jökulhlaup ensued which bore both water and hyaloclastite downslope, covering the subaerially-erupted lava which preceded it. The flame-like apophyses and other basalt disaggregation structures were then injected into the overlying hyaloclastite. This eruptive sequence occurred multiple times, with intervening periods of increased glaciation, stream flow, or non-eruptive-event jökulhlaups marked by deposition of diamictite (A17).

Alternatively, it is possible that the sequence of the eruption described above happened in reverse, such that eruption propagated from subglacial to subaerial, meaning hyaloclastite was deposited first, and was followed by subaerial basaltic lava which covered it. Since the lava was more dense than the hyaloclastite, it "burrowed" into the underlying hyaloclastite (cf. Duffield et al., 1986) and eventually sank to the base of the hyaloclastite unit (C.R. Bacon, pers.com. 2007). This is not the preferred interpretation of this author; however, further investigation is needed to rigorously evaluate this possibility.

Fluid-Mechanical Constraints on Apophysis Formation

It is clear from field observations (see Appendix A) that once hyaloclastite overlies basaltic lava, interaction between the two materials leads to the formation of flame-like apophyses composed of cube-jointed lava that invade the hyaloclastite host. Quickly after eruption, the lava presumably developed a chilled crust which insulated the inner portions of the flow and allowed it to propagate down valley. Evidence of this crust may be preserved at Kotafjall (Figures A19, A20, A21), where exposures display a combination of vesiculation and segregation veins that transported volatiles toward the outside of the flow. If these formations are indeed the first crust of the lava flow, they should be visible throughout the lava in the Siða-Fljotshverfi district—but they are not. This could be due to the limitations of the observations, since the majority of outcrops were high on cliffs and observed remotely, or because the crust was removed, perhaps due to cracking and being recycled into the interior of the flow, erosion during hyaloclastite deposition, or is simply very thin; the latter option seems most plausible. Conversely, lack of an initial subaerial crust may indicate that the lava flow was not subaerial (cf. Smellie, 2008), although this interpretation is not preferred (see below).

I propose the following sequence of events once lava was overlain by hyaloclastite. Even with an insulating crust present on the lava flow, heat diffused from the still-molten interior of the lava into the overlying hyaloclastite matrix, which still would have been saturated with water. As heat diffused upward, the hyaloclastite—and the water in the pore spaces—became heated, leading to thermal expansion of the interstitial water. This expansion resulted in an increase in the fluid pressure in the hyaloclastite. Since the lava under the crust was still molten, and the overlying

hyaloclastite still contained water, it is highly probable that both materials had dynamic

interiors. These disturbances led to fractures in the lava crust. It is likely that these

fractures occurred in groups, because field observations indicate that apophyses normally

occur in close proximity to other apophyses and disaggregation structures, and only

rarely as single intrusions. As soon as a crust fracture occurred, molten lava from the

interior of the flow injected upward into the weaker hyaloclastite matrix due to a

manometer effect (Figure 4.2) with local destabilization of the hyaloclastite. Rapid

introduction of molten (albeit fast-cooling post-injection) lava vaporized the water in the

hyaloclastite matrix, leading to a strong increase in the pore fluid. Since high pressure

tends to dissipate toward areas of lower pressure, the high-pressure fluids migrated away

from the injection location, dragging the hyaloclastite particles with it. The dragging

apart of the hyaloclastite matrix weakened it, allowing more injection to occur. The

apophyses propagated upward into the hyaloclastite not by a smooth injection, but

incrementally, due to tip propagation (Figure 4.3).

As the tip of the apophysis heated the surrounding pore water, internal pressure

increased and added torque on the tip. Diffusion of pressure away from the vicinity of

the lava led to dragging apart of the hyaloclastite matrix, allowing the apophysis to

intrude more, which temporarily relieved the internal pressure in the apophysis. This

repeated until the injecting lava could no longer overcome the tensile strength of the

hyaloclastite, which likely happened when the lava's heat diffused enough to allow a

thicker rind to form. Following work by Younes and Engelder (1999), in a system with a

lava-hyaloclastite boundary impermeable to mass transfer (Figure 4.3),

$$d\tau = pz'dz,$$
(4.2)
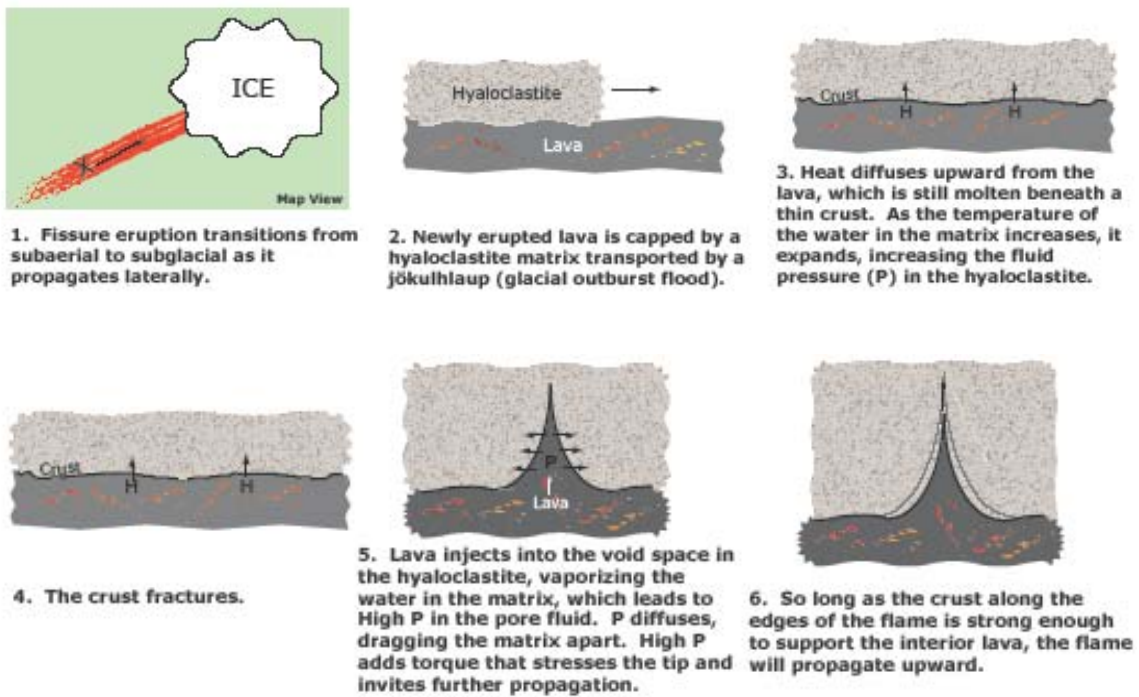
Figure 4.1: Cartoon illustrating probable general eruption sequence and flame-like apophysis formation mechanism.
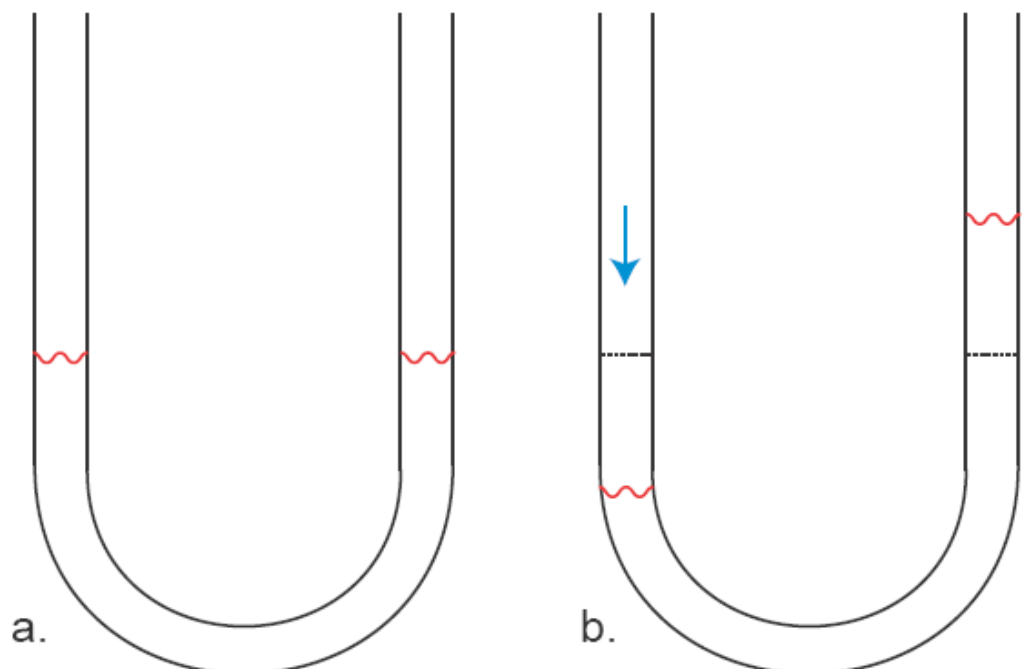
Figure 4.2: A simple manometer. a.) Liquid in a U-tube rises to the same height on both sides of the tube under normal conditions. b.) When a force is applied to the liquid on the left side of the tube, thereby lowering the level of the liquid, the liquid on the right side responds by rising the same amount the liquid on the left dropped.

where p is pressure in the lava, z' is the distance over which p diffuses, and z is length normal to τ torque, so that

$$\int_0^Z d\tau = p\int z'dz , \qquad (4.3)$$

where Z is a measure of the distance along which the hyaloclastite is behaving rigidly. However, lava intrusion into hyaloclastite results from a permeable boundary, so

$$d\tau = F_D z'dz , \text{ and } \int_0^Z d\tau = F_D \int z'dz , \qquad (4.4, 4.5)$$

where F_D is the force of drag exerted by the flux of fluid away from the lava. Following work by Furbish (pers.com. 2007), final apophysis height is dependent on a, thickness of the lava that has density ρ_a and flows over a surface inclined at an angle θ, and b, the thickness of the hyaloclastite layer with bulk density ρ_b (Figure 4.4). It is also necessary to consider γ, the residual head of the lava before loading by the hyaloclastite. Assuming intrusion at low Reynolds number, the maximum apophysis height $h_a(x)$ above the lava surface $\gamma(x)$ is

$$h_a(x) = \tan\theta x \qquad (4.6)$$

Once hyaloclastite loading is taken into account, maximum apophysis height, $h_b(x)$ is

$$h_b(x) = \tan\theta x + \frac{\rho_b}{\rho_a}b , \qquad (4.7)$$

which, if θ or x is very small, reduces to

$$h_b = \frac{\rho_b}{\rho_a}b \qquad (4.8)$$
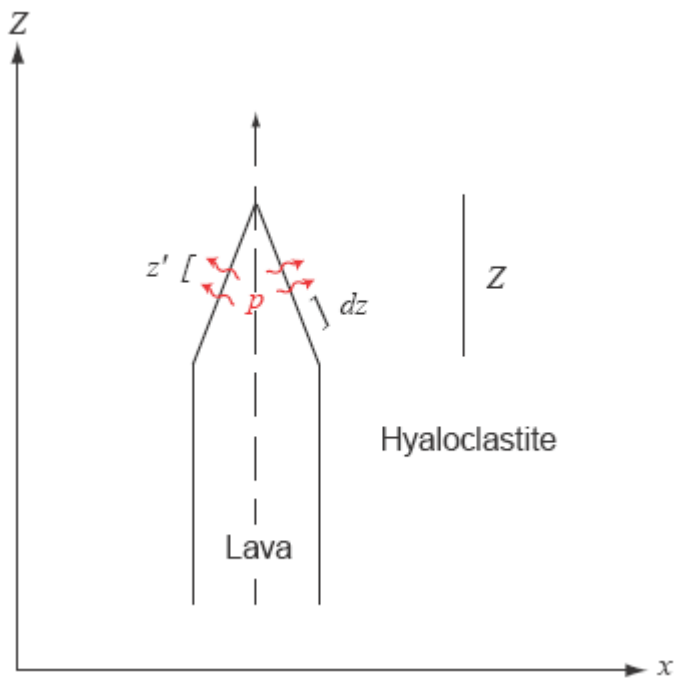
Figure 4.3: A propagating apophysis tip.

Figure 4.4: Diagram of lava-hyaloclastite system. From D.J. Furbish.
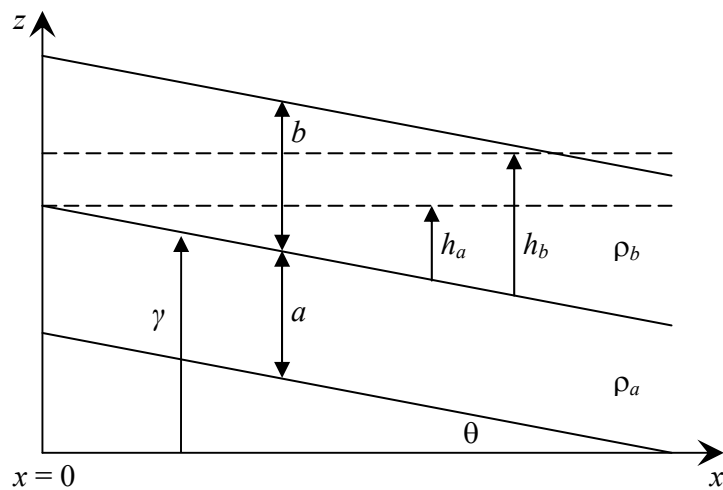
Discussion of Elemental Data

Major and trace element data obtained from glasses in field samples play an important role in determining eruption sequence and conditions. Performance of a 2-sample Student t-test and an ANOVA test for similarity for all major elements analyzed from Keldunúpur, Rauða Canyon, and Lómagnúpur lava and hyaloclastite glass samples show that lava glasses between locations are significantly different, as are hyaloclastites (see Appendix G). This is shown in the graphical presentation of the data. Among these localities, only Keldunúpur lava and hyaloclastite glasses are statistically the same; lava and hyaloclastite glasses from Rauða Canyon differ slightly and those from Lómagnúpur are very different. Additionally, lavas are different at each location, as are hyaloclastites, but samples at Rauða Canyon and Keldunúpur are much closer than those from Lómagnúpur.

Figure 3.6 illustrates the trend of increasing compositional evolution from Rauða Canyon hyaloclastites to lavas and Keldunúpur hyaloclastites and lavas, with Rauða lavas and Keldunúpur hyaloclastites overlapping. This pattern is also visible particularly with regard to MgO, FeO, and Al_2O_3. When considering other elements, Keldunúpur lavas always appear graphically as distinctly slightly more evolved than their hyaloclastites, while Rauða Canyon lavas and hyaloclastites commonly show no apparent distinction. REE patterns corroborate these findings. Keldunúpur and Rauða Canyon samples show very good correlation, with Rauða Canyon samples grouped tightly, independent of source material. Keldunúpur samples showed a wider range of variation both within and between materials, but still demonstrate a similarity to the Rauða Canyon eruptive products. Both materials from Keldunúpur and Rauða Canyon show compositions very

similar to those reported in glasses from the 1783 Laki eruption (Metrich et al., 1991), consistent with this study's assertion that the source fissures of the Siða-Fljotshverfi district were either proto-Laki, or in close proximity to Laki.

Since the Lómagnúpur samples deviate substantially from the others, particularly the lava glasses, it is likely that they had a distinctly different history. It is plausible that the same magma sourced both the lava and the hyaloclastite at Lómagnúpur, but if so, the lava fractionated further during flow and emplacement. The lava might also represent the upper, more evolved portion of a magma chamber that erupted first, and the hyaloclastite formed from the more primitive magma in the bottom of the chamber. However, a connection between the eruptive products at Lómagnúpur with those at Keldunúpur and Rauða Canyon is speculative at best.

It seems likely that the lava and hyaloclastite units sampled from Lómagnúpur were either not erupted as part of the same eruption, were from an eruption that was sourced from two separate chambers, or were from an entirely different set of fissures than the Keldunúpur and Rauða Canyon samples. Smellie (2008) obtained major element data from hyaloclastite glasses from a different outcrop at Lómagnúpur, and obtained compositions that were distinctly more evolved than my average values of Lómagnúpur hyaloclastites (higher SiO_2, FeO, Na_2O, K_2O; lower MgO, CaO). Although it is likely that Smellie (2008) and I sampled different depositional units, it is clear that Lómagnúpur has a complicated history and that will take more thorough investigation to do justice to its interpretation.

Summary

Geochemical analysis of glasses from lava and hyaloclastite samples from Rauða Canyon, Keldunúpur, and Lómagnúpur generally support the suggested eruptive sequence proposed at the beginning of this chapter. No dating technique currently exists that will give a resolution sufficient to determine if lava-forming or hyaloclastite-forming magma erupted and was emplaced first if they were indeed erupted almost concurrently. The coincidence of eruptive products sampled from Rauða Canyon and Keldunúpur suggests a close spatial and temporal eruptive relationship, and a source from a near-Laki system. The close relationship shown between eruptive products at these two locations supports this study's mechanism for basaltic apophysis formation, which requires a virtually concurrent emplacement of lava and hyaloclastite. The large difference between Rauða Canyon and Keldunúpur samples and the samples from Lómagnúpur suggests that the depositional unit sampled at Lómagnúpur was distinct in its source from those sampled at Rauða Canyon and Keldunúpur, which appear to be much more closely related.

CHAPTER V

A PLUTONIC EXAMPLE OF MAGMA-HOST INTERACTION: DISAGGREGATION
OF BASALT IN GRANITIC MAGMA, AZTEC WASH PLUTON, NEVADA

Geologic History

Aztec Wash pluton (AWP) is a mid-Miocene (15.75 Ma) pluton exposed over an

area of 50 km^2 (Falkner et al., 1995; Miller and Miller, 2002) in the Eldorado Mountains

of southern Nevada. It is part of the larger Colorado River Extensional Corridor

(CREC)(e.g. Falkner et al., 1995; Miller and Miller, 2002), a north trending, 50-100 km-

wide extensional zone that underwent large-magnitude regional extension 16-13 Ma (e.g.

Harper et al. 2004). Emplacement of AWP occurred concurrently with east-west

extension. The pluton now straddles a northwest-trending antiformal accommodation

zone (Miller et al. 2005). Large sections of the mid-to-upper crust 15 km thick [e.g.

Harper et al., 2004] are exposed and tilted up to 90°, and AWP itself is divided by

faulting into three structural blocks—western, central, and eastern (e.g. Harper et al.,

2004)(Figure 5.1). The western block, WNW of the Tule Wash Fault, has been tilted

slightly WNW; the central block, between the Tule Wash Fault and the Pipe Canyon

Fault, is dropped down and lacks tilt markers; and the eastern block is tilted steeply ENE

(e.g. Harper et al., 2004).
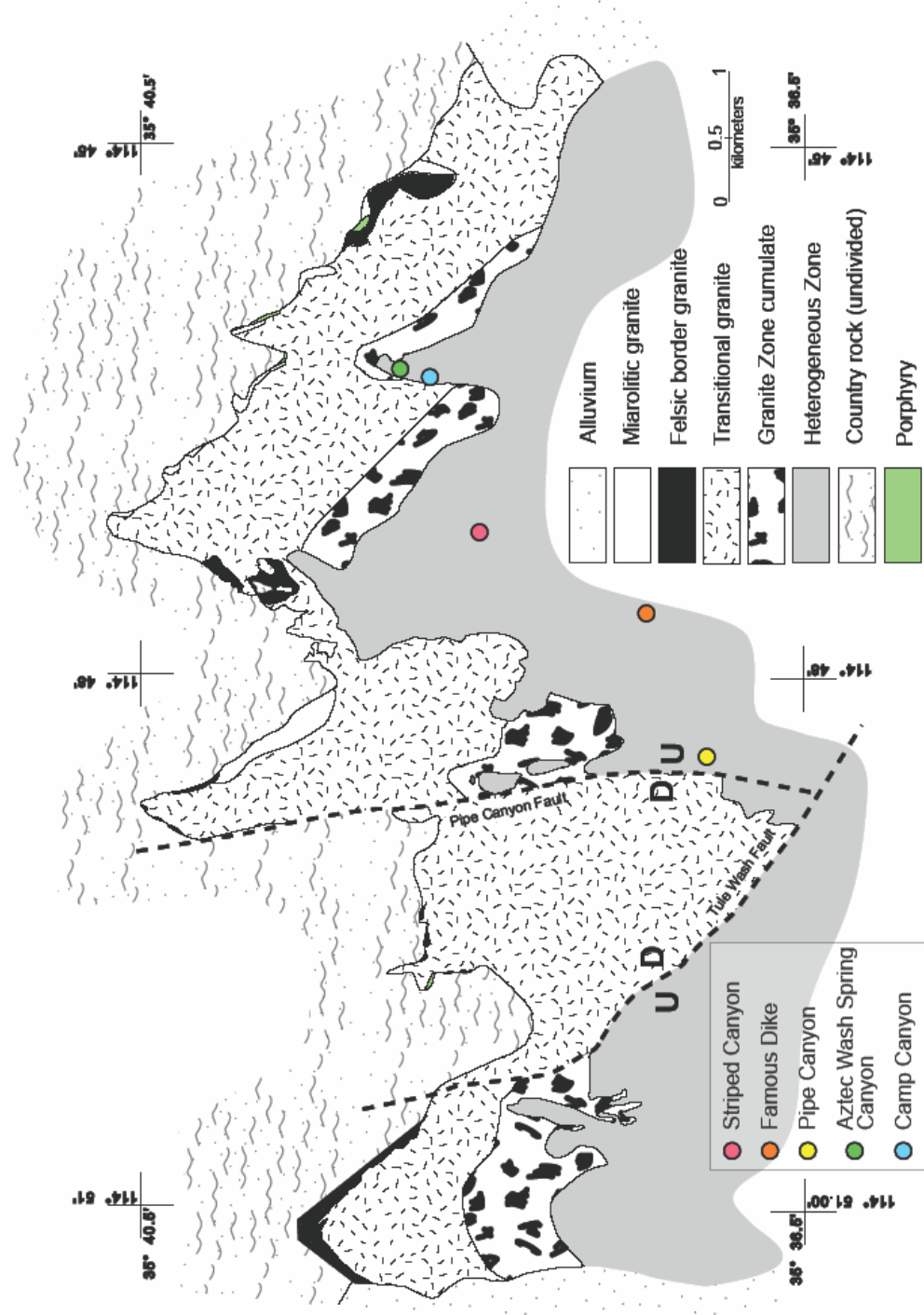
Figure 5.1: Map of granite zone in Aztec Wash pluton, NV. Modified from Harper et al., 2004.

Description of Field Area

Research for this study was carried out in several locations throughout the easternmost section of AWP: the informally name Pipe Canyon, Famous Dike, Striped Canyon, Aztec Wash Spring Canyon, and Camp Canyon (Figure 5.1). These locations were chosen because they each showed a different stage of the mafic magma disaggregation process. Pipe Canyon is notable for its intact mafic sheets and a small amount of pillow formation, while Striped Canyon, Aztec Wash Spring Canyon, and Camp Canyon display large, discrete pillow-like structures without the noticeable presence of well-defined mafic sheets. Famous Dike contains both basaltic sheets and pillows, but they are located within a felsic dike as opposed to in vertically stacked layers and may represent a different mechanism of formation and disaggregation. All locations are located in the heterogeneous zone (HZ) first identified by Falkner et al. (1995). The HZ is composed of interspersed mafic (basalt, gabbro, diabase), intermediate (diorite, quartz monzodiorite) and felsic (granite, quartz monzonite) rocks that show evidence of intermingling while still molten.

Previous studies of AWP (Falkner et al., 1995; Patrick and Miller, 1997; Miller and Miller, 2002; Harper et al., 2004) have interpreted basaltic intrusions to have spread laterally across the extant floor of the intrusion from feeder zones, younging upward as mafic sheet and accumulated granitic material built the floor upward. Therefore, basaltic sheets in this study are considered to have intruded sequentially to build up a basaltic sheet "pile" at a given location. Evidence of a potential basaltic sheet pile is most clearly seen at Pipe Canyon (see B13 in Appendix B).

Description of System Materials and Field Observations

This study focuses on interaction between basaltic pillow-like structures (PLS) and granites. Consequently, phenocrysts, textures, and relationships within and between mafic PLS and their felsic hosts in the immediate vicinity were the focus of both field and petrographic observations.

Basaltic Pillow-like Structures (PLS) and Sheets

Basaltic PLS (which may also be referred to as pillows, not to be confused with submarine pillow lavas) range from 10 cm to >5 m in length and width, and generally appear oblate (minimum dimension perpendicular to layering) to equidimensional when exposed in 2 dimensions (Figures B6 and B7 in Appendix B). Width (paleo-side-to-side) to height (paleo-top to –bottom) ratios range from 0.33 to 5, with the majority being >1 (Table 5.1). Some pillow interiors consist of fine-grained basalt lacking phenocrysts, but others contain up to ~10-20 % phenocrysts that become more abundant near the edges of the pillow, particularly of plagioclase, but also of hornblende and rarely of altered pyroxene. Most pillows, however, demonstrate a coarsening toward the center of the pillow. Pillow edges display varying stages of crenulation, indicative of liquid-liquid interaction (C.F. Miller, pers.com. 2007). A majority of observed pillows in AWP show more crenulation on the paleo-top, with the paleo-bottom of the pillow showing distinctly less—or even no—crenulation (Figures B4 and B11). Most pillows display chilled margins up to 2 cm wide (Figure B3 in Appendix B), which are more noticeable in areas with little or no crenulation.

Name	Width (cm)	Height (cm)	W:H ratio
B001	105	43	2.44
B002	230	240	0.96
B003	39	57	0.68
B004	150	42	3.57
B005	35	7	5.00
B006	20	4	5.00
ASC101	145	57	2.54
ASC102	81	70	1.16
ASC103	40	119	0.34
ASC201	44	72	0.61
ASC301	435	90	4.83

Table 5.1. Measurements of PLS from AWP, Nevada.

Basaltic sheets—presumably the precursor to PLS—display many of the same characteristics as the PLS. Sheets observed in Pipe Canyon are typically 0.2 to 1 m thick, and occur in a pile at least 50 m in height (Figure B13). Sheets within the pile are frequently interspersed with felsic layers parallel to the sheets. Felsic injections upward in the form of flame structures are also seen, but are less common. In general, thicker basaltic sheets have thinner felsic injections surrounding them than thinner basaltic sheets. It should also be noted that sheets themselves are not always continuous on an outcrop scale, in some cases displaying granite-filled discontinuities.

The basaltic sheets at Pipe Canyon display chilled margins of 2-5 mm on both the paleo-top and bottom of the sheet. Similarly to basalt PLS, the paleo-down edges of sheets tend to be smoother than the paleo-up edge, with the top appearing more crenulate than the bottom, and the bottom frequently being flat. When considering the entire pile, however, the bottom sheets in the pile appear much more disaggregated and rougher than the upper sheets.

Throughout the pluton, abundance of PLS decreases as distance from sheet piles increases. In close proximity to the sheets, pillows are small and concentrated, while

100s of m away, pillows are larger and more spread out (Figures B1, B2, B8).

Implications of these observations will be discussed in the next chapter.

Felsic Host

As previously mentioned, intermediate-to-felsic rocks in Aztec Wash pluton vary
in composition and texture; however, the rocks that host the mafic sheets and pillows
observed in this study are overwhelmingly granites and quartz monzonites, and
consequently the terms "felsic" and "granite" will be used interchangeably for the
duration of this report. The granite that hosts basalt sheets and disaggregation products
displays several interesting features that are ubiquitous in the 5 study areas of this
research.

Most notable are several characteristics of plagioclase and potassium feldspar
phenocrysts in the granite. The vast majority of feldspars are euhedral, though rounded
white "ghost" feldspars, which I interpret to result from replacement of potassium
feldspar by plagioclase during interaction with mafic magma, are commonly present in
the vicinity (several meters) of basaltic sheets or pillows. Rapakivi-textured feldspars
(potassium feldspar cores with plagioclase rims) appear to represent a less advanced stage
of this replacement process texture. Rapakivi phenocrysts are common in host granites,
with crystals reaching to 1 cm in length. Hornblende and biotite phenocrysts are also
present. Immediately beneath basaltic pillows, the granite host commonly displays a
zone ~2-3 mm wide that is slightly peach in color, fine-grained, and completely
phenocryst-free (Figures B18, B19). Abutting this phenocryst-free zone on its lower side
is a zone 2-3 cm wide that contains very densely-packed phenocrysts, primarily feldspars

with minor biotite and hornblende (Figures B3, B18, B19). This "feldspar packing" is also visible in the felsic material under basaltic sheets, although less pronounced. This phenomenon is sometimes present on the paleo- tops of pillows, but there a phenocryst-free zone is absent.

A striking feature in the granite present between successive basaltic sheets at Pipe Canyon is schlieren bands located in the middle of felsic material between sheets. Schlieren here may stretch for over 10 m (Figure B15).

Petrographic Observations

Petrographic analysis was carried out on 11 samples from Aztec Wash pluton. Please refer to Table 5.2 for a list of samples and their locations. Thin sections were obtained that encompassed the boundary between granite and basalt pillow in order to investigate changes or clues to the disaggregation process at the crystal scale. Felsic zones, mafic zones, and the boundary between the two in each section were examined individually, and the samples were taken from tops, bottoms, and sides of pillows (see Table 5.2).

The mafic rocks examined had 30-55% plagioclase feldspar, 0-20% clinopyroxene, 5-20% opaques (mainly magnetite, likely some ilmenite), 5-30% biotite, 15-30% hornblende, and trace amounts of sphene and apatite. Crystals are generally of similar size, with the exception of some larger (>400μm) pyroxene and plagioclase phenocrysts. Many plagioclase crystals show rims with opaque inclusions. Plagioclase crystals with opaque inclusions in their interiors are also not uncommon. Clinopyroxene

Table 5.2: Aztec Wash pluton, Nevada, sample locations and outcrop descriptions.

ID	Location Name	Latitude*	Longitude*	Description of Outcrop
#1	North of Pipe Canyon, AWP, NV	N35° 39.187'	W114° 48.649'	Partially exposed pillow, side
ASC202	Aztec Wash Spring Canyon, AWP, NV	N35° 39.589'	W114° 46.334'	Partially exp.pillow bottom, on north wall
ASC203	Aztec Wash Spring Canyon, AWP, NV	N35° 39.590'	W114° 46.332'	Partially exp.pillow top on north wall
ASC301	Aztec Wash Spring Canyon, AWP, NV	N35° 39.584'	W114° 46.331	South wall pillow field, side
ASC401	Aztec Wash Spring Canyon, AWP, NV	N35° 39.573'	W114° 46.376'	North wall angular pillow field, side
ASC501	Aztec Wash Spring Canyon, AWP, NV	N35° 39.558'	W114° 46.376'	South side pillow field, top
ASC502	Aztec Wash Spring Canyon, AWP, NV	N35° 39.561'	W114° 46.382	South side pillow field, bottom
SC001	Striped Canyon, AWP, NV	N35° 39.458'	W114° 47.398'	Exposed surface on canyon floor, side
SC002	Striped Canyon, AWP, NV	N35° 39.456'	W114° 47.333'	Exposed surface on canyon floor, top
SC003	Striped Canyon, AWP, NV	N35° 39.454'	W114° 47.300'	Exp. on canyon floor, bottom and top
SC004	Striped Canyon, AWP, NV	N35° 39.457'	W114° 47.149'	Exposed surface on canyon floor, top

* Datum: NAD1983

phenocryst concentrations increase in some samples with proximity to the mafic/felsic boundary.

Granites at the contacts with basalts also display marked variations in modal abundances, although it must be noted that the felsic material observed in thin section is located within 2 cm of the basalt boundary, so these compositions are in no way indicative of felsic rocks pluton-wide. These samples were specifically chosen because they are likely to have interacted with or been influenced by basalt injection. They contain 15-45% plagioclase feldspar, 25-40% potassium feldspar, 10-20% quartz, 0-10% biotite, 10-20% hornblende, 0-15% opaques (magnetite and ilmenite most likely), <2-3% each of sphene and apatite, and <1% zircon. As in the basalt portions observed in thin section, many plagioclase crystals in the felsic portion display rims, with some rim widths equaling the diameter of the crystal core they surround. Many feldspar crystals also display inclusions of opaques, and small intergrowths with quartz are common. Granophyric texture is present in at least one sample (Fig. B12), and these intergrowths may be the beginning stages of forming granophyric texture. Approximately half of all

feldspar grains in the felsic portion of any sample display some sort of disequilibrium texture.

Overall, felsic crystals are much larger than mafic ones, reaching >2 mm in diameter. Some exceptional samples, however, show a uniform felsic grain size of ~500 μm. Quartz appears to be the final phase crystallized in major amounts. Sphene is widely seen in small amounts, and sphene crystals frequently have opaque inclusions (likely ilmenite). For detailed petrographic descriptions of basalt/granite samples from AWP, please see Appendix C.

CHAPTER VI

DISCUSSION AND IMPLICATIONS OF PLUTONIC MAGMA-HOST
INTERACTION IN AZTEC WASH PLUTON, NEVADA

Intrusion of hotter, more dense, and less viscous basaltic magma into an ambient

cooler, less dense, more viscous granitic magma chamber creates a dynamic environment

which facilitates the disaggregation of intruding basaltic sheets into isolated pillow-like

structures (PLS). This disaggregation may be the result of multiple factors, including

instabilities arising from mafic-felsic magma interaction, collapse of the felsic crystal-

rich mush along the floor of the chamber (cf. Wiebe, 1994, 2001; Miller and Miller,

2002), and auto-acephalation (Parker, 2000).

Fluid Mechanical Constraints on Mafic Disaggregation

Instabilities Arising from Basalt-Granite Interaction

Instabilities arise from interactions between mafic magma and felsic magma due

to their greatly contrasting physical properties. Basaltic magma is hotter, more dense,

and less viscous than its granitic counterpart. These differences in density, viscosity, and

temperature all play important roles in determining the rheologies of both mafic and

felsic components.

Analogues of Saffman-Taylor flow-front instabilities have been experimentally

shown to induce fingering in intruding magma sheets (Snyder and Tait, 1995)(Figure

6.1). Saffman-Taylor instability results from a less viscous fluid, in this case the basaltic

62
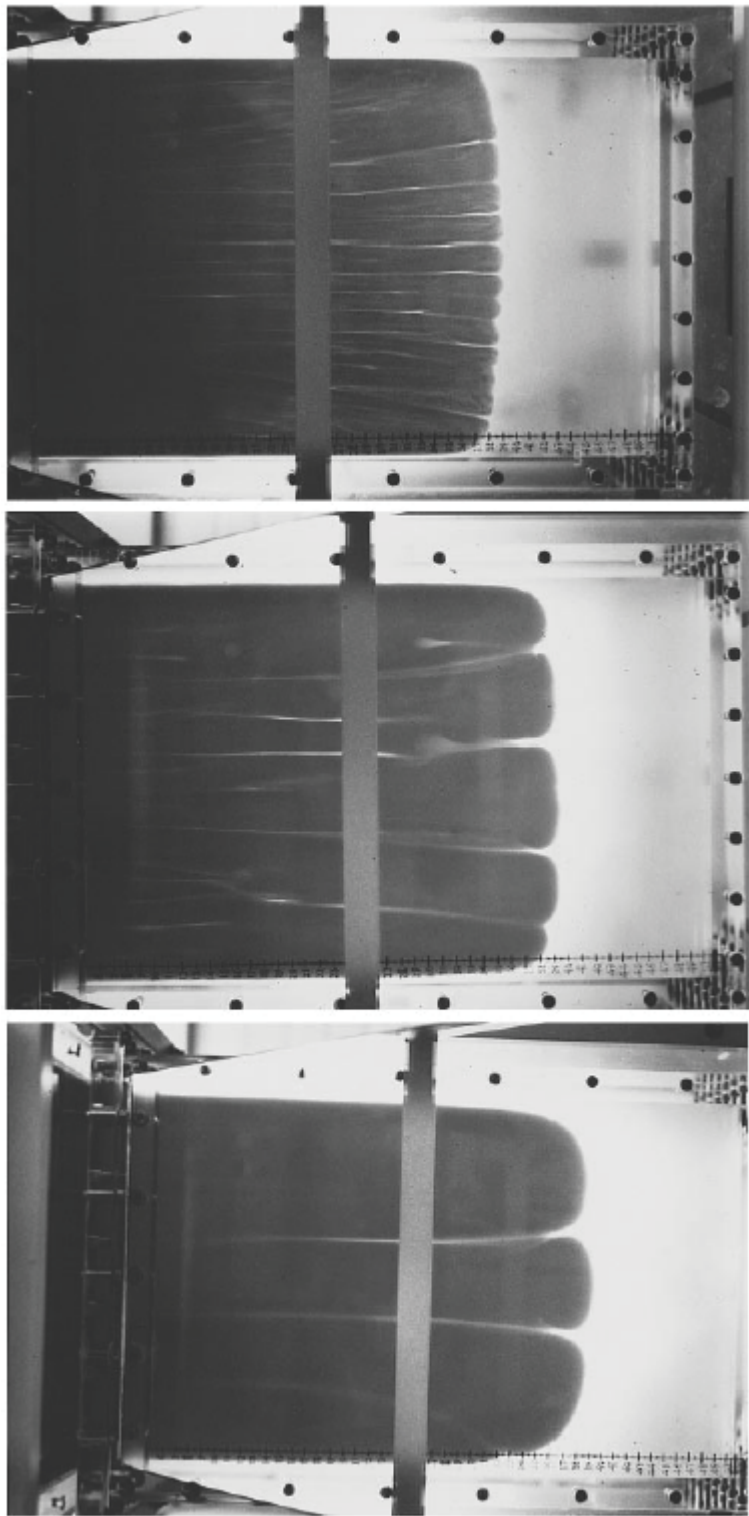
Figure 6.1: Experimental formation of fingers resulting from Saffman-Taylor instability. Pictures are in plan view; dark material is an analog for intruding basalt, and colorless material represents the ambient felsic magma. From Snyder and Tait, 1998.

magma, intruding at low Reynolds number and pushing on a more viscous fluid, which in this case is the ambient granitic magma, in a porous medium or Hele-Shaw cell (Snyder and Tait 1995, 1998; Paterson 1985). In this study, the ambient magma chamber acts like a Hele-Shaw cell (two plates separated by a thin gap), with the intruding basaltic magma bounded on the bottom by a crystal-rich mush and on the top by the more viscous felsic magma. These contrasting viscosities allow the development of "fingers" in the basaltic magma that extend parallel to the direction of the flow. Snyder and Tait (1995) found that finger width is proportional to intrusion rate, according to:

$$\lambda = 17.2 \left(\frac{\mu_f U w h}{g} \right)^{\frac{1}{3}}$$

where λ is the wavelength (i.e. finger width), μ_f is the dynamic viscosity of the ambient felsic magma, U is the injection velocity, w is the width of the basaltic injection, h is the thickness of the basaltic injection, and g is gravitational acceleration. Rapid intrusion yields relatively fewer fingers than slow intrusion, which yields many fingers. More fingers means more gaps between fingers, and the number of gaps must be sufficient to allow trapped felsic sublayer material underneath to rise buoyantly upward, which is important in facilitating both Darcy flux and mush compaction, which are described in the following paragraphs (Appendix F). While these fingers are not directly observed in AWP due to lack of paleohorizontal exposures, it is likely that they occurred during intrusion.

When a fluid A with density ρ_A [kg m^{-3}] overlies a fluid B with density ρ_B [kg m^{-3}], and $\rho_A > \rho_B$, a Rayleigh-Taylor instability develops. In this study, A is the intruding basaltic magma overlying B, the ambient felsic magma. As the basaltic sheet

intrudes the granitic magma chamber by flowing over a crystal-rich (but still deformable) mush that forms the floor of the chamber (cf. Wiebe, 1994; Miller and Miller, 2002), the leading edge of the sheet becomes elevated off the floor of the chamber (cf. Bleick, 2005)(Figure 6.2). This is due to the high viscous stresses associated with a thin sublayer—a no-slip condition exists at the mush boundary, and the intruding mafic magma is unable to intrude immediately next to the mush and must intrude slightly higher above the mush where the viscous stresses are spread over a larger area and the magma is more easily intruded. As a result, more buoyant felsic material becomes trapped underneath the more dense intruding mafic material, leading to density instability. Rayleigh-Taylor instability is critical both to the fingering process, because it selects the wavelength along which the intruding sheet will split into fingers (Snyder and Tait, 1995), and to the mechanism of auto-acephalation (Parker, 2000), which is discussed later in this section. In addition, Rayleigh-Taylor instabilities arising from the presence of a felsic sublayer have been shown experimentally to lead to the formation of felsic "pipes" (Bleick, 2005) that puncture the overlying mafic sheet. A similar mechanism plays a role in the migration of felsic liquid into piles of successive basaltic sheets, which will be discussed later in this chapter.

Mechanisms of Disaggregation

Mafic injection into a felsic host yields a broad spectrum of isolated mafic morphologies, crystal-scale reaction, and changes in the felsic host material. These processes are discussed in the following sections, with discussion of field evidence, since field and petrographic observations of PLS, basaltic sheets, and their felsic hosts lend
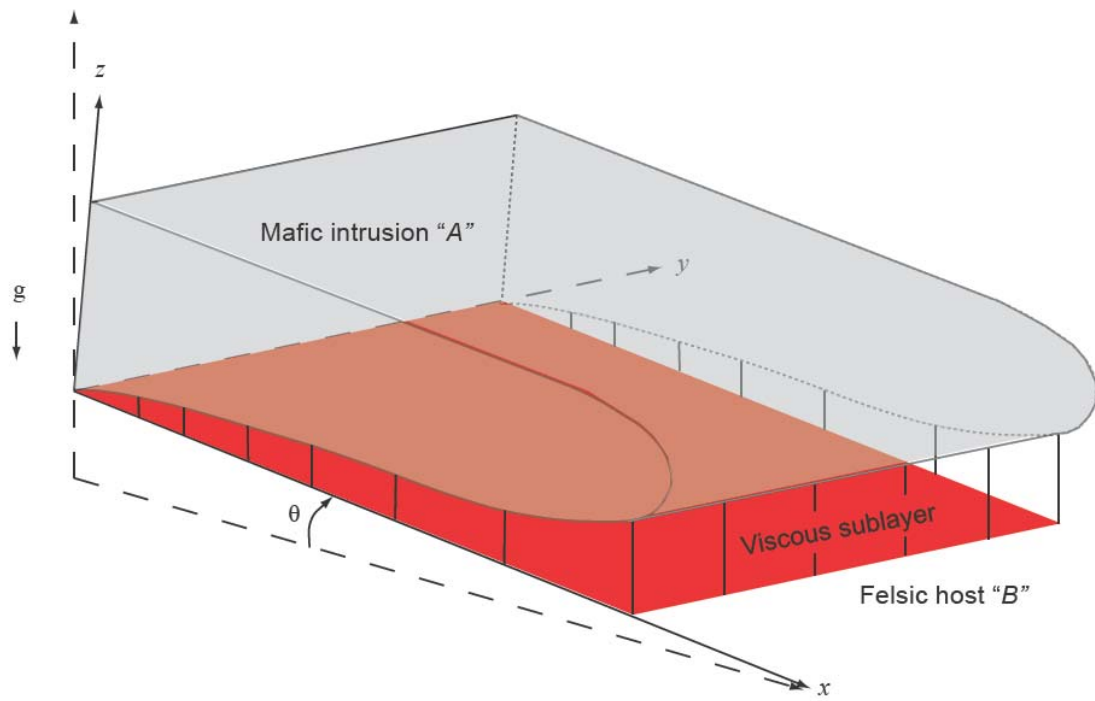
Figure 6.2: Schematic of development of felsic viscous sublayer. Modified from D.J. Furbish.

critical insight into resolving mafic disaggregation mechanisms in a felsic magma chamber.

Magma Chamber Processes: Migration of Melt and Instigation of Convection

In addition to differences in viscosity and density, the temperature difference between intruding basaltic magma and the ambient felsic magma is substantial and plays an important role in determining magma chamber dynamics. Intruding, hot basaltic magma at near-liquidus temperatures likely entered a chamber that was somewhat above solidus. For calculations in this study, basalt initial temperature was estimated at 1100°C, and felsic magma temperature was estimated at 800°C. An initial temperature difference of ~300°C substantially increases the amount of heat exchange occurring in the chamber, which can lead to some significant changes.

As heat diffuses from the intruding basalt into the underlying felsic crystal mush, it is probable that partial dissolution of the mush occurs. As heat is added from overlying mafic magma, crystals are resorbed, resulting in increased liquid in the portion of the mush nearest the overlying basalt. As the melt trapped in the mush becomes hotter, it also becomes more buoyant. As this buoyant melt rises, it becomes trapped unstably underneath the basalt sheet. The weight of the basalt sheet is also being borne by the crystal mush, which increases the pressure on the mush (compared to mush that underlies a less-dense felsic melt column). Since the felsic melt is more buoyant, it will exploit pathways to continue to rise upward—either by rising between the basaltic sheet "fingers" or by finding existing weaknesses in a sheet and injecting into them (Figure 6.3). Evidence of melt movement is seen at Pipe Canyon, where schlieren bands—bands of mafic minerals that result from differential movement within a crystal-bearing

magma—are evident for over 10 m (Figure B15). These structures may have formed

from felsic melt migrating upward or laterally between successive intrusive sheets, or

from shearing induced by an intruding basalt sheet above felsic magma that overlies a

stationary mush.

This felsic melt—which is under high pressure—will diffuse to areas of lower

pressure. This movement can be approximated by Darcy's law (see Appendix F), in

which fluid moves down a pressure gradient. In this system, a felsic melt flux in the

uppermost portion of the mush, q, is directed away from the area where intrusions first

start flowing across the mushy chamber floor (because more mafic, intruding material is

present there) and toward the "nose" of the basaltic sheet, which has split into "fingers".

This melt may also travel up in between the "fingers" to move to an area of lower

pressure. However, both q and the migration of felsic melt upward between successive

sheets and weak zones contribute very small amounts of material given the overall scale

of the system, and are not sufficient mechanisms on their own to incite mafic

disaggregation.

The migration is nonetheless important because diffusion of heat through moving

fluids is a critical mechanism of magma chamber disruption. Due to the large

temperature gradient between mafic and felsic magmas, a thermal boundary layer

(TBL)—a zone of steep temperature, crystal content, and viscosity gradients, and

characterized by crystal resorption as the TBL grows (Couch et al., 2001)—develops.

The more heated felsic melt is added inside the TBL, either from q or from increased

injection and heating of the ambient felsic magma, the larger the volume of heated

material the TBL can encompass. Even though the addition of heated material is small, it

may have large local effects for heating the TBL. Once a TBL has formed, instability may arise from accumulation of heated felsic material, resulting in convection along the top or sides of the injecting basalt sheets (Figure 6.3). Whether or not convection will occur in the vicinity of the TBL can be determined by calculating a critical Rayleigh number, Ra_c, according to

$$Ra_c = \frac{g\alpha\Delta T\delta^3\rho}{\kappa\mu},$$ (6.1)

where g is acceleration due to gravity, α is the coefficient of thermal expansion, ΔT is the temperature difference between the ambient felsic magma and the intruding basaltic magma, δ is the thickness of the TBL, ρ is density, κ is the thermal diffusivity, and μ is the dynamic viscosity (Couch et al., 2001)(Appendix F). For a system bounded on the bottom (in this case, the crystal mush), once $Ra_c >1101$, convection will begin. Once multiple intrusions have occurred, the TBL thickness will increase significantly, and convection will occur more quickly. Although convection itself is not likely to cause mafic disaggregation since only lateral and overlying magma convects, leaving the underlying mafic sheets unaltered, it is possible that convection in a magma chamber helps to disperse already-disaggregated pillows, carrying them away from their source location.

Collapse of the Crystal-Rich Granitic Mush

Rheology of the felsic crystal mush over which basaltic intrusion occurs likely plays a significant role in the disaggregation process. Once the mush is heated, dissolution of crystals and upward percolation of heated melts leads to growing instability of the mush. Alternatively, other intra-mush mechanisms may disturb the mush.
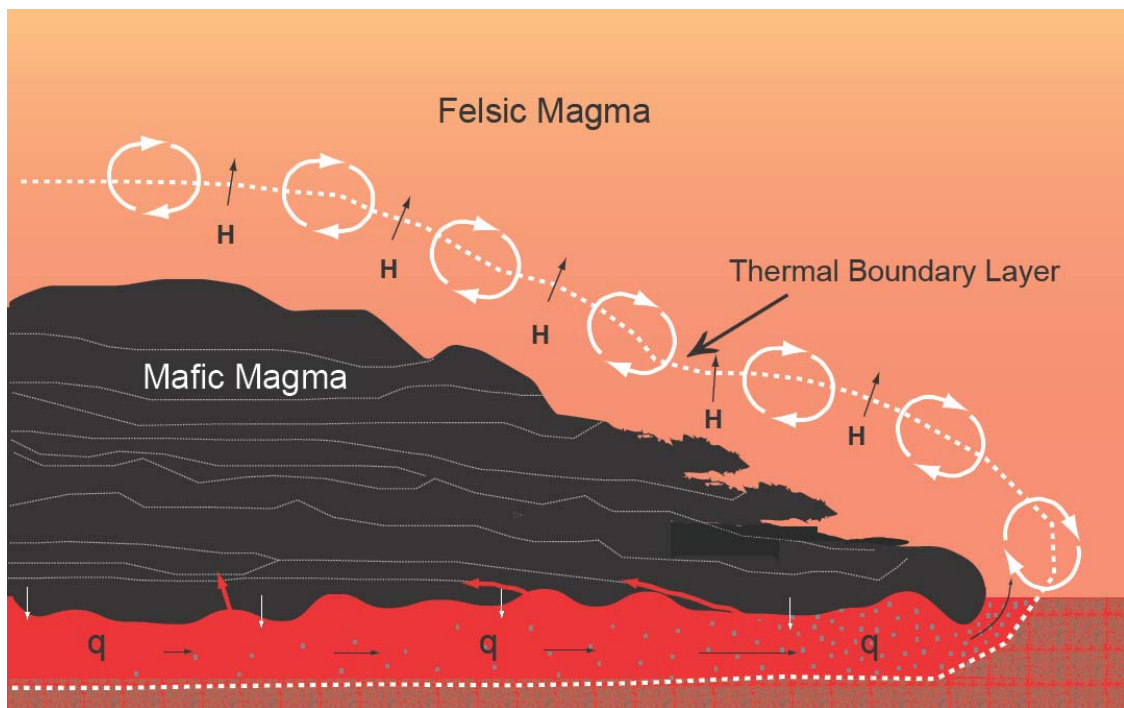
Figure 6.3: Summary of melt migration and convection processes in a felsic magma chamber during and after mafic magma injection.

Bachmann and Bergantz (2003) have proposed that mush rejuvenation can occur as a result of upward percolation of volatiles following intrusion of a hydrous mafic magma at the base of a mush. As volatiles rise, they induce partial dissolution of crystals and thus unlock the mush, facilitating melt circulation, which may lead to intra-mush convection. Although there is no field evidence for this process occurring in AWP, it is possible that mafic magma intruded into a deep portion of the mush column may have played a role in disturbing the previously quiescent mush.

Perturbation of the underlying mush may play a key role in disaggregation of mafic sheets. Once the mush becomes sufficiently disturbed, it will no longer be able to support the overlying sheet, which may lead to a local sheet collapse that results in disaggregation. This process is indicated in several locations throughout the pluton by the presence of "flame structures" of felsic material that inject overlying basalt pillows (Figure B16). In addition, "crystal packing"—the accumulation of felsic phenocrysts along the underside of a basaltic sheet or pillow (Figures B3, B18)—beneath still-intact basaltic sheets indicates that mush compaction may occur at any point post-injection.

Auto-acephalation

The term "auto-acephalation" was coined by Parker (2000) to describe phenomena associated with hydroplaning submarine debris flows. Parker (2000) observed that many debris flows undergo a separation of the "nose" of the flow from the remainder due to extensional flow, and the separated "nose" portion of the flow continues to move forward after separation. An analogous process is likely to contribute a large portion of disaggregated mafic pillows in a felsic magma chamber (Figure 6.4). As a
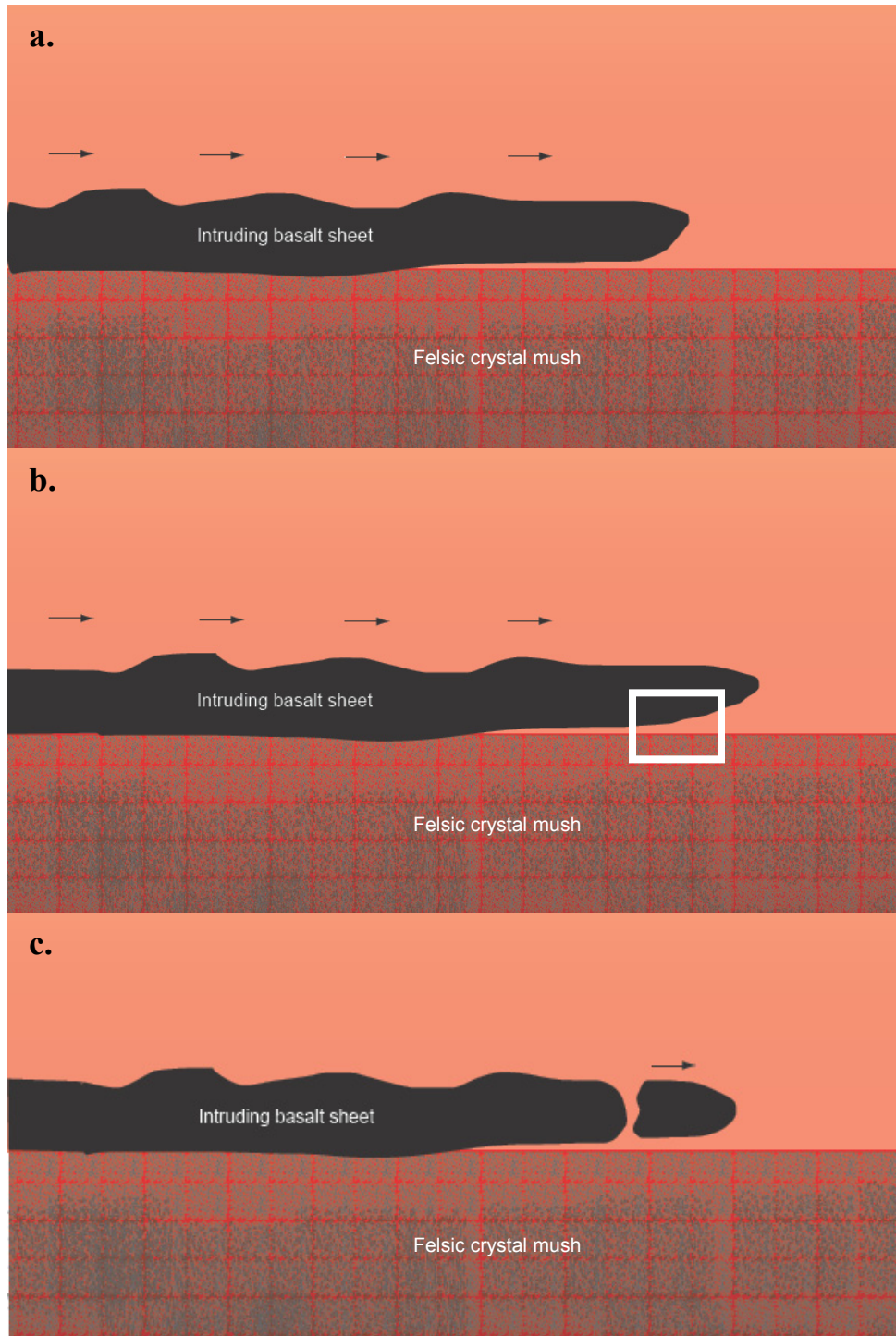
Figure 6.4: Auto-acephalation (Parker, 2000) as a mechanism for pillow formation.
a) Mafic sheet injects onto the slightly sloping crystal mush floor of a felsic magma chamber; a viscous sublayer, even if vanishingly thin, is present.
b) With a decrease in sublayer thickness (in box), viscous stresses increase;
c) Leading to extensional flow, and the front portion of the sheet breaks away from the back part. The disaggregated front portion of the flow is preserved as a pillow.
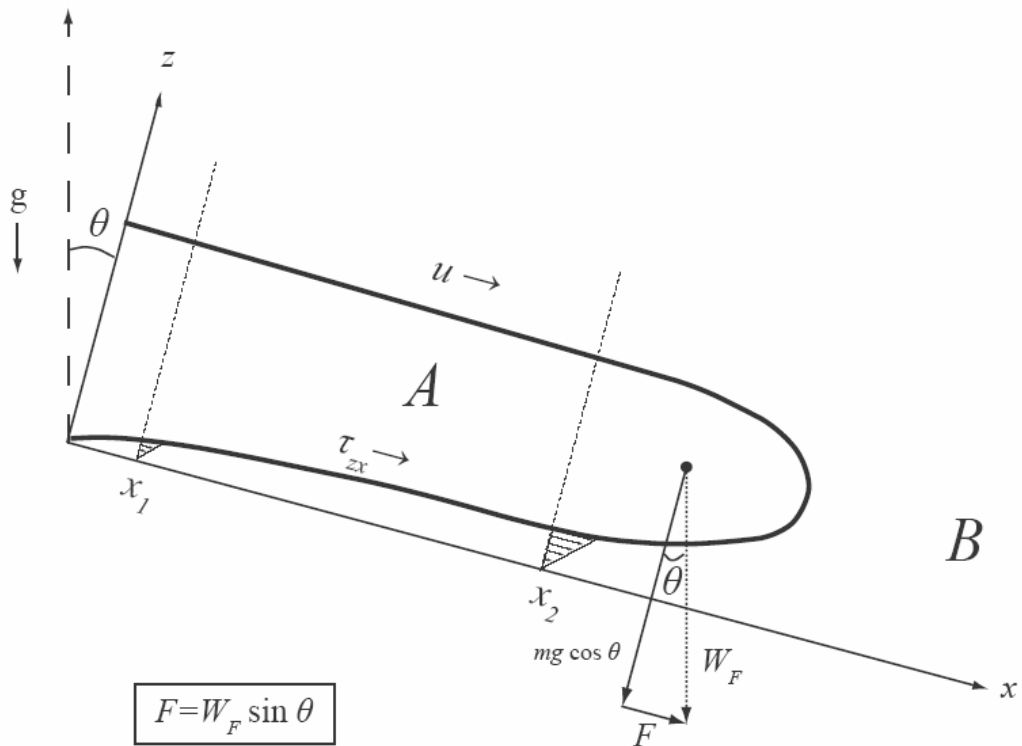
Figure 6.5: Diagram of forces acting on a basaltic magma sheet (*A*) as it intrudes a felsic magma chamber (*B*). Stress fields in the viscous sublayer are also shown.

basaltic sheet intrudes a felsic magma chamber by flowing over the top of a crystal-rich

mush, Rayleigh-Taylor and Saffman-Taylor instabilities develop, facilitating fingering of

the basaltic magma and the formation of a felsic sublayer. Since the felsic material

trapped underneath the intruding basalt is more buoyant than the basalt over it, the felsic

magma ascends between the fingers and into the overlying chamber (or subsequent

intrusions). This continued removal of underlying material slightly retards propagation

of the intruding fingered basaltic sheet due to drag from the differential melt movement,

and some felsic material is always trapped under the sheet due to the extreme resistance

to shear exhibited by a very thin sublayer. The thicker the sublayer, the easier it responds

to shear forces. Correspondingly, a basalt sheet intruding over a thin sublayer will be

impeded due to high friction with the sublayer, but once the sublayer thickness gradient

increases closer to the tip of the intruding sheet, the sheet moves more freely because the

sublayer is more easily sheared when it is thicker. This results in extensional flow in the

basalt fingered sheet. As the sheet intrudes, the felsic viscous sublayer reaches a critical

thickness (generally near the tips of the intruding fingered sheet (Parker, 2000)) where

the force exerted by the intruding magma overcomes the viscous stresses induced by the

sublayer (Figure 6.5). At this point, extensional flow in the basaltic sheet fingers occurs

quickly. Since the tips of the fingers are essentially moving faster than the back portion

of the flow, the tip "auto-acephalates" and continues moving downslope at its original

velocity.

Perrault (2006) noted that the sublayer acts as a lubricant and decreases the

friction that would otherwise occur with basalt sheet/crystal mush contact, which may

allow for viscous planing of auto-acephalated—and now discrete—flow tips to continue

moving away from their separation location. It is likely that tips may disaggregate

multiple times, if they are still moving downslope, by repeated auto-acephalation. Even

though the felsic sublayer acts somewhat as a lubricant, it seems that proximity to the

mush is critical to determining extent of auto-acephalation. In Pipe Canyon, bottom

sheets appear more disaggregated than upper ones. While this may just be a function of

age, its also likely that since sublayer shear is vital to disaggregation, upper sheets (which

intrude onto a more fluid-rich portion of felsic material) do not experience the magnitude

of sublayer effects that lower sheets do. Furthermore, since abundance of PLS decreases

with increasing distance from the parental sheet, it seems plausible that the first several

auto-acephalations occur in rapid succession, and diminish with distance from the sheet,

or that most PLS simply do not have enough energy to travel far from the source.

Thermal Contraction

Field and theoretical evidence suggests that thermal contraction of cooling

basaltic material contributes to its disaggregation. MELTS modeling (Ghiorso and Sack,

1995) shows that basalt cooling yields a volume decrease of ~10%. When temperature

change occurs at a non-linear rate, volume decrease may occur rapidly during some

intervals during cooling, resulting in fracture of the almost-cool basalt body. Evidence

for this is seen most commonly in AWP in pillows that have already disaggregated from

the parental magma sheet and subsequently become fractured. Figures B10 and B17 in

Appendix B illustrate the disaggregation from parental pillows caused by later thermal

contraction. Occurrences of fracturing are distinguished in the field by angular edges that

lack chilled margins; fractured pillows in some cases appear as "puzzle pieces" within

felsic host material (Figure B2, 20). This "puzzle-piece" formation may be due to

thermal contraction occurring on an outcrop scale. Although disaggregation due to

thermal contraction of cooling basalt appears to occur in mafic masses on a range of

scales, from thick sheets (10s of m) to minute pillow sizes (dm), it is most frequently

associated with smaller, isolated pillow groups that had already disaggregated from their

parental basaltic sheets prior to contraction. Therefore, although disaggregation due to

thermal contraction appears to be widespread, it seems to operate principally as a

secondary form of mafic disaggregation, and is not generally responsible for initial

disaggregation from the intruding basalt sheet. Field observations also suggest that once

a sheet has stopped intruding, it may thermally contract to produce local breaks in the

otherwise coherent sheet (Figure B9).

Post-Disaggregation Mafic-Felsic Interaction

Once basaltic pillows disaggregate from their parental sheets, they may be

dispersed by convection within the chamber, sink into the underlying mush (likely due to

mush collapse), or—in the case of auto-acephalated pillows—continue to move away

from the parent sheet. Post-disaggregation movement is evident around bottom edges of

pillows, which frequently display "feldspar packing" (Figures B3, B18), indicative of

downward movement of the isolated pillow. Also apparent are pillows with crenulated

tops and sides, and markedly less—or absent—crenulation on the paleo-bottom of a

pillow. It seems likely that any bottom crenulation is simply smoothed out due to

compaction with the underlying mush (R. Wiebe, pers.com., 2008). It is likely that as a

pillow disaggregates, some of the liquid interior is exposed to the ambient felsic liquid,

creating crenulation, while any surface perturbations along the bottom of the pillow are

lessened during descent into the underlying mush. Downward movement and settling of pillows post-disaggregation also may be responsible for the majority of pillows having a width: height ratio of >1, so that that pillows settle upon impact with the underlying and more solid crystal mush.

Alternate Explanations and Uncertainties

In addition to auto-acephalation and thermal contraction, other mechanisms of disaggregation from sheets to pillows have been suggested. Snyder and Tait (1995) suggest that pillows form directly as a result of flow-front instability, which results in "finger tips" shearing off during flow. Although this is a plausible mechanism of disaggregation and is similar to auto-acephalation, it was not investigated theoretically during this study.

In the course of this study, theoretical investigation of disaggregation processes provided insights and valuable constraints, but considerable uncertainty remains. There are enough variables in the system that the most rigorous modeling will not uniquely model processes associated with mafic intrusion into a felsic magma chamber. For this study, the goal was to model situations in a relatively simple but plausible way to evaluate the large-scale mechanisms and forces responsible for disaggregation. For example, 1-dimensional models were used to calculate magma flux and convection, when a 3-dimensional model is more realistic. However, the employment of a 1-D model is considerably simpler, and still gives a sufficient result resolution to get an idea of the scale of processes acting on the system.

Favored Model for Formation of Pillow-Like Structures in Aztec Wash Pluton

Crystal-poor basaltic magma enters the chamber in the form of sheets or sills, and interacts with ambient felsic liquid, as evidenced by crenulate margins present on most pillows and preserved sheet tops. Due to a large temperature difference between the two magmas (likely several 100s of degrees C), the basalt margins become chilled due to a rapid decrease in temperature. The ambient felsic magma in the chamber and the underlying crystal-rich mush are reheated and some mixing occurs (Bromley et al., 2008); the phases in the chamber are not in equilibrium, as evidenced by rapakivi texture and "ghost" feldspars that are observed in the host granite in close proximity to basaltic intrusions or pillows. It is evident that intruding basaltic sheets disaggregate to form isolated pillow-like structures, as suggested by PLS in close proximity to their parental sheets. Figures B5 and B13 provide good evidence of the relationship between basaltic sheets and PLS at the beginning stages of disaggregation, which ultimately produces isolated basaltic PLS. Although disaggregation and dispersal are likely the result of a combination of factors, including instabilities from differences in density, temperature, and viscosity; mush collapse; thermal contraction; convection; and finger-tip shear, I interpret the primary cause of mafic disaggregation to be auto-acephalation, which results from differing magnitudes of shear stresses acting on an intruding mafic sheet immediately adjacent to the felsic sublayer.

78

CHAPTER VII

CONCLUSIONS

In this thesis, I have examined two systems that each display evidence for disaggregation of mafic magma, but which contract greatly in the environments they represent. I interpret the processes of disaggregation to have been quite different in the two cases, but in combination the paired studies may shed light on physical behavior of magmas and their hosts over a wide range of conditions.

Processes in South Iceland

Disaggregation of basaltic lava into overlying hyaloclastite results primarily from changes in temperature and pressure, and to a lesser extent, kinematics. The results of this study suggest virtually concurrent emplacement of lava and hyaloclastite. I envision an eruption with both subglacial and subaerial phases (which was repeated multiple times), which is supported by the presence of a large volume of initially wet hyaloclastite, as well as extensive lava and chemically similar lava and hyaloclastite glass compositions from 2 locations. Once crusted lava was overlain by hyaloclastite, heat diffusion from the lava heated the pore water in the hyaloclastite, leading to volume expansion of the water and creating an increase in fluid pressure in the hyaloclastite. Fracturing of the lava crust led to exposure to the still-molten lava flow interior, which vaporized the water in the hyaloclastite matrix, leading to a strong increase in the pore fluid pressure. High-pressure fluids migrated away from the injection location, dragging the hyaloclastite

particles with them. The dragging apart of the hyaloclastite matrix created room for more injection to occur. Apophyses injected upward incrementally until they cooled sufficiently to develop a thick, rigid crust that impeded further ascent. Other injection geometries, particularly dikes, may occur by similar mechanisms but are not addressed further here.

Processes in Aztec Wash Pluton, Nevada

This study proposes that disaggregation of basalt from coherent sheets to discrete pillow-like structures in a felsic magma chamber occurs primarily as a result of auto-acephalation, and secondarily from thermal contraction during post-emplacement cooling. These disaggregation mechanisms result largely from differences in viscosity, density, and temperature, between more-dense/less-viscous basaltic magma and its less-dense/more-viscous felsic host. The instabilities that arise from these differences create a dynamic magma chamber environment that facilitates disaggregation of basaltic sheets into pillows and their dispersal. The formation of a felsic sublayer beneath the injecting basalt sheet, combined with formation of fingers due to flow-front instability and the diffusion of temperature into the host chamber, allow the intruding sheet to propagate over a crystal-rich mush which is the effective floor of the chamber. Movement of felsic liquid due to buoyancy and pressure-driven flux creates small disturbances that aid in the disaggregation process. Shearing of the sublayer leads to extensional flow in the injecting sheet, promoting auto-acephalation of the sheet tip.

APPENDIX A

Iceland Field Photographs and Descriptions

A1. Thin section photograph of hyaloclastite sample LOM405 at 4x magnification. Note the darker palagonite rim surrounding the sideromelane interior. White areas outside the glass pieces are zeolites.
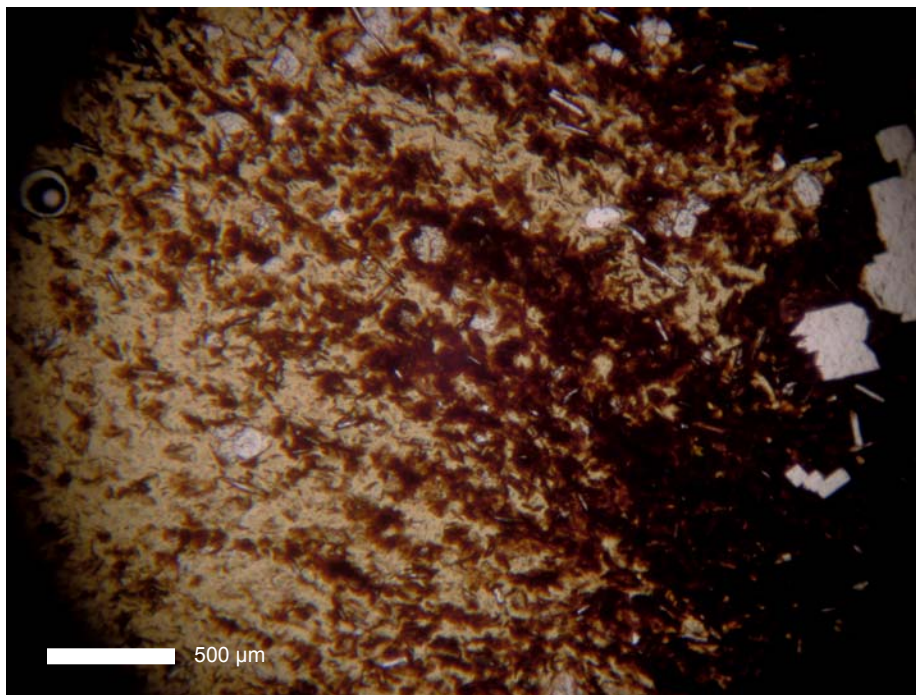
A2. Thin section photograph of RAUX01 at 4x magnification. Finger-like projections are basalt. The pale yellow area is hyaloclastite glass; most phenocrysts are plagioclase.
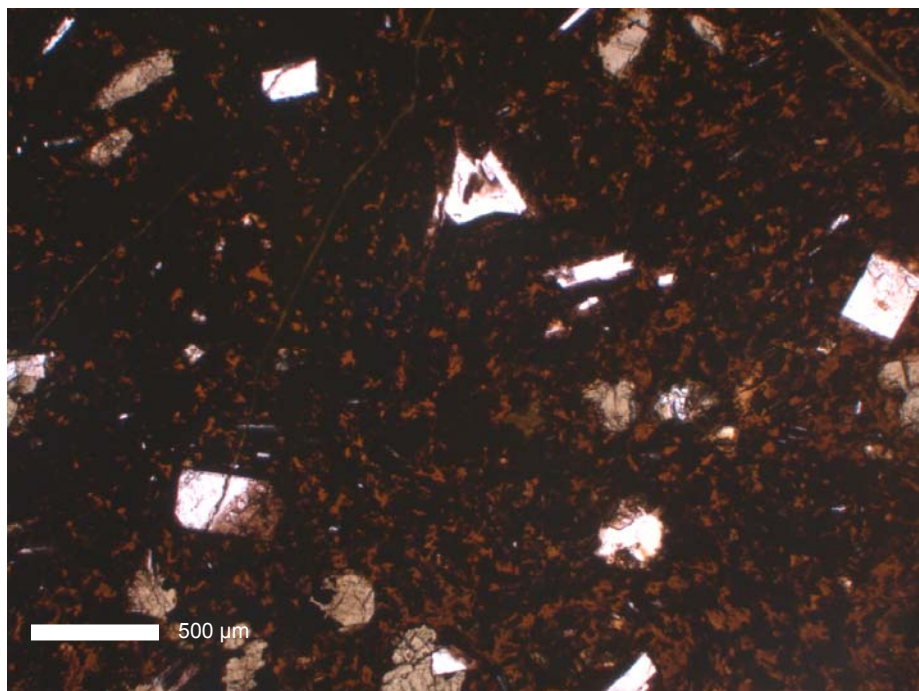
A3. Basaltic glass from thin section sample LOM410 at 4x magnification. Plane-polarized light. Phenocrysts are mostly plagioclase.
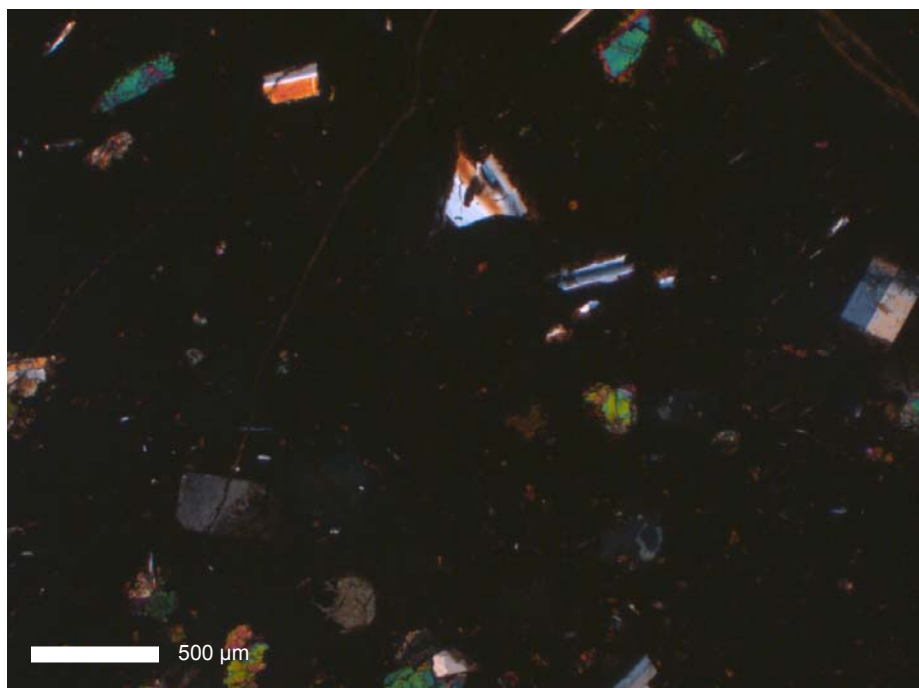
A4. Same as above, except under crossed polars.

A5. Concentric columnar basalt layers overlain by cubey basalt.

A6. Flame-like apophyses (shown by arrows) exposed in a cliff wall between Eystrikinnar and Lómagnúpur.

A7. Exposure at Keldunúpur.

Grass
Lava
Hyaloclastite
Diamictite
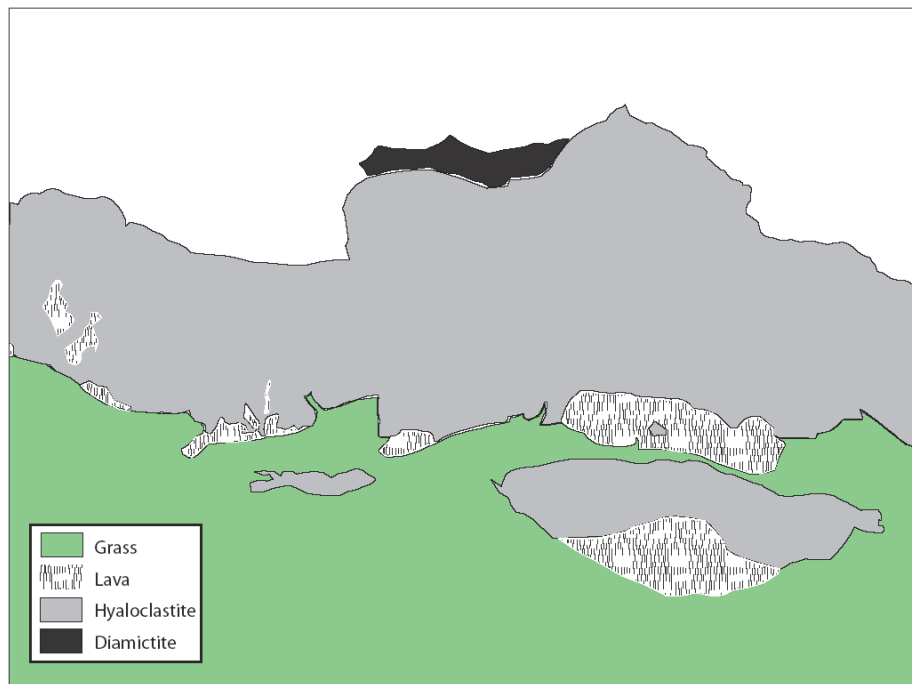
A8. Schematic of figure A7 showing location of depositional unit components.

A9. En echelon basaltic dikes in overlying hyaloclastite at Eystrikinnar.
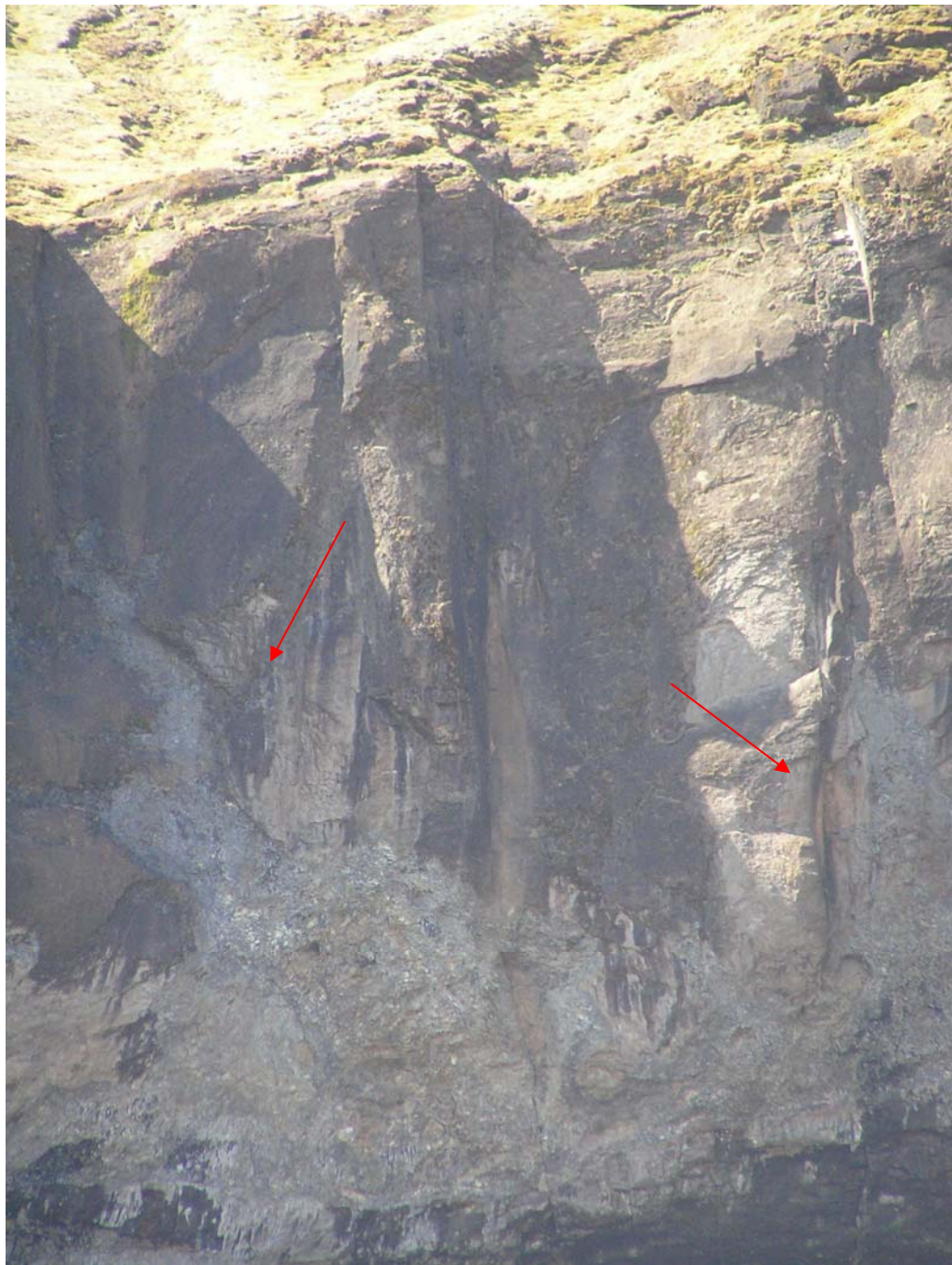
A10. Apophyses LOM302m (left) and LOM303m (right). Trend is 0-180°.

A11. Apophysis ÞVE103m at Þverárnúpur. Note the disaggregated base of the apophysis, and the small magma pods nearby.

A12. Standard lava sequence, with columnar-jointed basalt overlain by cube-jointed basalt. From Husheiði to Þverárnúpur section along Hwy 1.

A13. Burnt hyaloclastite margin where it came into contact with underlying hotter lava.

A14. Disaggregation of lava to form isolated pillow-like pods exposed at Þverárnúpur.

A15. Quenched margins on basalt clasts in hyaloclastite. Compass for scale.

A16. Quenched margins on basalt clasts in hyaloclastite. Large clast is ~2.5 cm wide.

A17. Fresh non-hyaloclastite-bearing jökulhlaup deposits at Mýrdalssandur. Diamictite deposits exposed in the Siða-Fljotshverfi district closely resemble this material.

A18. Apophysis LOM201m. Structure is ~15m high.

A19. Vesiculated basalt at Kotafjall.

A20. "Bubble dikes" in otherwise non-vesiculated basalt at Kotafjall.

A21. Vesiculated (center) and non-vesiculated (top and bottom) basalt in close proximity at Kotafjall. Photograph is approximately 25 cm wide.

A22. Upper margin of cube-jointed basalt and contact with hyaloclastite.

A23. Concentric columnar jointing in basalt. From Husheiði Canyon.

A24. Vesiculated basalt clasts in hyaloclastite. Photo is approximately 15 cm wide.

A25. Section of lower Djúpa River lava flow. Backpack for scale.

APPENDIX B

Aztec Wash Pluton Field Photographs and Descriptions

B1. Typical exposure of mafic pillow-like structures. Photo is ~3m across. From Aztec Wash Spring Canyon.

B2. Pillow-like structures exposed in the wall of Aztec Wash Spring Canyon. Photo is about 5m across.

B3. "Felsic packing" on the paleo-bottom edge of a mafic pillow. Note the approximately half-compass-width of densely-packed feldspar crystals next to the pillow. A chilled basalt margin is also visible Pillow is B004, Pipe Canyon Saddle Hill.

B4. Crenulate margin on paleo-up edge of pillow B005 (elongate center pillow). Pillow is 35 cm wide. From Pipe Canyon Saddle Hill.

B5. Mafic sheets in the initial stages of pillow formation. From Famous Dike (N35°38.383', W114°47.678').

B6. Pillow ASC102 in Aztec Wash Spring Canyon. Tape measure is on paleo-up side.

B7. Pillow ASC101 from Aztec Wash Spring Canyon. Tape measure is on paleo-up side.

B8. Exposure of mafic pillows in Aztec Wash Spring Canyon. Backpack for scale.

B9. Intra-sheet breaks interpreted to result from in situ thermal contraction. In Pipe Canyon.

B10. Thermal contraction of the main pillow body resulted in the fracturing of these mafic blobs, as evidenced by their extremely angular edges and intrusion of felsic material.

B11. Pillow displaying crenulate margins on the paleo-up side (left), while the paleo-down side is not crenulated. In Aztec Wash Spring Canyon.
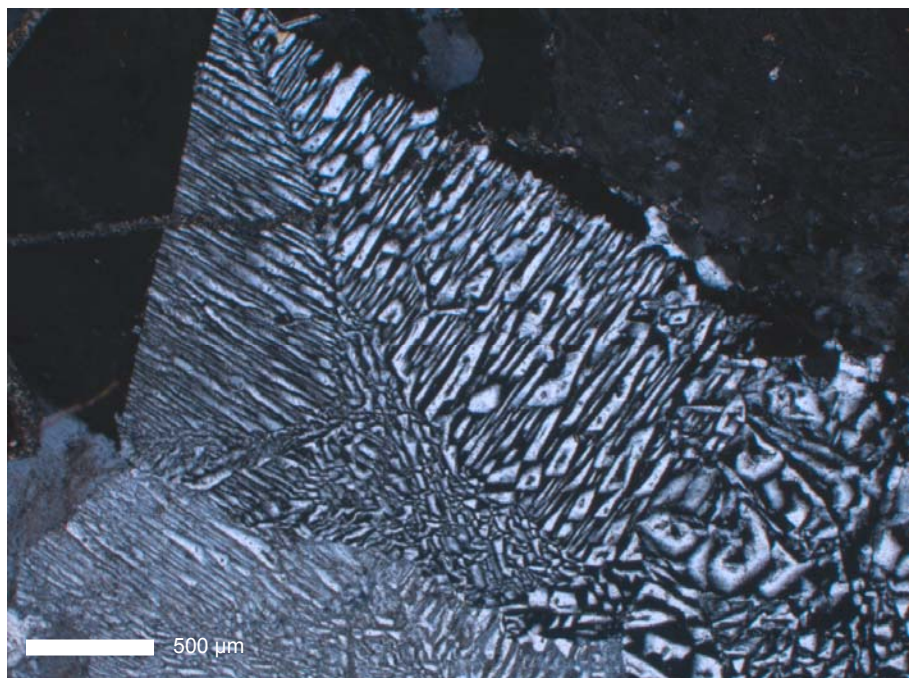
B12. Granophyric texture in thin section sample ASC501. Crossed polars at 5x magnification.

B13. Horizontally-intruding basaltic sheets exposed in Pipe Canyon. Paleo-up is roughly perpendicular to sheets.

B14. Disaggregation of basaltic pillows from intruding basaltic sheets. Note the post-disaggregation effects of gravity on the pillow above the field book. From Camp Canyon.

B15. Schlieren bands indicating differential fluid movement in the felsic cumulate between mafic sheets at Pipe Canyon.

B16. Pillows in Pipe Canyon. Note the flame structures indicated by the arrows.

B17. Three-dimensional view of a pillow portion disaggregated due to thermal contraction. Ruler is 15 cm. In Pipe Canyon.
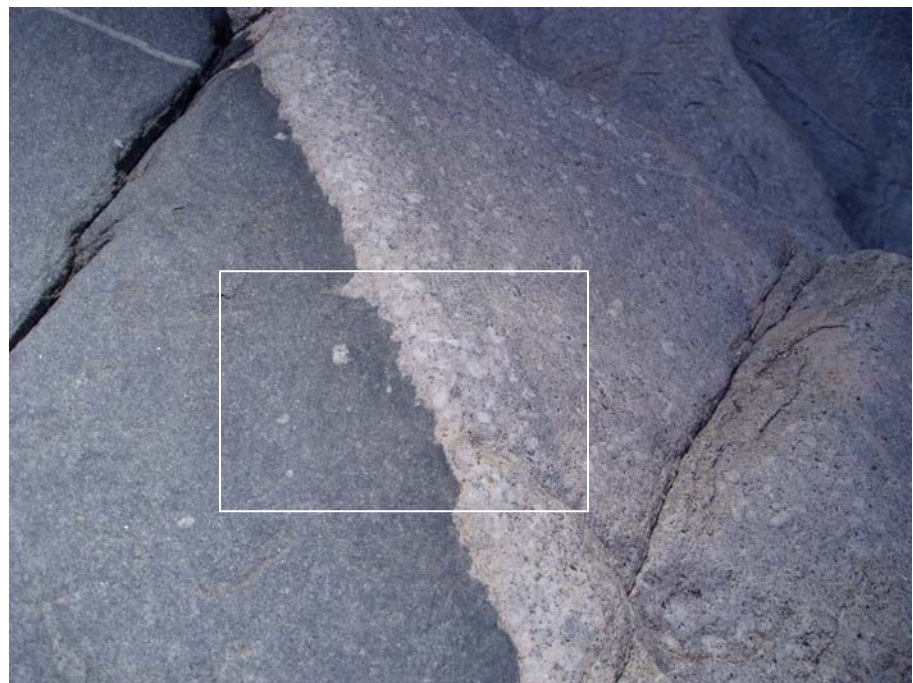
B18. Paleo-down pillow edge, with feldspar packing and thin (~2mm) aphanitic felsic rind at pillow edge. Picture is 10 cm acoss. In AWSC.

B19. Zoom of box in B17. Picture is ~5 cm across.

B20. Pillow pile in AWSC. Photo area is 3 m wide.

B21. Disaggregation due to thermal contraction exposed in AWSC. Mafic area is ~5 m wide. Paleo-up is to the right.

APPENDIX C

Petrographic Descriptions

APPENDIX C

PETROGRAPHIC DESCRIPTIONS

I examined 48 thin (30 μm) and thick (60 μm) sections cut from ~2cm x 3 cm billets. Samples came from both Iceland and Aztec Wash pluton, Nevada. Icelandic rocks were selected to sample varying areas of basalt, hyaloclastite, and the boundary between the two in and around apophyses, as illustrated by the diagram below (Figure C2). Samples with an identification name in the pattern of ABC-### were collected in May 2007, while samples with an identification of ABC-X## were gathered in October 2007 to replace earlier samples that did not contain sufficient glass. Samples gathered in May 2007 were turned into thick sections for possible usage on the EMP; all other sections are thin sections. Samples collected in AWP are of mafic-felsic boundaries, necessitating the petrography of both mafic and felsic components, as well as boundary analysis. Notes from microscope-oriented analysis are on the following pages. When describing hyaloclastites, please refer to Figure C1 to determine location and nomenclature of palagonization of sideromelane (glass).

Figure C1. Diagram of Palagonized Sideromelane Glass in Hyaloclastites
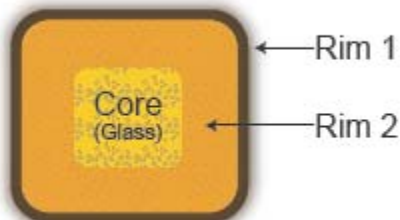
Figure C2. Ideal Sample-Taking Locales for Iceland Rocks
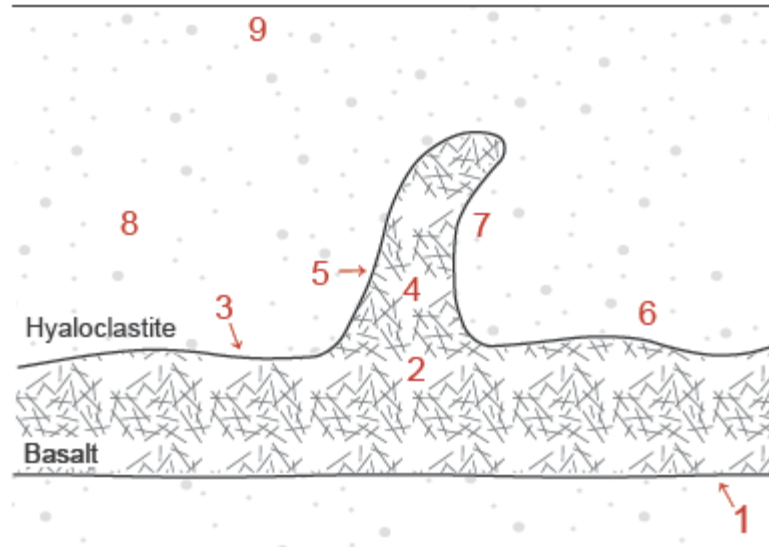
1: Base of cube-jointed basaltic unit (if exposed);
2: Interior of basalt;
3: Upper glassy margin of basalt;
4: Glassy margin of apophysis;
5: Interior of apophysis;
6: Hyaloclastite near the basalt lower boundary;
7: Hyaloclastite near apophysis;
8: Interior of hyaloclastite unit (if reachable);
9: Top of hyaloclastite unit (if reachable)

Sample ID/ Section ID	Field Area	Material	Phases Present					Vesiculation	Comments
			% plag	% ol	% px	% opaques	% glass		
KEL101	Iceland	Hyaloclastite	Trace	Trace	X	Trace	88%, with palagonite	Trace	Almost completely altered glass; Doubley rimmed, 1: tannish 25µm, 2: 100 µm; smectites visible; Super bright yellow-gold color
KEL102	Iceland	Hyaloclastite	Trace	Trace	X	Trace	88%, with palagonite	Trace	Virtually identical to KEL101, but with slightly more plag and ol phenocrysts
KEL103	Iceland	Lava	10%, in phenocrysts; 60% in matrix	5%, in phenocrysts	15% in matrix	10%	Maybe interstitially	20% of T.S. area; 200 µm diameter	Matrix has medium-sized xtals
KEL104	Iceland	Lava	2%, in phenocrysts; 50% in matrix	4% in matrix	14% in matrix	20%	X	Trace	Tri-modal: Layer 1: largest phenos, more opaques; Layer 2: more vesicles, large plag phenos, no ol/cpx in matrix; Layer 3: extremely aphanitic, no vesicles
KEL105	Iceland	Lava	20%, in phenocrysts; 60% in matrix	10%, in phenocrysts	8% in matrix	2%	X	X	Nice euhedral ol; oscillatory zoning in some plags; phenocrysts are large, dominant
KEL106	Iceland	Lava	50% in matrix	X	45% in matrix	5%	X	Trace	NO phenocrysts; Highly aphanitic and fine-grained groundmass (20µm xtals); Very slight vesiculation
KEL107	Iceland	Hyaloclastite	Trace	Trace	X	Trace	80%, with palagonite	Trace	Also 20% zeolites (in interstices); Tripley rimmed in some grains, 1: 25 µm, 2: 75 µm, 3 (if present): 50-100 µm (and darker than 2); grains look deteriorated
KEL108	Iceland	Hyaloclastite	Trace	Trace	X	Trace	95%, with palagonite	Trace	Also 5% zeolites (in interstices); Almost identical to KEL107 except for some large glass pieces; Rim1: 25µm and orangish, not brown; Rim 2: 50 µm

KELX02

Sample ID/Section ID	Field Area	Material	Phases Present						Comments
			% plag	% cpx	% opaques	% ol	% glass	% Others	
KELX02	Iceland	Lava	50%	10%	10%	20%	10%	X	Minor vesiculation; Fine-grained matrix, large amount of phenocrysts
			% glass/pala.	% zeolites		Rim 1 (µm):	Rim 2 (µm):	Other	
	Iceland	Hyaloclastite	90%	8%	Trace	<25	25	2% plag and ol	Pale yellow, looks relatively unaltered
	Iceland	Boundary	Huge boundary 3 mm wide; 20% of boundary is plag phenocrysts, 5% zeolites, 5% ol phenocrysts; about 625 µm of fragmentation into hyaloclastite						

KELX03a

Sample ID/Section ID	Field Area	Material	Phases Present						Comments
			% plag	% cpx	% opaques	% ol	% glass	% Others	
KELX03a	Iceland	Lava	50%	10%	13%	15%	12%	X	Looks fresh; Phenocrysts in good shape, euhedral; Plag and ol xtals up to 1mm²; Darkens toward boundary
			% glass/pala.	% zeolites		Rim 1 (µm):	Rim 2 (µm):	Other	
	Iceland	Hyaloclastite	60%	5%	X	X	X	20% plag; 15% ol	Virtually no hyaloclastite (~1mm); Glass has tons of inclusions of plag/ol
	Iceland	Boundary	Extremely phenocryst-rich; Phenocysts >100 µm long; Small amount of splintering (375 µm)						

KELX04

Sample ID/Section ID	Field Area	Material	Phases Present						Comments
			% plag	% cpx	% opaques	% ol	% glass	% Others	
KELX04	Iceland	Lava	40%	30%	10%	10%	10%	x	Very fine-grained matrix; Fairly vesiculated, bubbles ~125 μm wide and 15% of total T.S. area; Darkens toward boundary
			% glass/pala.	% zeolites	% opaques	Rim 1 (μm):	Rim 2 (μm):	Other	
	Iceland	Hyaloclastite	70%	23%	X	<25	25-250	5% plag, 2% ol	Big pieces look fresher, less altered; Many have bubbles in glass
	Iceland	Boundary							Thin quench layer (1mm), but disaggregation into hyaloclastite occurs over 1mm

KELX06

Sample ID/Section ID	Field Area	Material	Phases Present						Comments
			% plag	% cpx	% opaques	% ol	% glass	% Others	
KELX06	Iceland	Lava	30%	20%	15%	5%	30%	X	Very vesiculated (20% of total T.S. area) and glassy; Phenocrysts concentrate toward boundary
			% glass/pala.	% zeolites	% opaques	Rim 1 (μm):	Rim 2 (μm):	Other	
	Iceland	Hyaloclastite	60%	35%	X	10	X	5% plag inclusions	Super fragmented and beat-up; 500 μm max. xtal width; Only 1 rim; Tannish color
	Iceland	Boundary							Really rough, tons of phenocrysts (>50%); Can't discern fragmentation; 2 mm wide

117

Sample ID/ Section ID	Field Area	Material	Phases Present						Comments
			% plag	% cpx	% opaques	% ol	% glass	% Others	
KELX07	Iceland	Lava	3%	2%	Trace	Trace	55%	40% vesicles	All glassy, with some phenocrysts; looks like a lava-hy hybrid
RAU101	Iceland	Lava	5% in phenocrysts ≤ 500µm; 60% in matrix	3%, in phenocrysts, some beat-up	15%, in matrix	16%	1%, interstitial	Virtually none	Matrix composed of larger (100µm) elongate xtals
RAU102	Iceland	Lava	3% in phenocrysts; 60% in matrix	5%, in phenocrysts	15%, in matrix	16%	1%, interstitial	Slightly, ~100 µm diameter	Same as above, except with minor vesiculation
RAU103	Iceland	Lava	5%, in phenocrysts	5%, in phenocrysts	Likely in matrix	25%	X	Slightly, ~5% of T.S. area	Matrix is very fine-grained (but not as much as LOM406, 410,4 11a); Cannot tell mineralogy
RAU104	Iceland	Hyaloclastite	Trace	Trace; 2 large (100 µm) xtals in interstices	Trace	10%	70%, with palagonite	Trace	Also 20% zeolites (in interstices); several large basalt pieces; Doubley rimmed, 1: 50µm, 2: 125µm; Bright marigold color
RAU105	Iceland	Lava	5%, in phenocrysts; 50% in matrix	5% in phenocrysts (some twins); 20% in matrix	10% in matrix	10%, likely magnetite	X	X	Matrix has large (150µm) plags; some ol show partial magnetite rims; largely free of large phenocrysts
RAU106	Iceland	Hyaloclastite	Trace	Trace	X	Trace	80%, with palagonite	2% open space	Also 18% zeolites (in interstices); no phenocrysts; glass pieces smaller than usual (750µm); Doubley rimmed, 1: 25µm, 2: 63µm (bright marigold)
RAU107	Iceland	Hyaloclastite	Trace	Trace	X	Trace, with a few larger phenos (3-4mm)	85%, with palagonite	Trace	Also 15% zeolites (in interstices); Similar to RAU106; Rim1: 25µm, Rim 2 faint(25µm) or gone on a majority of grains; Bright marigold color

118

Sample ID/ Section ID	Field Area	Material	Phases Present						Comments
			% plag	% cpx	% opaques	% ol	% glass	% Others	
RAUX01	Iceland	Lava	30%	30%	20%	10%	10%	X	Fine-grained matrix; Basalt grades darker, more glassy, toward boundary
			% glass/pala.	% zeolites	% opaques	Rim 1 (µm):	Rim 2 (µm):	Other	
	Iceland	Hyaloclastite	90%	10%	X	25	50	Trace plag inclusions in glass	Nice pale yellow; Fresh looking;
	Iceland	Boundary	Extremely fragmented going into hyaloclastite; Maybe a bit angled? Fragmentation "fingers" reach 2.5mm into hyaloclastite						
Sample ID/ Section ID	Field Area	Material	Phases Present						Comments
			% plag	% cpx	% opaques	% ol	% glass	% Others	
RAUX03	Iceland	Lava	30%	25%	20%	10%	15%	X	Fine-grained matrix: Basalt grades darker, more glassy, toward boundary
			% glass/pala.	% zeolites	% opaques	Rim 1 (µm):	Rim 2 (µm):	Other	
	Iceland	Hyaloclastite	95%	5%	X	25	Usually not present; 40 when present	Trace plag inclusions in glass	Nice pale yellow; Fresh looking;
	Iceland	Boundary	Fragmented going into hyaloclastite, but much less pronounced than X01; Fragmentation "fingers" reach 375µm max. into hyaloclastite						

Sample ID/ Section ID	Field Area	Material	Phases Present						Comments
			% plag	% cpx	% opaques	% ol	% glass	% Others	
	Iceland	Lava	30%	25%	20%	10%	15%	X	Fine-grained matrix: Basalt grades darker, more glassy, toward boundary
			% glass/pala.	% zeolites	% opaques	Rim 1 (µm):	Rim 2 (µm):	Other	
RAUX04	Iceland	Hyaloclastite	95%	5%	X	25	X	Trace plag inclusions in glass	Not much to see, only 2.5mm; Fairly fresh looking
	Iceland	Boundary	Moderate fragmentation going into hyaloclastite, but much less pronounced than X01; Fragmentation "fingers" reach 525µm max. into hyaloclastite						

Sample ID/ Section ID	Field Area	Material	Phases Present						Comments
			% plag	% cpx	% opaques	% ol	% glass	% Others	
	Iceland	Lava	30%	25%	20%	10%	15%	X	Fine-grained matrix: Basalt grades darker, more glassy, toward boundary; Several large plag phenocrysts
			% glass/pala.	% zeolites	% opaques	Rim 1 (µm):	Rim 2 (µm):	Other	
RAUX05	Iceland	Hyaloclastite	75%	20%	X	25-75	40-175	Trace plag and ol inclusions in glass	Marigold color; looks more altered than previous RAUX; Also 5% smectites w/ rims ~100µm
	Iceland	Boundary	Lot of fragmentation going into hyaloclastite; Fragmentation "fingers" reach 1.25 into hyaloclastite; Maybe angled?						

Sample ID/Section ID	Field Area	Material	Phases Present					% Others	Comments
			% plag	% cpx	% opaques	% ol	% glass		
	Iceland	Lava	30%	25%	15%	10%	15%	5% zeolites in interstices	Basalt darkens toward rims, gains glass
			% glass/pala.	% zeolites	% opaques	Rim 1 (µm):	Rim 2 (µm):	Other	
RAUX06	Iceland	Hyaloclastite	88%	8%	X	25	25-50	2% ol, 2% plag	Bright yellow outside, pale yellow unaltered glass; Larger pieces less altered; Rim 1 oftern marigold to lite tan; Glass looks fresh; Some entrained ol, plag
	Iceland	Boundary	Moderate fragmentation going into hyaloclastite1; Fragmentation "fingers" reach 900 µm into hyaloclastite						

Sample ID/Section ID	Field Area	Material	Phases Present					Vesiculation	Comments
			% plag	% ol	% px	% opaques	% glass		
RAUX07	Iceland	Hyaloclastite	Trace, in glass	Trace, in glass and interstices	X	5%	75%, with palagonite	X	Also 20% zeolites in interstices; Rim 1: 25 µm, Rim 2: 75 µm; Grades from light yellow to marigold
LOM401	Iceland	Lava	7% in phenocrysts; 49% in matrix	3% in phenocrysts	cpx: 1% in phenocrysts; 15% in matrix	20%, likely magnetite	5%, interstitial	~5% of total T.S. area; ~250 µm diam.	Some ol looks burned and beat-up; plag frequently displays radial zoning habit; med-grained matrix (~100µm long plag)
LOM402	Iceland	Lava	5% in phenocrysts; 90% in matrix	5 % in phenocrysts; very euhedral	Likely trace amounts in matrix	X	X	~5% of total T.S. area; ~200 µm diam.	Very fine-grained matrix (~2µm long plag); Very few opaques
LOM403	Iceland	Lava	6% in phenocrysts, often broken; 90% in matrix	4% in phenocrysts; moderately euhedral	Likely trace amounts in matrix	Trace, interstitial	Trace, interstitial	~5% of total T.S. area; ~200 µm diam.	Very fine-grained matrix like LOM402 (~2µm long plag)

Sample ID/ Section ID	Field Area	Material	Phases Present					Vesiculation	Comments
			% plag	% ol	% px	% opaques	% glass		
LOM404	Iceland	Lava	10% in phenocrysts; 60% in matrix	7% in phenocrysts	1% in matrix	20%	2%, interstitial (~10μm diam.)	Moderate; 25% of T.S. area; ~150 μm diam.	Many phenocrysts appear to be a combination of ol and plag
LOM405	Iceland	Hyaloclastite	5%	X	X	10%	60%, with palagonite	Trace	Also 25% zeolites (in interstices); Palagonite "2" rims are 200 μm diam.; Moderate yellow color
		Hyaloclastite	5%	X	X	Trace	65%, with palagonite	Trace	Also 25% zeolites (in interstices); Palagonite "2" rims are 200 μm diam.; Moderate yellow color
LOM406	Iceland	Lava	10% in phenocrysts	2% in phenocyrsts; beat-up	Likely in matrix	Trace	X	Small amount; 100 μm diam.	Matrix is extremely fine-grained, cannot tell composition
LOM407	Iceland	Hyaloclastite	2%	1%; several 1 mm² pheno. throughout; euhedral	X	3%	75%, with palagonite	Trace, maybe up to 10%	Also 20% zeolites (in interstices); Palagonite "2" rims are 125 μm diam.; Very pale yellow color, almost greenish
LOM408	Iceland	Hyaloclastite	Trace	Trace	X	10%	80%, with palagonite	Trace	Also 10% zeolites (in interstices); Palagonite "2" rims are 125 μm diam.; Extremely burnt-orange in color; trace smectites around a few glass grains
LOM409	Iceland	Hyaloclastite	2%	3%; euhedral in glass	X	Trace	75%, with palagonite	Trace	Also 20% zeolites (in interstices); Palagonite "2" rims are 225 μm diam.; Very burnt-orange, but less that LOM409
LOM410	Iceland	Lava	10%, in elongate phenocrysts	5%; some euhedral, some beat-up	Likely in matrix	10%	5%, interstitial	X	Matrix is extremely fine-grained, cannot tell composition; glass layer in one corner with an orage matrix

Sample ID/Section ID	Field Area	Material	Phases Present					Vesiculation	Comments
			% plag	% ol	% px	% opaques	% glass		
LOM411a	Iceland	Lava	15%, in phenocrysts	5%, in phenocrysts; some beat-up	Likely in matrix	Trace	X	X	Matrix is extremely fine-grained, cannot tell composition; Matrix darker than other lavas

Sample ID/Section ID	Field Area	Material	Phases Present						Comments
			% plag	% cpx	% opaques	% biotite	% hbl	% Others	
SC001	AWP	Mafic	50%	15	5	15%	15%	X	Uniform composition; Many plags have sodic rims (probably gleaned from nearby felsic material; many rims have magnetite inclusions
			% plag	% kspar	% qz	% biotite	% hbl	% Others	
	AWP	Felsic	30%	30%	15%	10	10	3% sphene; 2% zircon; trace opaques	Xtals appear grown together, with qz filling in the last voids; xtals usually large (>50µm); Grains show disequil. textures
	AWP	Mafic/Felsic Boundary							No obvious quench zone visible; Mafic material appears to be entering felsic as evidenced by "mafic splintering"; Mafic edge more packed than center (?)

SC002

Sample ID/Section ID	Field Area	Material	Phases Present						Comments
			% plag	% cpx	% opaques	% biotite	% hbl	% Others	
	AWP	Mafic	50%	5%	5%	20%	20%	Trace sphene, interstitial	Uniform composition w/ the exception of some ~40µm augites; Magnetite frequently as small inclusions in plag; some plag have rims; Whole section looks "dirty"
			% plag	%qz	% kspar	% biotite	% hbl	% Others	
SC002	AWP	Felsic	30%	10%	40%	2%	10%	5% sphene; 3% opaques	Composition varies slightly depending on location; many plag have mag inclusions; plag rims are half the xtal radius; Large xtals; qz formed last
	AWP	Mafic/Felsic Boundary	Mafic splintering into felsic, hbl esp.; Some glass visible . . Quench areas?; General elongation of minerals (esp. hbl, plag) toward boundary into felsic; Magnetite more concentrated in boundary zone						

SC003

Sample ID/Section ID	Field Area	Material	Phases Present						Comments
			% plag	% cpx	% opaques	% biotite	% hbl	% Others	
	AWP	Mafic	40%	10%	20%	10%	20%	Trace sphene, interstitial	Magnetite extremely square
			% plag	%qz	% kspar	% biotite	% hbl	% Others	
SC003	AWP	Felsic	40%	15%	30%	X	10%	2% sphene; 3% opaques	Fairly large cpx and mag inclusions in felsic; Many plag have mag inclusions
	AWP	Mafic/Felsic Boundary	Definite mafic splintering; Magnetite seems slightly more concentrated; Elongated grains preferentially oriented perpendicular to boundary; Magnetite seems to bound the mafic advance						

Sample ID/ Section ID	Field Area	Material	Phases Present						Comments
			% plag	% cpx	% opaques	% biotite	% hbl	% Others	
SC004	AWP	Mafic	50%	X	20%	5%	25%	Trace sphene, interstitial	Plag show exsolution lamellae-like structures; Some very large (1.4mm x 1mm) plag
			% plag	%qz	% kspar	% biotite	% hbl	% Others	
	AWP	Felsic	30%	20%	25%	5	10%	5% sphene; 5% opaques	Many plag have "mottled" texture w/qz; Many plag >50µm
	AWP	Mafic/Felsic Boundary							Definite mafic splintering; Magnetite much more concentrated; Elongated grains preferentially oriented perpendicular to boundary; Magnetite seems to bound the mafic advance

Sample ID/ Section ID	Field Area	Material	Phases Present						Comments
			% plag	% cpx	% opaques	% biotite	% hbl	% Others	
ASC202	AWP	Mafic	45%	20%	10%	10%	15%	X	Slightly larger grains than SC samples; Plags are rimmed (sometimes)
			% plag	%qz	% kspar	% biotite	% hbl	% Others	
	AWP	Felsic	20%	15%	30%	10%	10%	5% sphene, 10% opaques	Many plag have "mottled" texture w/qz; Biotite very needley
	AWP	Mafic/Felsic Boundary							Definite mafic splintering; Magnetite much more concentrated; Elongated grains may be oriented perpendicular to boundary

ASC203

Sample ID/ Section ID	Field Area	Material	% plag	% cpx	% opaques	% biotite	% hbl	% Others	Comments
	AWP	Mafic	30%	5%	20%	25%	20%		Very needley bio; Bio needles and hbl increase markedly toward boundary
			% plag	%qz	% kspar	% biotite	% hbl	% Others	
ASC203	AWP	Felsic	15%	15%	25%	10%	20%	10% sphene; 5% opaques	Many plag have "mottled" texture w/qz
	AWP	Mafic/Felsic Boundary							Definite mafic splintering; No preferred orientation at boundary; Mafic splintering present

(Header: Phases Present)

ASC301

Sample ID/ Section ID	Field Area	Material	% plag	% cpx	% opaques	% biotite	% hbl	% Others	Comments
	AWP	Mafic	55%	5%	5%	20%	15%	Trace sphene, interstitial	Concentration of opx/bio increases toward boundary
			% plag	%qz	% kspar	% biotite	% hbl	% Others	
ASC301	AWP	Felsic	15%	15%	35%	10%	10%	15% opaques; trace sphene	Small xtals (500 µm max.)
	AWP	Mafic/Felsic Boundary							Mafic splintering minor; No preferential alignment

(Header: Phases Present)

ASC302

Sample ID/Section ID	Field Area	Material	Phases Present						Comments
			% plag	% cpx	% opaques	% biotite	% hbl	% Others	
	AWP	Mafic	30%	10%	10%	30%	20%	Trace sphene in interstices	A few rogue ol xtals present?
			% plag	%qz	% kspar	% biotite	% hbl	% Others	
ASC302	AWP	Felsic	25%	10%	35%	10%	10%	10% opaques, trace sphene	Feldspars and qz very large
	AWP	Mafic/Felsic Boundary	Some mafic splintering, not too pornounced; No preferential alignment						

ASC401

Sample ID/Section ID	Field Area	Material	Phases Present						Comments
			% plag	% cpx	% opaques	% biotite	% hbl	% Others	
	AWP	Mafic	45%	X	15%	20%	15%	5% apatite/sphene	Nondescript
			% plag	%qz	% kspar	% biotite	% hbl	% Others	
ASC401	AWP	Felsic	30%	15%	30%	5%	10%	5% sphene; 5% opaques	Many sphenes have ilmentite inclusions
	AWP	Mafic/Felsic Boundary	Minerals concentrate here, esp. magnetite; Definite mafic splintering; No preferential alignment of minerals						

ASC501

Sample ID/Section ID	Field Area	Material	Phases Present						Comments
			% plag	% cpx	% opaques	% biotite	% hbl	% Others	
ASC501	AWP	Mafic	50%	X	10%	10%	30%	Trace sphene, trace apatite	A few rogue ol xtals present
			% plag	%qz	% kspar	% biotite	% hbl	% Others	
	AWP	Felsic	45%	15%	30%	5%	5%	X	Rampant granophyric texture (>80% of spar/qz); Felsic is between 2 mafic lobes in the section
	AWP	Mafic/Felsic Boundary	Obvious mafic splintering; No preferential alignment						

ASC502

Sample ID/Section ID	Field Area	Material	Phases Present						Comments
			% plag	% cpx	% opaques	% biotite	% hbl	% Others	
ASC502	AWP	Mafic	40%	5%	5%	30%	20%	Trace sphene	Matrix has very small grains; Some large cpx phenocrysts; Looks dirty and altered
			% plag	%qz	% kspar	% biotite	% hbl	% Others	
	AWP	Felsic	30%	15%	40%	X	10%	1% opaque; 4% sphene; trace apatite	Large entrained hbl; Some plag show mottling; Some plag show resorbed cores?
	AWP	Mafic/Felsic Boundary	Minor mafic splintering, not too pornounced; No preferential alignment; Magnetite concentrated along boundary						

Sample ID/ Section ID	Field Area	Material	Phases Present						Comments
			% plag	% cpx	% opaques	% biotite	% hbl	% Others	
#1	AWP	Mafic	40%	X	5%	30%	20%	3% sphene; 2% apatite	Nondescript
			% plag	%qz	% kspar	% biotite	% hbl	% Others	
	AWP	Felsic	30%	15%	40%	10%	Trace	3% sphene; 2% opaques	Smaller grains; Mini-granophyre texture in some grains
	AWP	Mafic/Felsic Boundary	MInor mafic splintering, not too pornounced; No preferential alignment						

APPENDIX D

LA-ICP-MS Methods and Results

APPENDIX D

LA-ICP-MS METHODS AND RESULTS

Instrumentation and Operating Conditions

Two separate sets of operating conditions were used during LA-ICP-MS analysis.

Table D1 shows conditions used during July 2007, and Table D2 shows conditions used

during January 2008. The laser ablation system used was New Wave 213, and the ICP-

MS system was Perkin-Elmer Sciex ELAN 6100 DRCII. All LA-ICP-MS data reduction

was completed using the GLITTER software package for laser ablation microprobe.

Table D1. LA-ICP-MS Operating Conditions, July 2007 *(after Luo and Ayers, 2007)*

Perkin-Elmer Sciex ELAN 6100 DRCII	
Forward Power	1350-1400 W
Gas Flow Rate	
Nebulizer	0.9-1 L min^{-1}
Auxiliary	0.65-1 L min^{-1}
Plasma	~15.0 L min^{-1}
Lens Voltage	10.5 V
Auto Lens	OFF
New Wave 213 Laser Ablation System	
Wavelength	213 nm
Energy (26-30 kV, 10 Hz)	~14.5 J cm^2
Laser Frequency	10 Hz
Spot Size	60-140 µm
He Carrier Gas Flow	1 L min^{-1}
Pulse Duration	20 ns
Data acquisition	
Data Acquisition Protocol	Time resolved analysis
Scanning Mode	Peak hopping, 1 pt/peak
Dwell Time	30 s
Analysis Time	1 min
Replicates	1

Table D2. LA-ICP-MS Operating Conditions, January 2008 (*after Luo and Ayers, 2007*)

Perkin-Elmer Sciex ELAN 6100 DRCII

Forward Power	1350-1400 W
Gas Flow Rate	
Nebulizer	0.75 L min^{-1}
Auxiliary	0.65-1 L min^{-1}
Plasma	~15.0 L min^{-1}
Lens Voltage	10.5 V
Auto Lens	OFF

New Wave 213 Laser Ablation System

Wavelength	213 nm
Energy (26-30 Kv, 10 Hz)	~6 J cm^2
Laser Frequency	10 Hz
Spot Size	140 μm
He Carrier Gas Flow	0.85 L min^{-1}
Pulse Duration	20 ns

Data acquisition

Data Acquisition Protocol	Time resolved analysis
Scanning Mode	Peak hopping, 1 pt/peak
Dwell Time	30 s
Analysis Time	1 min
Replicates	1

LA-ICP-MS Methods and Results

LA-ICP-MS analysis is the most common way to attain trace element concentrations in individual minerals—or in this case—glasses (Bleick, 2005). As such, LA-ICP-MS was performed on 21 samples from Icelandic rocks, with multiple analyses from each sample (usually 5)(Table D3). NIST 610 was used as the primary external glass standard (500 ppm), but NIST 612 (50 ppm) and NIST 614 were used in addition (Pearce et al., 1997). The suite of 3 standards was run, with NIST 610 being duplicated, before any sample analyses. Sample analyses were then run, with 2 analyses of NIST 610 run after every 15 analyses. The full standard suite was run again before any further analyses after changing the mount, and again after the final sample analyses of the day. Samples were analyzed for the elements listed in Table D4.

Table D3. LA-ICP-MS Analyses

Date	Sample ID	Material	# of Analyses	Spot Size (µm)
July 9, 2007	LOM405	Hyaloclastite	5	140
July 10, 2007	LOM407	Hyaloclastite	5	140
	LOM409	Hyaloclastite	5	140
	LOM410	Lava	5	140
	LOM411a	Lava	5	140
	KEL102	Hyaloclastite	5	140
July 20, 2007	KEL107	Hyaloclastite	5	140
	KEL108	Hyaloclastite	5	140
	RAU106	Hyaloclastite	5	140
	RAU107	Hyaloclastite	5	140
January 23, 2008	KELX02	Lava	5	140
	KELX03a	Lava	5	140
	KELX04	Lava	5	140
	KELX06	Lava	5	140
	KELX07	Lava	5	140
	RAUX01	Lava	5	140
	RAUX03	Lava	5	140
	RAUX04	Lava	5	140
	RAUX05	Lava	5	140
	RAUX06	Lava	5	140
	RAUX07	Hyaloclastite	5	140

Table D4. Elements Analyzed For Using LA-ICP-MS

Element	Isotope Number	Element	Isotope Number	Element	Isotope Number
Si	29	Rb	85	Gd	155
P	31	Sr	88	Tb	159
Ca	42	Y	89	Dy	163
Sc	45	Zr	90	Ho	165
Ti	49	Nb	93	Er	166
V	51	Cs	133	Tm	169
Cr	52	Ba	137	Yb	173
Mn	55	La	139	Lu	175
Co	59	Ce	140	Hf	179
Ni	60	Pr	141	Ta	181
Cu	65	Nd	143	Pb	208
Zn	66	Sm	147	Th	232
Ga	71	Eu	151	U	238

After analysis was complete, the "counts" obtained and stored during analysis were reduced using GLITTER software to produce the Original data set. Although a the full complement of standard trace elements was analyzed for, only the rare earth elements (REE) have been examined in detail in this research. Table D5 lists the normalization values for REE used to normalize the original data to chondrite, and both the Original data set and the normalized values listed afterward.

Table D5. REE Normalization Factors

Element	Normalization Factor
La	0.310
Ce	0.808
Pr	0.122
Nd	0.600
Sm	0.195
Eu	0.074
Gd	0.259
Tb	0.047
Dy	0.322
Ho	0.072
Er	0.210
Tm	0.032
Yb	0.209
Lu	0.032

$$Normalized = \frac{Original}{NormFactor} \quad (A.1)$$

Original LA-ICP-MS Trace Element Data

	KEL102	KEL102	KEL102	KEL102	KEL102	KEL107	KEL107	KEL107	KEL107	KEL107	KEL108	KEL108	KEL108	KEL108	KEL108
Si29	219696.44	219696.44	219696.44	219696.44	219696.45	225773.2	225773.19	225773.19	225773.2	225773.2	226240.66	226240.66	226240.66	226240.66	226240.66
P31	1078.24	960.89	951.68	1087.29	1593.88	765.18	787.23	733.92	764.19	812.64	604.9	633.03	630.78	661.32	692.69
Ca42	85007.42	88753.07	89935.33	89170	69767.27	90906.82	91102.73	97397.16	89149.27	91474.37	70865.99	77377.41	79866.45	83970.64	81031.72
Sc45	46.92	44.41	43.34	48.32	15.85	47.14	47.25	52.21	47.1	47.94	38.11	40.58	44.12	45	42.64
Ti49	17102.73	15621	15725.85	17735.2	6027.08	14410.83	14726.97	13498.67	14402.12	14721.47	11445.63	12438.22	13257.39	12358.84	13120.38
V51	496.78	459.16	453.5	508.24	452.1	445.32	458.79	462.68	440.7	458.21	349.99	381.1	390.79	397.91	404.71
Cr52	52.64	59.36	58.69	49.97	21.35	126.74	127.89	281.87	137.74	131.3	105.63	116.54	131.63	222.32	115.24
Mn55	1679.74	1545.34	1565.95	1702.51	1322.47	1731.36	1761.5	1732.53	1747.18	1804.6	1378.35	1471.42	1542.95	1563.07	1609.04
Co59	45.65	42.83	44.32	44.87	25.38	54.48	55.8	55.69	58.56	58.92	44.51	45.55	52.09	51.32	50.92
Ni60	37.49	39.85	45.9	34.12	29.2	66.53	66.67	75.19	85.03	83.34	63.38	55.74	78.58	80.44	70.22
Cu65	222.35	198.51	195.31	224.33	103.63	215.56	221.16	204.24	217.96	221.35	170.5	183.82	199.8	184.19	197.64
Zn66	157.77	133.1	131.2	145.06	131.76	139.5	138.88	146.03	148.65	138.95	95.69	112.07	118.05	120.06	120.79
Ga71	20.22	19.96	19.86	20.1	21.29	22.62	22.64	22.23	23.24	22.14	17.34	19.04	18.68	18.89	19.49
Rb85	7.57	7.08	6.93	7.66	5.73	5.19	5.39	4.83	5.02	5.48	3.46	3.77	3.88	3.86	4.47
Sr88	187.13	201.75	204.66	193.86	427.47	218.56	217.36	195.91	210.95	222.11	150.47	171.56	166.53	177.06	183.15
Y89	37.43	32.87	32.25	38.35	15	37.42	37	33.55	36.54	37.74	24.67	27.51	30.8	28.57	30.35
Zr90	155.75	135	132.56	155.99	48.24	142.45	142.27	124.66	138.72	144.83	96.75	106.4	119.61	110.58	118.23
Nb93	13.47	12.04	11.98	13.72	4.65	11	11.16	9.75	11.02	11.11	7.66	8.67	9.4	8.53	9.43
Cs133	0.073	0.0712	0.0736	0.0762	0.0665	0.093	0.054	0.058	0.068	0.058	0.0309	0.0335	0.0426	0.0547	0.0457
Ba137	68.31	62.33	62.56	70.33	123.04	56.16	57.76	51.45	55.34	58.74	33.56	40.08	40.89	40.96	45.33
Hf179	3.37	3.66	3.56	3.82	1.043	3.93	3.86	3.86	3.98	4.03	2.36	2.98	3.27	3.16	3.35
Ta181	0.901	0.704	0.698	0.813	0.27	0.74	0.7	0.64	0.7	0.72	0.424	0.527	0.577	0.569	0.556
Pb208	0.996	0.865	0.855	0.925	0.533	0.88	0.88	0.82	0.99	0.96	0.515	0.599	0.619	0.678	0.662
Th232	1.004	0.932	0.993	1.135	0.318	0.84	0.82	0.76	0.85	0.86	0.506	0.584	0.73	0.633	0.622
U238	0.33	0.318	0.296	0.347	0.136	0.28	0.26	0.29	0.32	0.28	0.157	0.196	0.203	0.141	0.231
ThO248	<-NaN	<-NaN	<-NaN	<-NaN	<-NaN	<-NaN	<-NaN	<-NaN	<-NaN	<-NaN	<-NaN	<-NaN	<-NaN	<-NaN	<-NaN

Original LA-ICP-MS Trace Element Data

	KELX02	KELX02	KELX02	KELX02	KELX02	KELX03a	KELX03a	KELX03a	KELX03a	KELX03a	KELX03a	KELX03a
Mg24	22361.64	21071.01	23191.87	23195.57	24185.51	23032.26	23796.6	23091.45	23345.54	29396.21	23110.7	24292.19
Al27	39747.68	42017.09	39837.18	41723.31	41342.88	49372.33	41277.64	45272.69	39819.83	45630.46	42484.73	41173.54
Si29	229255.58	228867.63	229115.34	227395.17	228947.06	229213.52	229807.16	229171.45	230096.98	228830.2	229213.52	229807.16
P31	857.9	823.96	865.26	792.01	796.01	751.84	834.23	832.87	880.87	685.26	910.57	824.12
Ca42	79289.63	83670.79	80766.81	83594.59	84279.28	84400.63	86127.73	79944.66	80615.71	81392.59	80406.61	82727.04
Sc45	44.52	44.39	44.84	43.94	46.52	35.55	47.88	39	46.08	39.39	43.26	45.85
Ti49	15107.76	14145.7	14886.41	13725.33	14298.53	13168.31	14454.1	13420.56	14430.03	11005.12	14499.49	13975.93
V51	461.42	437.69	451.6	469.41	449.98	401.79	480.2	400.15	447.32	355.09	433.47	434.79
Cr52	70.92	91.18	73.15	115.24	120.05	50.96	126.02	52.13	101.5	100.41	62.01	115.7
Mn55	1734.49	1649.8	1755.26	1629.97	1698.82	1479.54	1702.55	1532.71	1699.48	1446.55	1670.35	1652.22
Y89	34.75	32.89	34.94	32.35	33.2	30.46	33.82	30.67	33.74	25.54	33.48	32.74
Zr90	141.15	127.17	137.88	128.63	128.66	120.53	131.41	124.55	131.51	99.43	132.22	128.03
Zr91	140.64	125.79	137.36	125.26	129	120.29	132.72	120.33	134.38	96.14	131.42	127.04
Nb93	10.58	9.51	10.34	9.73	9.51	9.45	10.13	9.41	9.93	7.25	10.06	9.52
Ba137	49.42	45.24	51.87	48.13	44.31	32.27	32.73	45.62	48.45	38.62	49.08	46.72
Hf179	3.99	3.3	3.85	3.57	3.49	3.21	3.66	3.53	3.84	2.89	3.69	3.68
Ta181	0.687	0.616	0.66	0.553	0.61	0.566	0.604	0.593	0.602	0.45	0.615	0.576
Pb208	0.845	0.74	0.755	0.693	0.676	0.651	0.695	0.663	0.744	0.658	0.741	0.696
Th232	0.735	0.713	0.754	0.653	0.675	0.647	0.691	0.647	0.688	0.503	0.733	0.634
U238	0.227	0.208	0.2093	0.1994	0.182	0.1793	0.1818	0.1827	0.23	0.112	0.217	0.2174
ThO248	<-NaN	<-NaN	<-NaN	<-NaN	<-NaN	<-NaN	<-NaN	<-NaN	<-NaN	<-NaN	<-NaN	<-NaN

Original LA-ICP-MS Trace Element Data

	KELX04	KELX04	KELX04	KELX04	KELX04	KELX06	KELX06	KELX06	KELX06	KELX06	KELX07	KELX07	KELX07	KELX07	KELX07
Mg24	21720.47	27787.64	26765.01	23042.2	25998.34	22919.51	23219.12	22306.7	23559.39	23255.08	24750.24	22542.75	22982.48	23946.85	24407.14
Al27	41835.34	41973.95	42225.2	41270.83	44776.43	39632.5	41760.06	51454.8	44026.46	41687.07	42261.32	60664.86	46415.06	52862.8	43003.27
Si29	229227.53	230078.28	233429.83	228652.59	230096.97	228652.59	229437.88	229568.78	229975.44	228549.75	229059.25	229269.61	228582.48	226712.72	228507.67
P31	789.83	825.44	802.67	806.69	781.94	621.26	798.31	560.41	777.15	809.11	780.54	552.29	728.24	644.35	812.97
Ca42	81803.45	80555.12	80915.38	80874.32	82495.15	79707.55	79730.55	86410.49	83323.34	80023.21	83818.45	94610.61	82311.52	82768.61	81447.66
Sc45	44.14	43.15	42.64	44.06	41.52	44.8	42.32	35.02	43.5	42.7	46.38	32.28	39.37	33.36	42.29
Ti49	13466.8	13389.3	13005.91	13144.01	12764.64	13366.77	13288.59	10902.32	12997.49	13204.98	12985.4	9849.74	12352.44	10386.09	13324.41
V51	412.26	412.06	405.1	408.78	390.57	395.86	400.22	293.59	401.06	401.06	410.16	306.99	380.12	311.54	409.26
Cr52	114.49	112.45	120.23	128.54	111.94	142.79	105.04	88.54	128.2	106.09	189.56	93.48	99.63	82.49	110.55
Mn55	1616.23	1595.97	1615.26	1564.46	1519.61	1632.61	1602.01	1275.52	1559.17	1582.08	1577.21	1201.12	1494.3	1225.56	1608.38
Y89	32.26	30.79	30.37	30.41	29.45	31.28	31.53	25.41	30.94	31.25	29.82	22.86	28.15	23.96	30.22
Zr90	126.17	121.83	117.98	120.37	116.46	120.68	121.82	97.96	118.83	122.1	115.87	89.56	111.02	93.44	119.68
Zr91	124.2	120.81	118.25	118.86	116.51	121.23	120.58	100.48	118.96	117.13	115.18	88.32	111.52	94.19	120.22
Nb93	9.64	9.06	9.13	8.88	8.83	9.33	9.16	7.61	8.98	9.06	8.74	6.61	8.64	7.01	9.22
Ba137	45.42	46.08	43.98	43.65	43.39	41.44	45.76	33.78	41.13	43.43	42.84	34.24	42.87	34.72	44.86
Hf179	3.3	3.57	3.41	3.19	3.01	3.45	3.9	2.78	3.13	3.22	3.11	2.65	3.15	2.56	3.42
Ta181	0.56	0.584	0.574	0.535	0.476	0.486	0.577	0.48	0.557	0.598	0.55	0.42	0.505	0.437	0.569
Pb208	0.631	0.639	0.662	0.626	0.591	0.671	0.653	0.553	0.683	0.626	0.68	0.477	0.643	0.555	0.646
Th232	0.613	0.533	0.618	0.603	0.679	0.615	0.619	0.539	0.601	0.62	0.594	0.457	0.575	0.478	0.637
U238	0.193	0.22	0.2093	0.182	0.189	0.199	0.23	0.1549	0.182	0.209	0.1956	0.1539	0.1928	0.163	0.1955
ThO248	<-NaN	<-NaN	<-NaN	<-NaN	<-NaN	<-NaN	<-NaN	<-NaN	<-NaN	<-NaN	<-NaN	<-NaN	<-NaN	<-NaN	<-NaN

Original LA-ICP-MS Trace Element Data

	RAU106	RAU106	RAU106	RAU106	RAU106	RAU107	RAU107	RAU107	Element	RAUX07	RAUX07	RAUX07	RAUX07	RAUX07
Si29	224838.34	224838.34	224838.34	224838.34	224838.34	225305.77	225305.75	225305.77	Si29	232354.72	229863.27	230662.58	233079.25	229900.66
P31	719.32	683.42	637.2	749.85	819.08	721.3	757.73	775.3	P31	807.41	825.7	789.88	780.48	834.44
Ca42	79778.09	82345.67	85565.83	81794.74	80719.7	81173.45	81880.41	80792.67	Ca42	82022.82	81690.93	78310.27	84529.34	83256.72
Sc45	41.43	42.98	38.05	44.11	42.48	40.71	43.16	44.91	Sc45	43.06	45.65	41.7	42.64	45.64
Ti49	12180.46	11697.77	11231.12	12926	12762	12156.1	12670.23	12995.27	Ti49	12689.99	13175.01	12055.51	12633.51	13346.45
V51	375.98	370.68	349.93	401.65	409.26	381.2	398.1	407.82	V51	392.24	409.35	376.28	390.78	413.17
Cr52	232.27	380.36	213.87	241.57	237.29	230.8	236.55	245.52	Cr52	228.03	247.79	243.48	239.28	248.02
Mn55	1487.29	1471.44	1335.6	1533.47	1530.31	1471.88	1506.47	1542.83	Mn55	1559.03	1582.28	1594.13	1506.69	1559.88
Co59	47.04	46.32	39.37	45.66	47.61	46.39	45.23	46.54						
Ni60	83.26	90.9	57.04	66.05	77.64	79.26	68.78	68.09						
Cu65	165.72	156.39	151.23	171.95	175.44	164.05	172.4	175.63						
Zn66	109.76	105.74	93.77	111.84	113.68	110.12	112.07	117.78	Mg24	27449.25	26625.9	33806.53	25154.13	24351.02
Ga71	19.31	18.19	20.3	19.55	21.17	19.9	20.37	20.97	Al27	44956.49	43276.84	42520.25	46566.22	43558.59
Rb85	5.03	4.9	4.96	5.57	5.45	5.38	5.26	5.6	Zr91	124.34	127.86	116.31	122.76	128.35
Sr88	172.96	172.08	194.55	176.28	136.93	180.13	179.33	173.96						
Y89	30.53	30.03	28.51	32.95	31.8	31.15	32.55	33.57	Y89	31.61	33.14	30.14	31.74	32.94
Zr90	120.54	114.89	109.43	128.88	123.69	119.94	124.96	128.34	Zr90	123.63	129.42	117.57	123.19	128.49
Nb93	10.14	9.5	9.15	10.82	10.84	10.21	10.74	10.97	Nb93	10.11	10.68	9.71	10.15	10.76
Cs133	0.0494	0.0474	0.0506	0.0665	0.071	0.0607	0.0481	0.0532						
Ba137	47.86	45.92	47.54	52.14	46.99	49.84	51.1	54.05	Ba137	49.16	50.03	46.19	49.4	51.05
Hf179	3.28	3.31	2.98	3.4	3.47	3.37	3.3	3.57	Hf179	3.44	3.51	3.19	3.49	3.43
Ta181	0.618	0.641	0.528	0.68	0.636	0.652	0.638	0.683	Ta181	0.635	0.663	0.555	0.645	0.644
Pb208	0.753	0.68	0.676	0.769	0.815	0.752	0.724	0.737	Pb208	0.64	0.729	0.642	0.691	0.699
Th232	0.752	0.904	0.718	0.813	0.79	0.777	0.808	0.786	Th232	0.754	0.784	0.694	0.729	0.801
U238	0.222	0.233	0.212	0.259	0.239	0.229	0.262	0.249	U238	0.228	0.224	0.22	0.219	0.238
ThO248	<-NaN	<-NaN	<-NaN	<-NaN	<-NaN	<-NaN	<-NaN	<-NaN	ThO248	<-NaN	<-NaN	<-NaN	<-NaN	<-NaN

Original LA-ICP-MS Trace Element Data

	RAUX01	RAUX01	RAUX01	RAUX01	RAUX01	RAUX03	RAUX03	RAUX03	RAUX03	RAUX03	RAUX04	RAUX04	RAUX04	RAUX04	RAUX04
Mg24	24956.3	23476.45	24316.16	25466.41	23877.89	23579.27	23792.18	25098.31	28452.52	26723.39	26193.12	25625.49	24857.85	24267.79	24281.08
Al27	43100.19	43648.25	44049.85	46155.7	45208.11	45671.52	44915.35	44992.88	43863.41	45088.61	45108.7	44248.08	45333.93	46681.79	44709.21
Si29	231429.17	231153.38	231606.8	234476.88	230597.14	229110.67	230699.97	230279.28	230489.61	228316.05	231681.58	231489.94	231999.44	233453.19	231363.72
P31	740.61	840.74	838.73	822.3	849.05	812.73	840.55	822.36	811.76	791.43	826.71	838.43	840.3	841.8	840.74
Ca42	80895.39	82882.08	82467.42	84685.68	85002.23	84107.89	84640.66	84296.07	83469.36	82443.97	83405.45	83450.54	85055.77	86312.56	84476.8
Sc45	42.31	43.12	43.91	43.4	44.58	43.66	45.74	45.19	45.32	42.6	45.01	45.65	45.87	45.44	45.38
Ti49	12633.22	13029.26	13048.74	12870.78	13014.45	12830.13	13399.91	13187.96	13128.85	12442.52	13114.16	13466.56	13414.38	13375.93	13363.77
V51	393.09	407.16	411.42	400.42	404.29	399.58	416.88	411.2	409.46	387.86	405.33	420.19	416.27	415.64	416.12
Cr52	239.55	243.69	243.58	241.53	238.64	237.71	247.15	243.47	248.1	240.81	243.25	249.45	247.08	244.96	247.25
Mn55	1544	1539.3	1560.5	1542.42	1523.38	1507.14	1562.22	1554.32	1604.15	1510.95	1562.38	1584.22	1575.51	1555.07	1554.99
Y89	30.99	31.97	32.28	31.66	32.19	32.24	33.4	33.35	33.19	30.57	33.4	33.83	33.71	33.62	33.4
Zr90	120.9	123.71	124.55	124.32	124.66	125.1	129.75	128.92	129.3	119.13	128.19	130.91	131.04	130.74	127.98
Zr91	119.76	122.08	124.47	123.35	122.72	124.98	129.2	128.29	127.09	117.92	127.87	130.88	130.8	128.58	127.89
Nb93	10.22	10.39	10.32	10.25	10.41	10.26	10.76	10.44	10.64	10.03	10.53	10.88	10.88	10.65	10.72
Ba137	48.69	50.43	50.77	49.8	48.43	49.92	51.99	50.13	51.22	45.91	50.85	51.89	51.21	51.47	51.47
Hf179	3.26	3.39	3.39	3.13	3.47	3.43	3.52	3.71	3.38	3.06	3.57	3.55	3.62	3.66	3.58
Ta181	0.591	0.609	0.643	0.603	0.624	0.627	0.649	0.617	0.648	0.588	0.642	0.664	0.693	0.661	0.676
Pb208	0.66	0.716	0.699	0.663	0.691	0.666	0.765	0.678	0.646	0.639	0.71	0.725	0.726	0.753	0.763
Th232	0.731	0.756	0.755	0.724	0.745	0.778	0.766	0.81	0.778	0.695	0.949	0.768	0.782	0.801	0.8
U238	0.221	0.24	0.244	0.2201	0.244	0.23	0.256	0.2266	0.236	0.223	0.243	0.257	0.244	0.26	0.242
ThO248	<-NaN	<-NaN	<-NaN	<-NaN	<-NaN	<-NaN	<-NaN	<-NaN	<-NaN	<-NaN	<-NaN	<-NaN	<-NaN	<-NaN	<-NaN

Original LA-ICP-MS Trace Element Data

	RAUX05	RAUX05	RAUX05	RAUX05	RAUX05	RAUX06	RAUX06	RAUX06	RAUX06	RAUX06
Mg24	28472.38	26961.99	27046.06	27455.26	30705.16	25313.78	23950.86	23795.24	23641.39	24869.54
Al27	44023.76	46442.69	44787.24	45480.46	43939.78	43113.75	43648.18	44119.03	41970.9	43964.59
Si29	229713.69	231316.98	232709.95	231293.61	231625.47	230255.89	228185.16	228414.2	225100.03	229489.31
P31	850.9	827.31	844.48	812.44	900.58	846.2	839.82	781.7	824.89	829.54
Ca42	80933.68	84664.28	83626.02	84078.73	82094.8	82013.98	82932.72	82343.05	81935.58	82636.85
Sc45	43.71	43.42	45.41	43.77	44.75	48.25	45.18	42.87	45.52	44.73
Ti49	13100.15	12926.24	13344.43	13118.08	13289.72	13976.41	13139.38	12772.55	13168.86	13013.59
V51	405.2	401.15	420.82	408.69	412.78	423.05	409.65	399.15	408.72	404.17
Cr52	247.31	238.71	248.22	241.2	245.35	255.06	242.38	237.03	244.37	245.39
Mn55	1576.34	1517.73	1574.39	1546.85	1566.64	1573.6	1537.96	1503.98	1550.61	1538.23
Y89	32.86	32.18	33	32.31	32.99	35.18	33.12	31.64	33.32	32.8
Zr90	127.99	125.28	128.12	125.89	129.11	136.91	127.67	123.41	129.18	126.47
Zr91	128.1	124.76	127.81	126.8	127.91	135.69	127.97	123.03	124.12	126.71
Nb93	10.85	10.29	10.58	10.53	10.63	11.13	10.6	10.13	10.55	10.52
Ba137	50.63	50.26	52.16	50.16	50.23	51.65	51.2	49.72	50.4	50.23
Hf179	3.5	3.17	3.4	3.52	3.33	3.57	3.54	3.25	3.65	3.4
Ta181	0.663	0.653	0.66	0.671	0.646	0.699	0.634	0.645	0.634	0.658
Pb208	0.735	0.815	0.719	0.752	0.717	0.758	0.714	0.7	0.692	0.688
Th232	1.655	0.759	0.818	0.803	0.78	0.823	0.783	0.743	0.798	0.76
U238	0.231	0.227	0.255	0.22	0.211	0.243	0.245	0.237	0.234	0.237
ThO248	<-NaN	<-NaN	<-NaN	<-NaN	<-NaN	<-NaN	<-NaN	<-NaN	<-NaN	<-NaN

Original LA-ICP-MS Trace Element Data

	LOM405	LOM405	LOM405	LOM405	LOM405	LOM407	LOM407	LOM407	LOM407	LOM407	LOM409	LOM409	LOM409	LOM409	LOM409
	226708.1	226708.1	226708.1	226708.1	226708.1	224370.8	224370.8	224370.8	224370.8	224370.9	221566.3	221566.3	221566.3	221566.3	221566.3
Si29	226708.1	226708.1	226708.1	226708.1	226708.1	224370.8	224370.8	224370.8	224370.8	224370.9	221566.3	221566.3	221566.3	221566.3	221566.3
P31	632.35	645.86	627.14	643.9	639.49	554.21	570.13	527.29	539.95	486.85	568.14	556.17	604.49	585.08	585.86
Ca42	105706	104107.9	104878.4	100477.8	100186.4	77717.53	76007.74	77738.43	77484.09	54807.26	88851.57	92640.04	94820.55	96673.7	100173.5
Sc45	44.62	44.28	47.32	42.95	41.48	39.59	39.65	38.52	38.89	1.61	41.19	42.99	45.77	44.47	45.05
Ti49	11706.39	11635.09	11389.29	11495.34	11349.23	10514.16	10623.55	10116.7	10214.89	426.1	10405.59	10718.86	11577.96	11152.4	10730.93
V51	357.43	356.74	363.08	349	346.53	337.61	340.67	331.94	333.85	135.98	331.54	340.47	362.05	355.44	347.55
Cr52	260.33	259.89	342.68	231.84	221.42	271.53	281.44	323.63	296.76	12.09	292.71	305.5	316.59	299.36	335.57
Mn55	1426.97	1418.34	1414.88	1437.32	1376.77	1392.86	1408.57	1369.26	1378.81	137.24	1406.78	1343.29	1406.52	1396.23	1357.53
Co59	45.76	45.16	46.13	49.02	45.28	50.14	49.67	49.6	49.08	3.83	53.18	45.44	48.24	46.22	45.44
Ni60	68.55	60.89	66.74	82.02	60.72	74.55	70.42	81.21	79.18	4.99	109.8	66.79	69.12	69.21	70.93
Cu65	139.85	144.17	139.48	144.09	148.04	161.38	166.65	153.75	158.54	19.08	134.59	142.54	145.38	139.05	134.2
Zn66	96.72	98.41	94.64	99.34	91.94	106.69	110.79	100.85	106.21	13.14	93.83	95.35	100.36	98.96	96.94
Ga71	17.63	18.24	17.44	17.78	18.2	20.08	19.65	19.14	19.42	3.97	16.56	17.57	17.51	17.24	17.18
Rb85	3.62	3.61	3.45	3.39	3.58	3.65	3.72	3.55	3.65	11.93	3.39	3.32	3.44	3.43	3.55
Sr88	196.86	193.51	186.33	190.09	191.52	180.15	174.45	179.2	179.3	481.72	178.66	180.46	179.73	184.53	185.4
Y89	24.02	23.76	23.32	23.25	23.03	24.68	23.7	22.85	23.5	1.335	22.16	22.33	24.16	23.27	22.23
Zr90	95.25	94.45	91.91	93.35	91.97	98.29	96.78	91.16	93.64	3.43	88.7	89.89	95.72	92.57	88.08
Nb93	7.21	7.37	7.12	7.31	7.3	7.61	7.66	7.31	7.49	0.372	6.87	6.75	7.44	7.19	6.85
Cs133	0.0325	0.0355	0.0369	0.0378	0.026	0.0428	0.0298	0.0381	0.0357	0.0291	0.0798	0.0233	0.0354	0.0336	0.0369
Ba137	38.35	39.48	36.89	37.38	38.85	39.35	39.17	39.5	38.14	66.88	36.29	35.51	38.44	37.07	35.9
La139	7.18	7.4	6.99	7.28	7.27	7.37	7.38	7.37	7.18	0.439	6.97	6.74	7.42	7.27	6.74
Ce140	18.17	18.29	17.66	18.4	18.18	18.53	18.9	18.4	17.97	0.838	17.1	17.49	19.1	18.26	17.12
Pr141	2.592	2.712	2.579	2.708	2.575	2.702	2.689	2.609	2.809	0.176	2.559	2.45	2.767	2.547	2.53
Nd143	13.34	13.02	13.06	13.2	13.31	13.54	13.75	13.15	13.16	0.677	13.13	12.44	13.29	12.85	12.54
Sm147	3.7	3.74	3.72	3.87	3.92	3.75	3.86	3.68	3.79	0.204	3.49	3.62	3.98	3.93	3.66
Eu151	1.45	1.529	1.402	1.364	1.404	1.475	1.384	1.434	1.45	0.0774	1.347	1.364	1.457	1.426	1.404
Gd155	4.68	4.14	4.55	4.18	4.17	4.22	4.31	3.96	4.32	0.166	3.92	4.37	3.96	4.03	3.97
Tb159	0.768	0.738	0.741	0.763	0.766	0.769	0.747	0.695	0.761	0.04	0.72	0.721	0.715	0.752	0.747
Dy163	4.56	4.63	4.42	4.38	4.3	4.73	4.46	4.45	4.62	0.233	4.21	4.06	4.62	4.66	4.21
Ho165	0.907	0.977	0.93	0.904	0.983	1.024	0.957	0.907	0.948	0.0481	0.883	0.937	0.925	0.935	0.837
Er166	2.433	2.458	2.456	2.372	2.414	2.559	2.474	2.447	2.628	0.108	2.246	2.353	2.596	2.413	2.245
Tm169	0.4	0.358	0.33	0.353	0.329	0.362	0.375	0.364	0.387	0.0165	0.322	0.33	0.343	0.32	0.333
Yb173	2.24	2.24	2.17	2.24	2.45	2.406	2.67	2.28	2.334	0.172	2.25	2.29	2.51	2.31	2.084
Lu175	0.339	0.35	0.343	0.326	0.332	0.333	0.34	0.308	0.349	0.0079	0.316	0.317	0.362	0.336	0.313
Hf179	2.29	2.6	2.56	2.53	2.69	2.74	2.69	2.55	2.36	0.065	2.37	2.35	2.59	2.46	2.25
Ta181	0.449	0.456	0.427	0.43	0.431	0.486	0.431	0.441	0.484	0.0156	0.399	0.437	0.379	0.409	0.408
Pb208	0.62	0.532	0.489	0.537	0.53	0.629	0.641	0.522	0.541	0.0391	0.469	0.526	0.535	0.538	0.598
Th232	0.483	0.521	0.714	0.487	0.496	0.596	0.527	0.558	0.507	0.0256	0.427	0.476	0.472	0.524	0.441
U238	0.1453	0.1557	0.1362	0.169	0.179	0.1768	0.1811	0.174	0.1619	0.153	0.1631	0.1464	0.1706	0.162	0.1604
ThO248	<-NaN	<-NaN	<-NaN	<-NaN	<-NaN	<-NaN	<-NaN	<-NaN	<-NaN	<-NaN	<-NaN	<-NaN	<-NaN	<-NaN	<-NaN

	Original LA-ICP-MS Trace Element Data								
	LOM410	LOM410	LOM410	LOM410	LOM410	LOM411a	LOM411a	LOM411a	LOM411a	LOM411a
Si29	224370.9	224370.9	224370.9	224370.9	224370.9	224370.8	224370.8	224370.9	224370.8	224370.8
P31	1449.7	1596.86	1710.89	36.87	1272.26	1409.86	1384.67	1632.92	1650.31	1437.46
Ca42	68923.66	71299.83	70124.71	140770.3	78155.84	56668.83	62530.62	67754.79	71243.82	63183.43
Sc45	35.5	38.76	37.46	142.14	31.32	32.56	31.34	36.17	38.69	32.67
Ti49	18131.56	19663.22	20160.81	8509.57	15483.18	17749.25	16991.28	19767.98	20015.85	18201.09
V51	377.81	402.75	404.68	461.41	319.24	372.35	349.71	399.27	409.05	375.12
Cr52	3.14	4.06	3.57	235.47	6.34	2.81	3.69	3.97	4.31	4.29
Mn55	1760.45	1867.52	1925.15	2161.43	1476.9	1722.68	1559.55	1711.66	1773.99	1655.2
Co59	41.21	38.26	42.25	57.07	30.88	41.39	36.76	36.32	38.27	36.35
Ni60	17.63	12.54	17.88	84.53	11.68	16.32	15.41	12.09	12.05	11.77
Cu65	124.33	134.6	136.03	7.45	98.99	141.55	120.78	131.81	130.95	129.58
Zn66	148.35	156.94	166.13	63.72	127.09	141.65	144.19	155	160.46	143.18
Ga71	20.94	20.07	20.39	8.85	19.12	22.5	21.86	22.2	21.97	23.66
Rb85	10.87	12.83	12.94	0.125	9.65	12.64	11.5	13.2	13.39	12.48
Sr88	228.18	215.02	214.92	12.76	254.12	214.06	234.55	229.29	231.21	241.48
Y89	43.99	48.54	47.85	26.62	36.97	47.46	41.55	48.54	48.42	45.36
Zr90	213.51	237.99	236.56	37.91	180.57	237.66	205.24	240.6	237.67	226.28
Nb93	17.55	19.2	19.43	0.274	14.42	19.42	16.82	19.07	19.16	18.79
Cs133	0.1222	0.1522	0.1467	0.00345	0.0887	0.1564	0.1361	0.1581	0.1334	0.1146
Ba137	105.44	121.09	119.27	0.54	96.76	122.53	114.98	125.91	125.49	123.99
La139	18.59	21.4	20.82	1.098	15.9	21.12	18.47	21.16	21.24	20.68
Ce140	43.77	49.52	49.29	4.64	37.14	48.19	42.26	48.43	49.72	47.23
Pr141	5.96	6.67	6.69	1.033	5.13	6.7	5.69	6.64	6.64	6.33
Nd143	28.2	31.98	32.02	6.86	24.24	30.75	26.06	31.5	31.09	29.84
Sm147	7.71	8.47	8.4	3.18	6.8	8.46	7.43	8.66	8.24	8.3
Eu151	2.714	3	3.02	1.157	2.241	3.069	2.604	2.933	2.887	2.763
Gd155	8.35	8.75	8.72	4.35	6.93	9.2	7.49	9.28	9.21	8.45
Tb159	1.435	1.547	1.499	0.784	1.23	1.556	1.315	1.538	1.54	1.469
Dy163	8.65	9.44	8.95	5.07	7.02	9.22	7.9	9.21	9.56	8.92
Ho165	1.736	1.89	1.853	1.074	1.419	1.947	1.591	1.917	1.779	1.821
Er166	4.48	4.77	4.95	2.774	3.86	5.1	4.02	4.81	4.91	4.56
Tm169	0.619	0.716	0.642	0.369	0.541	0.707	0.613	0.681	0.704	0.637
Yb173	4.06	4.66	4.53	2.58	3.4	4.83	4.17	4.56	4.75	4.48
Lu175	0.616	0.656	0.611	0.343	0.505	0.696	0.565	0.642	0.664	0.617
Hf179	5.23	6.02	5.75	1.749	4.37	6.24	5.01	6.21	6.02	6.06
Ta181	1.005	1.156	1.131	0.0294	0.856	1.213	0.985	1.143	1.083	1.06
Pb208	1.2	1.435	1.351	0.0492	1.14	1.296	1.202	1.383	1.475	1.32
Th232	1.509	1.835	1.73	0.0346	1.288	1.757	1.462	1.691	1.706	1.662
U238	0.489	0.552	0.551	0.0045	0.38	0.552	0.473	0.512	0.574	0.538
ThO248	<-NaN	<-NaN	<-NaN	<-NaN	<-NaN	<-NaN	<-NaN	<-NaN	<-NaN	<-NaN

Original Glass REE Data (ppm) obtained from GLITTER

Sample ID	Spot #	La	Ce	Pr	Nd	Sm	Eu	Gd	Tb	Dy	Ho	Er	Tm	Yb	Lu
KEL102	1	13.08	30.08	4.24	20.14	5.84	1.972	6.69	1.187	6.78	1.559	3.82	0.523	3.76	0.534
KEL102	2	11.85	27.62	3.77	18.5	5.53	1.946	5.77	0.996	6.13	1.309	3.28	0.472	3.06	0.494
KEL102	3	11.88	27.9	3.68	18.16	5.34	1.81	5.46	1.037	5.95	1.327	3.168	0.45	3.29	0.473
KEL102	4	13.46	31.32	4.24	20.38	5.8	2.1	6.81	1.173	6.95	1.459	3.81	0.56	3.85	0.521
KEL102	5	4.55	10.5	1.391	6.48	1.885	0.751	2.431	0.422	2.323	0.481	1.328	0.1899	1.159	0.2024
KEL107	1	11.8	28.37	4.25	19.73	6.05	2.2	6.7	1.27	7.44	1.54	4.01	0.61	3.91	0.55
KEL107	2	11.74	29.17	4.23	20.28	5.89	2.26	6.6	1.22	7.17	1.5	3.82	0.61	3.96	0.56
KEL107	3	10.45	26.96	3.87	18.9	5.72	1.98	6	1.14	6.77	1.46	3.8	0.59	3.59	0.52
KEL107	4	11.65	29.01	4.19	19.97	5.99	2.19	6.51	1.24	7.45	1.58	3.9	0.59	3.87	0.57
KEL107	5	12.27	30.16	4.36	20.62	6.32	2.25	6.79	1.26	7.64	1.6	4.15	0.63	3.8	0.58
KEL108	1	6.84	16.94	2.47	12.51	3.53	1.313	4.2	0.733	4.49	0.956	2.42	0.337	2.35	0.324
KEL108	2	8.11	20.13	2.95	14.43	4.2	1.58	4.79	0.867	5.06	1.063	2.86	0.394	2.66	0.395
KEL108	3	9.16	22.19	3.21	15.93	4.83	1.79	5.11	0.963	5.89	1.27	3.12	0.455	2.99	0.448
KEL108	4	8.47	21.53	2.99	15.42	4.38	1.66	4.75	0.954	5.77	1.174	3.11	0.448	3.15	0.443
KEL108	5	9.25	22.71	3.29	16.6	4.87	1.77	5.18	0.969	5.8	1.24	3.36	0.43	3.09	0.454
RAU106	1	9.63	22.6	3.19	16.19	4.46	1.67	5.23	0.932	5.74	1.22	3.1	0.474	3.29	0.429
RAU106	2	9.32	21.87	3.11	15.24	4.49	1.7	5	0.962	5.69	1.169	3.19	0.469	3.34	0.48
RAU106	3	9.15	21.34	3.11	14.61	4.32	1.63	4.85	0.982	5.23	1.26	3.1	0.465	2.82	0.454
RAU106	4	10.43	24.48	3.44	16.74	4.81	1.87	5.82	1.045	6.58	1.33	3.47	0.517	3.35	0.501
RAU106	5	9.84	23.88	3.35	16.08	5	1.75	5.22	0.966	5.92	1.28	3.43	0.5	3.31	0.464
RAU107	1	10.1	24.25	3.4	16.84	4.75	1.71	5.57	0.971	6.05	1.34	3.35	0.493	3.53	0.522
RAU107	2	10.19	23.89	3.41	16.21	4.82	1.78	5.82	0.993	6.07	1.34	3.43	0.503	3.4	0.482
RAU107	3	10.12	24.93	3.51	17.87	4.94	1.79	5.61	1.04	6.4	1.34	3.49	0.475	3.71	0.517
RAU107	4	10.35	24.65	3.35	16.59	5.14	1.76	5.54	1.02	5.95	1.36	3.47	0.503	3.3	0.469
RAU107	5	9.81	23.68	3.34	15.77	4.79	1.7	5.45	0.98	5.94	1.29	3.24	0.463	3.19	0.479
RAUX07	1	10.14	23.91	3.3	16.63	4.87	1.711	5.73	0.966	6.14	1.294	3.45	0.525	3.54	0.498
RAUX07	2	9.66	22.76	3.28	16.08	4.55	1.673	5.69	0.976	5.91	1.282	3.36	0.482	3.11	0.511
RAUX07	3	9.14	21.44	3.09	15.29	4.44	1.585	4.96	0.841	5.58	1.151	3.22	0.465	3.28	0.454
RAUX07	4	10.09	23.58	3.39	16.84	4.92	1.63	5.41	1.003	6.48	1.27	3.62	0.561	3.48	0.455
RAUX07	5	9.58	22.71	3.21	16.41	4.37	1.671	5.57	0.933	5.85	1.292	3.22	0.495	3.22	0.477
LOM405	1	7.18	18.17	2.592	13.34	3.7	1.45	4.68	0.768	4.56	0.907	2.433	0.4	2.24	0.339
LOM405	2	7.4	18.29	2.712	13.02	3.74	1.529	4.14	0.738	4.63	0.977	2.458	0.358	2.24	0.35
LOM405	3	6.99	17.66	2.579	13.06	3.72	1.402	4.55	0.741	4.42	0.93	2.456	0.33	2.17	0.343
LOM405	4	7.28	18.4	2.708	13.2	3.87	1.364	4.18	0.763	4.38	0.904	2.372	0.353	2.24	0.326
LOM405	5	7.27	18.18	2.575	13.31	3.92	1.404	4.17	0.766	4.3	0.983	2.414	0.329	2.45	0.332

143

Original Glass REE Data (ppm) obtained from GLITTER

Sample ID	Spot #	La	Ce	Pr	Nd	Sm	Eu	Gd	Tb	Dy	Ho	Er	Tm	Yb	Lu
LOM407	1	7.37	18.53	2.702	13.54	3.75	1.475	4.22	0.769	4.73	1.024	2.559	0.362	2.406	0.333
LOM407	2	7.38	18.9	2.689	13.75	3.86	1.384	4.31	0.747	4.46	0.957	2.474	0.375	2.67	0.34
LOM407	3	7.37	18.4	2.609	13.15	3.68	1.434	3.96	0.695	4.45	0.907	2.447	0.364	2.28	0.308
LOM407	4	7.18	17.97	2.809	13.16	3.79	1.45	4.32	0.761	4.62	0.948	2.628	0.387	2.334	0.349
LOM407	5	0.439	0.838	0.176	0.677	0.204	0.0774	0.166	0.04	0.233	0.0481	0.108	0.0165	0.172	0.0079
LOM409	1	6.97	17.1	2.559	13.13	3.49	1.347	3.92	0.72	4.21	0.883	2.246	0.322	2.25	0.316
LOM409	2	6.74	17.49	2.45	12.44	3.62	1.364	4.37	0.721	4.06	0.937	2.353	0.33	2.29	0.317
LOM409	3	7.42	19.1	2.767	13.29	3.98	1.457	3.96	0.715	4.62	0.925	2.596	0.343	2.51	0.362
LOM409	4	7.27	18.26	2.547	12.85	3.93	1.426	4.03	0.752	4.66	0.935	2.413	0.32	2.31	0.336
LOM409	5	6.74	17.12	2.53	12.54	3.66	1.404	3.97	0.747	4.21	0.837	2.245	0.333	2.084	0.313
KELX02	1	10.44	25.43	3.57	17.5	5.51	2.097	6.32	1.128	6.65	1.441	4.15	0.524	4.1	0.538
KELX02	2	9.79	24.2	3.45	18.34	5.36	1.878	6	1.075	6.43	1.398	3.5	0.519	3.39	0.514
KELX02	3	10.48	25.63	3.69	18.3	5.29	1.979	6.26	1.091	6.81	1.399	3.79	0.529	3.71	0.549
KELX02	4	9.74	23.2	3.4	17.2	4.92	1.833	5.65	0.994	6.17	1.296	3.48	0.522	3.39	0.5
KELX02	5	9.74	23.64	3.48	17.66	5.27	1.83	5.88	1.066	6.47	1.343	3.61	0.506	3.39	0.508
KELX03a	1	10.22	24.67	3.65	18.75	5.3	1.94	6.23	1.082	6.83	1.463	3.71	0.537	3.68	0.564
KELX03a	2	8.4	20.88	2.95	15.57	5.09	1.519	5.49	1.005	6.1	1.296	3.2	0.441	3.29	0.461
KELX03a	3	9.44	22.83	3.29	16.04	4.83	1.724	5.56	0.954	5.66	1.255	3.3	0.451	2.88	0.447
KELX03a	4	9.92	24.31	3.53	17.61	5.31	1.917	6.05	1.093	6.5	1.436	3.63	0.505	3.58	0.49
KELX03a	5	9.38	22.68	3.26	16.95	4.91	1.795	5.53	0.953	6.34	1.267	3.38	0.487	3.18	0.479
KELX03a	6	9.92	24.13	3.55	18	5.62	1.819	6.31	1.052	6.72	1.348	3.66	0.509	3.35	0.495
KELX03a	7	7.69	18.11	2.63	13.33	3.94	1.379	4.58	0.794	4.98	1.112	2.72	0.413	2.67	0.362
KELX03a	8	10.01	24.3	3.58	17.89	5.26	2.057	5.94	1.024	6.02	1.416	3.62	0.548	3.8	0.485
KELX03a	9	9.6	23.28	3.35	17.78	5.14	1.85	6.02	1.033	6.41	1.339	3.46	0.501	3.18	0.475
KELX04	1	9.44	22.46	3.17	16.21	5.16	1.786	5.49	1.014	6.17	1.315	3.52	0.491	3.11	0.521
KELX04	2	9.05	21.57	3.17	17.12	4.55	1.689	5.76	1.042	6.29	1.145	2.99	0.5	2.93	0.448
KELX04	3	8.73	21.15	3.08	15.77	4.76	1.683	5	0.882	5.67	1.235	3.21	0.454	3.03	0.413
KELX04	4	8.94	21.98	3.15	15.63	4.7	1.789	5.28	0.946	5.93	1.293	3.28	0.489	3.28	0.466
KELX04	5	8.4	21.59	3.21	15.66	5	1.541	5.12	0.931	5.51	1.269	3.34	0.503	2.92	0.451
KELX06	1	9.06	22.15	3.17	15.43	4.84	1.834	5.35	0.852	5.98	1.348	3.23	0.448	3.33	0.41
KELX06	2	8.74	21.48	3.11	15.97	4.9	1.604	5.51	0.959	5.85	1.33	3.2	0.476	3.39	0.526
KELX06	3	7.54	17.84	2.54	13.23	3.91	1.428	4.34	0.799	4.87	1.027	2.7	0.404	2.72	0.366
KELX06	4	8.77	21.39	3.08	15.81	4.52	1.642	5.8	0.887	5.67	1.273	3.33	0.468	3.4	0.471
KELX06	5	8.95	22.05	3.12	16.55	4.26	1.752	5.02	0.983	6.22	1.343	3.37	0.463	3.16	0.463
KELX07	1	8.62	21.32	3.08	16.02	4.44	1.671	5.24	0.957	5.74	1.186	3.23	0.437	2.98	0.455

Original Glass REE Data (ppm) obtained from GLITTER

Sample ID	Spot #	La	Ce	Pr	Nd	Sm	Eu	Gd	Tb	Dy	Ho	Er	Tm	Yb	Lu
KELX07	2	6.65	16.6	2.391	12.09	3.37	1.386	4.08	0.645	4.28	0.888	2.38	0.351	2.55	0.322
KELX07	3	8.4	20.54	2.89	15.31	4.37	1.55	5.08	0.912	5.37	1.178	2.98	0.382	2.78	0.404
KELX07	4	6.94	17.18	2.49	12.64	3.59	1.482	4.37	0.74	4.63	0.949	2.57	0.347	2.41	0.33
KELX07	5	8.91	21.84	3.07	15.98	4.77	1.694	5.55	0.935	5.95	1.205	3.42	0.443	3	0.453
RAUX01	1	9.43	22.35	3.16	15.63	4.53	1.669	5.16	0.923	5.58	1.204	3.42	0.473	3.32	0.43
RAUX01	2	9.96	23.32	3.31	16.15	4.69	1.717	5.66	0.938	6.23	1.276	3.43	0.472	3.4	0.473
RAUX01	3	9.8	23.59	3.4	16	4.54	1.653	5.53	0.957	6.02	1.265	3.44	0.514	3.27	0.462
RAUX01	4	9.93	22.99	3.23	16.12	4.71	1.651	5.48	0.955	6.09	1.296	3.36	0.487	3.31	0.458
RAUX01	5	9.76	23.21	3.37	16.59	4.61	1.746	5.35	1.002	5.94	1.293	3.33	0.469	3.15	0.502
RAUX03	1	9.6	22.3	3.21	16.02	4.76	1.702	5.35	0.93	6.04	1.321	3.41	0.483	3.38	0.478
RAUX03	2	10.15	23.95	3.33	16.96	5.02	1.747	5.43	1.007	6.43	1.358	3.46	0.501	3.52	0.49
RAUX03	3	10.03	23.31	3.29	16.06	4.72	1.717	5.55	0.988	6.28	1.314	3.49	0.509	3.36	0.504
RAUX03	4	9.87	23.46	3.26	16.68	4.72	1.753	5.61	1.008	6.11	1.32	3.56	0.515	3.42	0.482
RAUX03	5	9.25	21.92	3.06	15.62	4.48	1.686	5.27	0.88	5.57	1.207	3.27	0.449	3.26	0.475
RAUX04	1	9.85	23.37	3.31	16.52	4.71	1.718	5.3	0.978	6.01	1.384	3.5	0.514	3.42	0.492
RAUX04	2	10.1	24.43	3.35	17.16	4.95	1.689	5.43	0.972	6.45	1.325	3.63	0.526	3.54	0.539
RAUX04	3	10.12	24.07	3.43	17.16	4.92	1.765	5.54	0.996	6.25	1.353	3.57	0.502	3.47	0.506
RAUX04	4	10.01	23.65	3.37	16.8	5.22	1.748	5.65	1.025	6.19	1.333	3.59	0.507	3.33	0.514
RAUX04	5	10.07	23.99	3.38	16.95	4.79	1.836	5.75	1.023	6.22	1.296	3.64	0.516	3.52	0.518
RAUX05	1	9.79	23.41	3.24	15.9	4.65	1.691	5.43	0.989	6.31	1.271	3.39	0.523	3.61	0.478
RAUX05	2	9.73	23.54	3.24	16.68	4.82	1.779	5.43	0.968	6.01	1.3	3.33	0.469	3.38	0.497
RAUX05	3	10	23.98	3.35	16.16	4.85	1.707	5.9	0.992	6.16	1.351	3.53	0.518	3.49	0.476
RAUX05	4	9.73	23.32	3.31	16.27	4.82	1.675	5.7	1.022	5.95	1.232	3.45	0.486	3.53	0.483
RAUX05	5	9.82	23.62	3.22	16.52	4.64	1.728	5.49	1.006	6.22	1.319	3.6	0.496	3.56	0.475
RAUX06	1	9.98	23.6	3.33	16.51	5.04	1.703	5.47	1.051	6.31	1.328	3.62	0.505	3.51	0.513
RAUX06	2	9.8	23.19	3.2	16.65	4.64	1.75	5.65	0.985	6.33	1.275	3.38	0.506	3.51	0.475
RAUX06	3	10.58	25.44	3.5	17.46	5.4	1.781	5.94	1.007	6.76	1.458	3.73	0.54	3.52	0.538
RAUX06	4	9.85	23.34	3.29	16.21	4.89	1.627	5.64	0.977	6.16	1.316	3.43	0.492	3.33	0.465
RAUX06	5	9.64	23.04	3.26	16.44	4.71	1.767	5.31	0.966	5.92	1.309	3.31	0.509	3.25	0.496
LOM410	1	18.59	43.77	5.96	28.2	7.71	2.714	8.35	1.435	8.65	1.736	4.48	0.619	4.06	0.616
LOM410	2	21.4	49.52	6.67	31.98	8.47	3	8.75	1.547	9.44	1.89	4.77	0.716	4.66	0.656
LOM410	3	20.82	49.29	6.69	32.02	8.4	3.02	8.72	1.499	8.95	1.853	4.95	0.642	4.53	0.611
LOM410	4	1.098	4.64	1.033	6.86	3.18	1.157	4.35	0.784	5.07	1.074	2.774	0.369	2.58	0.343
LOM410	5	15.9	37.14	5.13	24.24	6.8	2.241	6.93	1.23	7.02	1.419	3.86	0.541	3.4	0.505
LOM411a	1	21.12	48.19	6.7	30.75	8.46	3.069	9.2	1.556	9.22	1.947	5.1	0.707	4.83	0.696

Original Glass REE Data (ppm) obtained from GLITTER																
Sample ID	Spot #	La	Ce	Pr	Nd	Sm	Eu	Gd	Tb	Dy	Ho	Er	Tm	Yb	Lu
LOM411a	2	18.47	42.26	5.69	26.06	7.43	2.604	7.49	1.315	7.9	1.591	4.02	0.613	4.17	0.565
LOM411a	3	21.16	48.43	6.64	31.5	8.66	2.933	9.28	1.538	9.21	1.917	4.81	0.681	4.56	0.642
LOM411a	4	21.24	49.72	6.64	31.09	8.24	2.887	9.21	1.54	9.56	1.779	4.91	0.704	4.75	0.664
LOM411a	5	20.68	47.23	6.33	29.84	8.3	2.763	8.45	1.469	8.92	1.821	4.56	0.637	4.48	0.617

146

Glass REE Data (ppm) Normalized to Chondrite

Sample ID	Spot #	La	Ce	Pr	Nd	Sm	Eu	Gd	Tb	Dy	Ho	Er	Tm	Yb	Lu
KEL102	1	42.194	37.22772	34.7541	33.56667	29.94872	26.64865	25.83012	25.25532	21.0559	21.65278	18.19048	16.34375	17.99043	16.6875
KEL102	2	38.226	34.18317	30.90164	30.83333	28.35897	26.2973	22.27799	21.19149	19.03727	18.18056	15.61905	14.75	14.64115	15.4375
KEL102	3	38.323	34.5297	30.16393	30.26667	27.38462	24.45946	21.08108	22.06383	18.47826	18.43056	15.08571	14.0625	15.74163	14.78125
KEL102	4	43.419	38.76238	34.7541	33.96667	29.74359	28.37838	26.29344	24.95745	21.58385	20.26389	18.14286	17.5	18.42105	16.28125
KEL102	5	14.677	12.99505	11.40164	10.8	9.666667	10.14865	9.3861	8.978723	7.214286	6.680556	6.32381	5.934375	5.545455	6.325
KEL107	1	38.065	35.11139	34.83607	32.88333	31.02564	29.72973	25.86873	27.02128	23.10559	21.38889	19.09524	19.0625	18.70813	17.1875
KEL107	2	37.871	36.10149	34.67213	33.8	30.20513	30.54054	25.48263	25.95745	22.26708	20.83333	18.19048	19.0625	18.94737	17.5
KEL107	3	33.71	33.36634	31.72131	31.5	29.33333	26.75676	23.16602	24.25532	21.02484	20.27778	18.09524	18.4375	17.17703	16.25
KEL107	4	37.581	35.90347	34.34426	33.28333	30.71795	29.59459	25.13514	26.38298	23.13665	21.94444	18.57143	18.4375	18.51675	17.8125
KEL107	5	39.581	37.32673	35.7377	34.36667	32.41026	30.40541	26.21622	26.80851	23.72671	22.22222	19.7619	19.6875	18.18182	18.125
KEL108	1	22.065	20.96535	20.2459	20.85	18.10256	17.74324	16.21622	15.59574	13.9441	13.27778	11.52381	10.53125	11.24402	10.125
KEL108	2	26.161	24.91337	24.18033	24.05	21.53846	21.35135	18.49421	18.44681	15.71429	14.76389	13.61905	12.3125	12.72727	12.34375
KEL108	3	29.548	27.46287	26.31148	26.55	24.76923	24.18919	19.72973	20.48936	18.29193	17.63889	14.85714	14.21875	14.30622	14
KEL108	4	27.323	26.64604	24.5082	25.7	22.46154	22.43243	18.33977	20.29787	17.91925	16.30556	14.80952	14	15.07177	13.84375
KEL108	5	29.839	28.10644	26.96721	27.66667	24.97436	23.91892	20	20.61702	18.01242	17.22222	16	13.4375	14.78469	14.1875
RAU106	1	31.065	27.9703	26.14754	26.98333	22.87179	22.56757	20.19305	19.82979	17.82609	16.94444	14.7619	14.8125	15.74163	13.40625
RAU106	2	30.065	27.06683	25.4918	25.4	23.02564	22.97297	19.30502	20.46809	17.67081	16.23611	15.19048	14.65625	15.98086	15
RAU106	3	29.516	26.41089	25.4918	24.35	22.15385	22.02703	18.72587	20.89362	16.24224	17.5	14.7619	14.53125	13.49282	14.1875
RAU106	4	33.645	30.29703	28.19672	27.9	24.66667	25.27027	22.47104	22.23404	20.43478	18.47222	16.52381	16.15625	16.02871	15.65625
RAU106	5	31.742	29.55446	27.45902	26.8	25.64103	23.64865	21.50579	20.55319	18.38509	17.77778	16.33333	15.625	15.83732	14.5
RAU107	1	32.581	30.01238	27.86885	28.06667	24.35897	23.10811	21.50579	20.65957	18.78882	18.61111	15.95238	15.40625	16.88995	16.3125
RAU107	2	32.871	29.56683	27.95082	27.01667	24.71795	24.05405	22.47104	21.12766	18.85093	18.61111	16.33333	15.71875	16.26794	15.0625
RAU107	3	32.645	30.85396	28.77049	29.78333	25.33333	24.18919	21.66023	22.12766	19.87578	18.61111	16.61905	14.84375	17.7512	16.15625
RAU107	4	33.387	30.50743	27.45902	27.65	26.35897	23.78378	21.38996	21.70213	18.47826	18.88889	16.52381	15.71875	15.78947	14.65625
RAU107	5	31.645	29.30693	27.37705	26.28333	24.5641	22.97297	21.04247	20.85106	18.4472	17.91667	15.42857	14.46875	15.26316	14.96875
RAUX07	1	32.71	29.59158	27.04918	27.71667	24.97436	23.12162	22.12355	20.55319	19.06832	17.97222	16.42857	16.40625	16.9378	15.5625
RAUX07	2	31.161	28.16832	26.88525	26.8	23.33333	22.60811	21.96911	20.76596	18.35404	17.80556	16	15.0625	14.88038	15.96875
RAUX07	3	29.484	26.53465	25.32787	25.48333	22.76923	21.41892	19.15058	17.89362	17.32919	15.98611	15.33333	14.53125	15.69378	14.1875
RAUX07	4	32.548	29.18317	27.78689	28.06667	25.23077	22.02703	20.88803	21.34043	20.12422	17.63889	17.2381	17.53125	16.65072	14.21875
RAUX07	5	30.903	28.10644	26.31148	27.35	22.41026	22.58108	21.50579	19.85106	18.1677	17.94444	15.33333	15.46875	15.4067	14.90625
LOM405	1	23.161	22.48762	21.2459	22.23333	18.97436	19.59459	18.0695	16.34043	14.16149	12.59722	11.58571	12.5	10.7177	10.59375
LOM405	2	23.871	22.63614	22.22951	21.7	19.17949	20.66216	15.98456	15.70213	14.37888	13.56944	11.70476	11.1875	10.7177	10.9375
LOM405	3	22.548	21.85644	21.13934	21.76667	19.07692	18.94595	17.56757	15.76596	13.72671	12.91667	11.69524	10.3125	10.38278	10.71875
LOM405	4	23.484	22.77228	22.19672	22	19.84615	18.43243	16.139	16.23404	13.60248	12.55556	11.29524	11.03125	10.7177	10.1875
LOM405	5	23.452	22.5	21.10656	22.18333	20.10256	18.97297	16.10039	16.29787	13.35404	13.65278	11.49524	10.28125	11.72249	10.375

Glass REE Data (ppm) Normalized to Chondrite															
Sample ID	Spot #	La	Ce	Pr	Nd	Sm	Eu	Gd	Tb	Dy	Ho	Er	Tm	Yb	Lu
LOM407	1	23.774	22.93317	22.14754	22.56667	19.23077	19.93243	16.29344	16.3617	14.68944	14.22222	12.18571	11.3125	11.51196	10.40625
LOM407	2	23.806	23.39109	22.04098	22.91667	19.79487	18.7027	16.64093	15.89362	13.85093	13.29167	11.78095	11.71875	12.77512	10.625
LOM407	3	23.774	22.77228	21.38525	21.91667	18.87179	19.37838	15.28958	14.78723	13.81988	12.59722	11.65238	11.375	10.90909	9.625
LOM407	4	23.161	22.2401	23.02459	21.93333	19.4359	19.59459	16.67954	16.19149	14.34783	13.16667	12.51429	12.09375	11.16746	10.90625
LOM407	5	1.4161	1.037129	1.442623	1.128333	1.046154	1.045946	0.640927	0.851064	0.723602	0.668056	0.514286	0.515625	0.822967	0.246875
LOM409	1	22.484	21.16337	20.97541	21.88333	17.89744	18.2027	15.13514	15.31915	13.07453	12.26389	10.69524	10.0625	10.76555	9.875
LOM409	2	21.742	21.64604	20.08197	20.73333	18.5641	18.43243	16.87259	15.34043	12.6087	13.01389	11.20476	10.3125	10.95694	9.90625
LOM409	3	23.935	23.63861	22.68033	22.15	20.41026	19.68919	15.28958	15.21277	14.34783	12.84722	12.3619	10.71875	12.00957	11.3125
LOM409	4	23.452	22.59901	20.87705	21.41667	20.15385	19.27027	15.55985	16	14.47205	12.98611	11.49048	10	11.05263	10.5
LOM409	5	21.742	21.18812	20.7377	20.9	18.76923	18.97297	15.32819	15.89362	13.07453	11.625	10.69048	10.40625	9.971292	9.78125
KELX02	1	33.677	31.47277	29.2623	29.16667	28.25641	28.33784	24.40154	24	20.65217	20.01389	19.7619	16.375	19.61722	16.8125
KELX02	2	31.581	29.9505	28.27869	30.56667	27.48718	25.37838	23.16602	22.87234	19.96894	19.41667	16.66667	16.21875	16.2201	16.0625
KELX02	3	33.806	31.7203	30.2459	30.5	27.12821	26.74324	24.16988	23.21277	21.14907	19.43056	18.04762	16.53125	17.7512	17.15625
KELX02	4	31.419	28.71287	27.86885	28.66667	25.23077	24.77027	21.81467	21.14894	19.16149	18	16.57143	16.3125	16.2201	15.625
KELX02	5	31.419	29.25743	28.52459	29.43333	27.02564	24.72973	22.7027	22.68085	20.09317	18.65278	17.19048	15.8125	16.2201	15.875
KELX03a	1	32.968	30.53218	29.91803	31.25	27.17949	26.21622	24.05405	23.02128	21.21118	20.31944	17.66667	16.78125	17.60766	17.625
KELX03a	2	27.097	25.84158	24.18033	25.95	26.10256	20.52703	21.19691	21.38298	18.9441	18	15.2381	13.78125	15.74163	14.40625
KELX03a	3	30.452	28.25495	26.96721	26.73333	24.76923	23.2973	21.46718	20.29787	17.57764	17.43056	15.71429	14.09375	13.7799	13.96875
KELX03a	4	32	30.08663	28.93443	29.35	27.23077	25.90541	23.35907	23.25532	20.18634	19.94444	17.28571	15.78125	17.12919	15.3125
KELX03a	5	30.258	28.06931	26.72131	28.25	25.17949	24.25676	21.35135	20.2766	19.68944	17.59722	16.09524	15.21875	15.21531	14.96875
KELX03a	6	32	29.86386	29.09836	30	28.82051	24.58108	24.36293	22.38298	20.86957	18.72222	17.42857	15.90625	16.02871	15.46875
KELX03a	7	24.806	22.41337	21.55738	22.21667	20.20513	18.63514	17.6834	16.89362	15.46584	15.44444	12.95238	12.90625	12.77512	11.3125
KELX03a	8	32.29	30.07426	29.34426	29.81667	26.97436	27.7973	22.93436	21.78723	18.69565	19.66667	17.2381	17.125	18.18182	15.15625
KELX03a	9	30.968	28.81188	27.45902	29.63333	26.35897	25	23.24324	21.97872	19.90683	18.59722	16.47619	15.65625	15.21531	14.84375
KELX04	1	30.452	27.79703	25.98361	27.01667	26.46154	24.13514	21.19691	21.57447	19.16149	18.26389	16.7619	15.34375	14.88038	16.28125
KELX04	2	29.194	26.69554	25.98361	28.53333	23.33333	22.82432	22.23938	22.17021	19.53416	15.90278	14.2381	15.625	14.01914	14
KELX04	3	28.161	26.17574	25.2459	26.28333	24.41026	22.74324	19.30502	18.76596	17.6087	17.15278	15.28571	14.1875	14.49761	12.90625
KELX04	4	28.839	27.20297	25.81967	26.05	24.10256	24.17568	20.3861	20.12766	18.41615	17.95833	15.61905	15.28125	15.69378	14.5625
KELX04	5	27.097	26.7203	26.31148	26.1	25.64103	20.82432	19.76834	19.80851	17.1118	17.625	15.90476	15.71875	13.97129	14.09375
KELX06	1	29.226	27.41337	25.98361	25.71667	24.82051	24.78378	20.65637	18.12766	18.57143	18.72222	15.38095	14	15.93301	12.8125
KELX06	2	28.194	26.58416	25.4918	26.61667	25.12821	21.67568	21.27413	20.40426	18.1677	18.47222	15.2381	14.875	16.2201	16.4375
KELX06	3	24.323	22.07921	20.81967	22.05	20.05128	19.2973	16.75676	17	15.12422	14.26389	12.85714	12.625	13.01435	11.4375
KELX06	4	28.29	26.47277	25.2459	26.35	23.17949	22.18919	22.39382	18.87234	17.6087	17.68056	15.85714	14.625	16.26794	14.71875
KELX06	5	28.871	27.2896	25.57377	27.58333	21.84615	23.67568	19.38224	20.91489	19.31677	18.65278	16.04762	14.46875	15.11962	14.46875
KELX07	1	27.806	26.38614	25.2459	26.7	22.76923	22.58108	20.23166	20.3617	17.82609	16.47222	15.38095	13.65625	14.25837	14.21875

148

Glass REE Data (ppm) Normalized to Chondrite

Sample ID	Spot #	La	Ce	Pr	Nd	Sm	Eu	Gd	Tb	Dy	Ho	Er	Tm	Yb	Lu
KELX07	2	21.452	20.54455	19.59836	20.15	17.28205	18.72973	15.7529	13.7234	13.29193	12.33333	11.33333	10.96875	12.20096	10.0625
KELX07	3	27.097	25.42079	23.68852	25.51667	22.41026	20.94595	19.6139	19.40426	16.67702	16.36111	14.19048	11.9375	13.30144	12.625
KELX07	4	22.387	21.26238	20.40984	21.06667	18.41026	20.02703	16.87259	15.74468	14.37888	13.18056	12.2381	10.84375	11.5311	10.3125
KELX07	5	28.742	27.0297	25.16393	26.63333	24.46154	22.89189	21.42857	19.89362	18.47826	16.73611	16.28571	13.84375	14.35407	14.15625
RAUX01	1	30.419	27.66089	25.90164	26.05	23.23077	22.55405	19.92278	19.6383	17.32919	16.72222	16.28571	14.78125	15.88517	13.4375
RAUX01	2	32.129	28.86139	27.13115	26.91667	24.05128	23.2027	21.85328	19.95745	19.34783	17.72222	16.33333	14.75	16.26794	14.78125
RAUX01	3	31.613	29.19554	27.86885	26.66667	23.28205	22.33784	21.35135	20.3617	18.69565	17.56944	16.38095	16.0625	15.64593	14.4375
RAUX01	4	32.032	28.45297	26.47541	26.86667	24.15385	22.31081	21.1583	20.31915	18.91304	18	16	15.21875	15.83732	14.3125
RAUX01	5	31.484	28.72525	27.62295	27.65	23.64103	23.59459	20.65637	21.31915	18.4472	17.95833	15.85714	14.65625	15.07177	15.6875
RAUX03	1	30.968	27.59901	26.31148	26.7	24.41026	23	20.65637	19.78723	18.75776	18.34722	16.2381	15.09375	16.17225	14.9375
RAUX03	2	32.742	29.64109	27.29508	28.26667	25.74359	23.60811	20.96525	21.42553	19.96894	18.86111	16.47619	15.65625	16.84211	15.3125
RAUX03	3	32.355	28.84901	26.96721	26.76667	24.20513	23.2027	21.42857	21.02128	19.50311	18.25	16.61905	15.90625	16.07656	15.75
RAUX03	4	31.839	29.03465	26.72131	27.8	24.20513	23.68919	21.66023	21.44681	18.97516	18.33333	16.95238	16.09375	16.36364	15.0625
RAUX03	5	29.839	27.12871	25.08197	26.03333	22.97436	22.78378	20.34749	18.7234	17.29814	16.76389	15.57143	14.03125	15.59809	14.84375
RAUX04	1	31.774	28.92327	27.13115	27.53333	24.15385	23.21622	20.46332	20.80851	18.6646	19.22222	16.66667	16.0625	16.36364	15.375
RAUX04	2	32.581	30.23515	27.45902	28.6	25.38462	22.82432	20.96525	20.68085	20.03106	18.40278	16.4375	16.0625	16.9378	16.84375
RAUX04	3	32.645	29.7896	28.11475	28.6	25.23077	23.85135	21.38996	21.19149	19.40994	18.79167	17.28571	15.6875	16.60287	15.8125
RAUX04	4	32.29	29.2698	27.62295	28	26.76923	23.62162	21.81467	21.80851	19.2236	18.51389	17	15.84375	15.93301	16.0625
RAUX04	5	32.484	29.69059	27.70492	28.25	24.5641	24.81081	22.20077	21.76596	19.31677	18	17.33333	16.125	16.84211	16.1875
RAUX05	1	31.581	28.97277	26.55738	26.5	23.84615	22.85135	20.96525	21.04255	19.59627	17.65278	16.14286	16.34375	17.27273	14.9375
RAUX05	2	31.387	29.13366	26.55738	27.8	24.71795	24.04054	20.96525	20.59574	18.6646	18.05556	15.85714	14.65625	16.17225	15.53125
RAUX05	3	32.258	29.67822	27.45902	26.93333	24.87179	23.06757	22.77992	21.10638	19.13043	18.76389	16.80952	16.1875	16.69856	14.875
RAUX05	4	31.387	28.86139	27.13115	27.11667	24.71795	22.63514	22.00772	21.74468	18.47826	17.11111	16.42857	15.1875	16.88995	15.09375
RAUX05	5	31.677	29.23267	26.39344	27.53333	23.79487	23.35135	21.19691	21.40426	19.31677	18.31944	17.14286	15.5	17.03349	14.84375
RAUX06	1	32.194	29.20792	27.29508	27.51667	25.84615	23.01351	21.11969	22.3617	19.59627	18.44444	17.2381	15.78125	16.79426	16.03125
RAUX06	2	31.613	28.7005	26.22951	27.75	23.79487	23.64865	21.81467	20.95745	19.65839	17.70833	16.09524	15.8125	16.79426	14.84375
RAUX06	3	34.129	31.48515	28.68852	29.1	27.69231	24.06757	22.93436	21.42553	20.99379	20.25	17.7619	16.875	16.84211	16.8125
RAUX06	4	31.774	28.88614	26.96721	27.01667	25.07692	21.98649	21.77606	20.78723	19.13043	18.27778	16.33333	15.375	15.93301	14.53125
RAUX06	5	31.097	28.51485	26.72131	27.4	24.15385	23.87838	20.50193	20.55319	18.38509	18.18056	15.7619	15.90625	15.55024	15.5
LOM410	1	59.968	54.17079	48.85246	47	39.53846	36.67568	32.23938	30.53191	26.86335	24.11111	21.33333	19.34375	19.42584	19.25
LOM410	2	69.032	61.28713	54.67213	53.3	43.4359	40.54054	33.78378	32.91489	29.31677	26.25	22.71429	22.375	22.29665	20.5
LOM410	3	67.161	61.00248	54.83607	53.36667	43.07692	40.81081	33.66795	31.89362	27.79503	25.73611	23.57143	20.0625	21.67464	19.09375
LOM410	4	3.5419	5.742574	8.467213	11.43333	16.30769	15.63514	16.79537	16.68085	15.74534	14.91667	13.20952	11.53125	12.3445	10.71875
LOM410	5	51.29	45.96535	42.04918	40.4	34.87179	30.28378	26.75676	26.17021	21.80124	19.70833	18.38095	16.90625	16.26794	15.78125
LOM411a	1	68.129	59.64109	54.91803	51.25	43.38462	41.47297	35.52124	33.10638	28.63354	27.04167	24.28571	22.09375	23.11005	21.75

149

Sample ID	Spot #	La	Ce	Pr	Nd	Sm	Eu	Gd	Tb	Dy	Ho	Er	Tm	Yb	Lu
								Glass REE Data (ppm) Normalized to Chondrite							
LOM411a	2	59.581	52.30198	46.63934	43.43333	38.10256	35.18919	28.91892	27.97872	24.53416	22.09722	19.14286	19.15625	19.95215	17.65625
LOM411a	3	68.258	59.93812	54.42623	52.5	44.41026	39.63514	35.83012	32.7234	28.60248	26.625	22.90476	21.28125	21.81818	20.0625
LOM411a	4	68.516	61.53465	54.42623	51.81667	42.25641	39.01351	35.55985	32.76596	29.68944	24.70833	23.38095	22	22.72727	20.75
LOM411a	5	66.71	58.45297	51.88525	49.73333	42.5641	37.33784	32.62548	31.25532	27.70186	25.29167	21.71429	19.90625	21.43541	19.28125

APPENDIX E

Electron Microprobe Methods and Results

APPENDIX E

ELECTRON MICROPROBE METHODS AND RESULTS

Instrumentation and Operating Conditions

Electron microprobe (EMP) analysis was conducted at the University of Tennessee-Knoxville EMP Laboratory. The UT EMP Lab houses a Cameca SX-50 microprobe outfitted with an energy dispersive system (EDS), which—coupled with Oxford Instruments software—permits detailed back-scattered electron (BSE) imaging. Although EMP analyses were obtained in both July and November 2007, the same settings were used for all samples (Table E1).

Table E1. EMP Operating Conditions for All Analyses

Parameter	Value
Spot Size	10 μm
Beam Voltage	15 kV
Current/Beam Intensity	10 nA
Counts/second	20
Dwell Time	1 ms

EMP Methods and Results

EMP analysis is the best way to attain accurate and extremely precise major element concentrations in individual minerals and glasses. Although LA-ICP-MS can be used to acquire major element concentrations, its minimum beam size is far greater than that of the EMP, which has a minimum beam size of 1 μm. Therefore, EMP usage is best when analyzing materials that may not be homogeneous or are present in small amounts.

The 22 Icelandic glass-bearing samples analyzed using the EMP contained not-insignificant amounts of microlites, which necessitated EMP precision to avoid them. I picked all spots to be analyzed and took BSE images of all samples, and the EMP was programmed to complete the analyses overnight. See Table E2 for a list of samples analyzed. Major elements analyzed in each sample are listed in Table E3.

Table E2. EMP Analyses

Date	Sample ID	Material	# of Analyses	Spot Size (μm)
July 17, 2007	KEL102	Hyaloclastite	8	10
	KEL107	Hyaloclastite	8	10
	KEL108	Hyaloclastite	10	10
	RAU104	Hyaloclastite	8	10
	RAU016	Hyaloclastite	10	10
	RAU107	Hyaloclastite	10	10
	LOM405	Hyaloclastite	8	10
	LOM407	Hyaloclastite	10	10
	LOM409	Hyaloclastite	8	10
	LOM410	Lava	8	10
	LOM411a	Lava	8	10
July 30, 2007	LOM410	Lava	6	12
	LOM411a	Lava	7	12
November 30, 2008	KELX02	Lava	5	10
	KELX03a	Lava	5	10
	KELX04	Lava	5	10
	KELX06	Lava	5	10
	KELX07	Lava	5	10
	RAUX01	Lava	5	10
	RAUX03	Lava	5	10
	RAUX04	Lava	5	10
	RAUX05	Lava	5	10
	RAUX06	Lava	5	10
	RAUX07	Hyaloclastite	5	10

Table E3. Major Elements Analyzed For Using EMP

Major Elements	
SiO_2	MgO
TiO_2	CaO
Al_2O_3	Na_2O
FeO	K_2O
MnO	P_2O_5
SO_2	Cr_2O_3

After analysis was complete, the original major element oxide percentages obtained were normalized to 100%. The Normalized data set was used to produce the major element graphs seen elsewhere in this manuscript. Both the Original and the Normalized data sets are listed on the following pages. In addition, BSE images of the samples analyzed with analytical spots shown are included following the data sets.

Original Major Element Data (oxide weight %)

Sample ID-Spot	SiO$_2$	TiO$_2$	Al$_2$O$_3$	FeO	MnO	MgO	CaO	Na$_2$O	K$_2$O	P$_2$O$_5$	Cr$_2$O$_3$	SO$_2$	Total
KEL102-8	45.649	3.214	11.724	15.357	0.251	5.299	9.977	2.558	0.387	0.260	0.064	0.081	94.821
KEL107-1	47.442	2.559	12.952	13.422	0.270	6.182	11.514	2.534	0.256	0.209	0.010	0.095	97.445
KEL107-2	48.675	2.650	13.112	13.465	0.208	6.275	11.647	2.500	0.232	0.256	0.000	0.120	99.140
KEL107-3	48.816	2.614	12.980	13.558	0.315	6.294	11.355	2.560	0.270	0.202	0.000	0.095	99.059
KEL107-4	48.326	2.598	12.846	12.891	0.348	6.425	11.164	2.510	0.303	0.258	0.016	0.025	97.710
KEL107-5	48.397	2.637	12.944	13.267	0.246	6.489	11.263	2.557	0.233	0.192	0.003	0.130	98.358
KEL107-6	48.296	2.580	12.961	13.082	0.222	6.345	11.325	2.526	0.283	0.236	0.049	0.100	98.005
KEL107-7	48.364	2.488	12.278	12.819	0.214	7.172	12.141	2.438	0.258	0.270	0.013	0.105	98.560
KEL107-8	48.093	2.489	12.948	13.627	0.310	6.464	11.424	2.571	0.267	0.209	0.010	0.000	98.412
KEL108-1	48.809	2.575	12.993	13.414	0.291	6.499	11.262	2.538	0.249	0.225	0.010	0.005	98.870
KEL108-2	48.431	2.582	12.891	13.340	0.275	6.422	11.038	2.618	0.234	0.234	0.000	0.065	98.130
KEL108-3	48.525	2.651	13.090	13.473	0.249	6.389	11.307	2.627	0.237	0.249	0.000	0.060	98.857
KEL108-4	48.566	2.657	13.043	13.552	0.179	6.545	11.195	2.524	0.254	0.241	0.003	0.100	98.859
KEL108-5	48.175	2.612	12.979	13.383	0.179	6.631	11.184	2.615	0.265	0.254	0.000	0.045	98.322
KEL108-6	48.701	2.542	13.109	13.481	0.257	6.392	11.000	2.572	0.239	0.255	0.016	0.080	98.644
KEL108-7	48.356	2.588	12.952	13.263	0.372	6.515	11.464	2.599	0.258	0.227	0.026	0.075	98.695
KEL108-8	48.737	2.461	14.325	12.534	0.273	5.926	11.450	2.598	0.285	0.206	0.000	0.030	98.825
KEL108-9	49.099	2.620	13.172	13.564	0.289	6.487	11.241	2.573	0.232	0.221	0.010	0.080	99.588
KEL108-10	48.494	2.561	13.039	13.451	0.265	6.381	11.485	2.647	0.233	0.229	0.000	0.035	98.820
KELX02-1	48.591	2.618	13.224	14.419	0.175	5.693	11.081	2.821	0.216	0.237	NA	NA	99.075
KELX02-2	48.425	2.662	13.222	14.114	0.249	5.994	11.154	2.683	0.201	0.200	NA	NA	98.904
KELX02-3	48.768	2.671	13.196	13.588	0.198	6.298	11.549	2.694	0.306	0.229	NA	NA	99.497
KELX02-4	48.039	2.943	13.202	14.300	0.253	5.831	11.094	2.639	0.231	0.219	NA	NA	98.751
KELX02-5	48.409	2.893	12.783	14.690	0.275	5.630	10.902	2.726	0.273	0.255	NA	NA	98.836
KELX03a-1	48.279	2.884	12.680	14.003	0.377	5.974	11.134	2.627	0.274	0.242	NA	NA	98.474
KELX03a-2	48.160	2.815	12.586	14.226	0.241	5.934	10.892	2.512	0.266	0.205	NA	NA	97.837
KELX03a-3	48.401	2.712	12.705	14.613	0.200	5.965	11.076	2.644	0.284	0.270	NA	NA	98.870
KELX03a-4	48.202	2.795	12.592	14.275	0.350	5.985	10.882	2.698	0.277	0.243	NA	NA	98.299
KELX03a-5	48.442	2.791	12.685	14.189	0.222	5.917	11.164	2.602	0.272	0.250	NA	NA	98.534
KELX04-1	48.209	2.526	13.009	13.435	0.241	6.372	11.398	2.581	0.280	0.257	NA	NA	98.308
KELX04-2	48.378	2.604	12.928	13.456	0.219	6.285	11.498	2.480	0.264	0.176	NA	NA	98.288
KELX04-3	47.925	2.642	13.056	13.434	0.245	6.387	11.237	2.505	0.227	0.272	NA	NA	97.930
KELX04-4	47.863	2.619	13.080	13.359	0.204	6.356	11.441	2.521	0.244	0.160	NA	NA	97.847
KELX04-5	48.280	2.641	13.138	13.374	0.147	6.181	11.410	2.436	0.284	0.190	NA	NA	98.081

NA--No data taken

155

Original Major Element Data (oxide weight %)

Sample ID-Spot	SiO$_2$	TiO$_2$	Al$_2$O$_3$	FeO	MnO	MgO	CaO	Na$_2$O	K$_2$O	P$_2$O$_5$	Cr$_2$O$_3$	SO$_2$	Total
KELX06-1	48.026	2.619	13.230	13.291	0.147	6.617	11.300	2.525	0.248	0.177	NA	NA	98.180
KELX06-2	48.156	2.481	13.189	13.188	0.211	6.642	11.183	2.573	0.225	0.261	NA	NA	98.109
KELX06-3	48.364	2.526	13.187	13.224	0.252	6.647	11.267	2.574	0.238	0.198	NA	NA	98.477
KELX06-4	48.607	2.448	13.291	13.256	0.248	6.644	11.288	2.585	0.256	0.174	NA	NA	98.797
KELX06-5	48.332	2.531	13.343	13.368	0.286	6.574	11.372	2.534	0.265	0.245	NA	NA	98.850
KELX07-1	48.739	2.403	13.137	13.902	0.259	6.654	11.357	2.550	0.259	0.201	NA	NA	99.461
KELX07-2	48.483	2.449	13.175	13.743	0.165	6.609	11.229	2.510	0.269	0.217	NA	NA	98.849
KELX07-3	48.621	2.474	13.489	13.560	0.210	6.592	11.465	2.586	0.273	0.157	NA	NA	99.427
KELX07-4	47.682	2.612	13.220	13.618	0.292	6.692	11.377	2.343	0.256	0.220	NA	NA	98.312
KELX07-5	48.439	2.632	13.443	13.418	0.213	6.678	11.283	2.552	0.239	0.191	NA	NA	99.088
RAU104-1	47.572	2.521	13.051	12.707	0.236	6.808	11.316	2.301	0.305	0.224	0.014	0.177	97.232
RAU104-2	45.571	2.520	12.841	12.473	0.236	6.628	11.241	2.350	0.297	0.223	0.046	0.071	94.497
RAU104-3	48.469	2.534	13.255	12.712	0.259	6.568	11.381	2.431	0.289	0.257	0.011	0.080	98.246
RAU104-4	47.148	2.554	12.857	12.051	0.183	7.396	11.974	2.223	0.243	0.244	0.049	0.022	96.944
RAU104-5	45.932	2.626	12.817	12.881	0.248	6.597	11.376	2.369	0.274	0.222	0.051	0.145	95.538
RAU104-6	47.213	2.552	13.258	12.959	0.243	6.404	11.171	2.518	0.271	0.220	0.000	0.092	96.901
RAU104-7	46.652	2.444	13.140	12.808	0.182	6.527	11.095	2.449	0.314	0.230	0.000	0.158	95.999
RAU104-8	47.922	2.585	13.477	12.350	0.206	6.485	11.357	2.359	0.302	0.236	0.043	0.140	97.462
RAU106-1	48.623	2.417	13.171	13.142	0.267	6.641	11.382	2.452	0.291	0.215	0.094	0.181	98.876
RAU106-2	48.671	2.460	13.168	12.503	0.252	6.621	11.374	2.369	0.312	0.224	0.120	0.116	98.190
RAU106-3	48.755	2.435	13.205	13.000	0.348	6.658	11.576	2.456	0.286	0.232	0.000	0.166	99.117
RAU106-4	47.786	2.506	13.068	12.296	0.203	6.610	11.490	2.315	0.284	0.219	0.006	0.115	96.898
RAU106-5	48.969	2.432	13.167	12.709	0.217	6.645	11.479	2.408	0.266	0.216	0.000	0.151	98.659
RAU106-6	48.555	2.558	13.306	12.573	0.248	6.866	11.552	2.513	0.273	0.240	0.042	0.020	98.746
RAU106-7	47.642	2.588	13.112	12.897	0.285	6.747	11.251	2.293	0.274	0.255	0.065	0.035	97.444
RAU106-8	47.104	2.445	12.858	13.034	0.256	6.704	11.515	2.376	0.283	0.208	0.000	0.095	96.878
RAU106-9	48.054	2.319	13.200	12.770	0.258	6.578	11.600	2.389	0.311	0.220	0.042	0.165	97.906
RAU106-10	47.988	2.473	13.132	12.826	0.221	6.784	11.273	2.398	0.289	0.211	0.078	0.130	97.803
RAU107-1	48.140	2.468	13.229	12.550	0.476	6.535	11.259	2.483	0.306	0.180	0.029	0.135	97.790
RAU107-2	49.118	2.504	13.397	12.571	0.447	6.769	11.455	2.278	0.292	0.231	0.019	0.000	99.081
RAU107-3	48.109	2.413	13.245	12.395	0.362	6.688	11.252	2.465	0.284	0.274	0.032	0.165	97.684
RAU107-4	48.564	2.350	14.126	12.117	0.383	6.362	11.537	2.421	0.278	0.252	0.071	0.065	98.526
RAU107-5	47.263	2.517	13.193	13.015	0.334	6.609	11.213	2.440	0.291	0.207	0.029	0.000	97.111
RAU107-6	46.584	2.470	12.976	12.571	0.331	6.742	11.386	2.321	0.275	0.181	0.077	0.209	96.123

NA--No data taken

Original Major Element Data (oxide weight %)

Sample ID-Spot	SiO$_2$	TiO$_2$	Al$_2$O$_3$	FeO	MnO	MgO	CaO	Na$_2$O	K$_2$O	P$_2$O$_5$	Cr$_2$O$_3$	SO$_2$	Total
RAU107-7	47.531	2.479	13.194	12.611	0.419	6.849	11.183	2.460	0.268	0.224	0.071	0.060	97.349
RAU107-8	48.138	2.418	13.025	12.748	0.387	6.835	11.460	2.480	0.305	0.245	0.039	0.075	98.155
RAU107-9	47.885	2.495	12.898	12.630	0.328	6.881	11.353	2.442	0.235	0.225	0.055	0.109	97.536
RAU107-10	47.469	2.476	12.992	12.833	0.352	6.782	11.432	2.498	0.305	0.238	0.029	0.109	97.515
RAUX01-1	48.736	2.515	13.001	13.615	0.263	6.389	11.246	2.294	0.277	0.219	NA	NA	98.555
RAUX01-2	48.975	2.477	13.175	13.602	0.254	6.596	11.299	2.017	0.289	0.236	NA	NA	98.920
RAUX01-3	49.109	2.575	13.248	13.189	0.207	6.565	11.430	2.272	0.268	0.250	NA	NA	99.113
RAUX01-4	49.476	2.340	14.248	10.976	0.291	6.291	11.848	2.744	0.225	0.193	NA	NA	98.632
RAUX01-5	48.808	2.412	13.328	13.139	0.235	6.627	11.506	2.372	0.251	0.260	NA	NA	98.938
RAUX03-1	48.230	2.419	13.370	13.075	0.245	6.571	11.582	2.510	0.196	0.202	NA	NA	98.400
RAUX03-2	49.147	2.603	13.455	12.957	0.274	6.375	11.714	2.635	0.165	0.256	NA	NA	99.581
RAUX03-3	48.413	2.467	13.483	12.948	0.196	6.269	11.261	2.412	0.610	0.213	NA	NA	98.272
RAUX03-4	48.380	2.543	12.978	12.947	0.222	6.536	11.486	2.587	0.204	0.233	NA	NA	98.116
RAUX03-5	49.002	2.600	13.767	13.199	0.288	6.646	11.955	2.472	0.194	0.200	NA	NA	100.323
RAUX04-1	49.127	2.500	13.316	12.736	0.185	6.611	11.681	2.425	0.291	0.246	NA	NA	99.118
RAUX04-2	49.084	2.511	13.253	12.837	0.245	6.644	11.639	2.370	0.305	0.225	NA	NA	99.113
RAUX04-3	49.238	2.504	13.271	12.914	0.291	6.538	11.504	2.440	0.272	0.234	NA	NA	99.206
RAUX04-4	48.951	2.442	13.263	12.941	0.230	6.479	11.676	2.403	0.292	0.276	NA	NA	98.953
RAUX04-5	49.284	1.934	17.154	10.051	0.119	4.957	12.041	2.696	0.249	0.195	NA	NA	98.680
RAUX05-1	47.694	2.583	13.180	12.569	0.213	6.421	11.492	2.390	0.248	0.262	NA	NA	97.052
RAUX05-2	48.929	2.563	13.253	12.823	0.289	6.678	11.482	2.352	0.274	0.232	NA	NA	98.875
RAUX05-3	48.913	2.415	13.221	12.561	0.194	6.467	11.615	2.370	0.286	0.208	NA	NA	98.250
RAUX05-4	48.700	2.449	13.339	12.817	0.217	6.611	11.558	2.249	0.244	0.238	NA	NA	98.422
RAUX05-5	48.596	2.508	13.362	12.697	0.186	6.417	11.383	2.338	0.288	0.296	NA	NA	98.071
RAUX06-1	47.364	2.714	13.117	12.961	0.236	6.972	12.212	2.323	0.190	0.266	NA	NA	98.355
RAUX06-2	48.398	2.624	13.326	12.673	0.285	6.802	11.726	2.431	0.155	0.161	NA	NA	98.581
RAUX06-3	49.427	1.789	19.155	9.067	0.232	4.594	12.927	2.844	0.142	0.164	NA	NA	100.341
RAUX06-4	48.435	2.637	13.309	13.221	0.126	6.696	11.704	2.639	0.160	0.292	NA	NA	99.219
RAUX06-5	48.408	2.606	13.338	12.347	0.240	7.024	12.137	2.531	0.168	0.266	NA	NA	99.065
RAUX07-1	48.038	2.368	13.003	13.181	0.326	6.519	11.266	2.455	0.266	0.249	NA	NA	97.671
RAUX07-2	48.672	2.489	12.940	12.589	0.251	6.569	11.256	2.337	0.292	0.217	NA	NA	97.612
RAUX07-3	48.203	2.547	12.907	12.648	0.289	6.716	11.515	2.304	0.307	0.248	NA	NA	97.684
RAUX07-4	48.653	2.568	13.241	13.234	0.233	6.571	11.480	2.426	0.269	0.263	NA	NA	98.938
RAUX07-5	48.914	2.532	12.970	12.953	0.138	6.531	11.492	2.337	0.313	0.223	NA	NA	98.403

NA--No data taken

157

Original Major Element Data (oxide weight %)

Sample ID-Spot	SiO$_2$	TiO$_2$	Al$_2$O$_3$	FeO	MnO	MgO	CaO	Na$_2$O	K$_2$O	P$_2$O$_5$	Cr$_2$O$_3$	SO$_2$	Total
LOM405-1	47.910	2.288	12.509	12.638	0.179	7.097	11.988	2.302	0.237	0.230	0.014	0.116	97.508
LOM405-2	47.003	2.434	12.960	12.965	0.216	6.816	11.736	2.402	0.225	0.188	0.084	0.067	97.096
LOM405-3	47.211	2.368	13.071	12.626	0.332	6.790	11.537	2.455	0.239	0.236	0.017	0.138	97.020
LOM405-4	46.447	2.287	13.212	12.565	0.299	6.568	11.837	2.409	0.225	0.225	0.000	0.040	96.114
LOM405-5	45.985	2.408	12.876	13.044	0.230	6.629	11.515	2.395	0.234	0.177	0.000	0.133	95.626
LOM405-6	47.508	2.320	13.133	13.024	0.235	6.664	11.872	2.368	0.239	0.209	0.009	0.031	97.612
LOM405-7	47.342	2.211	14.866	12.039	0.192	6.074	11.829	2.536	0.224	0.138	0.012	0.093	97.556
LOM405-8	47.394	1.962	16.333	10.483	0.168	5.395	12.223	2.579	0.182	0.199	0.040	0.058	97.016
LOM407-1	48.639	2.319	14.420	12.007	0.279	6.607	11.911	2.493	0.226	0.218	0.057	0.103	99.279
LOM407-2	48.586	2.330	13.314	12.967	0.286	6.869	11.790	2.395	0.252	0.250	0.000	0.083	99.122
LOM407-3	47.608	2.390	13.388	12.733	0.333	6.925	11.787	2.491	0.241	0.238	0.041	0.024	98.199
LOM407-4	47.598	2.301	12.657	12.746	0.275	7.468	12.135	2.357	0.233	0.207	0.085	0.131	98.193
LOM407-5	48.307	2.435	13.588	12.955	0.241	6.937	12.026	2.335	0.220	0.226	0.057	0.049	99.376
LOM407-6	47.377	2.259	12.331	12.528	0.264	7.483	12.362	2.330	0.209	0.203	0.044	0.092	97.482
LOM407-7	47.458	2.289	12.339	12.491	0.235	7.948	12.494	2.379	0.218	0.178	0.000	0.000	98.029
LOM407-8	46.449	2.342	13.283	13.015	0.237	6.717	11.594	2.490	0.247	0.174	0.006	0.106	96.660
LOM407-9	47.455	2.381	13.317	12.714	0.294	6.830	11.886	2.457	0.260	0.200	0.000	0.039	97.833
LOM407-10	45.494	1.780	11.147	14.151	0.241	13.462	9.841	1.943	0.214	0.186	0.034	0.058	98.551
LOM409-1	47.319	2.316	13.047	13.060	0.282	6.882	11.771	2.440	0.240	0.219	0.000	0.033	97.609
LOM409-2	47.365	2.351	13.076	12.939	0.206	6.805	11.816	2.388	0.221	0.200	0.015	0.071	97.453
LOM409-3	46.160	2.333	12.966	12.843	0.216	6.987	11.864	2.419	0.250	0.183	0.055	0.113	96.389
LOM409-4	47.287	2.373	13.040	12.391	0.189	6.930	11.867	2.449	0.253	0.216	0.034	0.005	97.034
LOM409-5	46.638	2.284	13.017	12.991	0.198	7.082	11.711	2.411	0.218	0.220	0.033	0.099	96.902
LOM409-6	46.644	2.145	12.341	12.444	0.228	7.734	12.388	2.294	0.218	0.200	0.073	0.042	96.751
LOM409-7	47.048	2.335	13.002	12.471	0.228	7.007	11.680	2.486	0.231	0.212	0.000	0.122	96.822
LOM409-8	47.578	2.260	13.635	12.227	0.251	6.818	11.882	2.475	0.232	0.206	0.030	0.127	97.721
LOM410-2	47.424	4.655	10.895	18.358	0.301	3.802	7.080	3.042	0.983	0.566	0.027	0.135	97.268
LOM410-5	47.720	4.745	11.202	18.175	0.269	2.594	7.116	3.139	1.067	0.572	0.000	0.218	96.817
LOM410-6	49.911	4.267	11.674	16.553	0.383	2.668	7.791	2.990	0.760	0.593	0.045	0.233	97.868
LOM410-2.1	49.669	4.116	10.694	16.415	0.406	3.346	8.428	2.754	0.700	0.525	NA	NA	97.053
LOM410-2.2	49.389	4.012	10.841	16.286	0.395	3.168	8.411	2.839	0.669	0.508	NA	NA	96.518
LOM410-2.3	49.649	4.081	10.575	16.449	0.473	3.317	8.255	2.899	0.712	0.511	NA	NA	96.921
LOM410-2.4	49.898	4.102	10.731	16.098	0.412	3.221	8.392	2.767	0.688	0.482	NA	NA	96.791
LOM410-2.5	49.760	4.125	10.948	16.542	0.512	3.219	8.386	2.744	0.787	0.512	NA	NA	97.535

NA--No data taken

158

Original Major Element Data (oxide weight %)

Sample ID-Spot	SiO_2	TiO_2	Al_2O_3	FeO	MnO	MgO	CaO	Na_2O	K_2O	P_2O_5	Cr_2O_3	SO_2	Total
LOM410-2.6	49.439	4.206	10.639	16.356	0.331	3.217	8.378	2.840	0.624	0.547	NA	NA	96.577
LOM411a-1	48.569	4.111	11.086	16.611	0.278	3.904	8.152	2.849	0.746	0.519	0.056	0.204	97.085
LOM411a-2	48.179	4.030	11.370	17.082	0.350	3.710	8.157	3.000	0.722	0.498	0.009	0.175	97.282
LOM411a-3	47.828	4.085	11.344	16.414	0.235	4.036	8.378	3.090	0.737	0.483	0.035	0.194	96.859
LOM411a-4	47.557	3.756	10.704	18.055	0.322	5.308	7.227	2.374	0.736	0.521	0.053	0.180	96.793
LOM411a-5	48.009	4.111	11.564	16.524	0.240	3.896	8.176	3.067	0.837	0.563	0.012	0.230	97.229
LOM411a-6	47.281	3.997	11.138	16.624	0.339	3.902	8.332	2.849	0.738	0.488	0.009	0.170	95.867
LOM411a-7	48.449	4.103	11.182	16.398	0.344	4.062	8.372	2.897	0.721	0.522	0.000	0.097	97.147
LOM411a-8	46.933	4.054	11.259	16.633	0.329	3.981	8.216	2.899	0.694	0.490	0.000	0.175	95.663
LOM411a-2.1	50.043	4.056	10.664	16.187	0.457	3.224	8.306	2.922	0.795	0.483	NA	NA	97.137
LOM411a-2.2	49.750	4.019	10.579	16.685	0.392	3.263	8.488	2.753	0.734	0.494	NA	NA	97.157
LOM411a-2.3	49.496	4.141	10.711	16.168	0.356	3.242	8.503	2.852	0.663	0.501	NA	NA	96.633
LOM411a-2.4	49.650	4.000	10.957	16.628	0.478	3.310	8.358	2.873	0.757	0.556	NA	NA	97.567
LOM411a-2.5	49.300	4.254	10.871	16.381	0.470	3.252	8.364	2.837	0.730	0.480	NA	NA	96.939
LOM411a-2.6	49.539	4.216	10.632	16.270	0.345	3.255	8.382	2.968	0.717	0.545	NA	NA	96.869
LOM411a-2.7	49.124	4.197	10.973	16.353	0.481	3.267	8.420	2.821	0.708	0.588	NA	NA	96.932

NA--No data taken

Major Elements (oxide weight %) Normalized to 100%

Sample ID-Spot	SiO$_2$	TiO$_2$	Al$_2$O$_3$	FeO	MnO	MgO	CaO	Na$_2$O	K$_2$O	P$_2$O$_5$	Cr$_2$O$_3$	SO$_2$	Total	PNT
KEL102-8	48.142	3.390	12.364	16.196	0.265	5.588	10.522	2.698	0.408	0.274	0.067	0.085	100	94.821
KEL107-1	48.686	2.626	13.292	13.774	0.277	6.344	11.816	2.600	0.263	0.214	0.010	0.097	100	97.445
KEL107-2	49.097	2.673	13.226	13.582	0.210	6.329	11.748	2.522	0.234	0.258	0.000	0.121	100	99.140
KEL107-3	49.280	2.639	13.103	13.687	0.318	6.354	11.463	2.584	0.273	0.204	0.000	0.096	100	99.059
KEL107-4	49.459	2.659	13.147	13.193	0.356	6.576	11.426	2.569	0.310	0.264	0.016	0.026	100	97.710
KEL107-5	49.205	2.681	13.160	13.488	0.250	6.597	11.451	2.600	0.237	0.196	0.003	0.132	100	98.358
KEL107-6	49.279	2.633	13.225	13.348	0.227	6.474	11.556	2.577	0.289	0.241	0.050	0.102	100	98.005
KEL107-7	49.071	2.524	12.457	13.006	0.217	7.277	12.318	2.474	0.262	0.274	0.013	0.107	100	98.560
KEL107-8	48.869	2.529	13.157	13.847	0.315	6.568	11.608	2.612	0.271	0.212	0.010	0.000	100	98.412
KEL108-1	49.367	2.604	13.141	13.567	0.294	6.573	11.391	2.567	0.252	0.229	0.010	0.005	100	98.870
KEL108-2	49.354	2.631	13.137	13.594	0.280	6.544	11.248	2.668	0.238	0.238	0.000	0.066	100	98.130
KEL108-3	49.086	2.682	13.241	13.629	0.252	6.463	11.438	2.657	0.240	0.249	0.000	0.061	100	98.857
KEL108-4	49.127	2.688	13.194	13.708	0.181	6.621	11.324	2.553	0.257	0.245	0.003	0.101	100	98.859
KEL108-5	48.997	2.657	13.201	13.611	0.182	6.744	11.375	2.660	0.270	0.258	0.000	0.046	100	98.322
KEL108-6	49.370	2.577	13.289	13.666	0.261	6.480	11.151	2.607	0.242	0.258	0.016	0.081	100	98.644
KEL108-7	48.995	2.622	13.123	13.438	0.377	6.601	11.616	2.633	0.261	0.230	0.026	0.076	100	98.695
KEL108-8	49.316	2.490	14.495	12.683	0.276	5.996	11.586	2.629	0.288	0.207	0.000	0.030	100	98.825
KEL108-9	49.302	2.631	13.226	13.620	0.290	6.514	11.288	2.584	0.233	0.222	0.010	0.080	100	99.588
KEL108-10	49.073	2.592	13.195	13.612	0.268	6.457	11.622	2.679	0.236	0.232	0.000	0.035	100	98.820
KELX02-1	49.045	2.642	13.347	14.554	0.177	5.746	11.184	2.847	0.218	0.239	NA	NA	100	99.075
KELX02-2	48.962	2.691	13.369	14.270	0.252	6.060	11.278	2.713	0.203	0.202	NA	NA	100	98.904
KELX02-3	49.015	2.685	13.263	13.657	0.199	6.330	11.607	2.708	0.308	0.230	NA	NA	100	99.497
KELX02-4	48.647	2.980	13.369	14.481	0.256	5.905	11.234	2.672	0.234	0.222	NA	NA	100	98.751
KELX02-5	48.979	2.927	12.934	14.863	0.278	5.696	11.030	2.758	0.276	0.258	NA	NA	100	98.836
KELX03a-1	49.027	2.929	12.876	14.220	0.383	6.067	11.307	2.668	0.278	0.246	NA	NA	100	98.474
KELX03a-2	49.225	2.877	12.864	14.541	0.246	6.065	11.133	2.568	0.272	0.210	NA	NA	100	97.837
KELX03a-3	48.954	2.743	12.850	14.780	0.202	6.033	11.203	2.674	0.287	0.273	NA	NA	100	98.870
KELX03a-4	49.036	2.843	12.810	14.522	0.356	6.089	11.070	2.745	0.282	0.247	NA	NA	100	98.299
KELX03a-5	49.163	2.833	12.874	14.400	0.225	6.005	11.330	2.641	0.276	0.254	NA	NA	100	98.534
KELX04-1	49.039	2.569	13.233	13.666	0.245	6.482	11.594	2.625	0.285	0.261	NA	NA	100	98.308
KELX04-2	49.221	2.649	13.153	13.690	0.223	6.394	11.698	2.523	0.269	0.179	NA	NA	100	98.288
KELX04-3	48.938	2.698	13.332	13.718	0.250	6.522	11.475	2.558	0.232	0.278	NA	NA	100	97.930
KELX04-4	48.916	2.677	13.368	13.653	0.208	6.496	11.693	2.576	0.249	0.164	NA	NA	100	97.847
KELX04-5	49.225	2.693	13.395	13.636	0.150	6.302	11.633	2.484	0.290	0.194	NA	NA	100	98.081

PNT--Pre-Normalization Total; NA--No data taken

160

Major Elements (oxide weight %) Normalized to 100%

Sample ID-Spot	SiO₂	TiO₂	Al₂O₃	FeO	MnO	MgO	CaO	Na₂O	K₂O	P₂O₅	Cr₂O₃	SO₂	Total	PNT
KELX06-1	48.916	2.668	13.475	13.537	0.150	6.740	11.509	2.572	0.253	0.180	NA	NA	100	98.180
KELX06-2	49.084	2.529	13.443	13.442	0.215	6.770	11.399	2.623	0.229	0.266	NA	NA	100	98.109
KELX06-3	49.112	2.565	13.391	13.429	0.256	6.750	11.441	2.614	0.242	0.201	NA	NA	100	98.477
KELX06-4	49.199	2.478	13.453	13.417	0.251	6.725	11.425	2.616	0.259	0.176	NA	NA	100	98.797
KELX06-5	48.894	2.560	13.498	13.524	0.289	6.650	11.504	2.563	0.268	0.248	NA	NA	100	98.850
KELX07-1	49.003	2.416	13.208	13.977	0.260	6.690	11.419	2.564	0.260	0.202	NA	NA	100	99.461
KELX07-2	49.048	2.478	13.328	13.903	0.167	6.686	11.360	2.539	0.272	0.220	NA	NA	100	98.849
KELX07-3	48.901	2.488	13.567	13.638	0.211	6.630	11.531	2.601	0.275	0.158	NA	NA	100	99.427
KELX07-4	48.501	2.657	13.447	13.852	0.297	6.807	11.572	2.383	0.260	0.224	NA	NA	100	98.312
KELX07-5	48.885	2.656	13.567	13.541	0.215	6.739	11.387	2.575	0.241	0.193	NA	NA	100	99.088
RAU104-1	48.926	2.593	13.423	13.069	0.243	7.002	11.638	2.367	0.314	0.237	0.014	0.182	100	97.232
RAU104-2	48.225	2.667	13.589	13.199	0.250	7.014	11.896	2.487	0.314	0.236	0.049	0.075	100	94.497
RAU104-3	49.334	2.579	13.492	12.939	0.264	6.685	11.584	2.474	0.294	0.265	0.011	0.081	100	98.246
RAU104-4	48.634	2.635	13.262	12.431	0.189	7.629	12.351	2.293	0.251	0.252	0.051	0.023	100	96.944
RAU104-5	48.077	2.749	13.416	13.483	0.260	6.905	11.907	2.480	0.287	0.229	0.053	0.152	100	95.538
RAU104-6	48.723	2.634	13.682	13.373	0.251	6.609	11.528	2.599	0.280	0.227	0.000	0.095	100	96.901
RAU104-7	48.596	2.546	13.688	13.342	0.190	6.799	11.557	2.551	0.327	0.240	0.000	0.165	100	95.999
RAU104-8	49.170	2.652	13.828	12.672	0.211	6.654	11.653	2.420	0.310	0.236	0.044	0.144	100	97.462
RAU106-1	49.176	2.444	13.321	13.291	0.270	6.716	11.511	2.480	0.294	0.217	0.095	0.183	100	98.876
RAU106-2	49.568	2.505	13.411	12.733	0.257	6.743	11.584	2.413	0.318	0.228	0.122	0.118	100	98.190
RAU106-3	49.189	2.457	13.323	13.116	0.351	6.717	11.679	2.478	0.289	0.235	0.000	0.167	100	99.117
RAU106-4	49.316	2.586	13.486	12.690	0.209	6.822	11.858	2.389	0.293	0.222	0.006	0.119	100	96.898
RAU106-5	49.635	2.465	13.346	12.882	0.220	6.735	11.635	2.441	0.270	0.219	0.000	0.153	100	98.659
RAU106-6	49.172	2.590	13.475	12.733	0.251	6.953	11.699	2.545	0.276	0.243	0.043	0.020	100	98.746
RAU106-7	48.892	2.656	13.456	13.235	0.292	6.924	11.546	2.353	0.281	0.263	0.067	0.036	100	97.444
RAU106-8	48.622	2.524	13.272	13.454	0.264	6.920	11.886	2.453	0.292	0.215	0.000	0.098	100	96.878
RAU106-9	49.082	2.369	13.482	13.043	0.264	6.719	11.848	2.440	0.318	0.225	0.043	0.169	100	97.906
RAU106-10	49.066	2.529	13.427	13.114	0.226	6.936	11.526	2.452	0.295	0.211	0.080	0.133	100	97.803
RAU107-1	49.228	2.524	13.528	12.834	0.487	6.683	11.513	2.539	0.313	0.184	0.030	0.138	100	97.790
RAU107-2	49.574	2.527	13.521	12.688	0.451	6.832	11.561	2.299	0.295	0.236	0.019	0.000	100	99.081
RAU107-3	49.250	2.470	13.559	12.689	0.371	6.847	11.519	2.523	0.291	0.280	0.033	0.169	100	97.684
RAU107-4	49.291	2.385	14.337	12.298	0.389	6.457	11.710	2.457	0.282	0.259	0.072	0.066	100	98.526
RAU107-5	48.669	2.592	13.585	13.402	0.344	6.806	11.547	2.513	0.300	0.213	0.030	0.000	100	97.111
RAU107-6	48.463	2.570	13.499	13.078	0.344	7.014	11.845	2.415	0.286	0.186	0.080	0.217	100	96.123

PNT--Pre-Normalization Total; NA--No data taken

Major Elements (oxide weight %) Normalized to 100%

Sample ID-Spot	SiO$_2$	TiO$_2$	Al$_2$O$_3$	FeO	MnO	MgO	CaO	Na$_2$O	K$_2$O	P$_2$O$_5$	Cr$_2$O$_3$	SO$_2$	Total	PNT
RAU107-7	48.825	2.547	13.553	12.954	0.430	7.036	11.488	2.527	0.275	0.230	0.073	0.062	100	97.349
RAU107-8	49.043	2.463	13.270	12.988	0.394	6.963	11.675	2.527	0.311	0.250	0.040	0.076	100	98.155
RAU107-9	49.095	2.558	13.224	12.949	0.336	7.055	11.640	2.504	0.241	0.231	0.056	0.112	100	97.536
RAU107-10	48.679	2.539	13.323	13.160	0.361	6.955	11.723	2.562	0.313	0.244	0.030	0.112	100	97.515
RAUX01-1	49.451	2.552	13.192	13.815	0.267	6.483	11.411	2.328	0.281	0.222	NA	NA	100	98.555
RAUX01-2	49.510	2.504	13.319	13.751	0.257	6.668	11.422	2.039	0.292	0.239	NA	NA	100	98.920
RAUX01-3	49.548	2.598	13.367	13.307	0.209	6.624	11.532	2.292	0.270	0.252	NA	NA	100	99.113
RAUX01-4	50.162	2.372	14.446	11.128	0.295	6.378	12.012	2.782	0.228	0.196	NA	NA	100	98.632
RAUX01-5	49.332	2.438	13.471	13.280	0.238	6.698	11.630	2.397	0.254	0.263	NA	NA	100	98.938
RAUX03-1	49.014	2.458	13.587	13.288	0.249	6.678	11.770	2.551	0.199	0.205	NA	NA	100	98.400
RAUX03-2	49.354	2.614	13.512	13.012	0.275	6.402	11.763	2.646	0.166	0.257	NA	NA	100	99.581
RAUX03-3	49.264	2.510	13.720	13.176	0.199	6.379	11.459	2.454	0.621	0.217	NA	NA	100	98.272
RAUX03-4	49.309	2.592	13.227	13.196	0.226	6.662	11.707	2.637	0.208	0.237	NA	NA	100	98.116
RAUX03-5	48.844	2.592	13.723	13.157	0.287	6.625	11.917	2.464	0.193	0.199	NA	NA	100	100.323
RAUX04-1	49.564	2.522	13.434	12.849	0.187	6.670	11.785	2.447	0.294	0.248	NA	NA	100	99.118
RAUX04-2	49.523	2.533	13.372	12.952	0.247	6.703	11.743	2.391	0.308	0.227	NA	NA	100	99.113
RAUX04-3	49.632	2.524	13.377	13.017	0.293	6.590	11.596	2.460	0.274	0.236	NA	NA	100	99.206
RAUX04-4	49.469	2.468	13.403	13.078	0.232	6.548	11.800	2.428	0.295	0.279	NA	NA	100	98.953
RAUX04-5	49.943	1.960	17.383	10.185	0.121	5.023	12.202	2.732	0.252	0.198	NA	NA	100	98.680
RAUX05-1	49.143	2.661	13.580	12.951	0.219	6.616	11.841	2.463	0.256	0.270	NA	NA	100	97.052
RAUX05-2	49.486	2.592	13.404	12.969	0.292	6.754	11.613	2.379	0.277	0.235	NA	NA	100	98.875
RAUX05-3	49.784	2.458	13.456	12.785	0.197	6.582	11.822	2.412	0.291	0.212	NA	NA	100	98.250
RAUX05-4	49.481	2.488	13.553	13.022	0.220	6.717	11.743	2.285	0.248	0.242	NA	NA	100	98.422
RAUX05-5	49.552	2.557	13.625	12.947	0.190	6.543	11.607	2.384	0.294	0.302	NA	NA	100	98.071
RAUX06-1	48.156	2.759	13.336	13.178	0.240	7.089	12.416	2.362	0.193	0.270	NA	NA	100	98.355
RAUX06-2	49.095	2.662	13.518	12.855	0.289	6.900	11.895	2.466	0.157	0.163	NA	NA	100	98.581
RAUX06-3	49.259	1.783	19.090	9.036	0.231	4.578	12.883	2.834	0.142	0.163	NA	NA	100	100.341
RAUX06-4	48.816	2.658	13.414	13.325	0.127	6.749	11.796	2.660	0.161	0.294	NA	NA	100	99.219
RAUX06-5	48.865	2.631	13.464	12.464	0.242	7.090	12.252	2.555	0.170	0.269	NA	NA	100	99.065
RAUX07-1	49.183	2.424	13.313	13.495	0.334	6.674	11.535	2.514	0.272	0.255	NA	NA	100	97.671
RAUX07-2	49.863	2.550	13.257	12.897	0.257	6.730	11.531	2.394	0.299	0.222	NA	NA	100	97.612
RAUX07-3	49.346	2.607	13.213	12.948	0.296	6.875	11.788	2.359	0.314	0.254	NA	NA	100	97.684
RAUX07-4	49.175	2.596	13.383	13.376	0.236	6.642	11.603	2.452	0.272	0.266	NA	NA	100	98.938
RAUX07-5	49.708	2.573	13.180	13.163	0.140	6.637	11.679	2.375	0.318	0.227	NA	NA	100	98.403

PNT--Pre-Normalization Total; NA--No data taken

162

Major Elements (oxide weight %) Normalized to 100%

Sample ID-Spot	SiO$_2$	TiO$_2$	Al$_2$O$_3$	FeO	MnO	MgO	CaO	Na$_2$O	K$_2$O	P$_2$O$_5$	Cr$_2$O$_3$	SO$_2$	Total	PNT
LOM405-1	49.134	2.346	12.829	12.961	0.184	7.278	12.294	2.361	0.243	0.236	0.014	0.119	100	97.508
LOM405-2	48.409	2.507	13.348	13.353	0.222	7.020	12.087	2.474	0.232	0.194	0.087	0.069	100	97.096
LOM405-3	48.661	2.441	13.472	13.014	0.342	6.999	11.891	2.530	0.246	0.243	0.018	0.142	100	97.020
LOM405-4	48.325	2.379	13.746	13.073	0.311	6.834	12.316	2.506	0.234	0.235	0.000	0.042	100	96.114
LOM405-5	48.088	2.518	13.465	13.641	0.241	6.932	12.042	2.505	0.245	0.185	0.000	0.139	100	95.626
LOM405-6	48.670	2.377	13.454	13.343	0.241	6.827	12.162	2.426	0.245	0.209	0.009	0.032	100	97.612
LOM405-7	48.528	2.266	15.238	12.341	0.197	6.226	12.125	2.600	0.230	0.142	0.012	0.095	100	97.556
LOM405-8	48.852	2.022	16.835	10.805	0.173	5.561	12.599	2.658	0.188	0.205	0.041	0.060	100	97.016
LOM407-1	48.992	2.336	14.525	12.094	0.281	6.655	11.998	2.511	0.228	0.220	0.057	0.104	100	99.279
LOM407-2	49.016	2.351	13.432	13.082	0.289	6.930	11.894	2.416	0.254	0.255	0.000	0.084	100	99.122
LOM407-3	48.481	2.434	13.634	12.967	0.339	7.052	12.003	2.537	0.245	0.242	0.042	0.024	100	98.199
LOM407-4	48.474	2.343	12.890	12.981	0.280	7.605	12.358	2.400	0.237	0.211	0.087	0.133	100	98.193
LOM407-5	48.610	2.450	13.673	13.036	0.243	6.981	12.102	2.350	0.221	0.232	0.057	0.049	100	99.376
LOM407-6	48.601	2.317	12.650	12.852	0.271	7.676	12.681	2.390	0.214	0.208	0.045	0.094	100	97.482
LOM407-7	48.412	2.335	12.587	12.742	0.240	8.108	12.745	2.427	0.222	0.184	0.000	0.000	100	98.029
LOM407-8	48.054	2.423	13.742	13.465	0.245	6.949	11.995	2.576	0.256	0.180	0.006	0.110	100	96.660
LOM407-9	48.506	2.434	13.612	12.996	0.301	6.981	12.149	2.511	0.266	0.203	0.000	0.040	100	97.833
LOM407-10	46.163	1.806	11.311	14.359	0.245	13.660	9.986	1.972	0.217	0.189	0.034	0.059	100	98.551
LOM409-1	48.478	2.373	13.367	13.380	0.289	7.051	12.059	2.500	0.246	0.225	0.000	0.034	100	97.609
LOM409-2	48.603	2.412	13.418	13.277	0.211	6.983	12.125	2.450	0.227	0.205	0.015	0.073	100	97.453
LOM409-3	47.889	2.420	13.452	13.324	0.224	7.249	12.308	2.510	0.259	0.189	0.057	0.117	100	96.389
LOM409-4	48.732	2.446	13.439	12.770	0.195	7.142	12.230	2.524	0.261	0.223	0.035	0.005	100	97.034
LOM409-5	48.129	2.357	13.433	13.406	0.204	7.308	12.085	2.488	0.225	0.227	0.034	0.102	100	96.902
LOM409-6	48.210	2.217	12.755	12.862	0.236	7.994	12.804	2.371	0.225	0.207	0.075	0.043	100	96.751
LOM409-7	48.592	2.412	13.429	12.880	0.235	7.237	12.063	2.568	0.239	0.212	0.000	0.126	100	96.822
LOM409-8	48.688	2.313	13.953	12.512	0.257	6.977	12.159	2.533	0.237	0.208	0.031	0.130	100	97.721
LOM410-2	48.756	4.786	11.201	18.874	0.309	3.909	7.279	3.127	1.011	0.575	0.028	0.139	100	97.268
LOM410-5	49.289	4.901	11.570	18.773	0.278	2.679	7.350	3.242	1.102	0.591	0.000	0.225	100	96.817
LOM410-6	50.998	4.360	11.928	16.914	0.391	2.726	7.961	3.055	0.777	0.593	0.046	0.238	100	97.868
LOM410-2.1	51.177	4.241	11.019	16.913	0.418	3.448	8.684	2.838	0.721	0.541	NA	NA	100	97.053
LOM410-2.2	51.171	4.157	11.232	16.874	0.409	3.282	8.714	2.941	0.693	0.526	NA	NA	100	96.518
LOM410-2.3	51.226	4.211	10.911	16.972	0.488	3.422	8.517	2.991	0.735	0.527	NA	NA	100	96.921
LOM410-2.4	51.552	4.238	11.087	16.632	0.426	3.328	8.670	2.859	0.711	0.498	NA	NA	100	96.791
LOM410-2.5	51.018	4.229	11.225	16.960	0.525	3.300	8.598	2.813	0.807	0.525	NA	NA	100	97.535

PNT--Pre-Normalization Total; NA--No data taken

163

Major Elements (oxide weight %) Normalized to 100%

Sample ID-Spot	SiO$_2$	TiO$_2$	Al$_2$O$_3$	FeO	MnO	MgO	CaO	Na$_2$O	K$_2$O	P$_2$O$_5$	Cr$_2$O$_3$	SO$_2$	Total	PNT
LOM410-2.6	51.191	4.355	11.016	16.936	0.343	3.331	8.675	2.941	0.646	0.566	NA	NA	100	96.577
LOM411a-1	50.027	4.234	11.419	17.110	0.286	4.021	8.397	2.935	0.768	0.534	0.058	0.210	100	97.085
LOM411a-2	49.525	4.143	11.688	17.559	0.360	3.814	8.385	3.084	0.742	0.512	0.009	0.180	100	97.282
LOM411a-3	49.379	4.217	11.712	16.946	0.243	4.167	8.650	3.190	0.761	0.499	0.036	0.200	100	96.859
LOM411a-4	49.133	3.880	11.059	18.653	0.333	5.484	7.466	2.453	0.760	0.538	0.055	0.186	100	96.793
LOM411a-5	49.377	4.228	11.894	16.995	0.247	4.007	8.409	3.154	0.861	0.587	0.012	0.237	100	97.229
LOM411a-6	49.319	4.169	11.618	17.341	0.354	4.070	8.691	2.972	0.770	0.509	0.009	0.177	100	95.867
LOM411a-7	49.872	4.223	11.510	16.880	0.354	4.181	8.618	2.982	0.742	0.522	0.000	0.100	100	97.147
LOM411a-8	49.061	4.238	11.769	17.387	0.344	4.161	8.588	3.030	0.725	0.538	0.000	0.183	100	95.663
LOM411a-2.1	51.518	4.176	10.978	16.664	0.470	3.319	8.551	3.008	0.818	0.497	NA	NA	100	97.137
LOM411a-2.2	51.206	4.137	10.889	17.173	0.403	3.358	8.736	2.834	0.755	0.508	NA	NA	100	97.157
LOM411a-2.3	51.221	4.285	11.084	16.731	0.368	3.355	8.799	2.951	0.686	0.518	NA	NA	100	96.633
LOM411a-2.4	50.888	4.100	11.230	17.043	0.490	3.393	8.566	2.945	0.776	0.570	NA	NA	100	97.567
LOM411a-2.5	50.857	4.388	11.214	16.898	0.485	3.355	8.628	2.927	0.753	0.495	NA	NA	100	96.939
LOM411a-2.6	51.140	4.352	10.976	16.796	0.356	3.360	8.653	3.064	0.740	0.563	NA	NA	100	96.869
LOM411a-2.7	50.679	4.330	11.320	16.871	0.496	3.370	8.687	2.910	0.730	0.607	NA	NA	100	96.932

PNT--Pre-Normalization Total; NA--No data taken

164

BSE Image of Sample KEL102
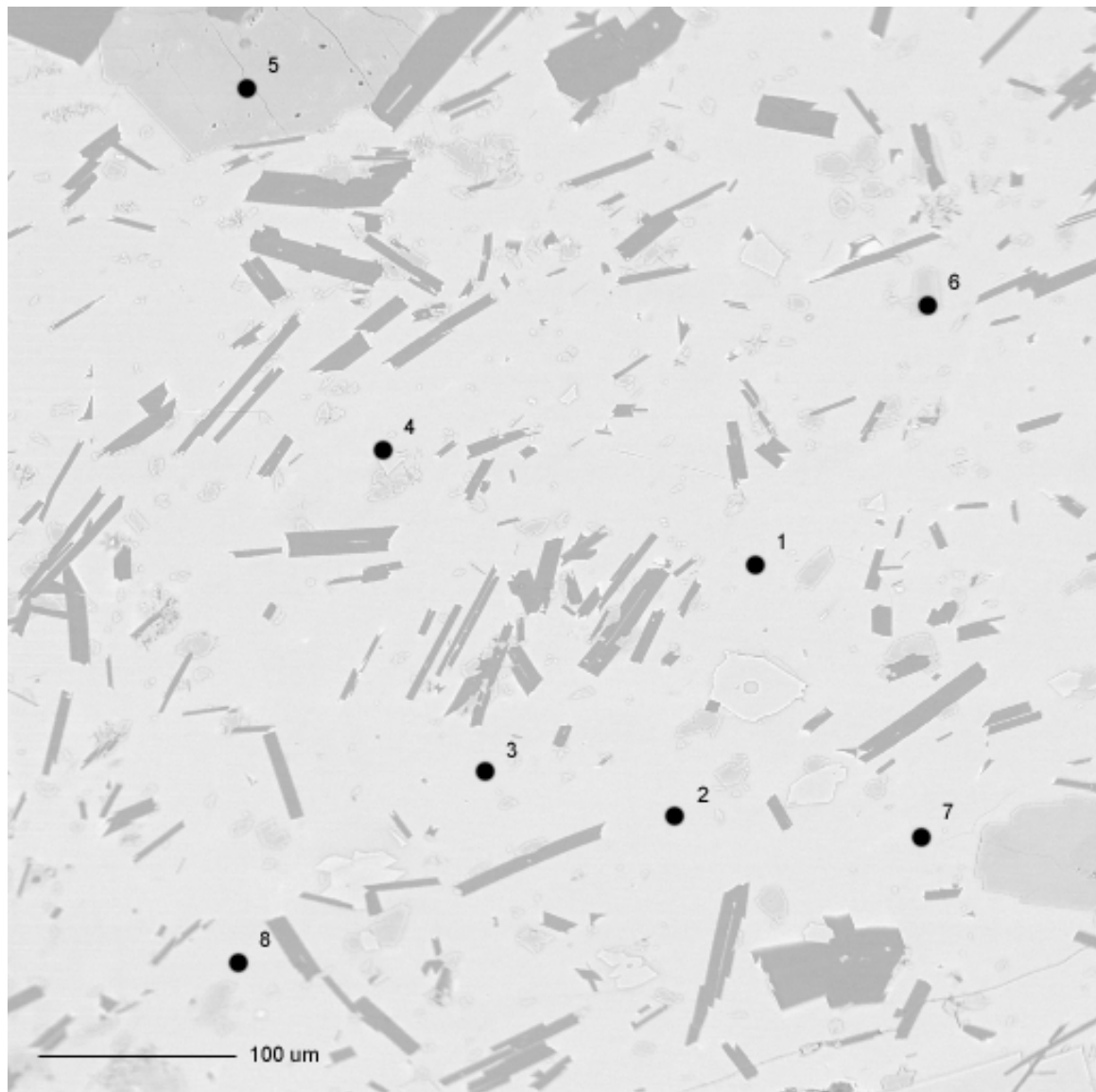
BSE Image of Sample KEL 107
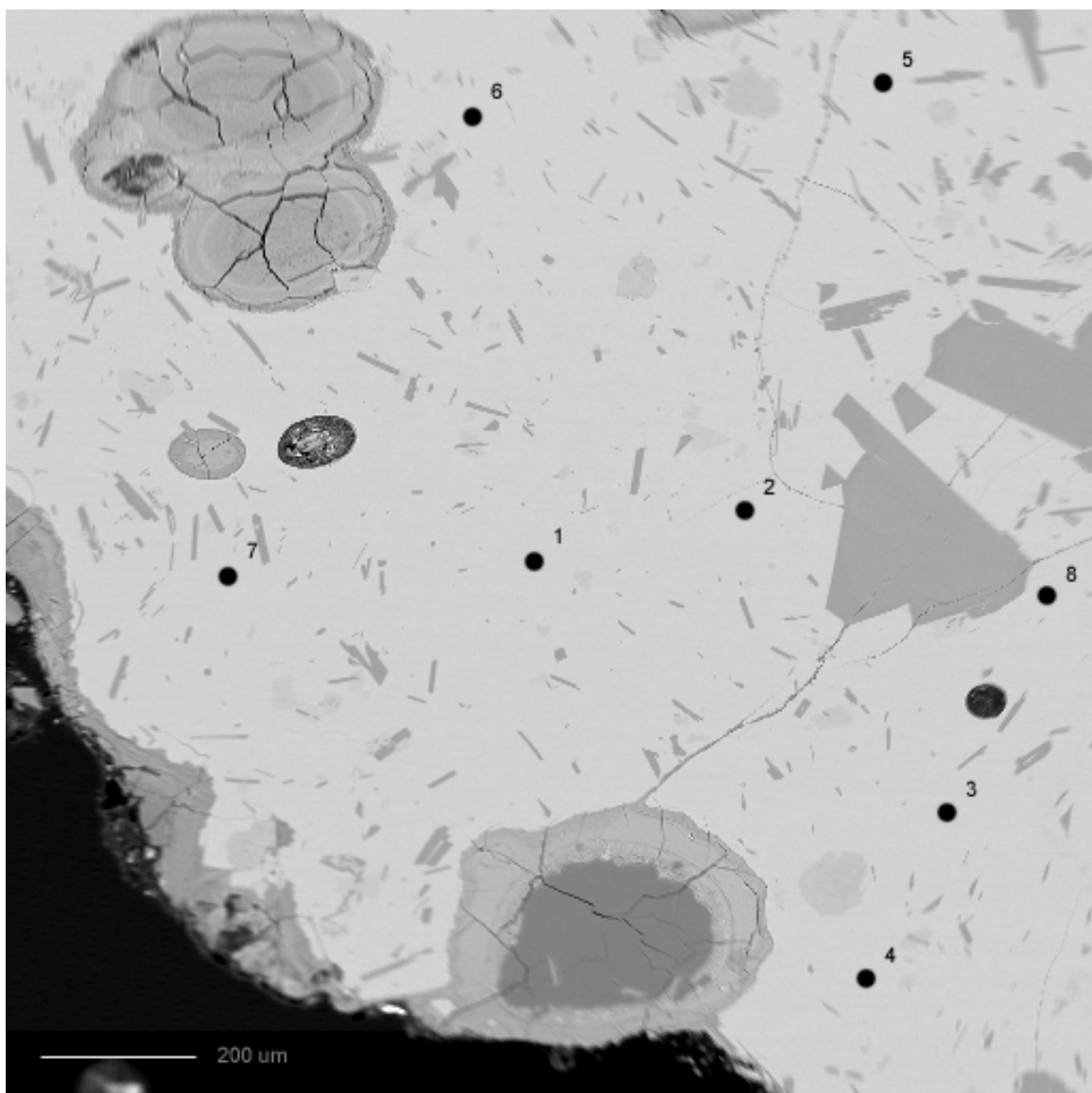
BSE Image of Sample KEL 108, Area 1 (Spots 1-5)
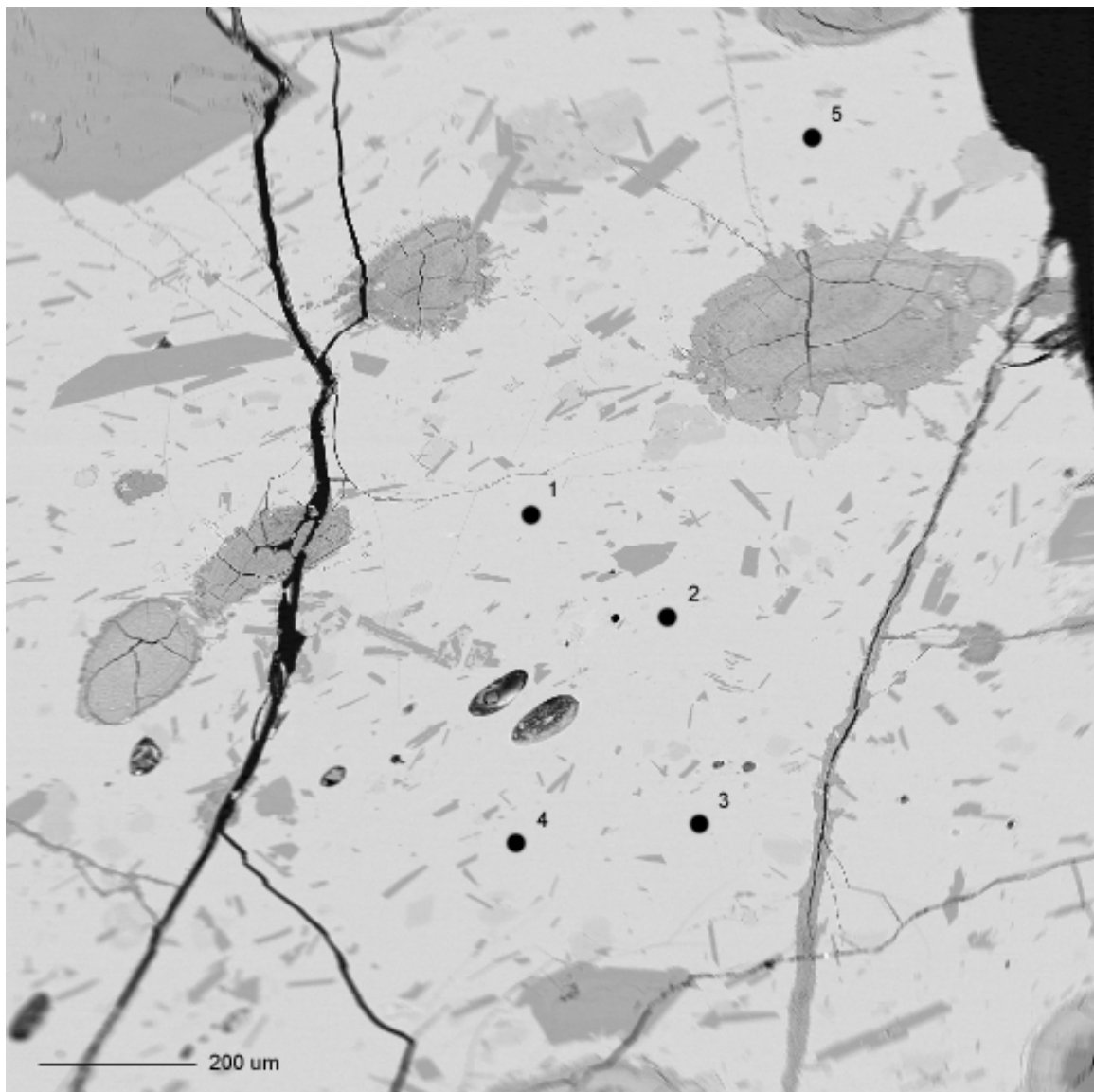
**BSE Image of Sample KEL108, Area 2 (Spots 6-10)**
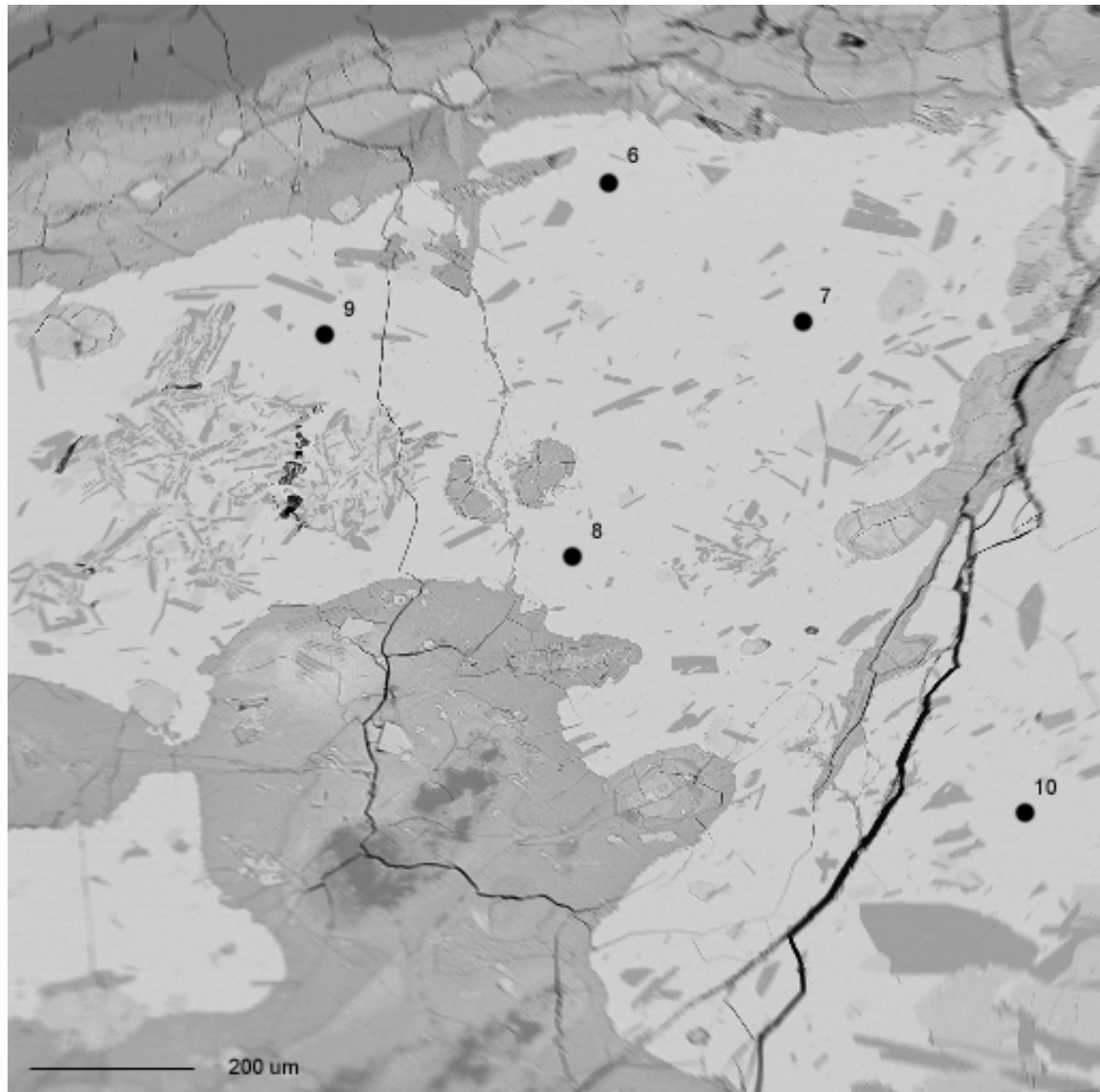
**BSE Image of Sample KELX02**
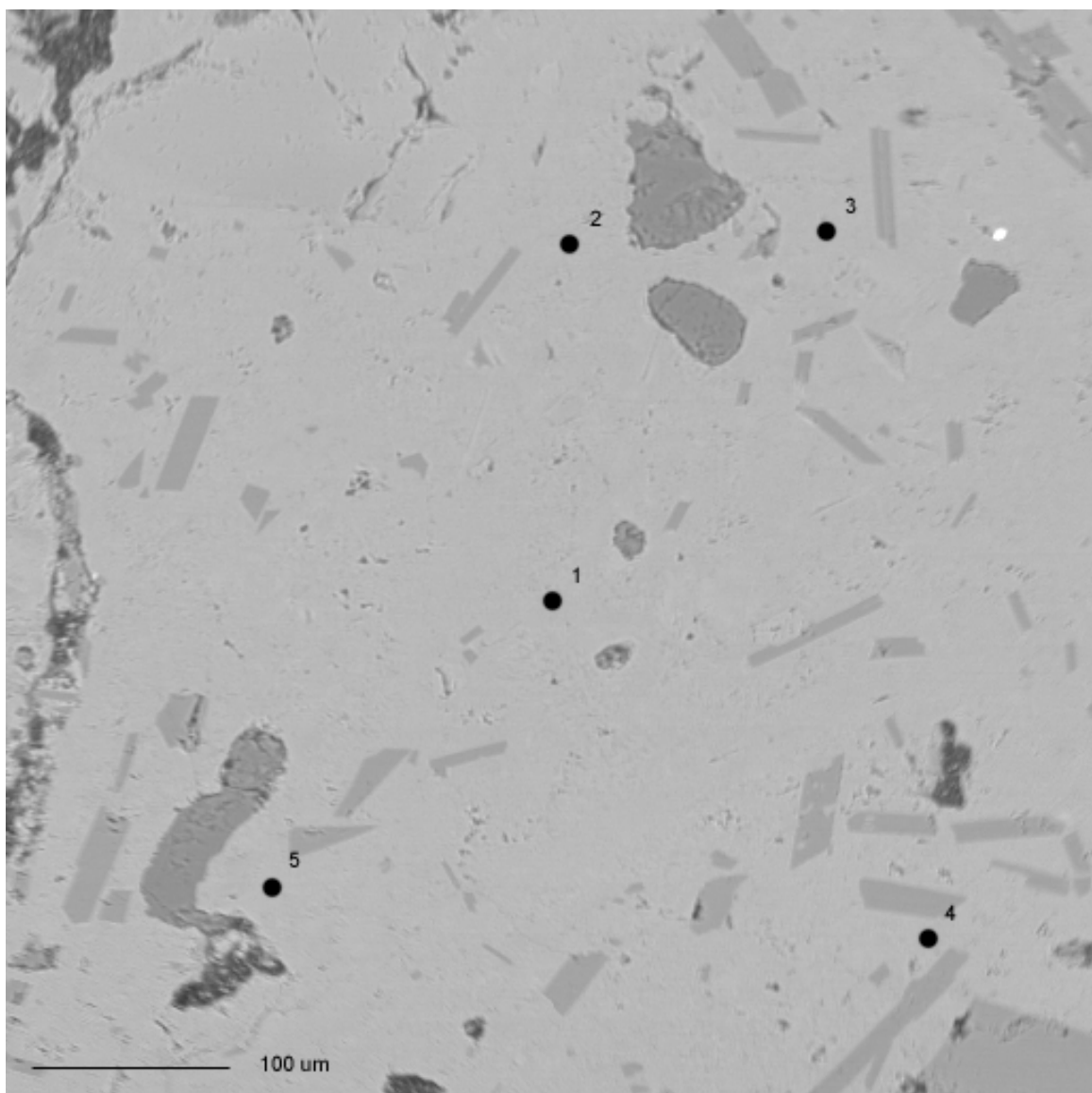
**BSE Image of Sample KELX03a**
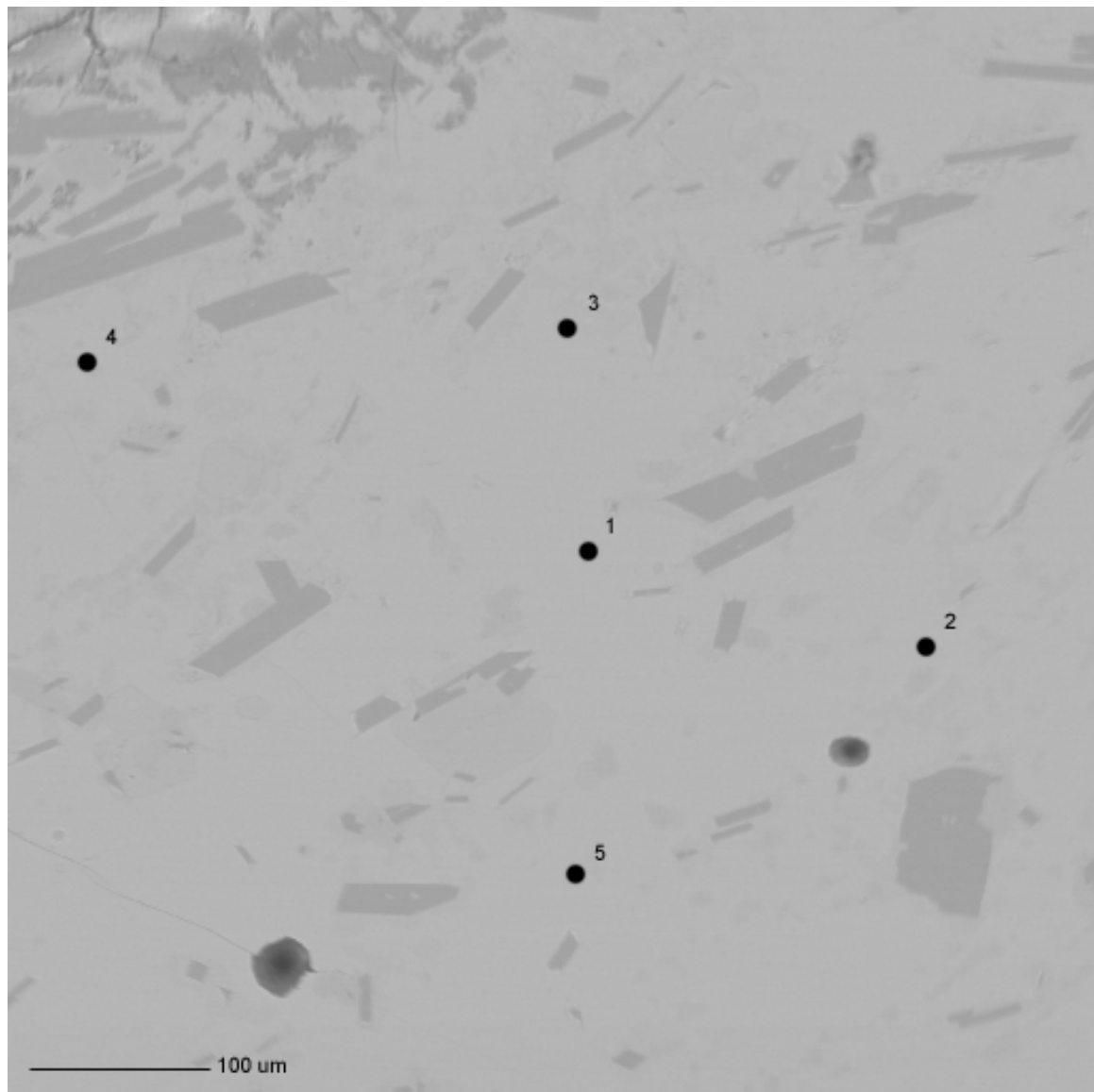
BSE Image of Sample KELX04
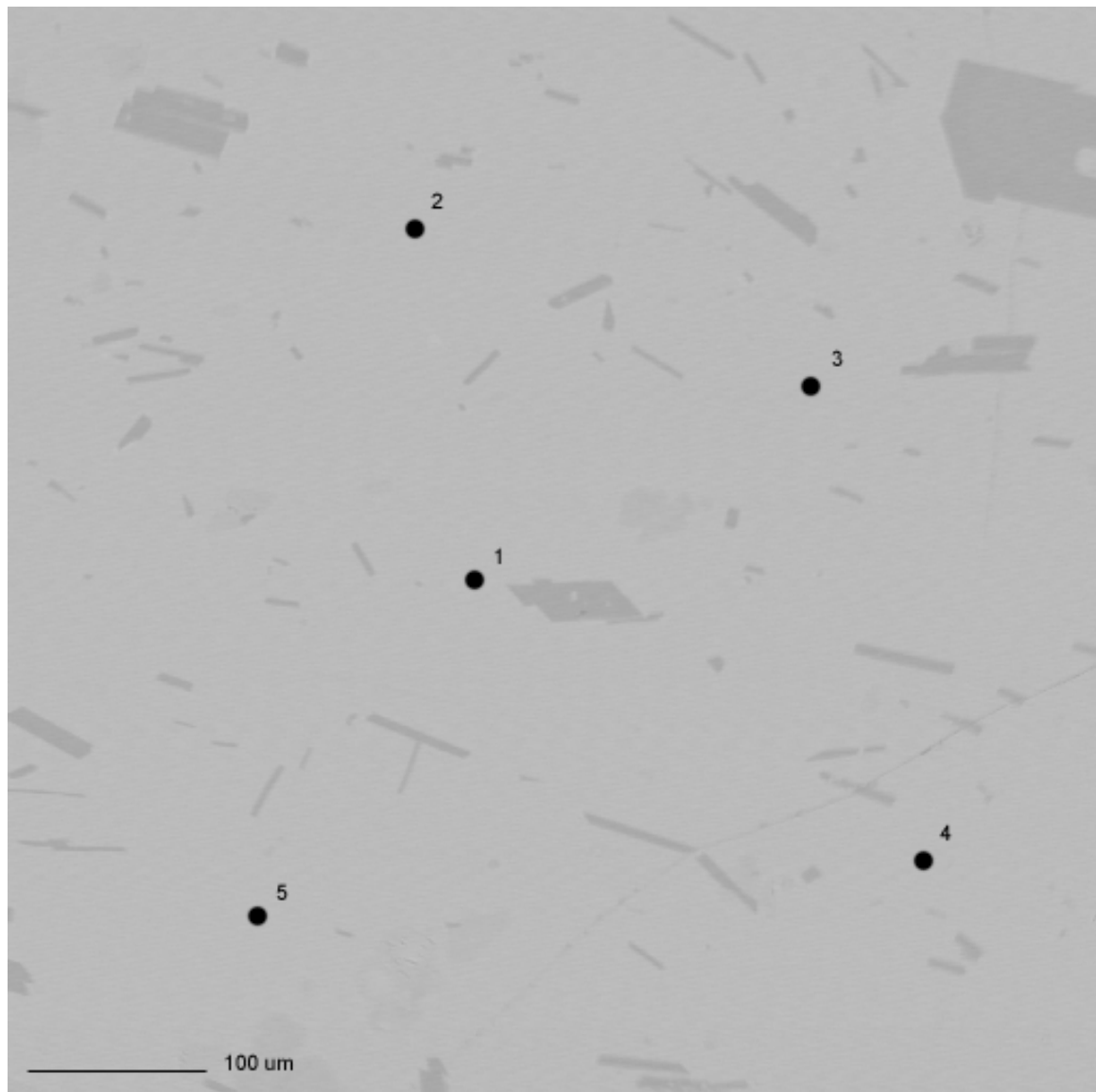
BSE Image of Sample KELX06
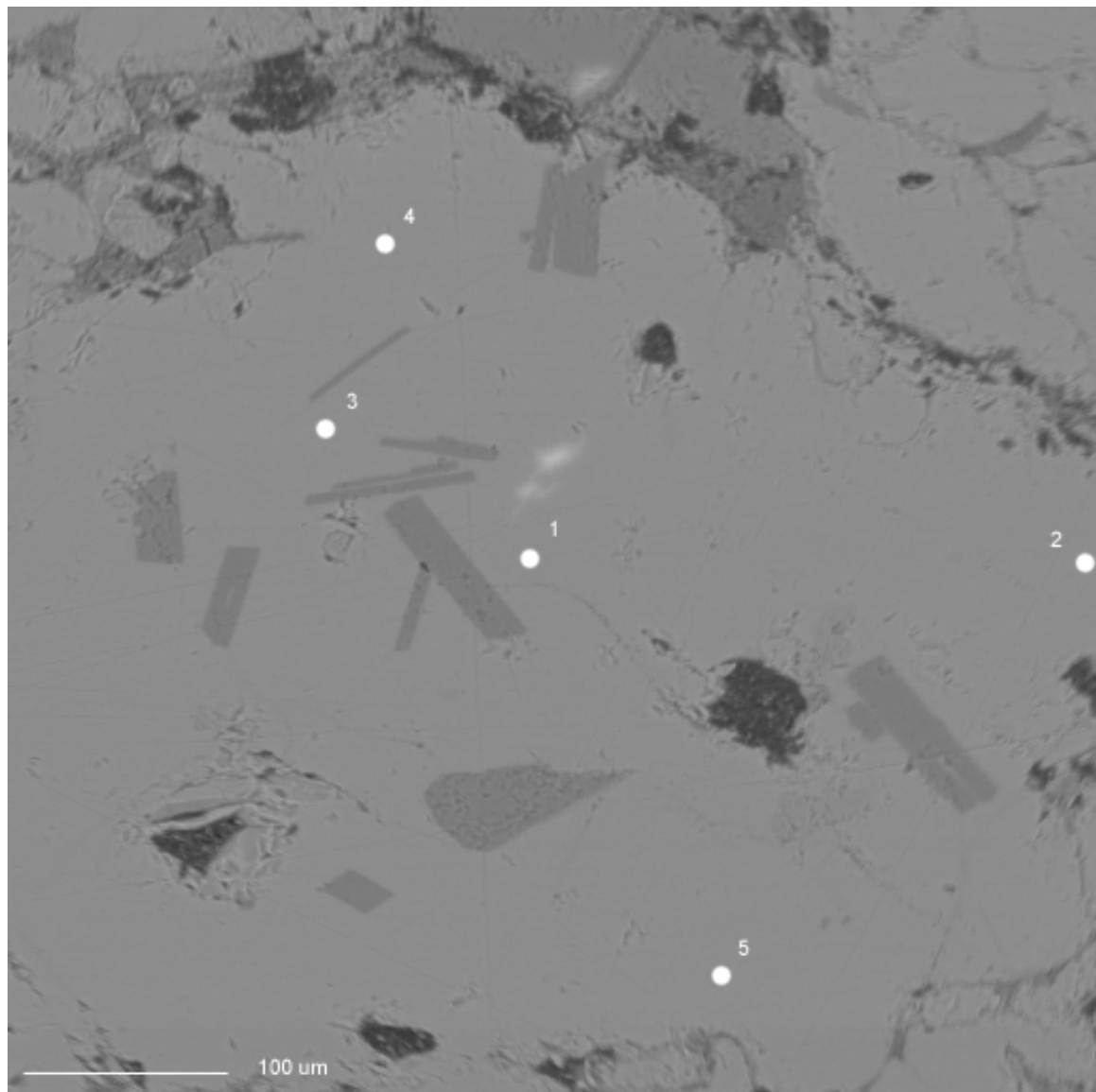
BSE Image of Sample KELX07
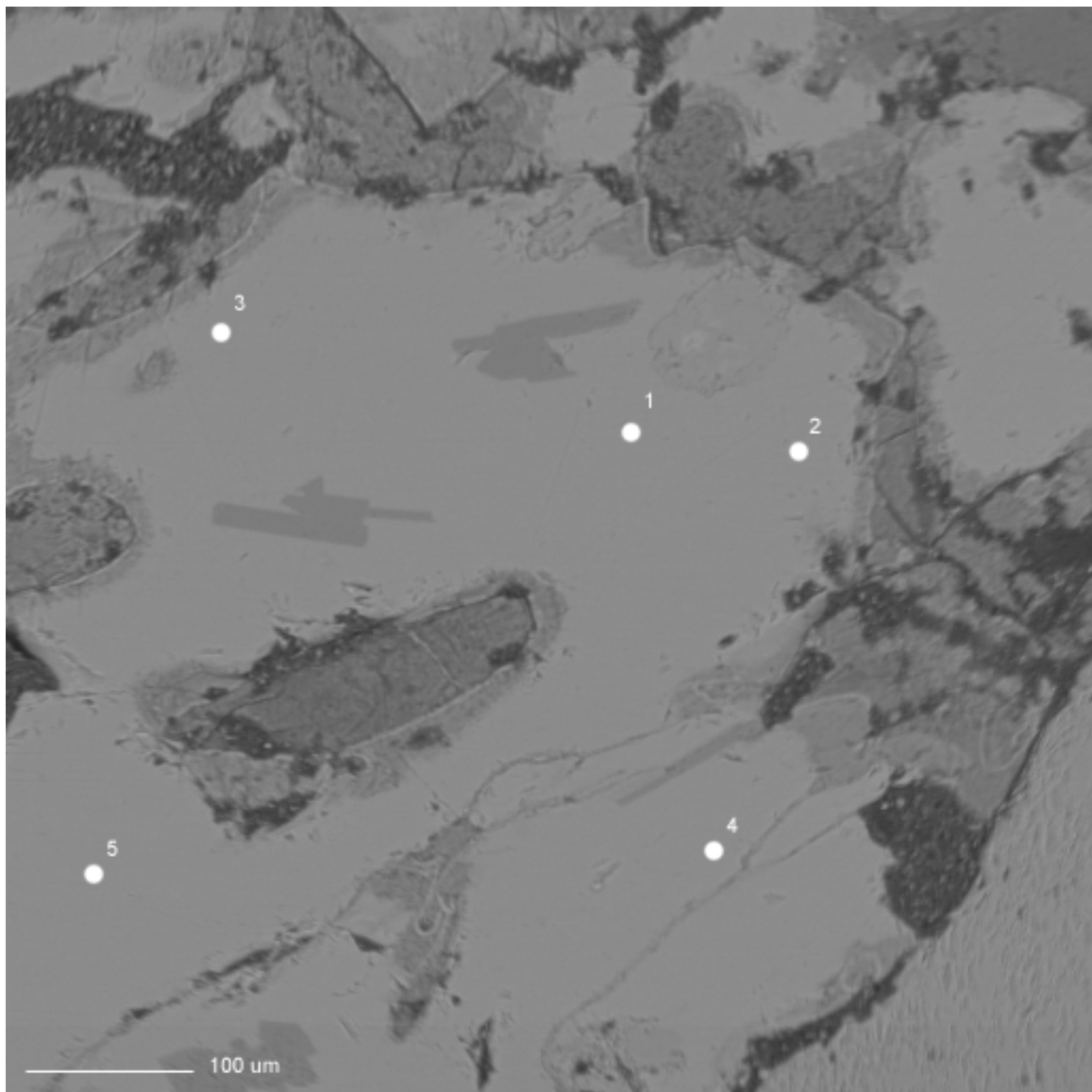
BSE Image of Sample RAU104
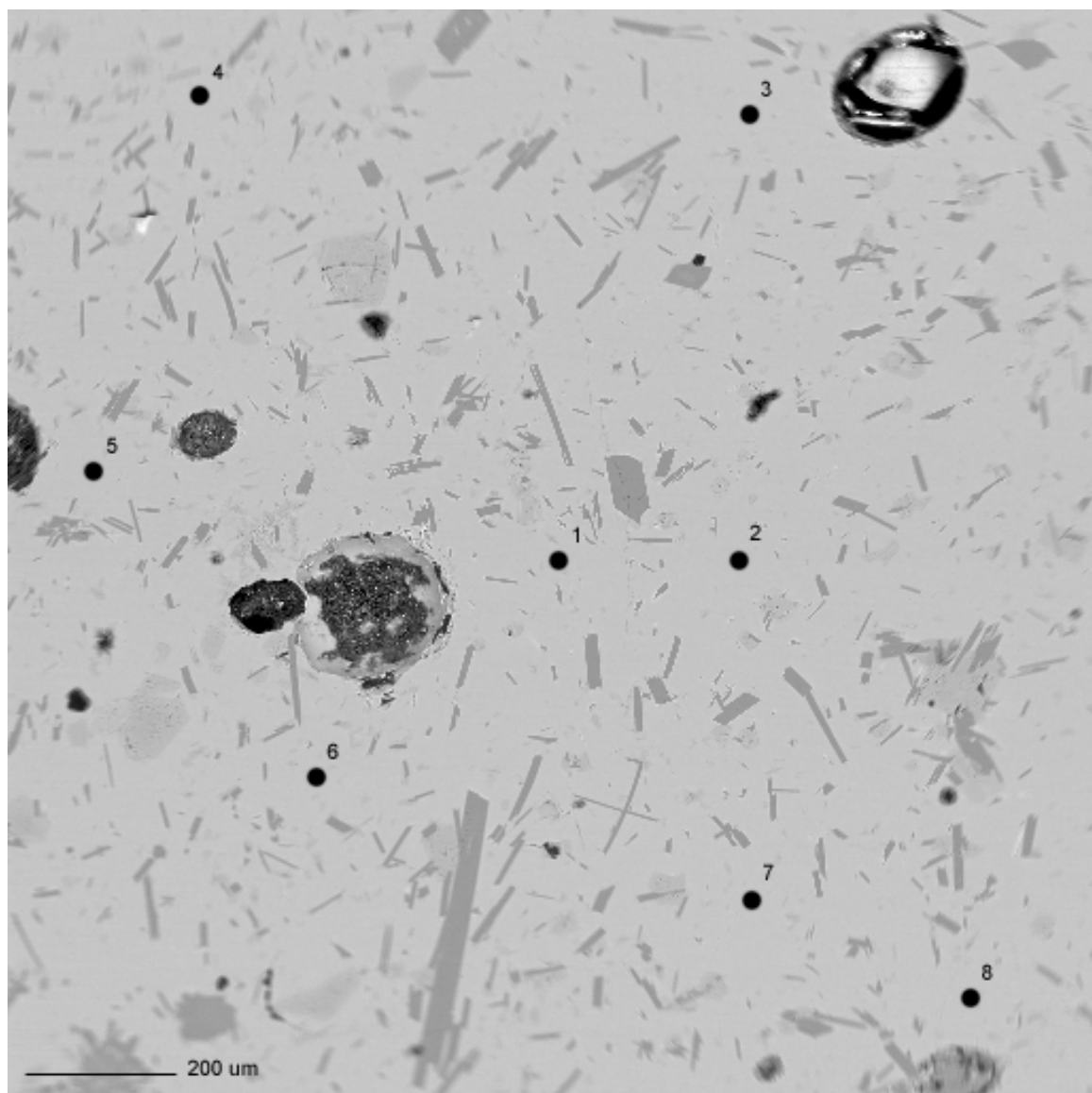
BSE Image of Sample RAU106, Area 1 (Spots 1-5)
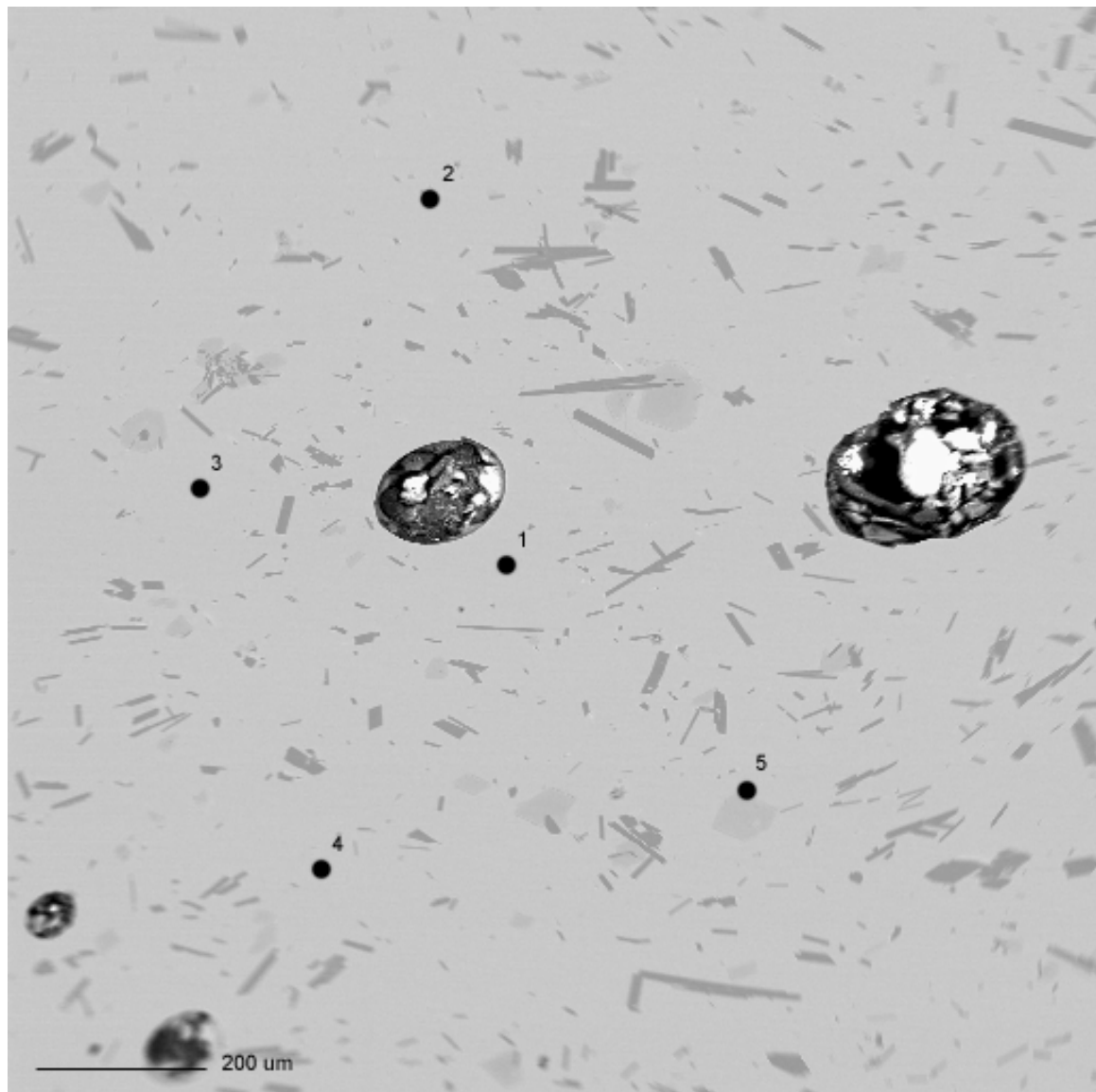
BSE Image of Sample RAU106, Area 2 (Spots 6-10)
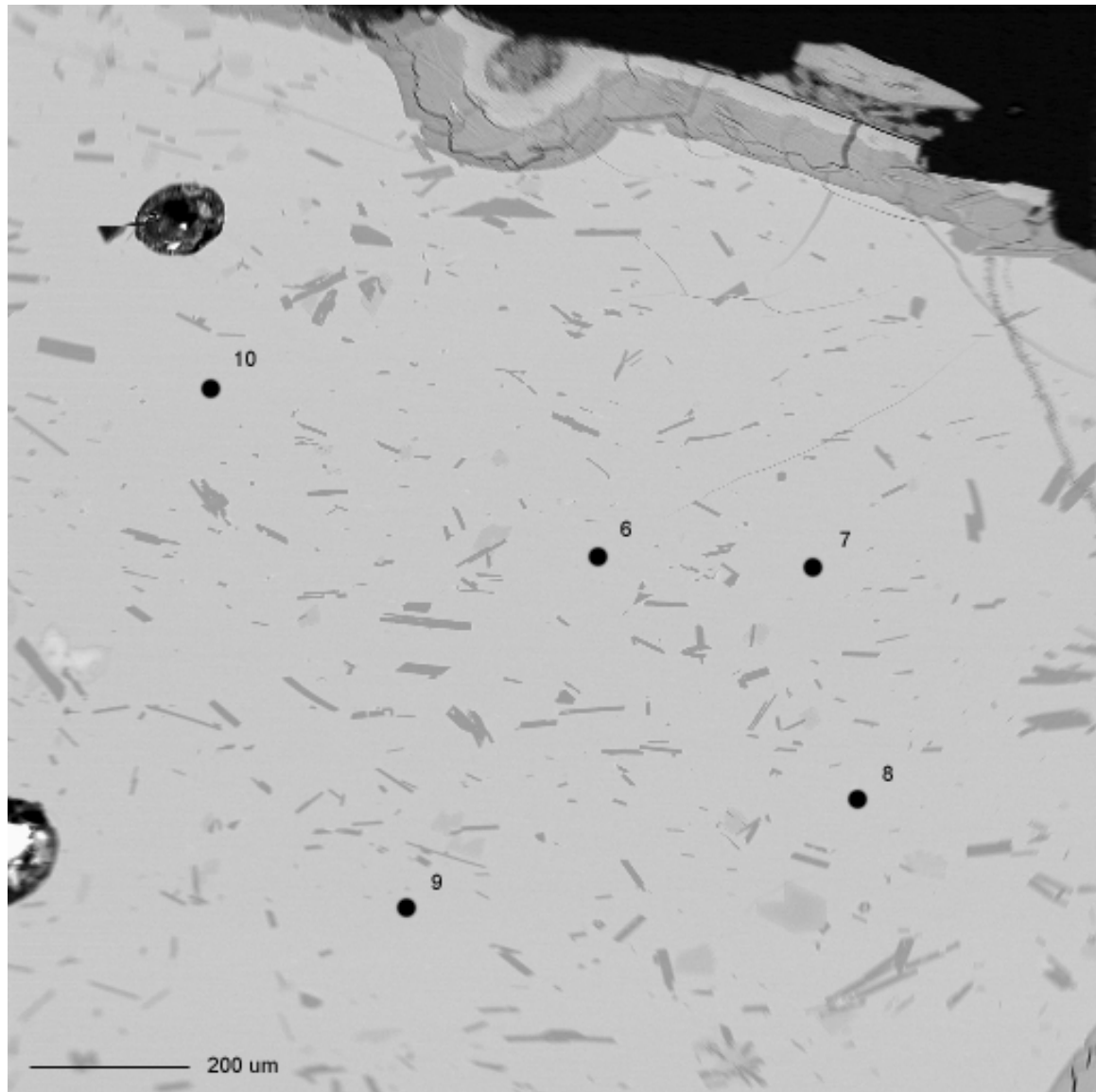
BSE Image of Sample RAU107, Area 1 (Spots 1-5)
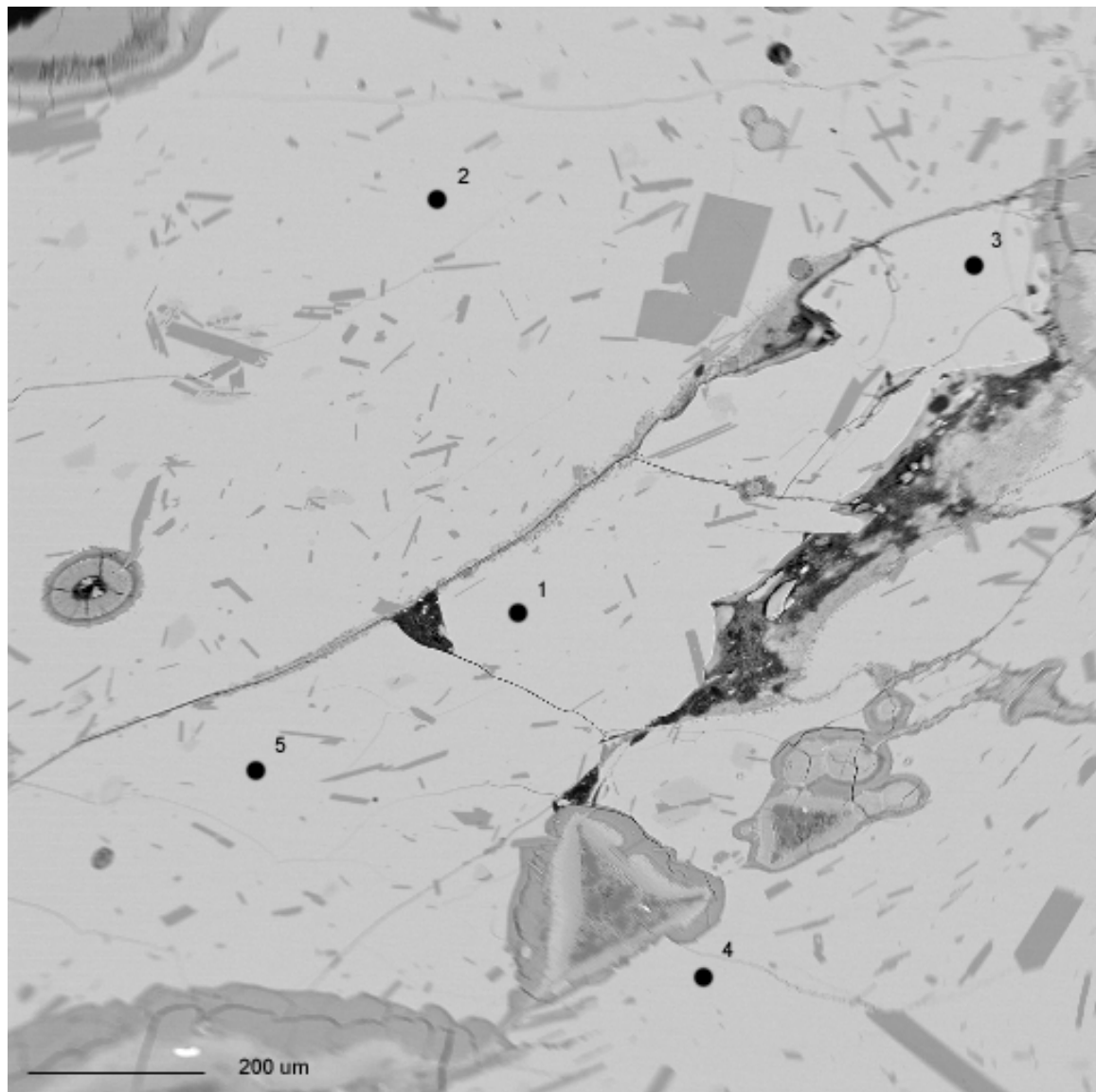
BSE Image of Sample RAU107, Area 2 (Spots 6-10)
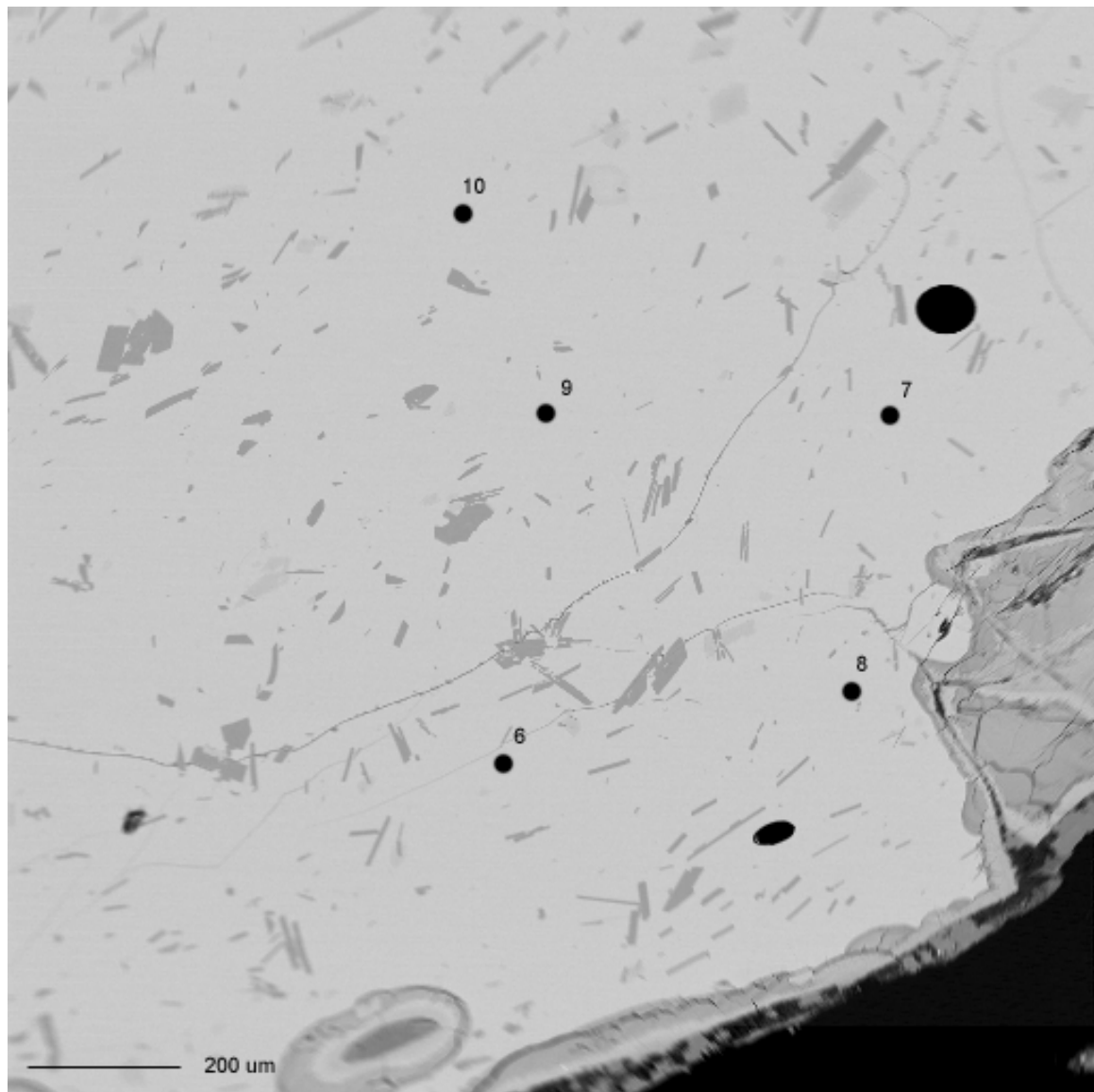
BSE Image of Sample RAUX01
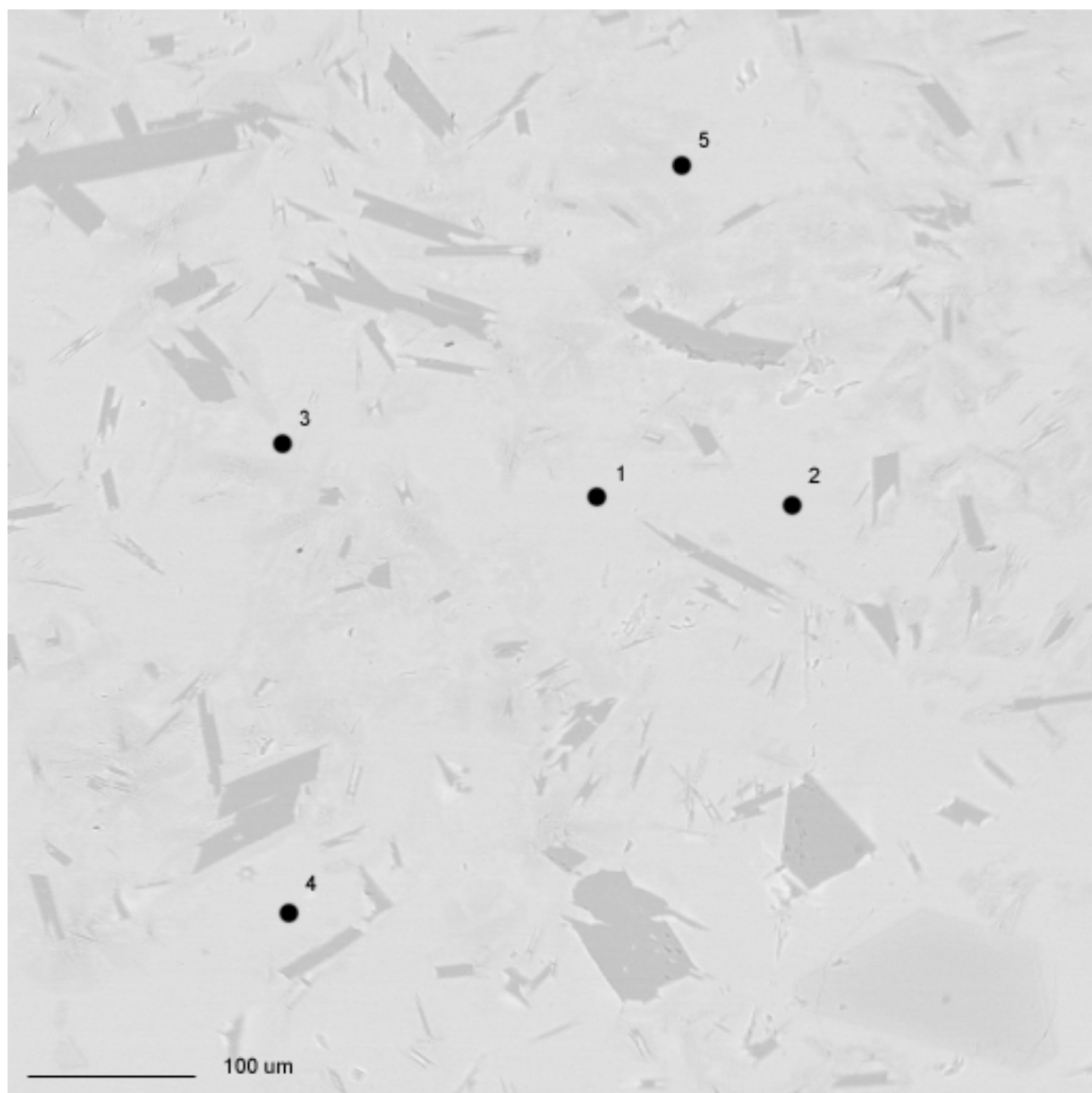
BSE Image of Sample RAUX03
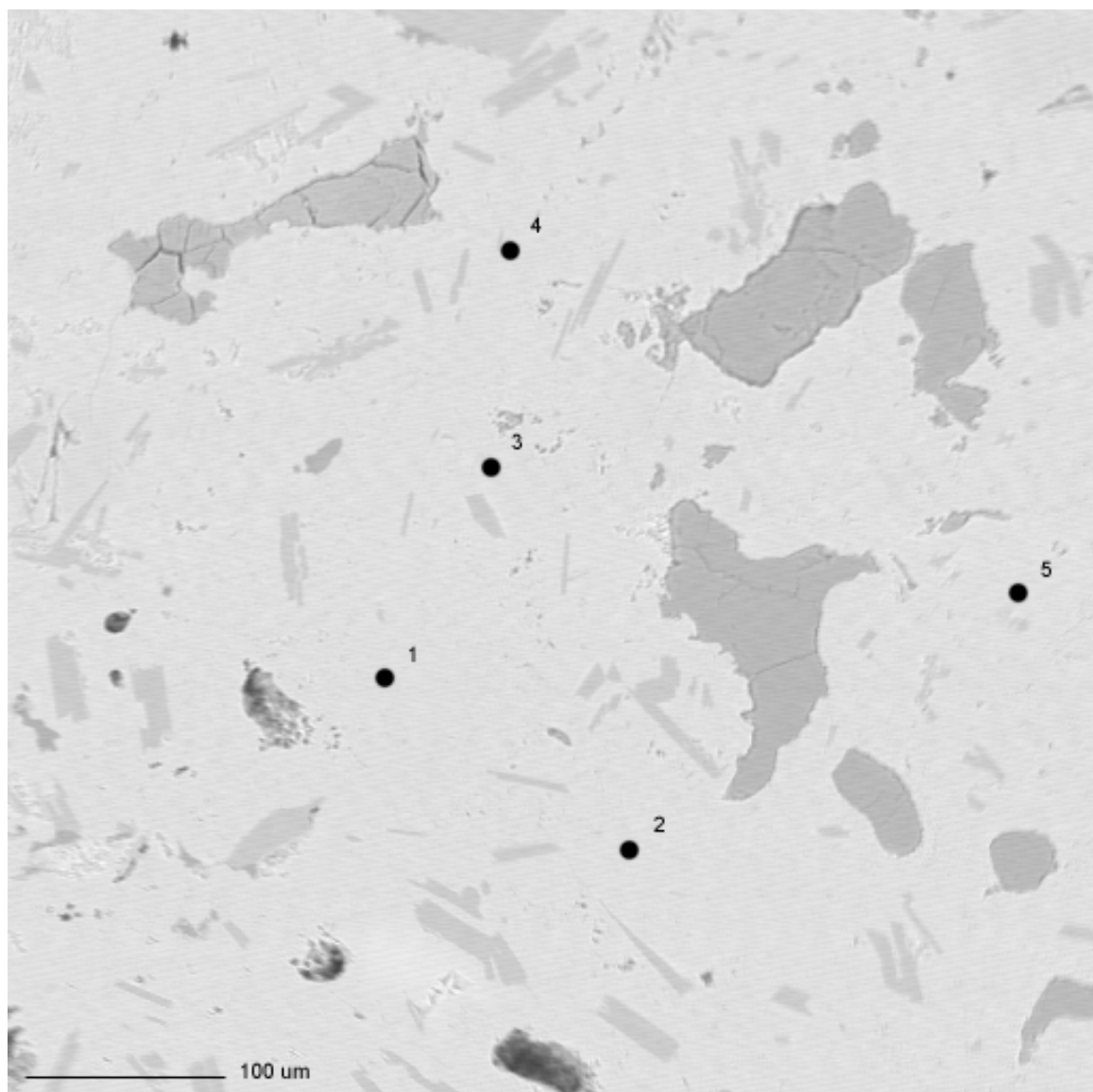
BSE Image of Sample RAUX04
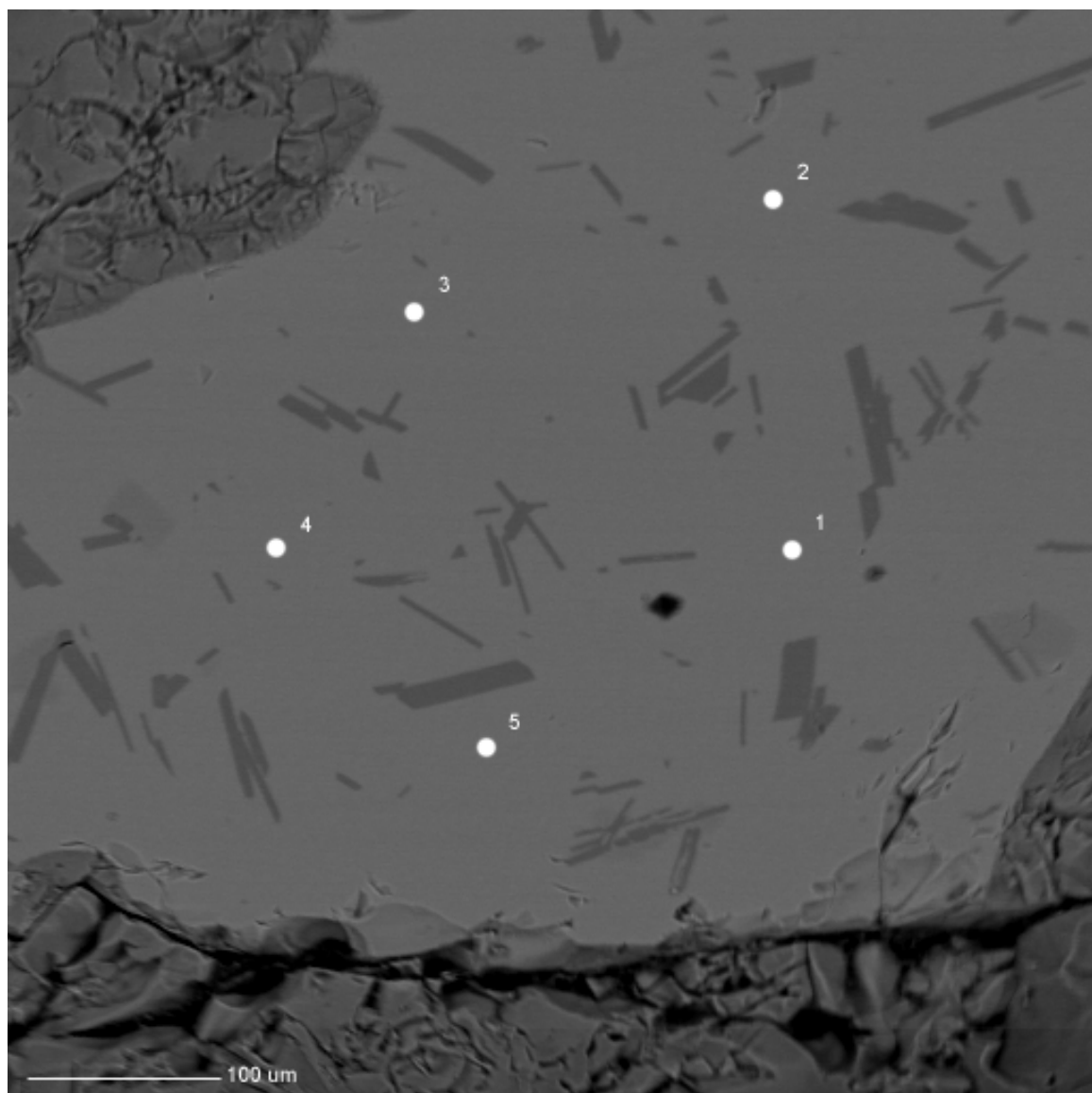
BSE Image of Sample RAUX05
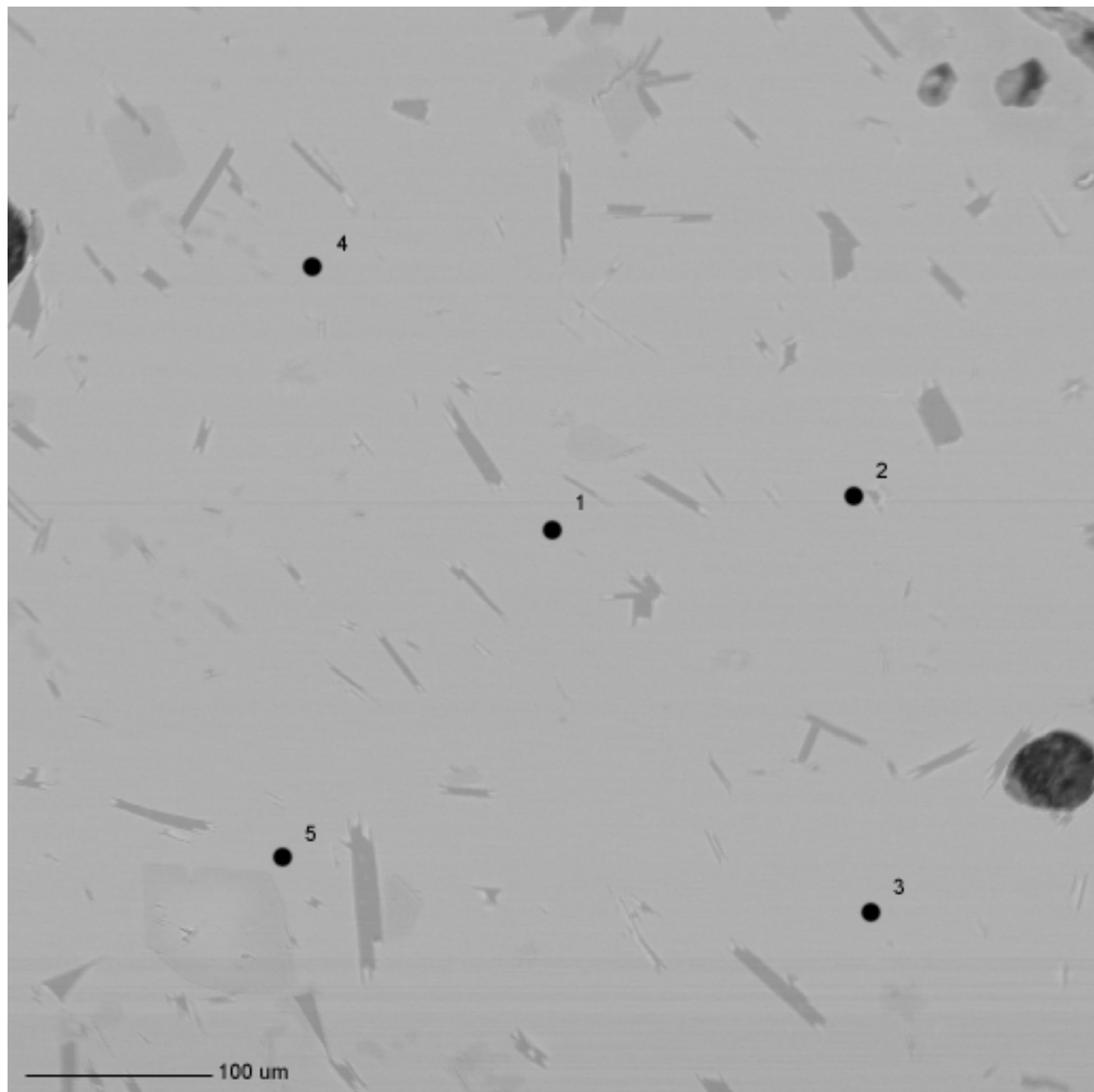
BSE Image of Sample RAUX06
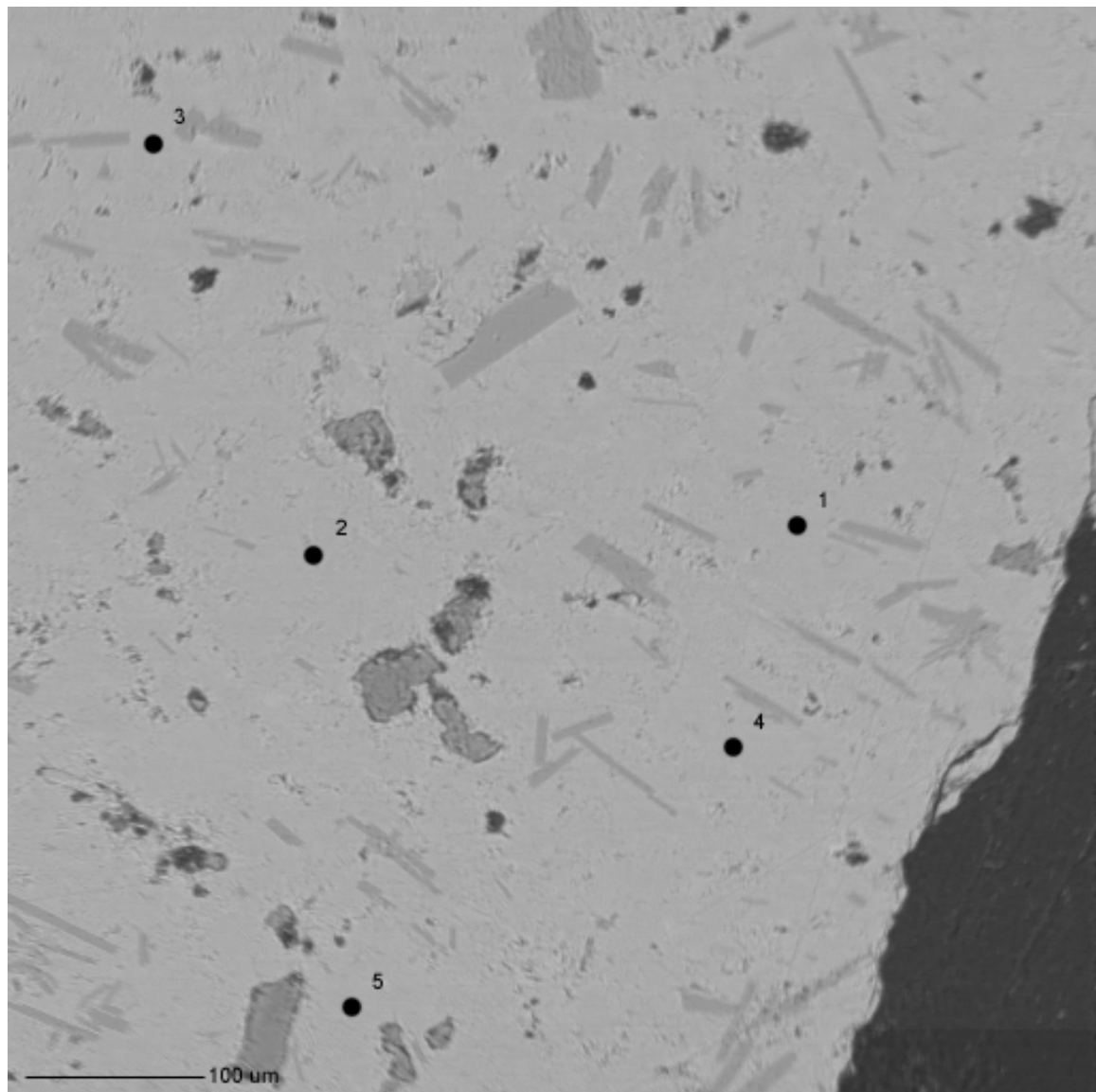
BSE Image of Sample RAUX07
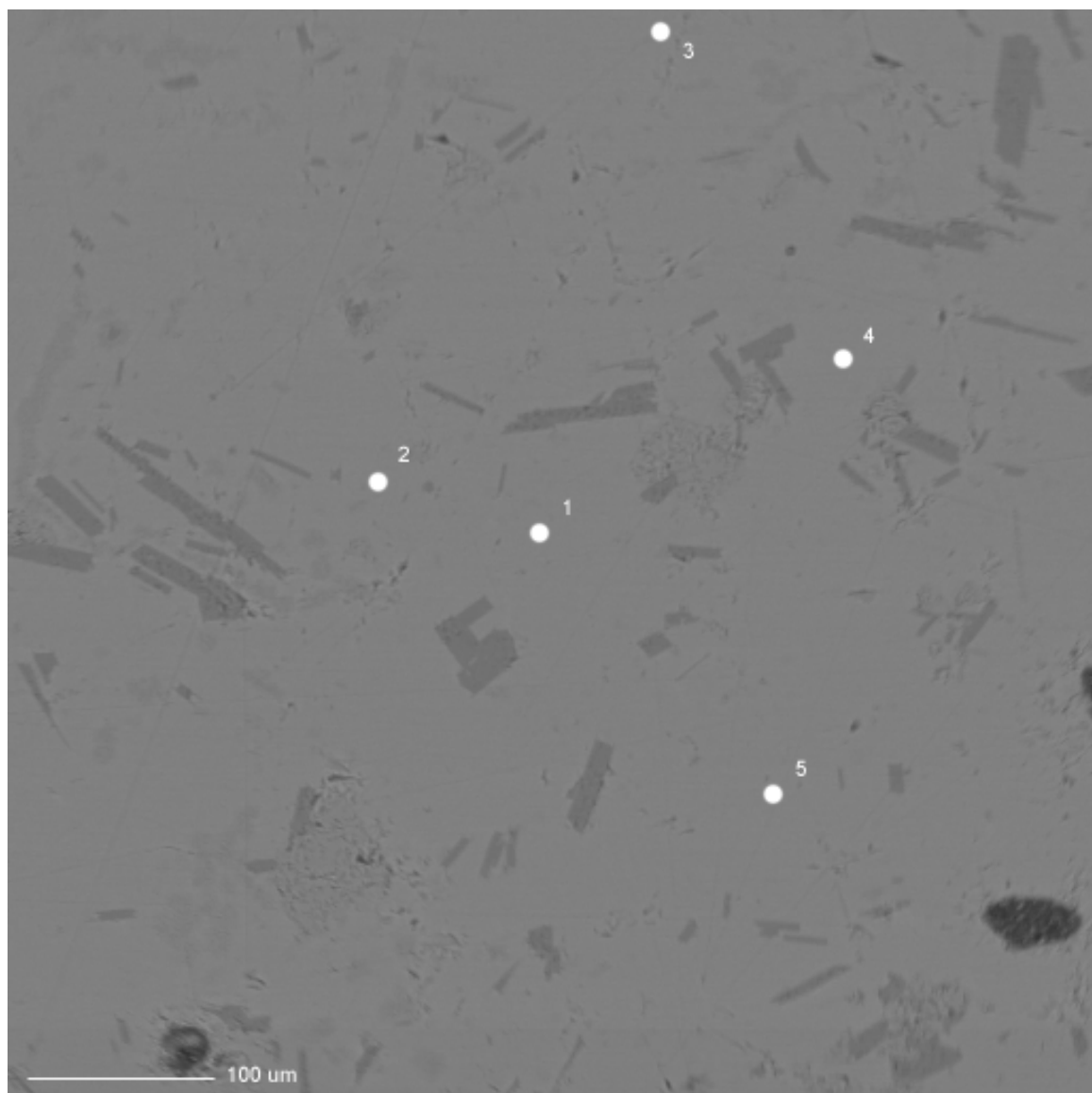
BSE Image of Sample LOM405
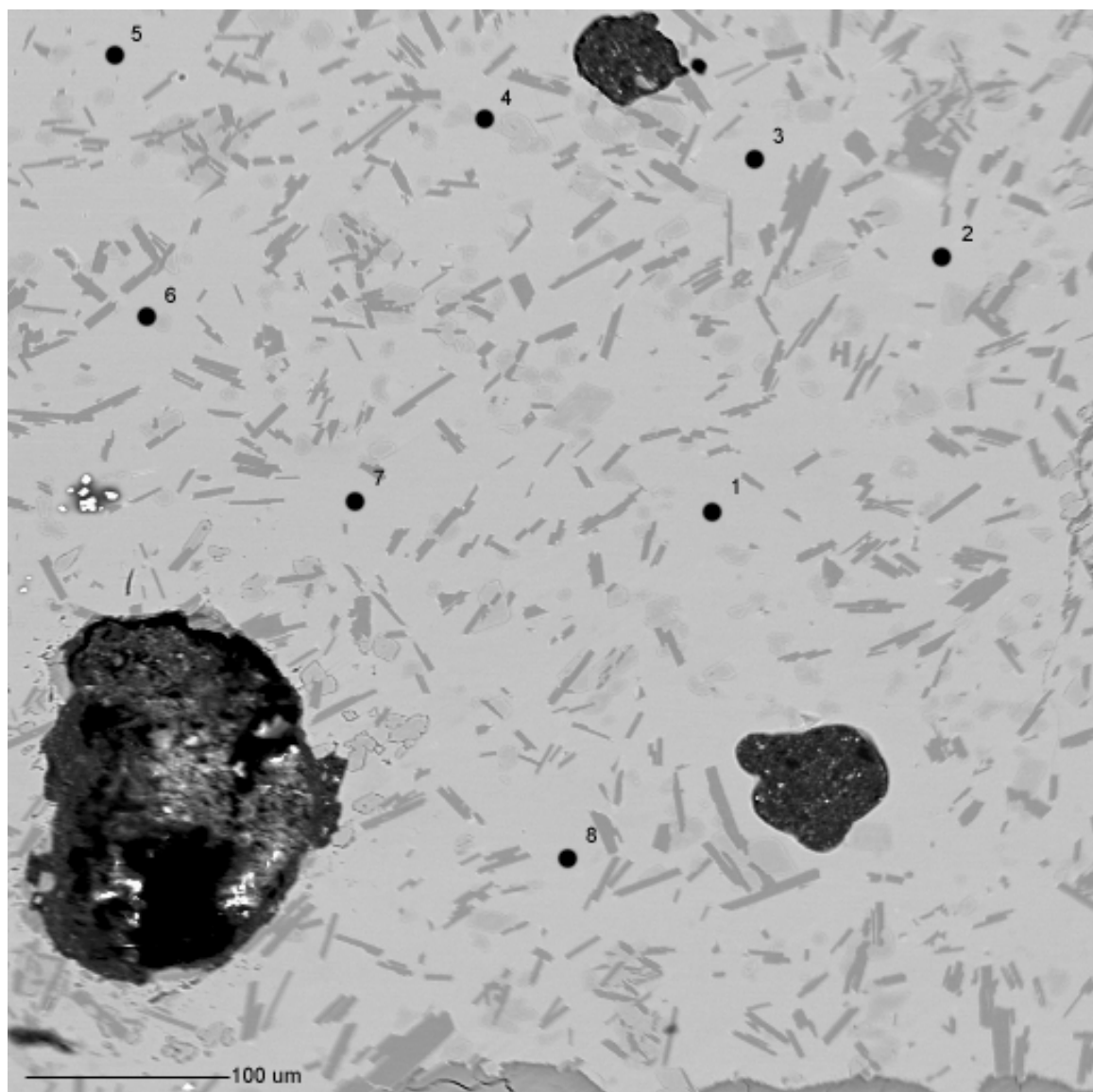
BSE Image of Sample LOM407, Area 1 (Spots 1-5)
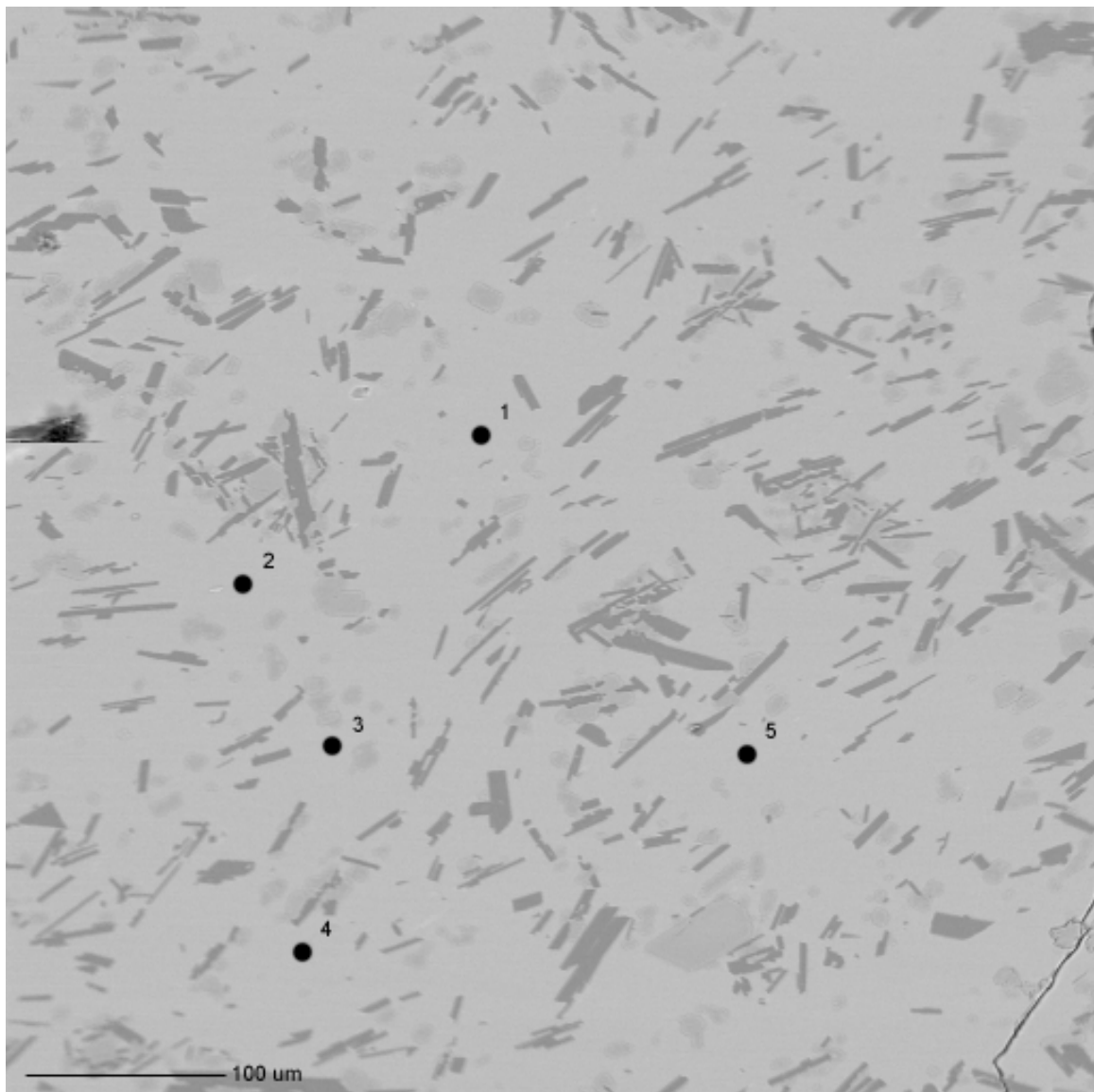
BSE Image of Sample LOM407, Area 2 (Spots 6-10)
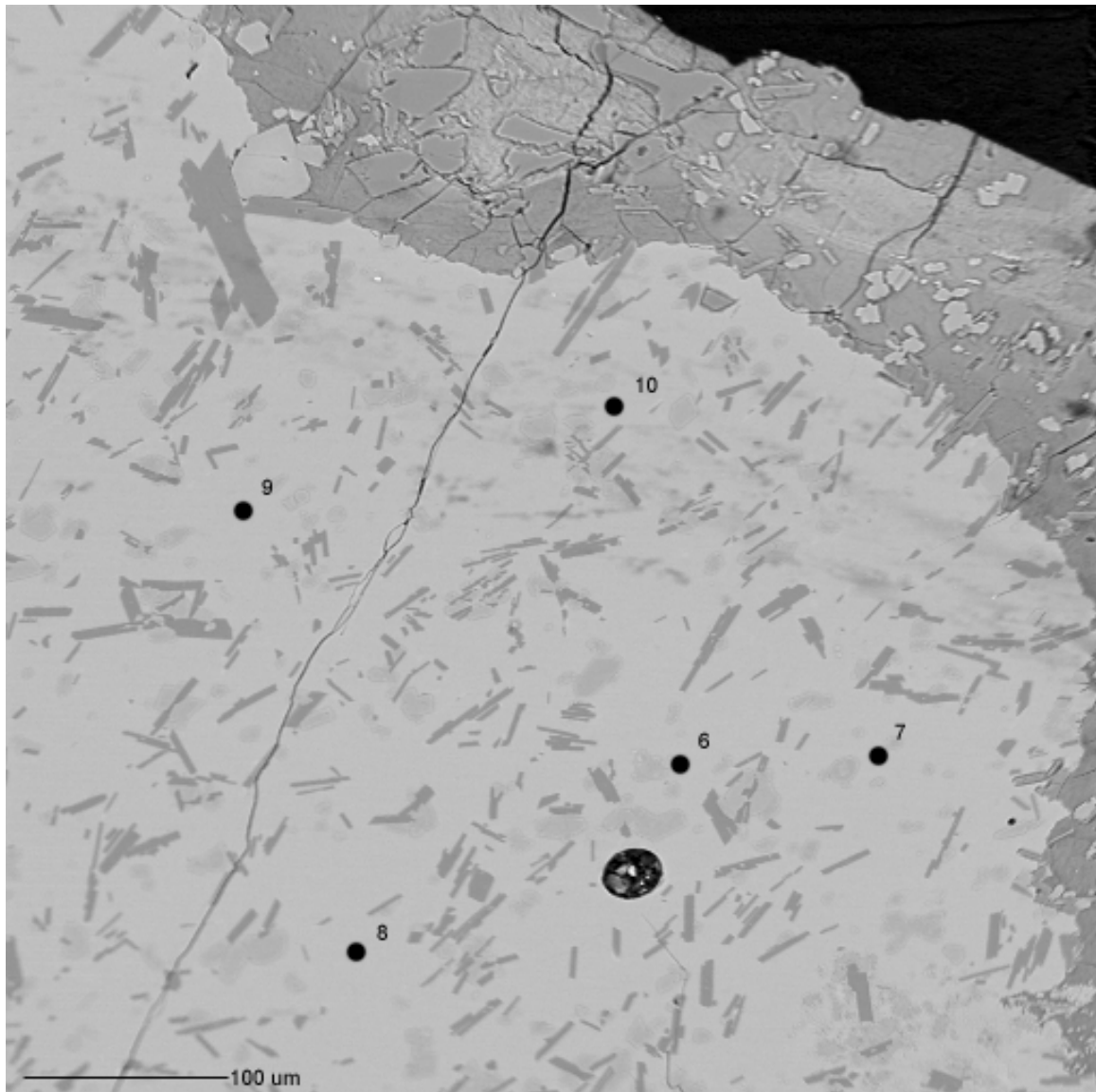
BSE Image of Sample LOM409
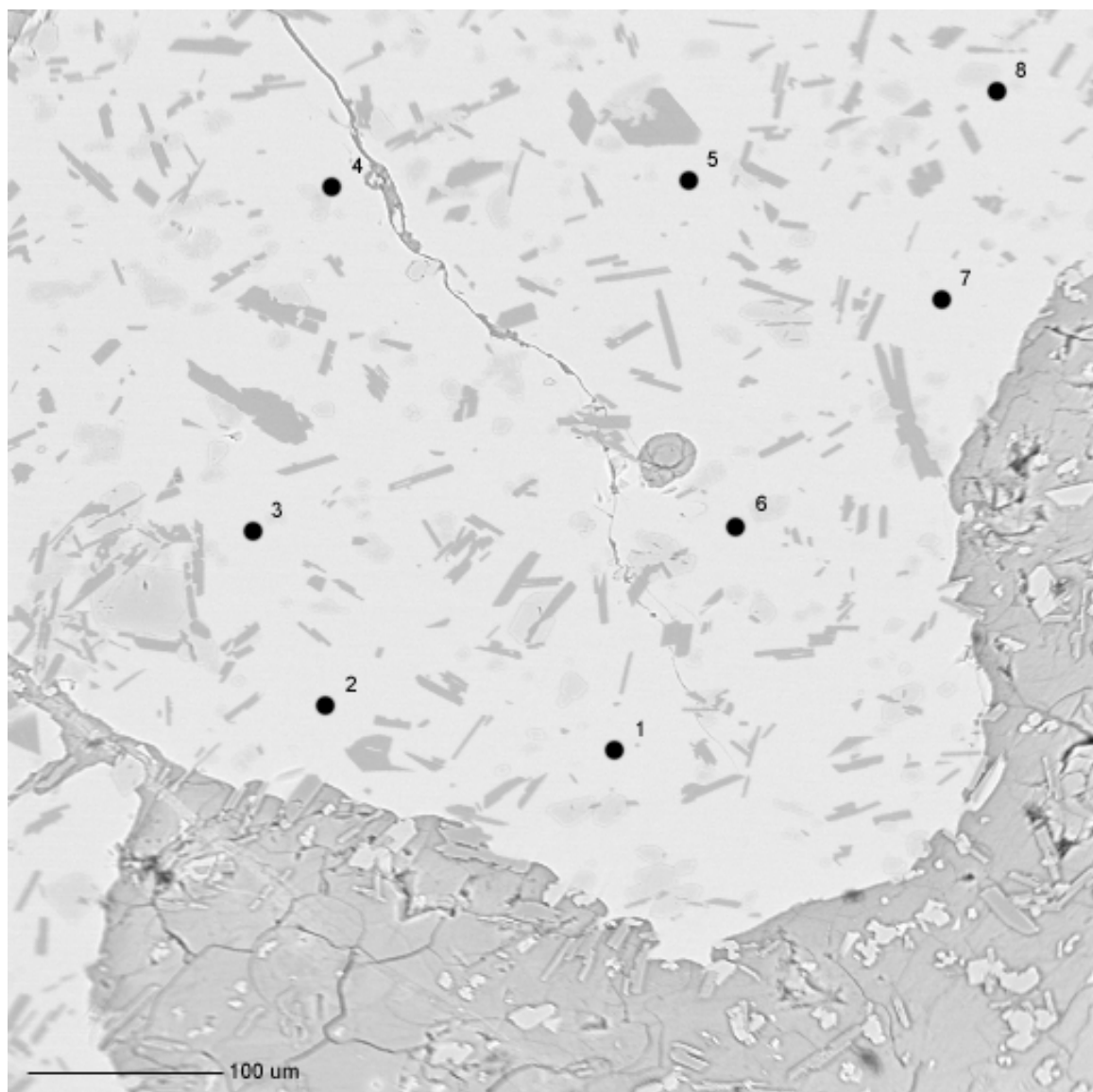
BSE Image of Sample LOM410
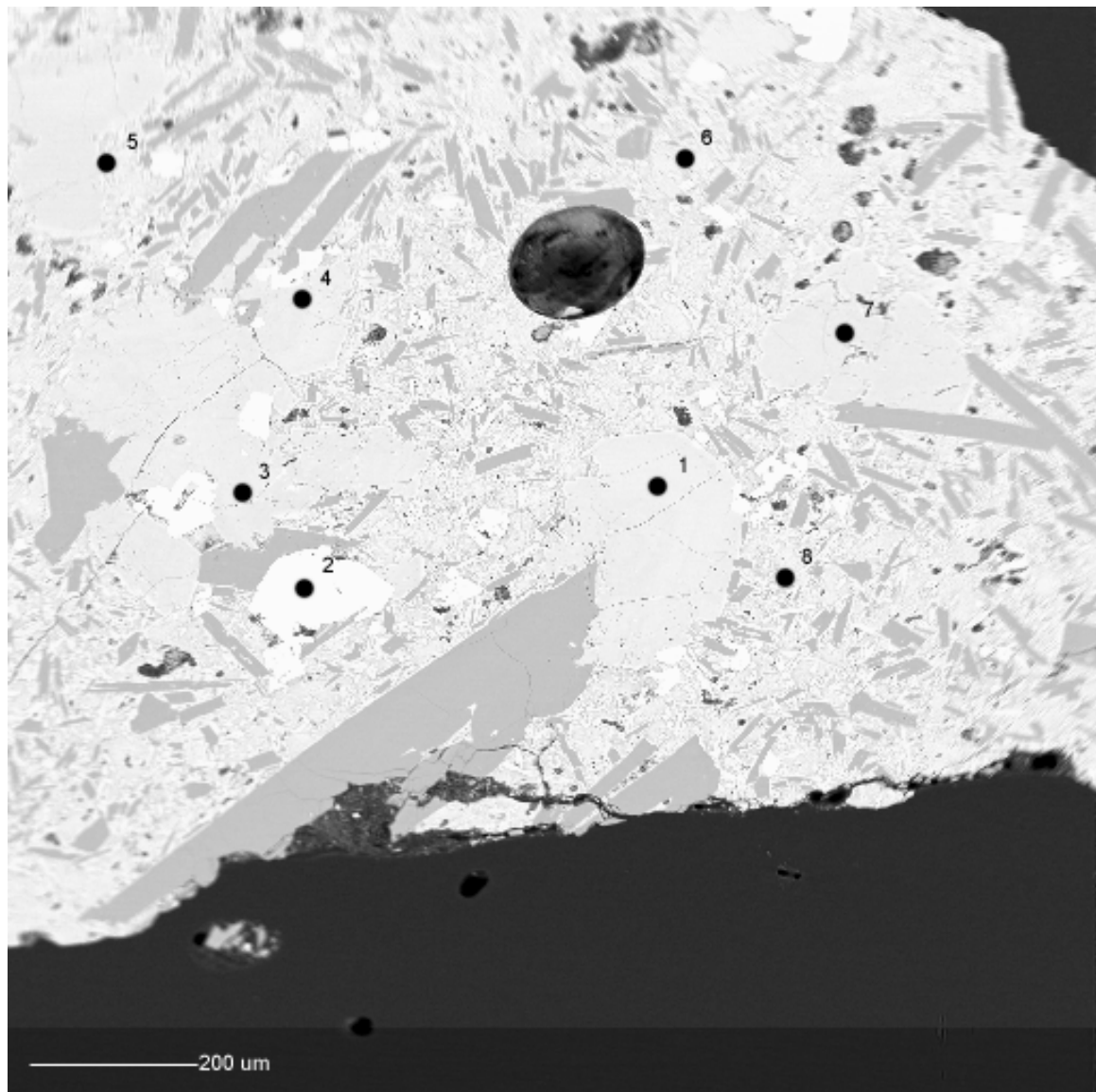
BSE Image of Sample LOM410-2
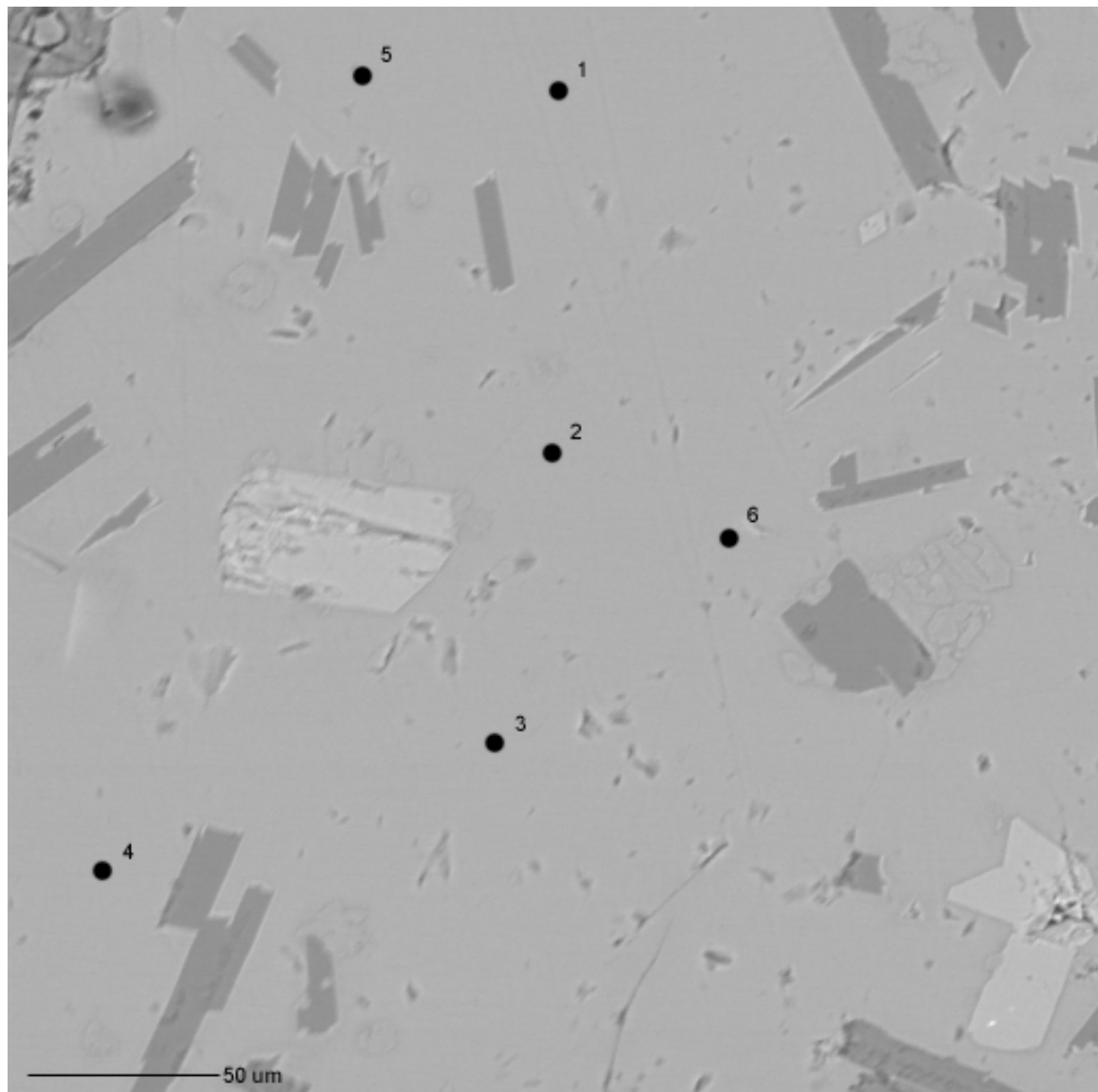
BSE Image of Sample LOM411a
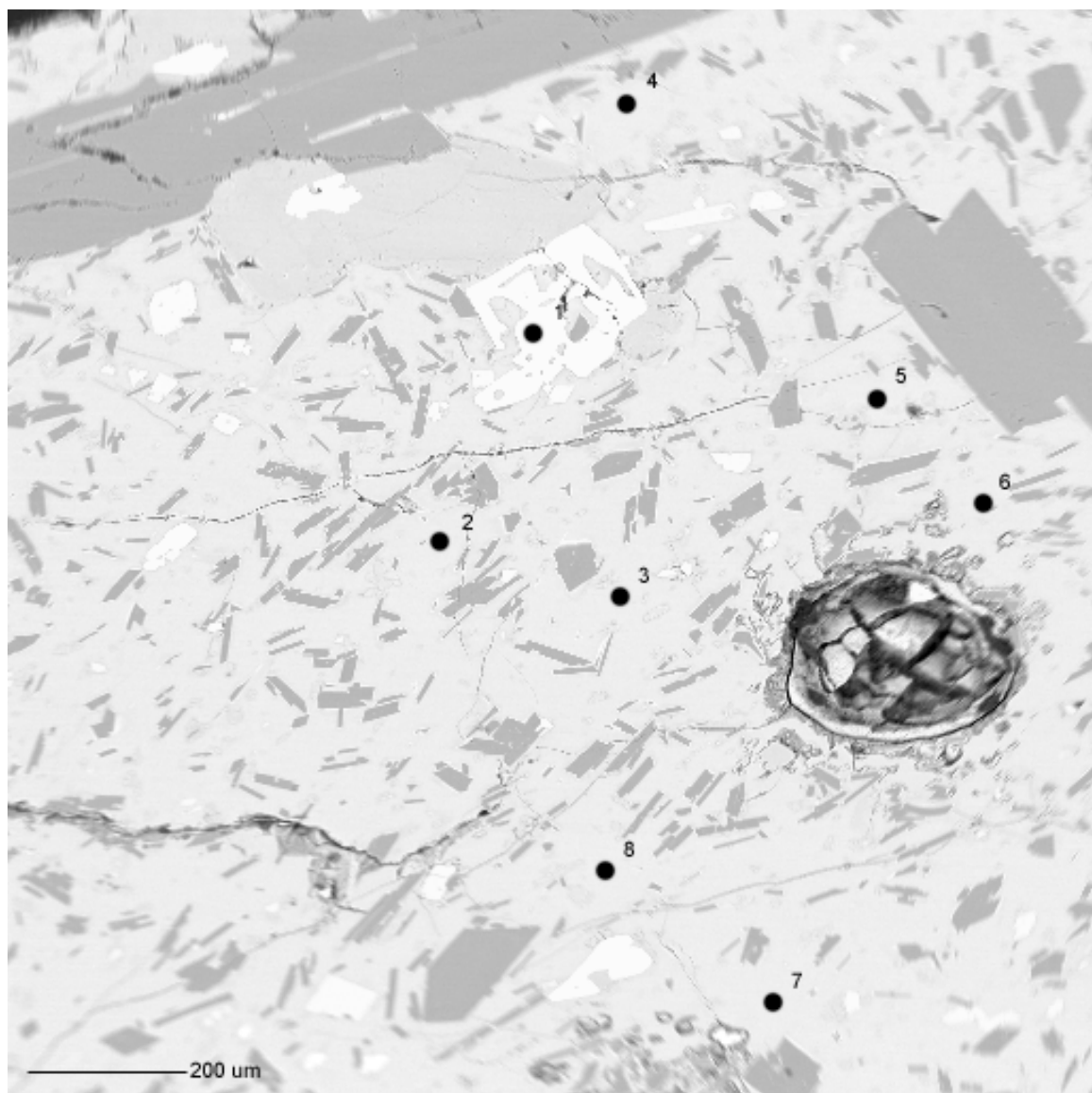
BSE Image of Sample LOM411a-2
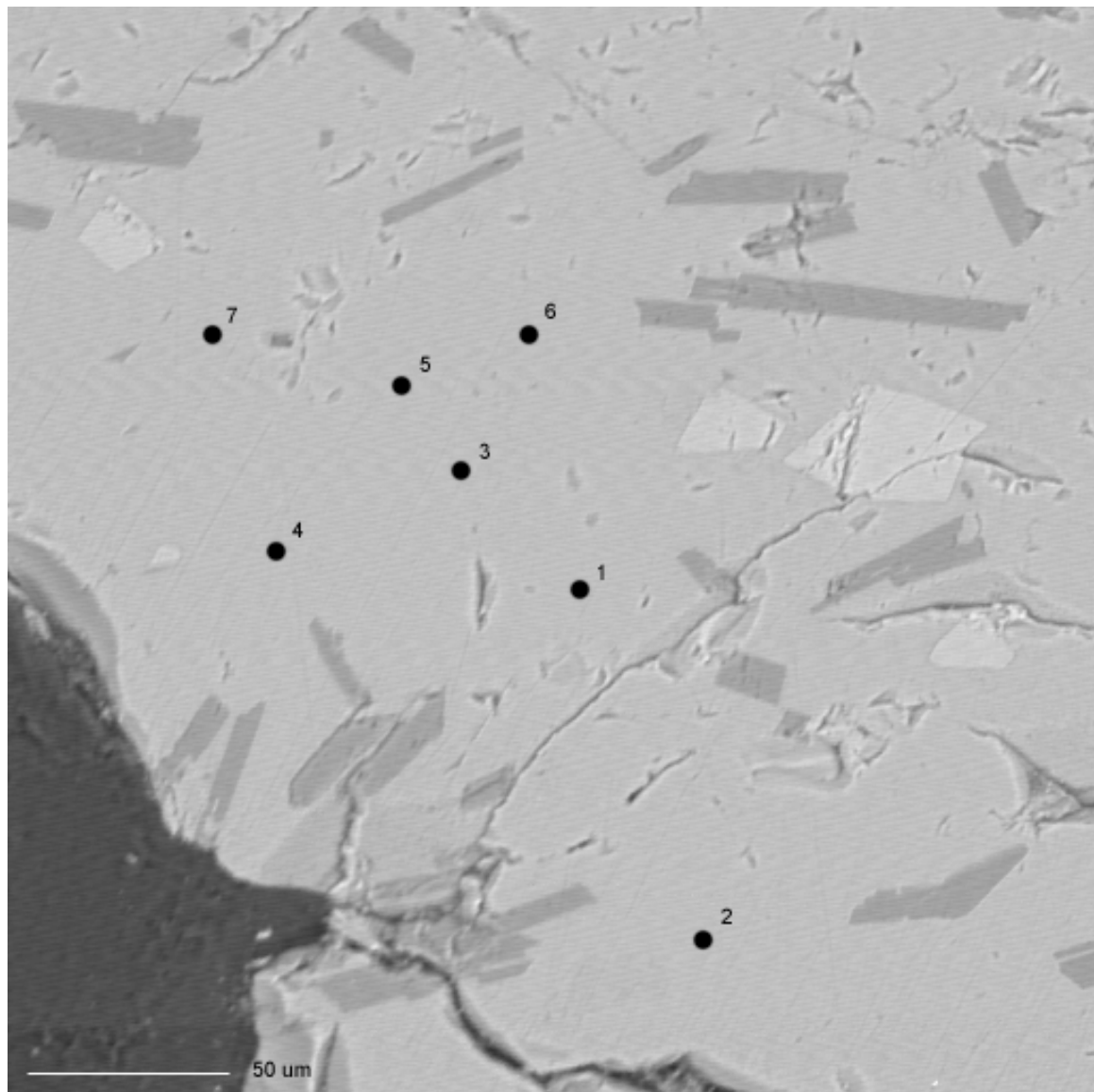
APPENDIX F

Equations for Determination of Mafic Disaggregation in Nevada

EQUATIONS FOR DETERMINATION OF MAFIC DISAGGREGATION IN

NEVADA

Darcy Flux of Mush-Originated Magma

The flux q of a volume of fluid per unit area per time is determined by Darcy's Law,

$$q = -K \frac{\partial h}{\partial x},$$ (F.1)

where K is hydraulic conductivity and h is hydraulic head. In order to determine q, which is this study is the flux of felsic magma from underneath the intruding basalt sheet upward, (F.1) needs to be arranged into a more meaningful description. Starting with (F.1), $k\,\rho g \mu^{-1}$—where k is permeability, ρ is density, g is gravitational acceleration, and μ is dynamic viscosity—can be substituted for K, yielding

$$q = k \frac{\rho g}{\mu} \frac{\partial h}{\partial x}$$ (F.2)

By assuming velocity head, a component of h, is zero, (F.2) becomes

$$q = k \frac{\rho g}{\mu} \frac{\partial \left(\frac{p}{\rho g} \right)}{\partial x},$$ (F.3)

where p is pressure, which simplifies to

$$q = \frac{k}{\mu} \frac{\partial p}{\partial x}$$ (F.4)

At this point, q is in a more intuitive arrangement for this system. k and μ may be obtained from the literature, but $\partial p / \partial x$ must be discovered through other means. In a magma chamber where a mafic layer with density ρ_2 and thickness h_2 intrudes felsic fluid with density ρ_1, and rides over a crystal mush with density ρ_3 (Figure F.1), and $\rho_2 > \rho_1$, felsic fluid from remelting of the underlying crystal mush is trapped beneath a more
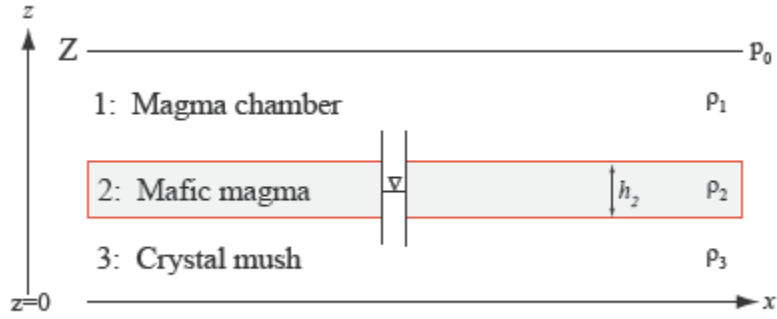
Figure F.1: Diagram of idealized Aztec Wash pluton during mafic sheet intrusion. Realistically, the *x*-axis is slightly inclined, a viscous sublayer exists between layers 2 and 3, and layer 2 is tapered toward the intrusion direction. Intrusion direction in this diagram is left to right.

dense material and wants to rise, resulting in a Rayleigh-Taylor instability. Concurrently, the weight of the intruding basalt sheet is pushing down on the felsic fluid, and the fluid migrates buoyantly upward as the mafic sheet sinks slightly, replacing the upper fluid layer on the mush. If we say that $\psi = Z - z$, where z is an arbitrary point within a layer, and we know that generally

$$\frac{\partial p}{\partial z} = -\rho g, \tag{F.5}$$

then the pressure p_1 in the upper portion of the magma chamber is

$$p_1 = p_0 + \rho_1 g \psi_1, \tag{F.6}$$

the pressure p_2 in the mafic sheet is

$$p_2 = p_1 + \rho_2 g \psi_2 \tag{F.7}$$

$$p_2 = p_0 + \rho_1 g (Z - h_2) + \rho_2 g \psi_2, \tag{F.8}$$

and the pressure p_3 in the crystal mush is

$$p_3 = p_1 + p_2 + \rho_3 g \psi_3 \tag{F.9}$$

$$p_3 = p_0 + \rho_1 g (Z - h_2) + \rho_2 g h_2 + \rho_3 g \psi_3 \tag{F.10}$$

At this point, $\rho_3 g \psi_3$ and p_0 are constants, and can be removed. Therefore, the change in p of the whole system is

$$\frac{\partial p}{\partial x} = -\rho_1 g \frac{\partial h_2}{\partial x} + \rho_2 g \frac{\partial h_2}{\partial x} \tag{F.11}$$

$$\frac{\partial p}{\partial x} = (\rho_2 - \rho_1)g\frac{\partial h_2}{\partial x} \tag{F.12}$$

Now that we have $\partial p/\partial x$, and we can obtain k and μ from the literature, q may be obtained. If ρ_2=2700 kg m^{-3}, ρ_1 =2200 kg m^{-3}, h_2=0.5 m, k=10^{-10} m^2 (estimated from values provided in Bachmann and Bergantz, 2003), and μ=10^5 Pa s,

$$q = 4.9 \times 10^{-14}\, m^3\, m^{-2}\, s^{-1}$$

Clearly, this is a vanishingly small flux, and plays no role in physically disaggregating basaltic sheets into isolated pillow-like structures. It is important, however, in delivering heated fluid up between the fingered basalt sheet and out by the edges of the sheet, which facilitates convection in the surrounding magma chamber.

Wavelength Determination of Finger Width

The following is followed from Snyder and Tait (1995). As basaltic sheets intrude a felsic magma chamber a flow-front instability analogous to a Saffman-Taylor instability develops, which allows the basalt sheet to split into "fingers". The finger width, λ, is determined by a Rayleigh-Taylor instability (as shown below) that results from having less-dense felsic magma overlain by more-dense basaltic magma. Seven independent variables describe this system: mafic and felsic densities (ρ_m and ρ_f) and dynamic viscosities (μ_m and μ_f)(which combine as ρ/μ to give v, the kinematic viscosity) , gravity g, flow rate Q, and height of the intruding sheet (h). According to Buckingham's Pi theorem, four independent, dimensionless variables are need to describe the system, in this case

$$\left(\frac{v_f}{v_m}\right), \left(\frac{\rho_m - \rho_f}{\rho_m}\right), \left(\frac{Q}{v_f}\right), and \left(\frac{Q}{\sqrt{(g'h^3)}}\right), \tag{F.13}$$

where g' is the reduced gravity, $g(\rho_m - \rho_f)/\rho_m$. These ratios are kinematic viscosity, dimensionless buoyancy, Reynold's number (Re), and the Froude number (Fr). These can be incorporated into a model that describes their influence on λ, such that

$$\frac{\lambda}{h} = \phi\left(\frac{v_f}{v_m}\right)^a \left(\frac{\rho_m - \rho_f}{\rho_m}\right)^b \left(\frac{Q}{v_f}\right)^c \left(\frac{Q}{\sqrt{(g'h^3)}}\right)^d \tag{F.14}$$

Based on experimental results, the viscosity ratio term is insignificant, and the buoyancy term cancels, which leaves

$$\lambda \propto h \left(\frac{\rho_m - \rho_f}{\rho_m} \right)^{1/4} \left(\frac{Q}{v_f} \right)^{-1/4} \left(\frac{Q}{\sqrt{(g'h^3)}} \right)^{1/2} \propto \left(\frac{v_f h Q}{g} \right)^{1/4}$$ (F.15)

Examination of this relationship shows a very weak time dependence, which, when combined with analysis done in a previous portion of Snyder and Tait (1995),

$$h = c_1 \left(\frac{\mu_f t Q^2}{\rho_m g'} \right)^{1/5},$$ (F.16)

yields (within the resolution of the data)

$$\left(\frac{v_f h Q}{g} \right)^{1/4} \propto \left(\frac{v_f Q}{g} \right)^{1/3}$$ (F.17)

$$\lambda = 17.2 \left(\frac{v_f Q}{g} \right)^{1/3}$$ (F.18)

Since this equation fits experimental data, they deduce that only one instability—Rayleigh-Taylor—selects finger width. Based on this scaling, a basalt sheet 10 m wide and 1 m thick injecting at a rate of 10 m/yr with a v_f=45.5 m^2 s^{-1} will develop fingers 0.4 m wide.

Intra-Chamber Convection Instigated by Mafic Magma Injection

Occurrence of convection can be assessed using the Rayleigh number,

$$Ra_c = \frac{g \alpha \Delta T \delta^3 \rho}{\kappa \mu}$$ (F.19)

where g is acceleration due to gravity, α is the coefficient of thermal expansion, ΔT is the temperature difference between the ambient felsic magma and the intruding basaltic magma, δ is the thickness of the thermal boundary layer (TBL), ρ is density, κ is the thermal diffusivity, and μ is the dynamic viscosity (Couch et al., 2001). In order to achieve convection in a system with one boundary (in this case, the crystal mush as the effective floor), the critical Rayleigh number, Ra_c, must be >1101 (D. Furbish, pers.com.,

2007). For conservative values (g=9.8 m s^{-2}, α=8.5 × 10^{-5} °C^{-1}, ΔT=100°C, δ=1.69 m, ρ =2200 kg m^{-3}, κ=8 × 10^{-7}, and μ=10^{5} Pa s), most notably for ΔT, of basaltic magma intruding a felsic magma chamber at Aztec Wash pluton, Ra_c=1105.7. In areas of the felsic magma chamber that do not underlie the basalt intrusion, convection will occur within 1.69 m of the intruding basalt sheet. With a larger ΔT, convection will occur faster.

δ, the thickness of the thermal boundary layer, may be calculated using

$$\delta = \sqrt{\kappa U} ,$$
(F.20)

where U is the rate of injection. Therefore, a basaltic sheet with U=10m/yr and κ=10^{-6} (estimate) yields a TBL whose thickness increases ~17.75 m/yr.

APPENDIX G

Results of Statistical Comparison of Iceland Glass Chemistry

RESULTS OF STATISTICAL COMPARISON OF ICELAND GLASS

CHEMISTRY

To assess the similarity of glasses gathered from Keldunúpur, Rauða Canyon, and Lomagnúpur, two statistical tests were used to compare the samples. A Student t-test was used when comparing lavas and hyaloclastites from within a location or when comparing one lithology at two locations. An ANOVA test was performed on each lithology to compare lavas and hyaloclastites at all three locations. Both methods were carried out using the built-in data analysis tools in Microsoft Excel. The results of these tests are listed below.

Table G1. t-test comparing lavas and hyaloclastites at Keldunúpur.

	SiO_2	P_2O_5	TiO_2	Al_2O_3	MgO	CaO	MnO	FeO	Na_2O	K_2O
Test Statistic	1.446	1.821	-0.343	-0.751	1.018	0.804	1.815	-1.722	-0.545	0.551
Critical 2-Tail t value	2.055	2.018	2.030	2.048	2.021	2.056	2.021	2.042	2.021	2.048
Outcome	Same	Same	Same	Same	Same	Same	Same	Same	Same	Same

Table G2. t-test comparing lavas and hyaloclastites at Rauða Canyon.

	SiO_2	P_2O_5	TiO_2	Al_2O_3	MgO	CaO	MnO	FeO	Na_2O	K_2O
Test Statistic	-2.654	-0.162	1.109	-1.537	2.858	-2.068	3.463	1.234	-0.463	2.151
Critical 2-Tail t value	2.007	2.028	2.042	2.060	2.045	2.032	2.006	2.052	2.040	2.056
Outcome	Different	Same	Same	Same	Different	Different	Different	Same	Same	Different

Table G3. t-test comparing lavas and hyaloclastites at Lomagnúpur.

	SiO_2	P_2O_5	TiO_2	Al_2O_3	MgO	CaO	MnO	FeO	Na_2O	K_2O
Test Statistic	-9.378	-38.554	-41.074	12.341	22.216	36.434	-7.014	-24.696	-13.583	-26.447
Critical 2-Tail t value	2.048	2.018	2.035	2.040	2.013	2.028	2.028	2.013	2.035	2.064
Outcome	Different	Different	Different	Different	Different	Different	Different	Different	Different	Different

Table G4. t-test comparing lavas at Keldunúpur and Rauða Canyon.

	SiO$_2$	P$_2$O$_5$	TiO$_2$	Al$_2$O$_3$	MgO	CaO	MnO	FeO	Na$_2$O	K$_2$O
Test Statistic	-3.926	-1.465	3.432	-2.260	-1.036	-5.580	0.362	5.165	3.592	0.406
Critical 2-Tail t value	2.037	2.011	2.015	2.056	2.020	2.024	2.012	2.035	2.026	2.052
Outcome	Different	Same	Different	Different	Same	Different	Same	Different	Different	Same

Table G5. t-test comparing hyaloclastites at Keldunúpur and Rauða Canyon.

	SiO$_2$	P$_2$O$_5$	TiO$_2$	Al$_2$O$_3$	MgO	CaO	MnO	FeO	Na$_2$O	K$_2$O
Test Statistic	0.548	0.417	2.463	-2.791	-4.387	-2.403	-1.276	3.794	8.021	-2.718
Critical 2-Tail t value	2.012	2.032	2.074	2.064	2.056	2.064	2.010	2.074	2.012	2.069
Outcome	Same	Same	Different	Different	Different	Different	Same	Different	Different	Different

Table G6. ANOVA comparing hyaloclastites at Keldunúpur, Rauða Canyon, and Lomagnúpur.

	SiO$_2$	P$_2$O$_5$	TiO$_2$	Al$_2$O$_3$	MgO	CaO	MnO	FeO	Na$_2$O	K$_2$O
F Test Statistic	20.291	9.536	32.945	3.393	14.628	54.072	3.036	12.600	26.276	34.142
Critical F value	3.120	3.120	3.120	3.120	3.120	3.120	3.120	3.120	3.120	3.120
Outcome	Different	Different	Different	Different	Different	Different	Same	Different	Different	Different

Table G7. ANOVA comparing lavas at Keldunúpur, Rauða Canyon, and Lomagnúpur.

	SiO$_2$	P$_2$O$_5$	TiO$_2$	Al$_2$O$_3$	MgO	CaO	MnO	FeO	Na$_2$O	K$_2$O
F Test Statistic	37.472	629.111	640.609	64.612	409.867	739.671	44.540	217.355	74.289	349.159
Critical F value	3.126	3.126	3.126	3.126	3.130	3.126	3.126	3.126	3.126	3.126
Outcome	Different	Different	Different	Different	Different	Different	Different	Different	Different	Different

REFERENCES

Bachmann, O. and Bergantz, G.W. 2003. Rejuvenation of the Fish Canyon magma body: A window into the evolution of large-volume silicic magma systems. *Geology* **31**: 789-792.

Batiza, R. and White, J.D.L. Submarine lavas and hyaloclastite, pp. 361-380 in *Encyclopedia of Volcanoes*: Academic Press, 2000.

Bergh, S.G. 1985. Structure, depositional environment and mode of emplacement of basaltic hyaloclastites and related lavas and sedimentary rocks: Plio-Pleistocene of the Eastern Volcanic rift zone, southern Iceland. PhD Dissertation, University of Iceland, Reykjavík, Iceland.

Bergh, S.G. and Sigvaldason, G.E. 1991. Pleistocene mass-flow deposits of basaltic hyaloclastite on a shallow submarine shelf. *Bulletin of Volcanology* **53**: 597-611.

Bleick, H.A. 2005. Production and redistribution of hybridized magma in a replenished, open-system magma chamber: Aztec Wash pluton Eldorado Mountains, Nevada. Master's thesis, Vanderbilt University, Nashville, TN, USA.

Cas, R.A.F. and Wright, J.V. Volcanic successions, modern and ancient: a geological approach to processes, products, and successions. London: Allen & Unwin, 1987.

Duffield, W.A., Bacon, C.R., and Delaney, P.T. 1986. Deformation of poorly consolidated sediment during shallow emplacement of a basalt sill, Coso Range, California. *Bulletin of Volcanology* **48**: 97-107.

Falkner, C.M., Miller, C.F., Wooden, J.L., and Heizler, M.T. 1995. Petrogenesis and tectonic significance of the calc-alkaline, bimodal Aztec Wash pluton, Eldorado Mountains, Colorado River extensional corridor. *Journal of Geophysical Research* **100**: 10,453-10,476,

Frolova, J., Ladygin, V., Franzson, H., Sigurðsson, Stefánsson, V., and Shustrov, V. 2005. Petrophysical properties of fresh to mildly altered hyaloclastite tuffs. Proceedings of the World Geothermal Congress, Antalya, Turkey, 24-29 April 2005: 1-15.

Gass, I.G. 1968. Pillow Lavas. *Transactions of the Leeds Geological Association* **7,** Ninety-fourth session: 251-260.

Ghiorso, M.S. and Sack, R.O. 1995. Chemical mass transfer in magmatic processes. IV. A revised and internally consistent thermodynamic model for the interpolation and extrapolation of liquid-solid equilibria in magmatic systems at elevated

temperatures and pressures. *Contributions to Mineralogy and Petrology* **119**: 197-212.

Harper, B.E., Miller, C.F., Koteas, G.C., Cates, N.L., Wiebe, R.A., Lazzareschi, D.S., and Cribb, J.W. 2004. Granites, dynamic magma chamber processes and pluton construction: the Aztec Wash pluton, Eldorado Mountains, Nevada, USA. *Transactions of the Royal Society of Edinburgh: Earth Sciences* **95**: 277-295.

Hawkins, D.P. and Wiebe, R.A. 2004. Discrete stoping events in granite plutons: A signature of eruptions from silicic magma chambers? *Geology* **32**: 1021-1024.

Luo, Y. and Ayers, J.C. 2007. Instructions for in-situ LA-ICP-MS analysis, Version 2. Vanderbilt University Dept. of Earth and Environmental Sciences.

Metrich, N., Sigurdsson, H., Meyer, P.S., and Devine, J.D. 1991. The 1783 Lakagigar eruption in Iceland: geochemistry, CO_2 and sulfur degassing. *Contributions to Mineralogy and Petrology* **107**: 435-447.

Miller, C.F. and Miller, J.S. 2002. Contrasting stratified plutons exposed in tilt blocks, Eldorado Mountains, Colorado River Rift, NV, USA. *Lithos* **61**: 209-224.

Moore, J.G. 1975. Mechanism of Formation of Pillow Lava. *American Scientist* **63**: 269-277.

Noe-Nygaard, A. 1940. Sub-glacial volcanic activity in ancient and recent times. *Folia Geographica Danica* **1**: 5-65.

Pallister, J.S., Hoblitt, R.P., and Reyes, A.G. 1992. A basalt trigger for the 1991 eruptions of Pinatubo Volcano? *Nature* 356: 426-428.

Parker, G. 2000. Hydroplaning outrunner blocks from auto-acephalated subaqueous debris flows and landslides, *Eos* Transactions, AGU, 81(48), Fall Meet. Suppl., Abstract OS51D-08.

Patrick, D.W., and Miller, C.F. 1997. Processes in a composite, recharging magma chamber: evidence from magmatic structures in the Aztec Wash pluton, Nevada: Proceedings of the 30th International Geological Congress **30** (15), pp. 121-135.

Paterson, L. 1985. Fingering with miscible fluids in a Hele Shaw cell. *Physics of Fluids* **28**: 26-30.

Pearce N.J.G., Perkins W.T., Westgate J.A., Gorton M.P., Jackson S.E., Neal C.R. and Chenery S.P. 1997. A compilation of new and published major and trace element data for NIST SRM 610 and NIST SRM 612 glass reference materials. *Geostandards Newsletter: The Journal of Geostandards and Geoanalysis* **21**: 115-144.

Perrault, D.S. 2006. Giant country rock blocks within Searchlight pluton, southern Nevada. Master's thesis, Vanderbilt University, Nashville, TN, USA.

Sigmundsson, F. 1991. Post-glacial rebound and asthenosphere viscosity in Iceland. *Geophysical Research Letters* **18**: 1131-1134.

Skilling, I.P., White, J.D.L., and McPhie, J. 2002. Peperite: a review of magma-sediemnt mingling. *Journal of Volcanology and Geothermal Research* **114**: 1-17.

Smellie, J.L. Subglacial eruptions. pp.403-417 in *Encyclopedia of Volcanoes*: Academic Press, 2000.

Smellie, J.L. 2008. Basaltic subglacial sheet-like sequences: evidence for two types with different implications for the inferred thickness of associated ice. *Earth Science Reviews*: DOI 10.1016/j.earscirev.2008.01.004.

Snyder, D. and Tait, S. 1995. Replenishment of magma chambers: comparison of fluid-mechanic experiments with field relations. *Contributions to Mineralogy and Petrology* **122**: 230-240.

Snyder, D. and Tait, S. 1998. A flow-front instability in viscous gravity currents. *Journal of Fluid Mechanics* **369**: 1-21.

Sparks, R.S.J. and Sigurdsson, H. 1977. Magma mixing: a mechanism for triggering acid explosive eruptions. *Nature* **267**: 315-318.

Sparks, R.S.J. and Marshall, L.A. 1986. Thermal and mechanical constraints on mixing between mafic and silicic magmas. *Journal of Volcanology and Geothermal Research* **29**: 99-124.

Squire, R.J. and McPhie, J. 2002. Characteristics and origin of peperite involving coarse-grained host sediment. *Journal of Volcanology and Geothermal Research* **114**: 45-61.

Stroncik, N.A. and Schmincke, H.-U. 2001. Evolution of palagonite: Crystallization, chemical changes, and element budget. *Geochemistry Geophysics Geosystems* **2**, Paper number 2000GC000102.

Thordarson, T. and Höskuldsson, Á. *Classic Geology in Europe 3: Iceland*. Hertfordshire, England: Terra Publishing, 2002.

Walker, G.P.L. and Blake, D.H. 1966. The formation of a palagonite breccia mass beneath a valley glacier in Iceland. *Quarterly Journal of the Geological Society of London* **122**: 45-61.

Walker, G.P.L. 1992. Morphometric study of pillow-size spectrum among pillow lavas. *Bulletin of Volcanology* **54**: 459-474.

White, J.D.L. and Houghton, B.F. 2006. Primary volcaniclastic rocks. *Geology* **34**: 677-680.

Whitehead, J.A. 1988. Fluid models of geological hotspots. *Annual Reviews of Fluid Mechanics* **20**: 61-87.

Whitehead, J.A. and Luther, D.S. 1975. Dynamics of laboratory diapir and plume models. *Journal of Geological Research* **80**: 705-717.

Wiebe, R.A. 1994. Silicic magma chambers as traps for basaltic magmas; the Cadillac Mountain intrusive complex, Mount Desert Island, Maine. *Journal of Geology* **102**: 423-437.

Wiebe, R.A. 1996. Mafic-silicic layered intrusions: the role of basaltic injections on magmatic processes and the evolution of silicic magma chambers. *Transactions of the Royal Society of Edinburgh: Earth Sciences* **87**: 233-242.

Wiebe, R.A., Frey, H., and Hawkins, D.P. 2001. Basaltic pillow mounds in the Vinalhaven intrusion, Maine. *Journal of Volcanology and Geothermal Research* **107**: 171-184.

Younes, A.I. and Engelder, T. 1999. Fringe cracks: Key structures for the interpretation of progressive Alleghanian deformation of the Appalachian plateau. *GSA Bulletin* **111**: 219-239.